UNIVERSITY OF IOANNINA
SCHOOL OF SCIENCE
DEPARTMENT OF MATERIALS SCIENCE AND ENGINEERING

Wide-band gap semiconductors with noble metals for photonic applications

ANASTASIOS K. SIOZIOS

Doctoral Dissertation

IOANNINA 2015

UNIVERSITY OF IOANNINA
SCHOOL OF SCIENCE
DEPARTMENT OF MATERIALS SCIENCE AND ENGINEERING

Wide-band gap semiconductors with noble metals for photonic applications

ANASTASIOS K. SIOZIOS

Doctoral Dissertation

IOANNINA 2015

«Η έγκριση της διδακτορικής διατριβής από το Τμήμα Μηχανικών Επιστήμης Υλικών της Σχολής Θετικών Επιστημών του Πανεπιστημίου Ιωαννίνων δεν υποδηλώνει αποδοχή των γνωμών του συγγραφέα Ν. 5343/32, άρθρο 202, παράγραφος 2».

Ημερομηνία αίτησης του κ. Σιώζιου Αναστάσιου: 13.02.2009

Ημερομηνία ορισμού Τριμελούς Συμβουλευτικής Επιτροπής: **06.03.2009**

Μέλη Τριμελούς Συμβουλευτικής Επιτροπής:

Επιβλέπων: **Παναγιώτης Πατσαλάς,** Επίκουρος Καθηγητής του ΤΜΕΥ της Σχολής

Επιστημών & Τεχνολογιών του Παν/μίου Ιωαννίνων

Μέλη: **Απόστολος Αυγερόπουλος,** Επίκουρος Καθηγητής του ΤΜΕΥ της Σχολής

Επιστημών & Τεχνολογιών του Παν/μίου Ιωαννίνων

Gregory Abadias, Καθηγητής του University Poitiers της Γαλλίας.

Ημερομηνία ορισμού θέματος: **06.03.2009**

"Νανοσύνθετα Υμένια Μήτρας Ημιαγωγών Ευρέως Χάσματος με Εγκλείσματα Μετάλλων για Φωτονικές Εφαρμογές"

Ημερομηνία Ανασυγκρότησης Τριμελούς Συμβουλευτικής Επιτροπής: **24.04.2013**

Μέλη Τριμελούς Συμβουλευτικής Επιτροπής:

Επιβλέπων: **Απόστολος Αυγερόπουλος,** Αναπληρωτής Καθηγητής του ΤΜΕΥ της Σ.Θ.Ε. του Παν/μίου Ιωαννίνων.

Μέλη: **Παναγιώτης Πατσαλάς,** Αναπληρωτής Καθηγητής του Τμήματος Φυσικής της Σ.Θ.Ε. του Α.Π.Θ.

Gregory Abadias, Καθηγητής του University Poitiers της Γαλλίας.

ΔΙΟΡΙΣΜΟΣ ΕΠΤΑΜΕΛΟΥΣ ΕΞΕΤΑΣΤΙΚΗΣ ΕΠΙΤΡΟΠΗΣ : 12.11.2013

1. **Απόστολος Αυγερόπουλος,** Καθηγητής του ΤΜΕΥ της Σ.Θ.Ε. του Παν/μίου Ιωαννίνων
2. **Gregory Abadias,** Καθηγητής του University Poitiers της Γαλλίας
3. **Κων/νος Κοσμίδης,** Καθηγητής του Τμήματος Φυσικής της Σ.Θ.Ε. του Παν/μίου Ιωαννίνων
4. **Γεώργιος Ευαγγελάκης,** Καθηγητής του Τμήματος Φυσικής της Σ.Θ.Ε. του Παν/μίου Ιωαννίνων
5. **Δημοσθένης Κουτσογεώργης,** Αναπληρωτής Καθηγητής του College of Arts and Science, School of Science and Technology, Physics and Mathematics του Παν/μίου Nottingham Trent του Ηνωμένου Βασιλείου.
6. **Παναγιώτης Πατσαλάς,** Αναπληρωτής Καθηγητής του Τμήματος Φυσικής της Σ.Θ.Ε. του Α.Π.Θ.
7. **Ελευθέριος Λοιδωρίκης,** Καθηγητής του ΤΜΕΥ της Σ.Θ.Ε. του Παν/μίου Ιωαννίνων

Έγκριση Διδακτορικής Διατριβής με βαθμό **«ΑΡΙΣΤΑ»** στις **28.08.2014**

Ο Πρόεδρος του Τμήματος	**Η Γραμματέας του Τμήματος**
Καρακασίδης Μιχαήλ **Καθηγητής**	**Ξανθή Τουτουνζόγλου**

PREFACE

This thesis focuses in the growth and characterization of the structural, morphological and optical properties of nanocomposite films consisting of transparent, hard and inorganic matrices with metal inclusion which are suitable candidates in photonics for light manipulation, antireflection coatings, color patterning etc.

Within PhD framework nanocomposite binary and ternary systems consisting of III-nitrides matrices (AlN, $Al_{1-x}In_xN$) with silver inclusions were carried out by means of two widespread PVD techniques, Pulsed Laser Deposition (PLD) and Reactive Magnetron Sputtering (RMS). In particular in case of binary systems three different approaches were considered:

i) Nanocomposite films consisting of AlN matrix with silver nanoparticles

ii) Co sputtered AlN:Ag where Ag was atomically dispersed

iii) Multilayers of alternative thin AlN and Ag layers

On the contrary in case of ternary systems pure Al-rich $Al_{1-x}In_xN$ and nanocomposite $Al_{1-x}In_xN$/Ag were grown respectively.

The as grown films were subjected in both thermal annealing and UV-laser annealing, a new very promising technique, in an effort to understand their self-organization and optical properties due to the different mechanisms that occurs

On the other hand the optical properties of Ag, as our inclusions, were prerequisite in order to understand the optical properties of the nanocomposite films. Thus, the optical properties of laser annealed thin silver films grown by magnetron sputtering was also studied in this thesis

The structural and compositional characterization of the samples was performed by X-Ray Diffraction (XRD) and X-ray Photoelectron Spectroscopy (XPS) technique respectively, while X-Ray Reflectivity (XRR), Electron Microscopy (SEM, TEM) and Atomic Force Microscopy (AFM) measurements were performed for the morphological features of the samples.

The alterations of the optical properties of the samples were investigated by Optical Reflectance Spectroscopy (ORS) measurements.

TABLE OF CONTENTS

ACKNOWLEDGEMENTS

I would like to thank all the people whose contribution was crucial for the completion of my PhD thesis.

First of all I would like to thank my advisor Assoc. Prof. P. Patsalas for the award of this topic and his guidance on the approach, analysis and optimization of the experimental results as well as for funding a financial support through the Irakleitos II program.

I would like to express my thanks to Prof. A. Avgeropoulos and Prof. G. Abadias, member of the consultant committee, for their efforts and time they devoted in reading and commenting this thesis.

My special thanks to Sen. Lec. D.C. Koutsogeorgis who introduced me in laser annealing technique during my visit to Nottingham Trent University through Life Long Learning Programme/Erasmus LLP of the International and Public Relations Directorate of the University of Ioannina. My collaboration with him was special.

I would like to express my thank to Assoc. Prof. E. Lidorikis for his thorough discussion regarding the optical properties of solids and light-matter interactions as well as their FDTD simulations in order to support the experimental results.

I would also like to thank Prof. G.A. Evangelakis for his cooperation throughout my PhD thesis and for his confidence showed on me during the experiments and the analysis that took place in the thin films lab of the physics department.

I would like to gratitude Dr. D. Anagnostopoulos for his contribution on this PhD thesis although he wasn't directly involved as well as the cooperation we had during my master and undergraduate thesis.

I would also like to thank Pr. C. Kosmidis and the laser facility of Physics department of the University of Ioannina for providing the Nd:YaG laser source for the needs of the pulsed laser deposition techniques, as well as, Dr. Spyros Kaziannis for the operation of laser sources.

I would like to express my thank to Assoc. Prof. G. Dimitrakopoulos for the TEM observations which had a significant role in understanding the effect of laser annealing in the structural properties of the nanocomposite films of this thesis.

I would like to thanks Dr. N. Kalfagiannis for the excellent cooperation throughout this PhD thesis in various subjects as well as for the AFM measurements in the pure Ag thin films after laser annealing.

I would like to express my cordial thanks to Dr. Matenoglou, Dr. Koutsokeras and Dr. Panagiotopoulos for their contribution in my familiarity with experimental techniques such as Magnetron Sputtering, PLD, XRD, XPS, SEM and data analysis.

I would like to thank Dr. H. Zoubos for providing me some of his AlN:Ag nanocomposite films in order to study the effect of the laser annealing.

I would also like to thank PhD candidate D. Bellas for his contribution in this thesis through FDTD simulation and PhD candidate N. Pliatsikas for providing me XPS depth profiling measurements when it was needed and the tandem we had all these year.

Finally, I want to attribute my extent gratitude to my family for providing me the chance to continue my education and for their endless support all these years of my studies.

This research has been co-financed by the European Union (European Social Fund – ESF) and Greek national funds through the Operational Program "Education and Lifelong Learning" of the National Strategic Reference Framework (NSRF) - Research Funding Program: Heracleitus II. Investing in knowledge society through the European Social Fund.

List of Publications

1. "*Optical Encoding by Plasmon-Based Patterning: Hard and Inorganic Materials Become Photosensitive*"
A. Siozios, D.C. Koutsogeorgis et al. Nanoletters 12 (1), pp. 259-263 (2012).

2. "*Growth and annealing strategies to control the microstructure of AlN:Ag nanocomposite films for plasmonic applications*"
A.Siozios, H. Zoubos et al., Surface and Coating technology 225, pp. 28-36 (2014).

3. "*Influence of laser annealing on the structural properties of sputtered AlN:Ag plasmonic nanocomposites*" ,
Bazioti, C, Dimitrakopulos, G.P, … , **A.Siozios** et al. , Journal of Materials Science 49 (11), Pages 3996-4006. (2014).

4. "*Sub-surface laser nanostructuring in stratified metal/dielectric media: a versatile platform towards flexible, durable and large-scale plasmonic writing*".
A. Siozios, N. Kalfagiannis, D. Bellas et al. Nanotechnology 26,155301 (2015)

5. "*Laser-matter interactions, phase changes and diffusion phenomena during laser annealing of plasmonic AlN:Ag templates and their applications in optical encoding*".
A. Siozios, D.C. Koutsogeorgis et al. **submitted (2015)**

6. "Selective Modification of Nanoparticle Arrays by Laser-Induced Self Assembly *(MONA-LISA): putting control into bottom-up plasmonic nanostructuring*"
N. Kalfagiannis, **A. Siozios** et al. **submitted (2015).**

INTRODUCTION

Entry into the 21st century revealed new requirements into materials sciences as new applications and technologies were developed and thus materials with new improved properties, or predefined some times, required.

These requirements led the scientific community on develop and continued study of nanocomposite materials in order to yield the desired properties in each case. Therefore an important and rapidly growing chapter *Nanotechnology* was created.

Part of this huge chapter is this PhD thesis where the growth of nanocomposite films consisting of a semiconductor matrix with metal inclusions is attempted.

Although this kind of nanocomposite films have been studied in depth the last decades, however this study revealed results that reported for first time in the literature.

The materials grown in this thesis target in optical applications such color pattering, optical encoding (overt or covert), waveguides, optical sensors etc. , so the optical properties is mainly investigated while at the same time a correlation with the structural features is attempted.

Aim of thesis

Aim of this study is the growth of nanocomposite films consisting of a semiconductor matrix with metal inclusions. These materials are candidates for photonic applications based on the Surface Plasmon Resonance manifestation that the metallic phase exhibits. Furthermore, the inorganic, hard semiconductor host gives extra stability and strength so that they can be used even in the most demanding applications such as aerospace.

Materials Involved

The materials involved in this PhD framework can categorized into two sections:

- Materials that used for the matrix
- Materials that used as inclusions.

In the first section, III- nitride semiconductors (Figure 1) were used as matrix materials, in binary or ternary systems, due to their exceptional optical properties. Specifically, AlN was the main candidate for the binary systems while AlInN alloys were grown as a case study of ternary compounds.

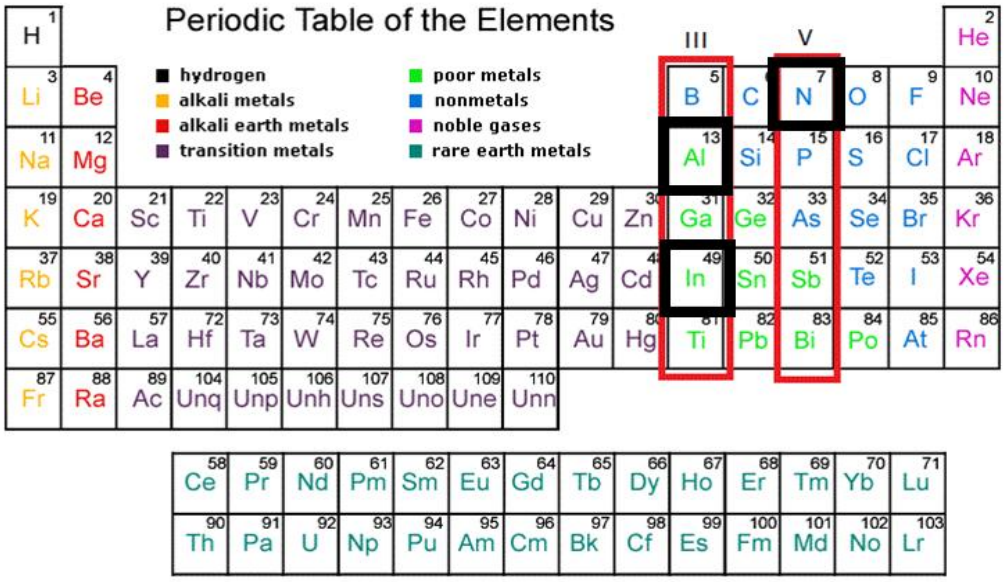

Figure 1.1. Periodic Table of elements.

Aluminum nitride (AlN) is an interesting optical material due to its wide direct band gap (E_g=6.2eV) [1,2] which exhibits absorption in the far UV spectral range, while being totally transparent in the visible spectral region and having refractive index n=2 [2]. In addition, it has excellent physical properties such as high melting point (2200 ^{o}C) [3] and thermal conductivity (285 $Wm^{-1}K^{-1}$)[4], mechanical properties and substantial chemical and metallurgical stability, making it suitable for various applications in coatings' industry as antireflective coatings[5], protective coating[6,7], opto-electronic devices[8] and in surface acoustic waves (SAW)[6].

Structurally, AlN crystallizes, in equilibrium conditions, in the *Hexagonal Wurtzite* (HCP) structure (Figure 2) while there are cases where a totally amorphous AlN has been grown in numerous works.

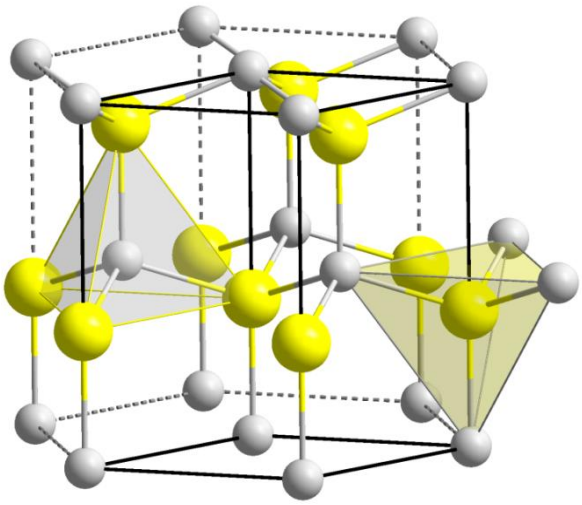

Figure 1.2. Schematic illustration of wurtzite structure.

Indium nitride (InN) is a narrow direct band gap with (E_g= 0.77eV) [9] group-III nitride semiconductor, optical denser that AlN (n=2.95) [10], which crystallizes in the same crystal structure with Aluminum Nitride. It displays high electron mobility (3200 $cm^2V^{-1}s^{-1}$) [11] low thermal conductivity (45 $Wm^{-1}K^{-1}$) [12] and melting point (1100^{o}C) [13] respectively. Due to these optical and physical properties InN presents enormous potential for device applications such as near-infrared optoelectronics [15], high-efficiency solar cells [14], and high-speed electronics [16]. The structural and optical parameters of both AlN and InN respectively are provided in table I.

The structural relevance that AlN and InN showing to each other allows their mixture and the creation of solid solutions $Al_{1-x}In_xN$.

Table I. Structural Physical and Optical properties of the involved materials.

	Materials		Units (SI)
	AlN	InN	
Structural Properties			
Crystal structure	Wurtzite	Wurtzite	-
Lattice constant a_0	0.311	0.354	nm
Lattice constant c_0	0.498	0.570	nm
Lattice mismatch a_0	-13.82 %		-
Lattice mismatch c_0	-14.45 %		-
Physical Properties			
Melting Point	2200	1100	^oC
Thermal Conductivity	285	45	$Wm^{-1}K^{-1}$
Optical Properties			
Gap	Direct	Direct	-
Bandgap Energy (E_g)	6.2	0.77	eV
Refractive index (n)	1.9-2.1	2.95	
Absorption coefficient (α)	$3x10^{-5}$	$0.6x10^{-5}$	cm^{-1}
Relative dielectric constant (ε_r)	8.5	15.3	-
Electron mobility	300	3200	$cm^2V^{-1}s^{-1}$
Mechanical Properties			
Density	3.26	6.81	$grcm^{-3}$
Elastic Modulus	330		GPa
Hardness	1100		Kg/mm^2

This ternary compounds constitute a new, very promising field as by varying the compositions between AlN and InN respectively we can tune the optical parameters such as the optical band gap without important differences in the structural parameters as it is clearly observed in figure 3. However the lattice mismatch of AlN and InN (-14.45% at c axes) makes $Al_{1-x}In_xN$ rather unstable at high temperatures and spinodul decomposition may occurs [17].

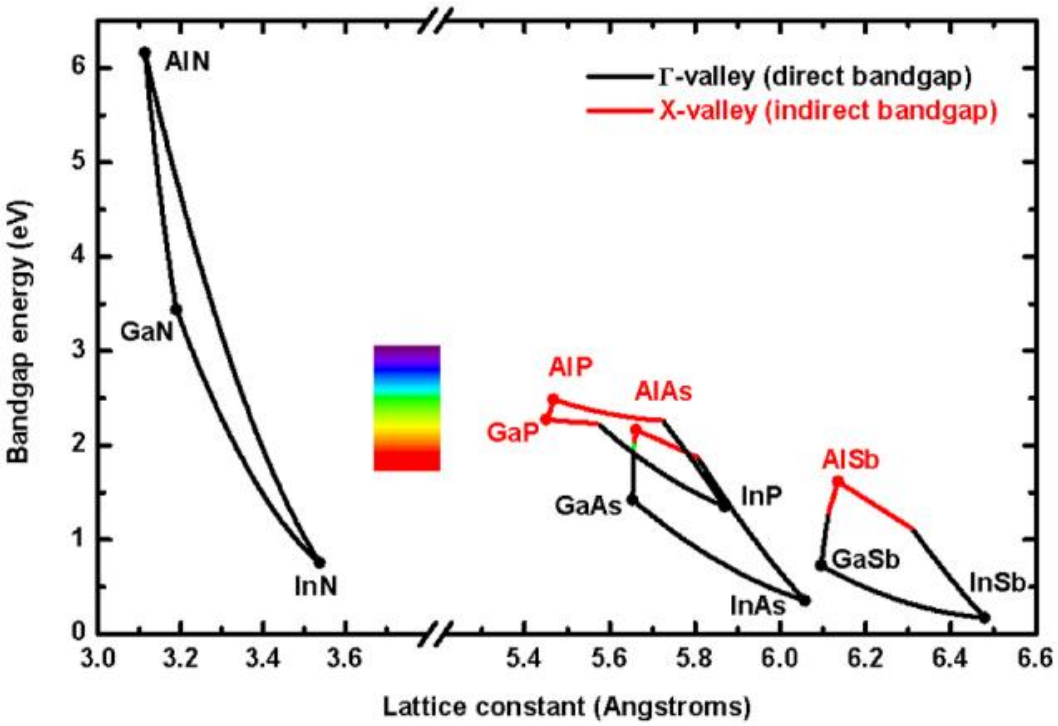

Figure 1.3. Optical band gap with respect to the lattice constant for III-V compound semiconductors and their alloys [18]

On the other hand, silver (Ag) was used as phase dispersion into the transparent matrix in both binary and ternary systems while the optical properties of Ag were an individual field of research in this PhD thesis. Silver is a well known material and of metals, is considered a very promising candidate for PNPs, due to its stability when formed into nanoparticles and its strong LSPR absorption bands in the visible region of the spectrum [19-27].

Thesis Outline

This thesis is composed of seven chapters from which the first three are the theoretical and technical background needed in order to be able to extract the results obtained from the analysis of the experimental data.

Specifically, Chapter 1 is referred to the optical properties of materials in the nanoscale. Drude and Lorentz models are presenting while a discussion about light matter interactions is performed presenting the key points.

Chapter 2 is devoted to thin film growth techniques that were used in the framework of this PhD. Sputtering technology is discussed in depth, presenting the basic modes that can be used while the growth of thin films and the influence of the deposition parameters are presented. Finally, Pulsed Laser Deposition (PLD) technique (instrumentation and principles) are discussed. In particular various laser sources used in our days are presented as well as the effect of various laser parameters.

In Chapter 3 an overview of the characterization methods employed in this study is provided focusing on the basic principles of each technique. In particular, structural and morphological characterization techniques such as X-ray diffraction (XRD), X-ray reflectivity (XRR) and X-ray Photoelectron spectroscopy (XPS) Scanning Electron Microscopy (SEM), Transmission Electron Microscopy (TEM) and Atomic Force Microscopy (AFM) are also presented.

Subsequently, chapters 4, chapter5 and chapter 6 are the experimental part of the PhD where the results and the analysis that took place are presenting in detail.

Chapter 4 provides a detailed analysis of the optical properties of silver thin films that have been subjected to UV-laser annealing. A correlation of LSPR with various processing parameters is attempted.

Chapter 5 is the main core of this thesis, three different formations of AlN:Ag systems are discussed. The initial formation consists from Ag nanoparticles embedded into AlN host by alternating PLD of Al and Ag in N_2 ambient. The second formation corresponds to Ag which is finely dispersed into AlN matrix of various crystallinities by sputter co-deposition of Al and Ag in Ar/N_2 plasma. Finally, multilayers of alternative ceramic (AlN) and metal (Ag) layers respectively are studied.

Ternary $Al_{1-x}In_xN$ alloys are studied in chapter 6 with In concentration x varying in the range 0%at <x< 20%at. The structural and optical features of the films are studying in terms of different In compositions, whereas the effect of the In concentration in the LSPR behavior is also investigating.

Finally, PhD thesis ends with a combined summary and outlook in chapter 7.

References

[1] Christensen, N.E., Gorczyca, I. , *Phys. Review B*, **50** (1994), pp 4397-4415.

[2] Baek J., Ma J., *et al., Thin Solid Films* **515** (2007), pp. 7096–7104.

[3] MacChesney, J.B., Bridenbaugh, P.M., O'Connor, P.B, *Mater.Res. Bul.* **5**(1970), pp. 783-791.

[4] Slack, G.A., Tanzilli, R.A., et al., *J. Phys. Chem. Sol.*, **48** (1987), pp. 641-647.

[5] Claudio G., Kaminski P., and Bass K., *Phys. Stat. Sol. C*, **6** (2009), pp. 2665–2667.

[6] Belyanin, A.F. Bouilov, L.L. *et al., Diam. Relat. Mater.*, **8** (1999), pp. 369-372.

[7] Godpole V.P., Narayan J., *Mater. Scien. Engin. B*, **39**, (1996), pp. 153-159.

[8] Taniyasu Y, Kasu M., Makimoto T, *Nature*, **441** (2006),pp 325-328.

[9] V. Yu. Davydov1, A. A. Klochikhin, R. P. Seisyan, *et al., Phys. Stat. Sol. B,* **229**, R1-R3.

[10] Djurišić, A.B. , Li, E.H , *J. App. Phys*. **85** (1999), pp. 2848-2853.

[11] Tansley, T.L., Foley, C.P., *J. App. Phys.*, **59** (1986), pp. 3241-3244.

[12] Krukowski, S. Witek, A., *et al*., J. Phys. Chem. Sol., **59** (1998), pp. 289-295.

[13] MacChesney J.B., Bridenbaugh P.M. *et al., Mat. Res. Bulletin*, **5** (1970), pp 783-792.

[14] Neil, M.E., Bamett, A.M., *IEEE Trans. Electron. Devices*, 1987, ED-34,257.

[15] Nakamura, S., Senoh, M., *et al., Jpn. J. Appl.* Phys., **34** (1995), L1332.

[16] Oseki M., Okubo K., *et al.*, *Scientific Reports* 4 (2014), article number 3951

[17] Mayrhofer H.P., Hultman L., et al., Intern. Journ. Mater. Resear.98 (2007), pp. 1054-1059.

[18] Zhu D., Wallis D. J., Humphreys C. J., *Rep. Prog. Phys*. **76** (2013) 106501 (31pp).

[19] Bohren C.F., Huffman D.R., *Absorption and scattering of light by small particles*, Wiley Interscience, New York (1983).

[20] Genzel L., Martin T.P., Kreibig U., *Z. Physic B*, **21** (1975), pp.339-346.

[21] Little S. A., Collins R. W., Marsillac S., App. Phys. Lett. **98** (2011), pp. 101910_1-3.

[22] Marsillac S., Little S.A., Collins R.W., *Thin Solid Films*, **519** (2011), pp.2936–2940.

[23] Kreibig U, Genzel .L., *Surface Science*, **156** (1985), pp. 678-700.

[24] Lance Kelly K., Coronado E., *et al., J. Phys. Chem. B,* ***107*** (2003),pp. 668-677.

[25] Moores A., Goettmann F., *New J. Chem.*, **30** (2006), pp.1121–1132.

[26] F. Stietz, *Appl. Phys. A*, **72** (2001), pp. 381–394.

[27] Tomchuk P. M., Tomchuk B. P., *JETP* **85** (1997), pp. 360-369.

Chapter 1 *OPTICAL PROPERTIES OF NANOSTRUCTURED MATERIALS*

1.1 Introduction

The development of nanotechnology has led in utilization of nanoscale materials e.g. metals or semiconductors in a wide variety of applications, such as biosensors [1.1-1.3, 1.22], protective coatings [1.4], antireflection coatings [1.5], opto-electronics [1.6, 1.7] *etc*. based on different properties that these materials present when in nanoscale dimensions. Of special interest are the optical properties which might be extraordinarily different in the nanoscale, because of the LSPR in metal nanoparticles and of the quantum confinement effects in semiconductor quantum dots.

Firstly, we present the classical Drude-Lorentz models that describe the intraband and interband transitions, respectively, as the starting point of understanding the optical properties of the nanomaterials. Then, we briefly review the individual light-matter interactions for semiconductors and nanomaterials.

1.2 Lorentz Oscillator-Dielectric Function

Lorentz model, which used to describe the electrons that are bound to the nuclei in semiconductors and insulators, can easily be compared with a small mass atom which is connected to another one with bigger mass using a linear spring, i.e it is based on the description of the equations of motion of an electron under light illumination as a harmonic oscillator.

In that case and under a electromagnetic wave the atom will act as an electric dipole and the electron cloud, until that moment is evenly distributed around the nuclei, will shifted, for example at a distance r.

Then electron motion can be described using the equation:

$$m\frac{d^2r}{dt^2} + m\gamma\frac{dr}{dt} + m\omega_0^2\, r = -eE_{loc} \qquad (1.1)$$

where E_{loc} the local electric field, the second term represents a viscous damping and provides for an energy loss mechanism, γ the damping constant and the third term of the equation is a restore force from Hooke's law while the first term is the Newton's second law.

In order the equation 1.1 to be valid, two assumptions should be fulfilled: Firstly that the nuclei mass is infinite compared to the electron mass therefore being still even within the field, and secondly that the electron motion is not affected from the electromagnetic field.

Considering that the electron cloud shift is altered harmonically by time, that means that $\vec{E} = \vec{E}e^{-i\omega t}$ and $\vec{r} = \vec{r}e^{-i\omega t}$, we can rewrite the equation 1.1 as:

$$m\omega^2\vec{r} - im\omega\gamma\vec{r} + m\omega_0^2\vec{r} = -e\vec{E} \quad (1.2)$$

and

$$\|\vec{r}\| = \frac{-eE/m}{\omega_0^2 - \omega^2 - i\gamma\omega} \quad (1.3)$$

Then the dipole is described from the equation:

$$\vec{p} = -e\vec{r} \xrightarrow{(1.3)} \vec{p} = \frac{e^2\vec{E}}{m}\frac{1}{(\omega_0^2 - \omega^2) - i\gamma\omega} \quad (1.4)$$

Assuming that that the oscillator is in the linear region (i.e. for small electric fields such as those of usual light sources-not lasers) we can write:

$$\vec{p} = \alpha(\omega)E \quad (1.5)$$

where $\alpha(\omega)$ is the atomic polarizability

$$\alpha = \frac{e^2}{m}\frac{1}{\omega_0^2 - \omega^2 - i\gamma\omega} \quad (1.6)$$

If there are N atoms per volume unity then we can write:

$$P = N < p >= NaE = x_e E \quad (1.7)$$

where P is the macroscopic polarization, $< p >$ is the dipole moment and x_e is the electrical permittivity.

We can now determine the dielectric function (Eqn 1.8):

$$D = \varepsilon E = E + 4\pi P = (1 + 4\pi\chi_e)\vec{E} \quad \rightarrow \quad \varepsilon(\omega) = 1 + 4\pi\chi_e(\omega) \quad \rightarrow$$

$$\varepsilon = 1 + \frac{4\pi Ne^2}{m}\sum_j \frac{N_j}{\omega_j^2 - \omega^2 - i\gamma_j\omega} \qquad \text{where } \sum_j N_j = N \qquad (1.8)$$

where j is the number of the oscillators, ω_j is the resonant frequency , γ_j the dumping factor for each oscillator and $\sum_j N_J$ the sum of density of electrons.

A detailed analysis of the light-matter interaction using the Maxwell's macroscopic equations leads to the equations:

$$\varepsilon_1 = \frac{n^2 - k^2}{\mu} \qquad (1.9) \qquad \text{and} \qquad \varepsilon_2 = \frac{2nk}{\mu} \qquad (1.10)$$

and for non-magnetic materials (μ=1) we get:

$$\varepsilon_1 = n^2 - k^2 \qquad (1.11)$$

$$\varepsilon_2 = 2nk \qquad (1.12)$$

Then we can define a complex refractive index $\tilde{n} = (n + ik)$ (1.13)

where n is the real refractive index and k is the extinction coefficient through complex dielectric function

$$\tilde{\varepsilon} = \varepsilon_1 + i\varepsilon_2 = \tilde{n}^2 \qquad (1.14)$$

Substituting (1.13) into (1.14) we get:

$$\varepsilon = (\varepsilon_1 + i\varepsilon_2) = (n + ik)^2 = n^2 - k^2 + i2nk \qquad (1.15)$$

We can now determine the real ε_1 and the imaginary ε_2 part (of the dielectric function ε, respectively, for the Lorentzian model as below:

$$\varepsilon_1 = n^2 - k^2 = 1 + \frac{4\pi Ne^2}{m}\frac{\omega_0^2 - \omega^2}{(\omega_0^2 - \omega^2)^2 + \gamma\omega^2} \qquad (1.16)$$

$$\varepsilon_2 = 2nk = \frac{4\pi Ne^2}{m}\frac{\gamma\omega}{(\omega_0^2-\omega^2)^2+\gamma^2\omega^2} \quad (1.17)$$

The refractive index n and the extinction coefficient k can also been extracted from equations 1.15:

$$n = \sqrt{\frac{\left[(\varepsilon_1^2+\varepsilon_2^2)^{1/2}+\varepsilon_1\right]}{2}} \quad (1.18)$$

$$k = \sqrt{\frac{\left[(\varepsilon_1^2+\varepsilon_2^2)^{1/2}-\varepsilon_1\right]}{2}} \quad (1.19)$$

The quantities n, k can easily be calculated from the reflectivity measurements of a material as a function of the polarization of the incidence light and the incidence angle in the surface. For normal incidence the reflectivity can be defined as:

$$R = \left|\frac{n-1+ik}{n-1-ik}\right|^2 = \frac{(n-1)^2+k^2}{(n+1)^2+k^2} \quad (1.20)$$

1.3 Drude Oscillator

Drude model describes accurately the metals in contrast to Lorentz model that usually is used to describe semiconductors and insulators [1.8, 1.9, and 1.31].

Following the same classical picture as in Lorentz's model in metals the conduction electrons are not bound to the nuclei, thus there is no restoring force. So, Drude model can be exported from Lorentz oscillator setting ω_0=0 (Eqn. 1.21):

$$\varepsilon = 1 - \frac{4\pi Ne^2}{m}\frac{1}{(\omega^2+i\gamma\omega)} \quad (1.21)$$

with the real and imaginary part of the dielectric function being:

$$\varepsilon_1 = 1 - \frac{4\pi Ne^2}{m}\frac{1}{(\omega^2 - \gamma)} \quad (1.22)$$

$$\varepsilon_2 = 1 - \frac{4\pi Ne^2}{m}\frac{\gamma}{\omega(\omega^2 - \gamma^2)} \quad (1.23)$$

Equations 1.22 and 1.23 can be simplified if we define the bulk plasma frequency (it corresponds to the energy of the bulk plasmon) as:

$$\omega_p = \sqrt{\frac{4\pi Ne^2}{m}} \quad (1.24)$$

The damping factor γ for metals is associated with the electron relaxation time τ:

$$\tau = \frac{1}{\gamma} \quad (1.25).$$

Taking into account 1.24 and 1.25 eqn. 1.21 becomes:

$$\varepsilon = 1 - \frac{\omega_p^2}{(\omega^2 + {}^{i\omega}/_{\tau})} \quad (1.26)$$

Especially in the case of a nanomaterial τ is determined by [1.31, 1.44 and 1.45]:

$$\frac{1}{\tau} = \frac{1}{\tau_{Bulk}} + \frac{1}{\tau_{defects}} + \frac{U_F}{L} \quad (1.27)$$

Where $\tau_{Bulk}$is the τ of the infinite metal without any structural defects and it is associated with the conduction electron mean free path, $\tau_{defects}$ is the working function of the defects, U_F is the Fermi velocity [1.45] and L is the particles size.

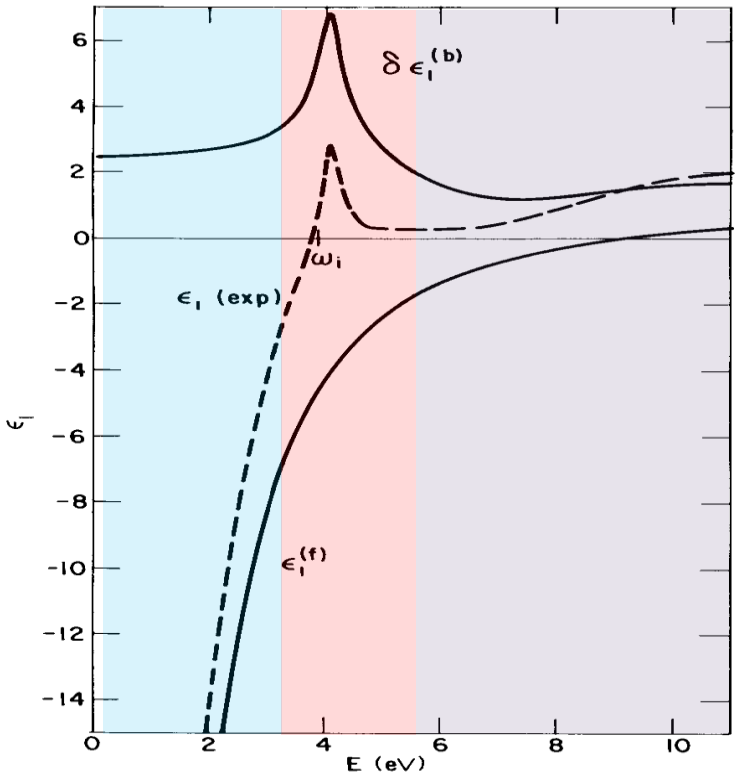

Figure 1.1. Dielectric function of Ag. The l dielectric function of Ag (ε_1 (exp)) is the result of the contribution of the intraband ($\varepsilon_1^{(f)}$) and interband transitions ($\delta\varepsilon_1^{(b)}$). [1.9]

From plasma frequency equation we can identify three regions (Figure 1.1)

- for $\omega < \omega_p$ the ε_1 is negative (characteristic of metals) that implies a strong reflection and no transmission of light (blue color).
- for $\omega > \omega_p$ the $\varepsilon_1$now is positive. In those frequencies the metal is transparent and the light can pass through it (violet region).
- for $\omega = \omega_p$ (red region) a harmonic oscillation of the conduction electrons in phase with the electric field of light is observed and it is called plasmon oscillation.

Its energy is:

$$E_{pl} = \hbar\omega_p \qquad (1.28)$$

1.4 Thin Films interaction with light

The determination of the optical properties of thin films is usually performed by measuring the reflection and transmission of the film when it is illuminated by light. For this reason, it is important to know how the light propagates into a film.

In the general case, where light (independent of polarization[1]) enters from a region with refractive index n_1 into another region having a refractive index n_2 with an angle of incidence θ (Figure 1.2).

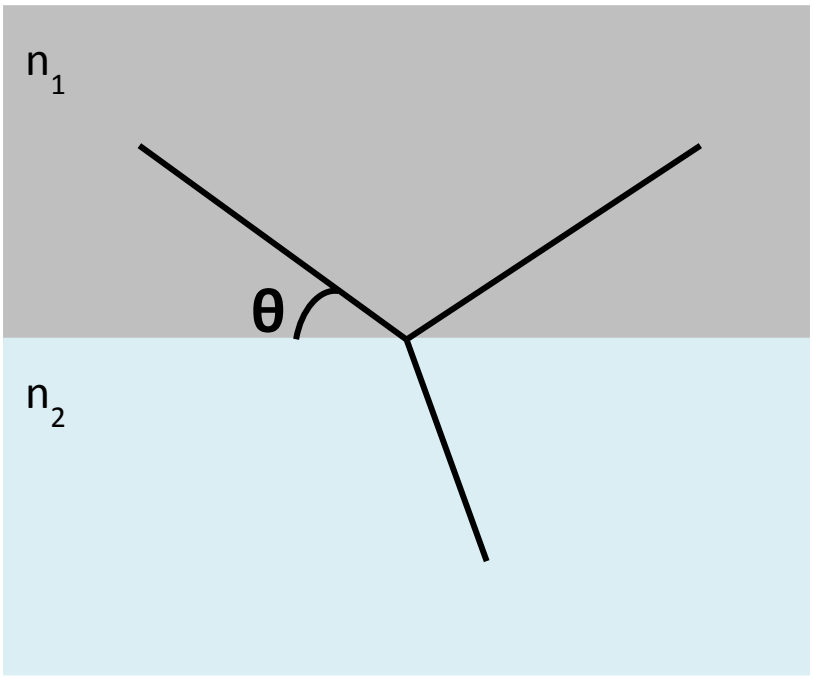

Figure 1.2. When light propagates from a region to another with different refractive indices, in the interface one part of the wave is reflected and the other transmitted with a different angle.

Fresnel reflection (r) and transmission (τ) coefficients can be calculated respectively. Thus for p and s components we get [1.11, 1.12]:

$$r_p = \frac{n_1\cos\theta_2 - n_2\cos\theta_1}{n_1\cos\theta_2 + n_2\cos\theta_1} \quad (1.29) \qquad \tau_p = \frac{2n_1\cos\theta_1}{n_1\cos\theta_2 + n_2\cos\theta_1} \quad (1.30)$$

$$r_s = \frac{n_1\cos\theta_1 - n_2\cos\theta_2}{n_1\cos\theta_1 + n_2\cos\theta_2} \quad (1.31) \qquad \tau_s = \frac{2n_1\cos\theta_1}{n_1\cos\theta_1 + n_2\cos\theta_2} \quad (1.32)$$

[1] The incidence wave can be parallel (s-polarization) or perpendicular (p-polarization) to the plane of incidence.

In the case of single non-absorbing film with thickness $\boldsymbol{d}$ and index of refraction $\boldsymbol{n_f}$ which is deposited on a substrate with refractive index $\boldsymbol{n_s}$ and above there is ambient with a refractive index $\boldsymbol{n_a}$ (Figure 1.3) we can apply the equations 1.29-1.32 for the ambient-film and film-substrate interfaces respectively and by adding the individual contributions we can conclude to the equations that describe the Reflection (R) (1.33) and Transmission (T) (1.34) that corresponds to the film:

$$R = \frac{r_{fs} + r_{af}\exp(-2i\varphi)}{1 + r_{fs}r_{af}\exp(-i\varphi)} \quad (1.33) \qquad T = \frac{\tau_{af} + \tau_{fs}\exp(-i\varphi)}{1 + r_{fs}r_{af}\exp(-i\varphi)} \quad (1.34)$$

where $\boldsymbol{\varphi = \frac{2\pi}{\lambda} n_f d\cos\theta_1}$ is the phase change that occurs when the light wave traverses the film from one boundary to the other.

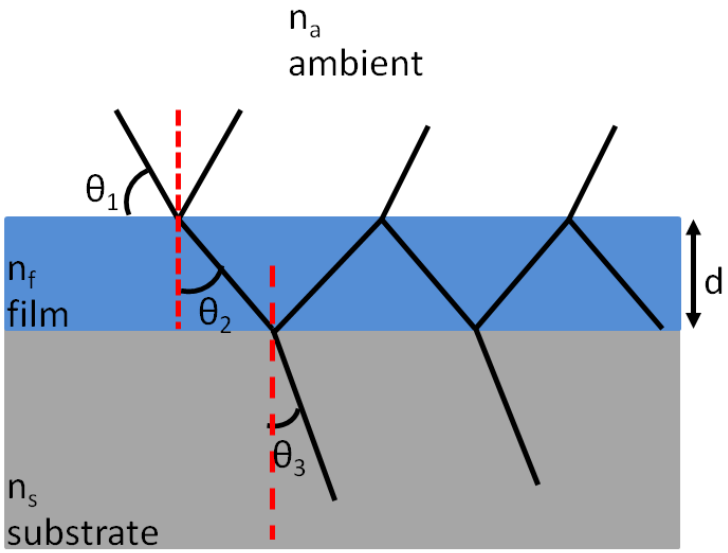

Figure 1.3. A uniform non-absorbing film grown on a substrate. The electromagnetic wave subjected to reflections, refraction and transmission in each interface.

At normal incidence ($\boldsymbol{\theta_1 = 0}$) the Fresnel reflection and transmission coefficients at the interfaces are simplified to:

$$r_{fs} = \frac{n_f - n_s}{n_f + n_s} \quad (1.35) \qquad \tau_{fs} = \frac{2n_f}{n_f + n_s} \quad (1.36)$$

$$r_{vf} = \frac{n_a - n_f}{n_f + n_a} \quad (1.37) \qquad \tau_{vf} = \frac{2n_a}{n_f + n_a} \quad (1.38)$$

and equations (1.33),(1.34) are now:

$$R = \frac{(n_s^2 + n_f^2)(n_f^2 + n_a^2) - 4n_s n_a n_f^2 + (n_s^2 - n_f^2)(n_f^2 - n_a^2)\cos 2\varphi}{(n_s^2 + n_f^2)(n_f^2 + n_a^2) + 4n_s n_a n_f^2 + (n_s^2 - n_f^2)(n_f^2 - n_a^2)\cos 2\varphi} \qquad (1.39)$$

$$T = \frac{8n_s n_a n_f^2}{(n_s^2 + n_f^2)(n_f^2 + n_a^2) - 4n_s n_a n_f^2 + (n_s^2 - n_f^2)(n_f^2 - n_a^2)\cos 2\varphi} \qquad (1.40)$$

The equations above are for a non-absorbing film. If the absorption of the light is taken into account then the real refractive index have to be replaced from the complex index of refraction (Eqn. 1.13) that includes the extinction coefficient k as well.

For the determination of the reflection and transmittance of multilayer structures the *Matrix Method* [1.11-1.15] has been developed. In that method tables 2x2 [1.13, 1.15] or 4x4 [1.14] are used to describe the reflection and transmission coefficients of each individual layer. Then, the final optical response of the multilayer is determined by multiplication of all the individual matrices

A very short description of that method is presented by O.S. Heavens [1.12] where he uses the electric vector $\boldsymbol{E_m^+}$ of the wave travelling in the direction of incidence in the m_{th} layer and $\boldsymbol{E_m^-}$ for the opposite direction. Each of these propagating waves can be described from equations 1.41 and 1.42 respectively.

$$E_m^+ = \frac{1}{\tau_m}\left[E_{m-1}^- \exp(i\varphi_{m-1}) + r_m E_{m-1}^- \exp(-i\varphi_{m-1})\right] \qquad (1.41)$$

$$E_m^- = \frac{1}{\tau_m}\left[r_m E_{m-1}^+ \exp(i\varphi_{m-1}) + E_{m-1}^- \exp(-i\varphi_{m-1})\right] \qquad (1.42)$$

The equations 1.41 and 1.42 can be rewritten in matrix form as:

$$\begin{pmatrix} E_m^+ \\ E_m^- \end{pmatrix} = \frac{1}{\tau_m}\begin{pmatrix} \exp(i\varphi_{m-1}) & r_m \exp(-i\varphi_{m-1}) \\ r_m \exp(i\varphi_{m-1}) & \exp(-i\varphi_{m-1}) \end{pmatrix}\begin{pmatrix} E_{m-1}^+ \\ E_{m-1}^- \end{pmatrix}$$

$$= \frac{1}{\tau_m} M_{m-1} \begin{pmatrix} E_{m-1}^+ \\ E_{m-1}^- \end{pmatrix} \qquad (1.43)$$

So, for a stack of N layers we get (eqn 1.44):

$$\begin{pmatrix} E_{N+1}^{+} \\ E_{N+1}^{-} \end{pmatrix} = \frac{M_N M_{N-1} \ldots\ldots M_2 M_1}{\tau_N \tau_{N-1} \ldots\ldots \tau_2 \tau_1} \begin{pmatrix} E_0^{+} \\ E_0^{-} \end{pmatrix} \qquad (1.44)$$

and finally the reflectance (Eqn. 1.45) and the transmittance (Eqn 1.46) can be calculated as:

$$R = \frac{|E_{N+1}^{-}|^2}{\left|E_{N+1}^{+}\right|^2} \qquad (1.45)$$

$$T = \frac{n_0 \cos^2\theta_{N+1}}{n_{N+1}\cos^2\theta_0} \frac{|E_0^{+}|^2}{\left|E_{N+1}^{+}\right|^2} \qquad (1.46)$$

where all the parameters with indicator zero correspond to the substrate.

1.5 Optical Properties of Semiconductors

The optical properties of semiconductors are based on the ability to absorb a photon with energy $\hbar\omega$ by switching an electron to switch from one state in the valence band to another state in the conduction band and creating an electron-hole pair.

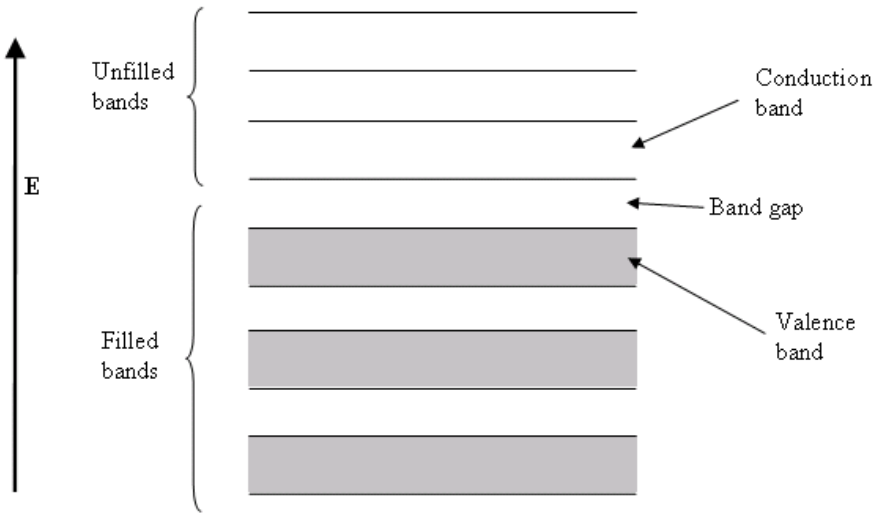

Figure 1.4. Energy diagram of a semiconductor.

1.5.1 Direct and Indirect semiconductors

The relative position in the k-space of the valence band maximum and conduction band minimum has a strong consequence on the energy gap and thus in the optical properties of semiconductors. So, based on this criterion semiconductors can be distinguished in two categories [1.11, 1.16]:

- Direct Band Gap Semiconductors
- Indirect Band Gap Semiconductors

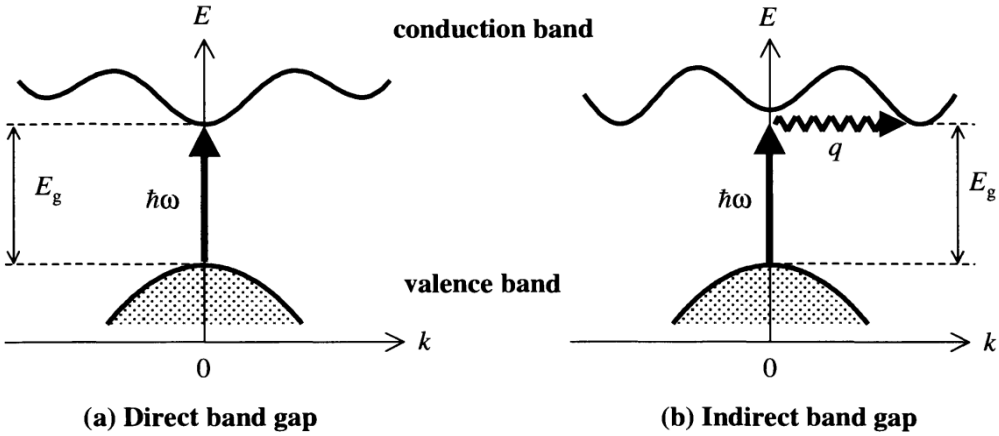

Figure 1.5. E-k diagrams for a direct (a) and indirect (b) band gap semiconductor. Indirect transition require a phonon absorption or emission in order to conserve the total momentum of the system [1.16]

As it is shown in picture 1.5a, in the case of a direct band gap semiconductor the conduction band minimum and valence band maximum occur at the zone center where k=0. Thus, when a photon is absorbed a direct transition of an electron from the valence band to the empty conduction band occurs and therefore no phonon participation in the process is necessary.

Instead, in the case of indirect band gap semiconductor (Picture 1.5b) the conduction band minimum and valence band maximum are not positioned at the same electron wave vector k. Now the transition is not direct and a phonon absorption or emission is required in order to have energy and momentum conservation during the absorption of the light.

In the following will elaborate more to the case of direct transitions since all the used semiconductors of this study (AlN, InN, $Al_xIn_{1-x}N$) exhibit direct optical gap.

1.5.2 Absorption of direct band gap semiconductors-Interband transitions

The interband transitions play important role in the optical properties of a semiconductor namely the excitation of an electron from the valence band to the conduction band and they are critical to determine the absorption coefficient α. The absorption coefficient α is related to the join density of states g(E). Join density of states can be expressed as (Eqn. 1.47) [1.12, 1.16],

$$g(E) = \frac{1}{2\pi^2}\left(\frac{2m^*}{\hbar^2}\right)^{3/2} E^{1/2} \qquad (1.47)$$

where m^* is the electron effective mass.

During the transition from the valence band to the conduction band the electron and the hole have a kinetic energy described from equations 1.48 and 1.49 respectively:

$$E_c(k) = E_g + \frac{\hbar^2 k^2}{2m_e^*} \qquad (1.48)$$

$$E_v(k) = \frac{\hbar^2 k^2}{2m_h^*} \qquad (1.49)$$

From the conservation of energy we get:

$$\hbar\omega = E_g + \frac{\hbar^2 k^2}{2m_e^*} + \frac{\hbar^2 k^2}{2m_h^*} \qquad (1.50)$$

If we define the reduced electron hole mass μ according to:

$$\frac{1}{\mu} = \frac{1}{m_e^*} + \frac{1}{m_h^*} \qquad (1.51)$$

The equation 1.49 can be rewritten as

$$\hbar\omega = E_g + \frac{\hbar^2 k^2}{2\mu} \qquad (1.52)$$

Substituting eqn. (1.49) into eqn. (1.47) we get that:

- For $\hbar\omega < E_g \Rightarrow g(E) = 0 \Rightarrow \alpha = 0$

- For $\hbar\omega \geq E_g \Rightarrow g(E) = \frac{1}{2\pi}\left(\frac{2\mu}{\hbar^2}\right)^{3/2}\left(\hbar\omega - E_g\right)^{1/2}$

$$\Rightarrow \alpha \propto \left(\hbar\omega - E_g\right)^{1/2} \quad (1.53)$$

From above we can see that when the energy of the photon is lower than the E_g the photon is not absorbed and the material is totally transparent in the appropriate wavelength. On the contrary, when the photon energy is equal or greater than the E_g the photon is absorbed and we have the creation of electron-hole pair. The analysis based in equation 1.56 is called "Tauc analysis" and it is used to determine the optical band gap from absorption spectra [1.47].

1.6 The case of Exciton

As stated above when a photon is absorbed from a semiconductor an electron is excited from the valence band to the conduction band leaving a positive hole in the valence band. This approach presupposes that the Coulomb forces between electron and hole are not taken into account. If the Coulomb interaction counted, then we have the case of *exciton*.

As exciton we can define a bound state of an electron and electron hole state, which attract each other by the electrostatic Coulomb force.

Excitons can affect the optical properties of materials. We can distinguish two basic types of excitons:

- Wannier-Mott excitons or free excitons
- Frenkel excitons or tightly bound excitons

The Wannier-Mott excitons are mainly observed in semiconductors in contrast to Frenkel excitons that are presented in insulators and some organic crystals.

The exciton absorption is given from the equation 1.54 [1.16]

$$E_n = E_g - \frac{R_X}{n^2} \quad (1.54)$$

where E_g is the fundamental energy gap and $\frac{R_X}{n^2}$ is the exciton Rydberg constant.

From equations 1.59 we can observe that the exciton energy is lower than the energy gap thus we could expect optical absorption that corresponds to exciton formation at energies just below the band gap.

1.7 Interaction of metal nanostructures with light

Metal nanostructure exhibit extra ordinary optical properties because of the interfacial phenomena that occur due to the fact that otherwise free conduction electrons are bonded by the physical dimensions of the nanostructures. This gives rise to surface plasmon (at metal surfaces) and localized surface plasmon (at metal nanoparticles) in contrast to bulk plasmon. Although a variety of metals can be used to form nanoparticles, Ag and Au are widely preferred owing to their low dielectric losses.

1.7.1 Surface Plasmons

An interesting case of a special optical behavior of a metal is the surface plasmon polariton that implies it is a surface electromagnetic wave which is guided by the coherent oscillation of conduction electrons at the interface metal-dielectric, as figure 1.6 shows.

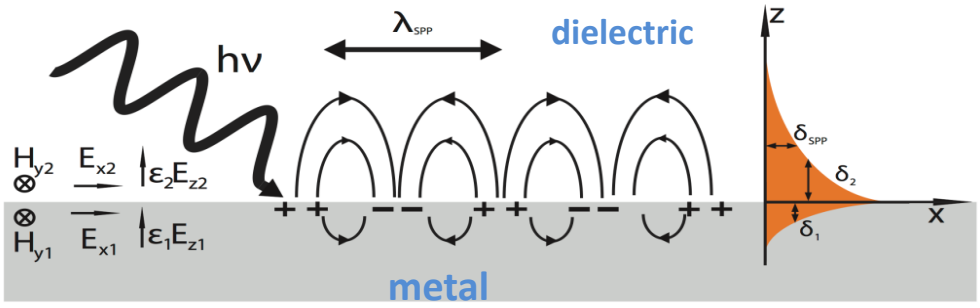

Figure 1.6. Schematically illustration of the surface plasmon

The electric field of the propagating electromagnetic wave can be described as follow:

$$E = E_0 \exp[i(k_x x + k_z z - \omega t)] \qquad (1.55)$$

Solving the Maxwell's equations for the propagating electromagnetic wave at the interface of the metal-dielectric, with ε_1 and ε_2 being the real and the imaginary part of the dielectric functions respectively, we lead to boundary conditions:

$$\frac{k_{z1}}{\varepsilon_1} + \frac{k_{z2}}{\varepsilon_2} = 0 \Longrightarrow \frac{k_{z1}}{\varepsilon_1} = -\frac{k_{z2}}{\varepsilon_2} \qquad (1.56)$$

And

$$k_x^2 + k_i^2 = \varepsilon_i(\frac{\omega}{c})^2 \quad i = 1,2, \tag{1.57}$$

The combination of equations 1.56 and 1.57 leads to equation 1.58 which describes the dispersion of surface plasmon:

$$k_x = \frac{\omega}{c}\left(\frac{\varepsilon_1\varepsilon_2}{\varepsilon_1 + \varepsilon_2}\right)^2 \tag{1.58}$$

And easily we can see that: $\varepsilon_1 \leq \varepsilon_2$ and as a result we can extract the boundary condition for surface plasmon which is (Eqn 1.59):

$$\varepsilon_{metal}(\omega) = -\varepsilon_{dielectric} \tag{1.59}$$

If the metal-vacuum (ε_1=1) boundary conditions are applied we take:

$$\omega_{sp} = \frac{\omega_p}{\sqrt{2}} \tag{1.60}$$

and in the case of dielectric ($\varepsilon_d \neq 1$) we have:

$$\omega_{sp} = \frac{\omega_p}{\sqrt{1 + \varepsilon_{dielectric}}} \tag{1.61}$$

1.8 Absorption on metal nanoparticles

Another important case that includes interaction with light is the interaction of small (smaller than the wavelength of the light) metallic particles with light.

When a nanoparticle is illuminated by light absorbs and scatters the radiation leading to a non-propagating collective oscillation of the conduction electrons at a specific frequency known as *Localized Surface Plasmon Resonance* ***(LSPR)***. During the light illumination the nanoparticle acts as an electric dipole and surface charges are created, because of the electron oscillation in the particle (Figure 1.7).

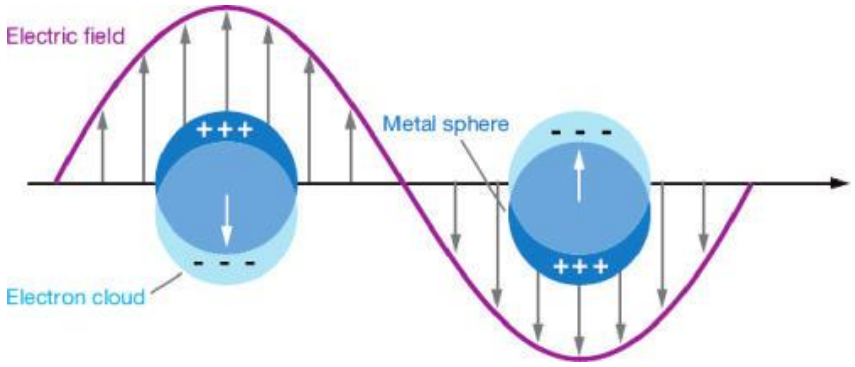

Figure 1.7. Metal nanoparticles converted in electric dipole while irradiated with light.

Historically the first approaches for describing interactions between light and nanostructures were published in the very beginning of the XXth century, some sixty years before those theories started to be exploited in the field of nanochemistry. These approaches enabled the complete description of the problem without having to proceed to complicated approximations. First in 1904–1905, Maxwell–Garnett described the so called ‘‘Effective medium theory’’ [1.26, 1.33]. The model developed gives the expression of the dielectric constant within a matrix (dielectric constant ε_m) containing small metallic spheres, provided that the size of the spheres is small compared to the wavelength and the material under consideration has a spatial extension larger than the wavelength. However, the most popular theory is without contest the one Mie published in 1908 concerning the absorption and scattering behavior of a small metal nanoparticle when illuminated by light [1.17] while several groups followed in the coming years [1.18, 1.21, 1.22, 1.23, and 1.33]. All studies were based on the *Quasi-Static approximation* i.e. that the particle size is smaller than the wavelength of light.

In order to calculate the electric filed that applied to the particle we solve Laplace equation $\boldsymbol{\nabla^2\Phi = 0}$ [1.10], where Φ is the electric potential, and we conclude to equation 1.37 [1.62] that correlates the dipole moment with the electric field including the atomic polarizability α (Eqn. 1.63).

$$p = \varepsilon_0 \varepsilon_m \alpha E_0 \qquad (1.62)$$

$$\alpha = 4\pi r^3 \frac{\varepsilon - \varepsilon_m}{\varepsilon + 2\varepsilon_m} \qquad (1.63)$$

where r is the nanoparticles radius, ε is the dielectric function of the metal and ε_m the dielectric constant of the medium (isotropic and non-absorbing).

The atomic polarizability gives us a straight answer that a resonance enhancement caused when the denominator of the equation 1.67 $|\boldsymbol{\varepsilon + 2\varepsilon_m}|$ is minimum. That leads to the resonance condition (Eqn 1.64)

$$\mathrm{Re}[\varepsilon(\omega)] = -2\varepsilon_\mathrm{m} \tag{1.64}$$

which is known as the Fröilich condition. For a metallic sphere located in the air the resonance criterion is

$$\omega_0 = \frac{\omega_\mathrm{p}}{\sqrt{3}} \tag{1.65}$$

where ω_p is the plasma frequency of the bulk metal.

The polarizability that is observed in metal nanoparticles effect in the absorption and scattering of the light from the particle.

Thus expressions for both components can be deduced respectively [1.10]:

$$\mathrm{C_{sca}} = \frac{8\pi}{3}\mathrm{k^4a^6}\left|\frac{\varepsilon - \varepsilon_\mathrm{m}}{\varepsilon + 2\varepsilon_\mathrm{m}}\right|^2 \tag{1.66}$$

$$\mathrm{C_{abs}} = 4\pi\mathrm{ka^3Im}\left|\frac{\varepsilon - \varepsilon_\mathrm{m}}{\varepsilon + 2\varepsilon_\mathrm{m}}\right| \tag{1.67}$$

Cross section extinction coefficient is the summary of the two components and is described from the equation 1.68 [1.10, 1.33]

$$\mathrm{C_{ext}} = 9\frac{\omega}{c}\varepsilon_\mathrm{m}^{3/2}\mathrm{V}\frac{\varepsilon_2}{(\varepsilon_1 + 2\varepsilon_\mathrm{m})^2 + \varepsilon_2} \tag{1.68}$$

where V is the volume of the nanoparticles, ε_m is the dielectric constant of the environment and $\varepsilon_1, \varepsilon_2$ are the real and imaginary part of the dielectric constant of the metallic nanoparticles.

It is important to note that for particles with larger dimensions the Quasi-static approximation fails, so it is necessary to use an electrodynamic approach for describing the

interaction of those particles with light because now quadrupole or higher order momentum are observed.

It is obvious from the expression of the Mie extinction cross section (Eqn. 1.68) that the dielectric constant of the surrounding medium plays a predominant role in determining both the plasmon peak position and intensity. Changing the medium surrounding the NPs for another medium having a markedly different refractive index strongly alters the plasmon behavior of the NPs. In particular increasing the refractive index of the medium a red shift is observed. Contrariwise, decreasing the refractive index of the surrounding LSPR peak is shifted to lower wavelengths [1.7, 1.35, 1.19- 1.22, 1.24, 1.28, 1.32 1.36].

The influence of the size of the NPs on the LSPR peak position is a question that has arisen very early. As the diameter R of the nanoparticles appears in its equation through sphere volume V, the Mie theory predicts a size dependence of the intensity of the LSPR (Eqn 1.68). Position and bandwidth are also affected by R, but through intrinsic effects, which means that R modifies the expression of the dielectric constant of the metal and thus alters the resonance condition expressed as $\varepsilon_1 = -2\varepsilon_m$. Classically it is admitted that as NPs size becomes small enough (typically under 50 nm) the size of the NP becomes of the order of the mean free path, or even smaller, which strongly affects the dynamics of the system. Thus, increasing particles size a red shift of the LSPR spectral position is expected while dissolution of the existing nanoparticles into smaller induces a blue shift in LSPR peak position [1.19, 1.21, 1.22, 1.27, 1.31, 1.34, 1.37].

Although the resonant condition calculated based on the simplest form of nanoparticles (sphere) previsions, impact of the NPs shape on the LSPR behavior has been also considered [1.25, 1.29 and 1.33]. Thus, nanotechnology has enabled researchers to synthesize nanoparticles featuring original shapes such as ellipsoids [1.42, 1.43], cubes [1.25, 1.38], triangles [1.25], rods [1.39, 1.40], stars [1.41] etc. are also made and studied. The main conclusion that was pointed out of the SPR peak for different configurations (except sphere) is that the number of the LSPR peaks is proportional to the number of the individual polarizations that a particle can develop. For example, for an ellipsoid having three different axis $\alpha_1 < \alpha_2 < \alpha_3$ (triaxial ellipsoid, figure 1.8) three LSPR peaks are expected [1.10, 1.19] while for a prolate ellipsoid, where the two minor axis are equal two LSPR peaks are expected, one for the minor and one for the major axis respectively.

Figure 1.8. A triaxial ellipsoid can lead to three different SPR peaks through to three different axis a, b, c.

It is worth noticing that in case of triangles, cubes and stars important role in the LSPR peak position and intensity plays the sharpness of the corners [1.25, 1.27]. In particular, LSPR peaks red shift with increasing the corner sharpness and particle anisotropy.

Finally, it has been demonstrated bimodal systems mainly due to the broad particles size distribution [].

1.9 Effect of the particle size in metal dielectric function

As it was discussed in previous sections the optical properties of a metal is described accurately through Drude oscillator (Eqn. 1.21). Drude term is characterized by the unscreened plasma energy $E_{pu} = \hbar\omega_p$ (Eqn. 1.24) and the damping factor Γ_D. E_{pu} depends on the concentration of the conduction electrons in the film and is defined by the relation

$$\omega_p{}^2 = \frac{\mathrm{Ne}^2}{\varepsilon_0 \mathrm{m}^*} \tag{1.69}$$

where N is the conduction electron density, e is the electron charge, $\varepsilon_0$is the permittivity of free space, and m^* is the electron effective mass. In adittion, Γ_D is due to the scattering of electrons and according to the free-electron theory it is related to the electron relaxation time through the relation

$$\tau_D = \frac{\hbar}{\Gamma_D(eV)} \tag{1.70}$$

Each atom of the metal contributes with one free electron to and thus the electron density remains constant for different sizes. For this reason the plasma frequency ω_p is assumed independent of the size. However, the damping factor, related to the mean free path for free electrons, is strongly affected by the size through relaxation time (Eqn. 1.32). In particles smaller than the mean free path of conduction electrons in the bulk metal, the mean free path is dominated by collisions with the particle boundary. For small particles, the damping constant for the free electron contribution is increased due to additional collisions with the boundary of the particle and thus we can write via equation 1.32:

$$\Gamma_{D\,FREE}(R) = \Gamma_{D\,BULK} + \frac{U_F}{R} \tag{1.71}$$

where U_F is the Fermi velocity and R is the radius of the particle.

References

[1.1] Panagiotopoulos, N.T., Patsalas P. *et al., ACS Applied Materials and Interfaces,* **2** (2010), pp. 3052-3058.

[1.2] Liedberg B., Nylander C., Lundstrom I., *Sensors and Actuators,* **4** (1983), pp. 299-304.

[1.3] Nikitin P.I., Beloglazov A.A., *et al*., *Sensors and Actuators B,* **54** (1999), pp. 43-50.

[1.4] Godbole V.P., Narayan J., *Materials Science and Engineering B,* **39** (1996), pp. 153-159.

[1.5] Kaminski P.M., Bass K., Claudio G., *Phys. Status Solid C,* **8** (2011), pp. 1311-1314.

[1.6] Taniyasu Y., Kasu M. and Makimoto T., *Nature Letters,* **441** (2006), pp. 325-328.

[1.7] Siozios A., Koutsogeorgis D.C. *et al*., *NanoLetters*, **12** (2012), pp. 259-263.

[1.8] Jackson J.D., *Classical Electrodynamics,* John Wiley& Sons, Inc., New York 1962.

[1.9] Wooten F., *Optical Properties of Solids,* Academic Press, New York, 1972.

[1.10] Maier S. *Plasmonic: Fundamentals and Applications*, Springer, New York, 2007.

[1.11] Singh Jai, *Optical Properties of Condensed Matter and Applications*, John Wiley& Sons, 2006.

[1.12] Heavens O.S., *Optical Properties of Thin Films.*

[1.13] Mansuripur M., *J. Appl. Phys*, **67** (1990), pp. 6466-6475.

[1.14] Abdulhalim I., *Journal of Optics A: Pure Appl. Opt.*, **1**(1999), pp. 646-653.

[1.15] Katsidis C.C., Siapkas I.D., *Applied Optics*, **41** (2002), pp. 3978-3987.

[1.16] Fox Mark*, Optical Properties of Solids,* Oxford University Press, New York, 2001.

[1.17] Mie G., Ann. Phys. **25** (1908).

[1.18] Bohren C.F., Huffman D.R., *Absorption and Scattering of Light by Small Particles*, Wiley Interscience, New York 1983.

[1.19] Kelly K.L., Coronado E., Zhao L.L., Schatz G., *J. Phys. Chem*., **107** (2003), pp. 668-677.

[1.20] Miller M.M, Lazarides A.A., *J. Phys. Chem*., **109** (2005), pp. 21556-21565.

[1.21] Kreibig U., Genzel L., *Surface Science*, **156** (1985), pp. 678-700.

[1.22] Moores A., Goettmann F., *New Journal of Chemistry*, **30** (2006), pp. 1121-1132.

[1.23] Doremus H.R., *Langmuir*, **18** (2002), pp. 2436-2437.

[1.24] Walters G, Parkin P.I., J. *Mater. Chem*., **19** (2009), pp. 574-590.

[1.25] Lu X., Rycenga M., *et al*., *Annu. Rev. Phys. Chem*., **60** (2009), pp, 167-192.

[1.26] Aspnes D.E., *Thin Solid Films*, **89** (1982), pp. 249-262.

[1.27] Mock J.J., Barbic M. *et al. J. Chem. Phys*., **116** (2002), pp. 6755-6759.

[1.28] Mock J.J., Smith R.D., Schultz S., *NanoLetters*, **3** (2003), pp. 485-491.

[1.29] Filippo E., Manno D. *et al*., *Superlattices and Microstrucrture*, **47** (2010), pp. 66-71.

[1.30] Liedberg B., Nylander C., Lundstrom I., *Sensors and Actuators*, **4**(1983), pp. 299-304.

[1.31] Genzel L., Martin T.P., Kreibig U., Z. *Physik B*, **21** (1975), pp. 339-346

[1.32] Persson B.N.J., *Surface Science*, **281** (1993), pp. 153-162.

[1.33] Link S., El-Sayed A.M., *Int. Reviews in Physical Chemistry*, **19** (2000), pp. 409-453.

[1.34] Kolwas K., Derkachova A., Shopa M., *Journal of Quantitative and Radiative Transfer*, **110** (2009), pp. 1490-1501.

[1.35] Underwood S., Mulvaney P., *Langmuir*, **10** (1994), pp. 3427-3430.

[1.36] Prodan E., Lee A., Nordlander P., *Chemical Physics Letters*, **360** (2002), pp. 325-332.

[1.37] Fu Hong-Bing, Yao Jian-Nian, *J. Am. Chem. Soc.*, **123** (2001), pp. 1434-1439.

[1.38] Sherry J.L., Chang Shih-Hui *et al*., *NanoLetters*, **5** (2005), pp. 2034-2038.

[1.39] Kimling J., Maier M. *et al*., *J. Phys. Chem.*, **110** (2006), pp. 15700-15707.

[1.40] Tsuji M., Hashimoto M., *et al*., *Chem-Eur. J.*, **11** (2005), pp. 440-452.

[1.41] Eustis S., Al-Sayed M.A., *Chem. Soc. Rev*., **35** (2006), pp. 209-217.

[1.42] Pustovalov V.K., Babenko V.A., *Laser Physics Letters*, **2** (2005), pp. 84-88.

[1.43] Oraevsky A.A., Oraevsky, A.N, *Quantum Electronics*, **32** (2002), pp. 79-82.

[1.44] G. M. Matenoglou, Ch. E. Lekka, *et al*., *J. Appl. Phys.*, **105** (2009), 103714.

[1.45] P. Patsalas,. Logothetidis S., *J. Appl. Phys.*, **90**, (2001), 4725.

[1.46] Ascroft N.W., Mermin N.D., Solid State Physics, Saunders, 1976.

[1.47] Tauc J., Grigorovici R., Vancu A., *Phys. Stat. Sol*., **15** (1966), pp. 627-637.

Chapter 2 *THIN FILMS GROWTH AND PROCESSING*

2.1 Introduction

In our days thin film growth plays a significant role in the development of the materials science as it is possible to create new structures with new exceptional properties and functionalities which can make them suitable for a wide range of applications in nanoscience and nanotechnologies. Sometimes the properties of thin films are totally different to the bulk, so it is possible new phenomena to occur.

Through the years thin film deposition techniques developed to meet any requirement regarding film's structural and optical properties. The most widespread methods are Physical Vapor Deposition (PVD) and Chemical Vapor Deposition (CVD) techniques. In vapor deposition the material transfers to the solid surface through the vapor face. If the vapor is created by physical means the process is classified as PVD. Instead, if the vapor is the result of a chemical reaction the process is classified as CVD.

Techniques that include in the two categories and were used for thin film growth in this thesis are discussed, presenting the main characteristics of each one.

In addition, we discuss the modes of film growth that mainly occur in both PVD and CVD techniques.

Furthermore, the microstructure of the films can be also altered by exploiting the diffusion and de-wetting phenomena occurring during thermal and laser annealing.

2.2 Modes of film growth by vapor deposition

2.2.1 Nucleation

In PVD and CVD techniques the vapor condensation and its transformation to solid state phase usually occur. This process is extensively described by nucleation theory that is based on the growth of nucleus in the early stage of thin film growth. During nucleation new surface and interfaces are formed and it is an important process because the grain structure that ultimately develops in a given deposition process. Although it is rare, homogeneous nucleation is the one of the two categories of nucleation that can take place. This kind is observed in "perfect" and clean substrates and the total free energy change in forming the nucleus is thus given by:

$$\Delta G = \frac{4}{3}\pi r^3 \Delta G_v + 4\pi r^2 \gamma \qquad (2.1)$$

In equation 2.1 the first term is related with the volume change during solidification and the second term is the result of the increase in the surface energy of the system due to new surface and interface formation respectively (Figure 2.1), while ΔG_v corresponds to the change in chemical free energy per unit volume and is given by:

$$\Delta G_v = \frac{k_B T}{\Omega} \ln \frac{P_s}{P_V} = -\frac{k_B T}{\Omega} \ln(1 + S) \qquad (2.2)$$

where Ω is the atomic volume, P_v is the pressure of the supersaturated vapor, P_s is the pressure above the solid and S is equal to $(P_v\text{-}P_s)/P_s$.

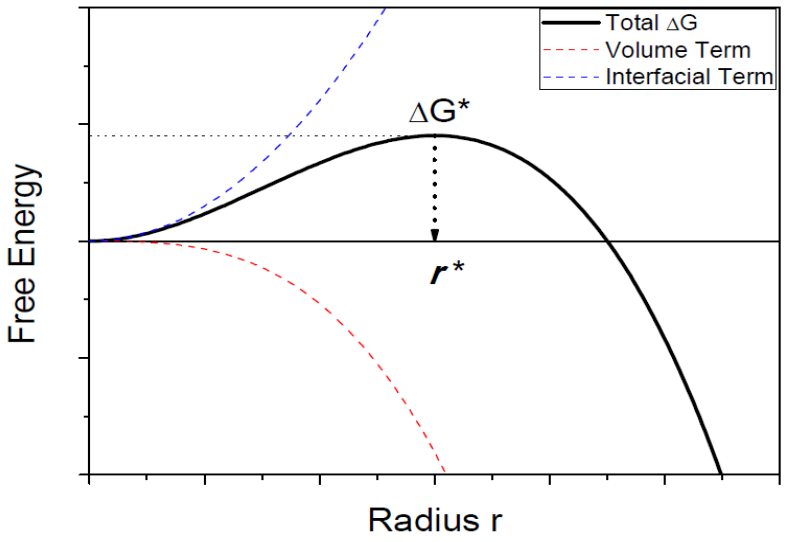

Figure 2.1. Change of the free energy as a function of the radius r. The total energy ΔG is the summary of the interface free energy (blue dash line) and the volume energy (red dash line).

Minimization of ΔG with respect to r ($\frac{d(\Delta G)}{dr} = 0$) yields the equilibrium size r^*

$$r^* = -\frac{2\gamma}{\Delta G_v} \qquad (2.3)$$

Finally if we substitute equation 2.2 to equation 2.1 we get:

$$\Delta G^* = \frac{16\pi\gamma^3}{3(\Delta G_v)^2} \qquad (2.4)$$

As it is illustrated in figure 2.1, ΔG^* represents an energy barrier to the nucleation process. It is also clear that nucleus with radius less than r^* are unstable and will shrink while clusters with radius larger than r^* have surmounted the energy barrier and are stable.

Heterogeneous nucleation occurs much more often than homogeneous nucleation. It forms at preferential sites such as phase boundaries or impurities like dust of a substrate. At such preferential sites, the effective surface energy is lower, thus diminishing the free energy barrier and facilitating nucleation and thus and requires less energy than homogeneous nucleation.

Assuming that nucleus is created in a substrate, as schematically presented in figure 2.2, and heterogeneous nucleation occurs, then the free energy change accompanying this formation is:

$$\Delta G = a_3 r^3 \Delta G_v + a_1 r^2 \gamma_{fv} + a_2 r^2 \gamma_{fs} + a_2 r^2 \gamma_{sv} \quad (2.5)$$

where $a_1 r^2$ is the curved surface, $a_2 r^2$ is the projected circular area, $a_3 r^3$ is the volume and γ are interfacial tensions that developed between the substrate and the deposited nuclei. Finally subscripts fv, fs and sv referred to film-vapor, film-substrate and substrate-vapor interfaces that formed during nucleation respectively.

We can also export the geometrical constants as:

$$a_1 = 2\pi(1 - \cos\theta_c) \quad (2.6)$$

$$a_2 = \pi \sin^2\theta_c \quad (2.7)$$

$$a_3 = \frac{\pi}{3}(2 - 3\cos\theta_c + \cos^3\theta_c) \quad (2.8)$$

where θ_c is the contact angle which measures the affinity of the deposited melt on the specific surface (note that the contact angle is exceptionally important for the annealing process as well).

Following the same step as we did in homogeneous nucleation we can estimate the critical nucleus size r^* for heterogeneous nucleation requiring thermodynamic equilibrium that is achieved when $\frac{d(\Delta G)}{dr} = 0$.

Using equation 2.5 that time we conclude to the critical nucleus radius r^*:

$$r^* = \frac{-2(a_1\gamma_{fv} + a_2\gamma_{fs} - a_2\gamma_{sv})}{3a_3\Delta G_v} \quad (2.9)$$

Correspondingly, ΔG evaluated at $r = r^*$ is

$$\Delta G^* = \frac{4(a_1\gamma_{fv} + a_2\gamma_{fs} - a_2\gamma_{sv})^3}{27a_3^2\Delta G_v{}^2} \quad (2.10)$$

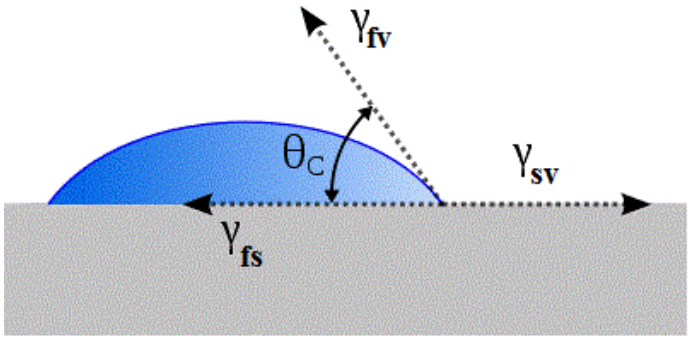

Figure 2.2. Growth of nuclei upon a substrate. γ_{fv}, γ_{fs} and γ_{sv} are interfacial tensions that formed between film-vapor, film-substrate and substrate-vapor interfaces during nucleation, θ_C is the contact angle between nuclei and substrate [2.36].

Substituting the geometrical constants a_1, a_2, a_3 into the equation 2.10 we get:

$$\Delta G^* = \frac{16\pi\gamma^3}{3(\Delta G_v)^2}\left(\frac{2 - 3\cos\theta_c + \cos^3\theta_c}{4}\right) \quad (2.11)$$

Comparing the equation above with that of homogeneous nucleation (equation 2.4) we can see that the free energy in heterogeneous nucleation is that of the homogeneous nucleation modified by a factor associated with contact angle. We can say then that the energy barrier for starting heterogeneous nucleation is less than that in the homogenous (Figure 2.3). It is also important to note that the free energy is strongly related to the contact angle[2] θ_c

[2] The contact angle is the angle, conventionally measured through the liquid, where a liquid-vapor interface meets a solid surface

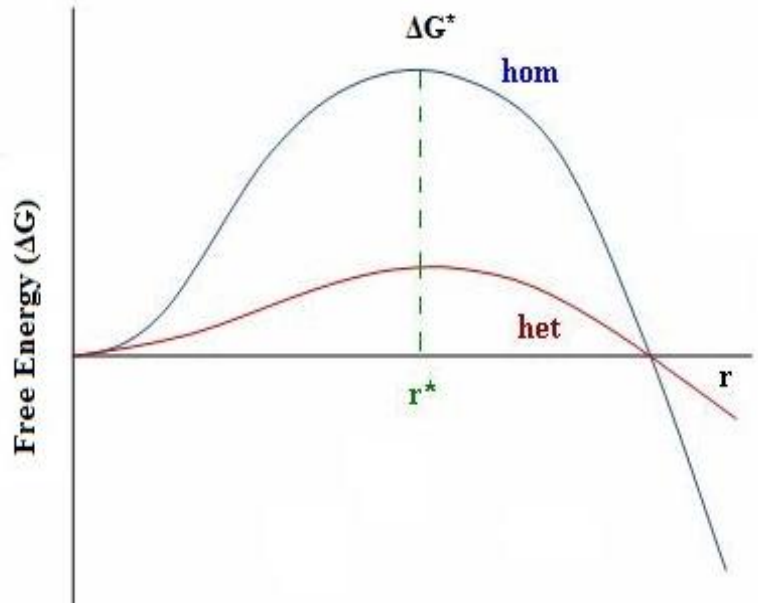

Figure 2.3. Comparison of the free energy (ΔG) for homogeneous (blue line) and heterogeneous (red line) nucleation. The contact angle factor that involving in the heterogeneous nucleation reduces the energy barrier for starting nucleation.

2.2.2 Film growth modes

As stated above during growth of nuclei onto a substrate interfacial tensions are developing. The equilibrium among the horizontal components of that tensions yields Young's equation:

$$\gamma_{sv} = \gamma_{fs} + \gamma_{fv}\cos\theta_c \qquad (2.12)$$

where γ_{fv}, γ_{fs} and γ_{sv} are interfacial tensions that formed between film-vapor, film-substrate and substrate-vapor interfaces respectively during nucleation.

This equation can help us distinguish three different modes (Figure 2.4) of film growth with respect to the wetting angle:

- When $\theta_c > 0 \Longrightarrow \gamma_{sv} < \gamma_{fs} + \gamma_{fv}$ island growth is promoted (*Volmer-Weber growth*). The deposited atoms interact strongly with each other than with substrate atoms. This leads in island growth which becomes larger with time up to their coalescence.
- When $\theta_c \cong 0 \Longrightarrow \gamma_{sv} \geq \gamma_{fs} + \gamma_{fv}$ layer growth is observed (*Frank-Van der Merwe growth*). Now the wetting is better and the deposited atoms interact mostly with the substrate atoms.

  A special case of this condition is the ideal homo-epitaxy, because the interface between film and substrate essentially vanishes.

- Finally, there is an intermediate state known as *Stranki-Krastanov growth*. In this case, a layer of the deposited atoms is initially formed and then island growth occurs. In this mode $\gamma_{sv} > \gamma_{fs} + \gamma_{fv}$.

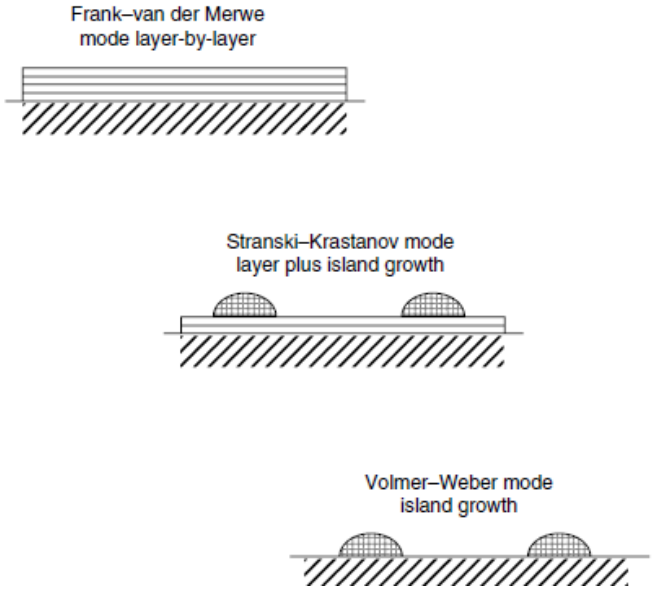

Figure 2.4. Three different modes of growth with respect to the contact angle. [2.4]

2.2.3 Film growth and microstructure

During film growth atoms that arrive in the substrate surface, from vapor condensation, diffuse over it. These atoms that now are adatoms can be absorbed on the substrate surface, interact with other atoms of the substrate or being trapped at low-energy sites until they finally find their equilibrium positions. Each of these processes that can take place is related to a corresponding activation energy which has a good correlation with the melting point T_m of the deposited material. Furthermore, the dominant process depends mostly on the substrate temperature T.

On the other hand, polycrystalline films structurally are described in terms of grain size, grain boundary morphology and film texture. Thus it is needed to describe their structural characteristics as a function of the process that is taking place.

This correlation was the motivation for Movchan and Demchishin to propose a Structure Zone Model (SZM) [2.36] for evaporated thick coatings (Figure 2.5) where the microstructure of the film is presented as a function of T/T_m ratio. This model is consisting from three zones. In zone 1 ($T/T_m < 0.25$) tapered columnar crystals are observed with domed tops that are separated

by void boundaries. In this region very little surface diffusion occurs. In zone 2 ($0.25<T/T_m<0.5$) columnar grains are separated by distant and dense grain boundaries. In this case the dislocations appear to be mainly concentrated in the boundary regions. Finally, in zone 3 ($0.50<T/T_m<1$) the grains are equiaxed and reveal a bright surface. Bulk diffusion is the mechanism that occurs now.

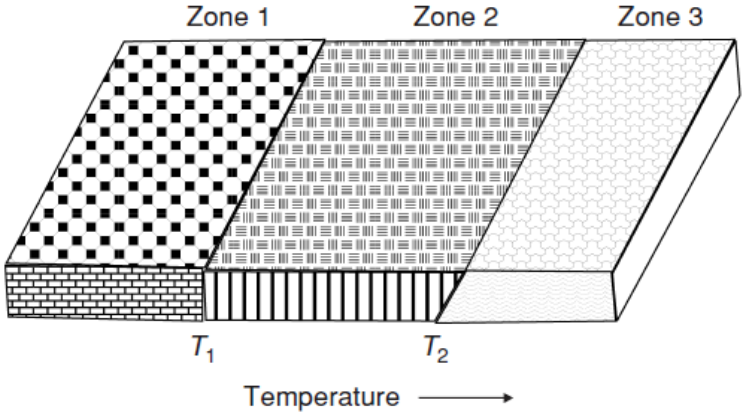

Figure 2.5. Structural Zone Model (SZM) that was first proposed from Movchan and Demchishin. Thin film microstructure is related with T/T_m ratio [2.4].

The SZM proposed by Movchan and Demchishin was later extended by Thornton [2.37] (Figure 2.6), who added another parameter, inert sputtering gas pressure (P), in order to describe the morphologies of sputtered films.

Broadly, pressure seems to increase the temperature boundaries that every zone occurs. If the pressure is increased, that means that mean free path of elastic collisions between sputtering species and inert gas increases, the oblique component of the deposition flux increases and thus a more open zone 1 results. On the other hand, if pressure is decreased, particles gain energy, less collisions occur, and become more active. This leads to more dense films.

Finally, Thornton was also introduce a new transition region in his revised SZM called T zone which represents the going from zone 1 to zone 2.T zone is between zones 1 and 2 and comprised of a dense array of poorly defined fibrous grains.

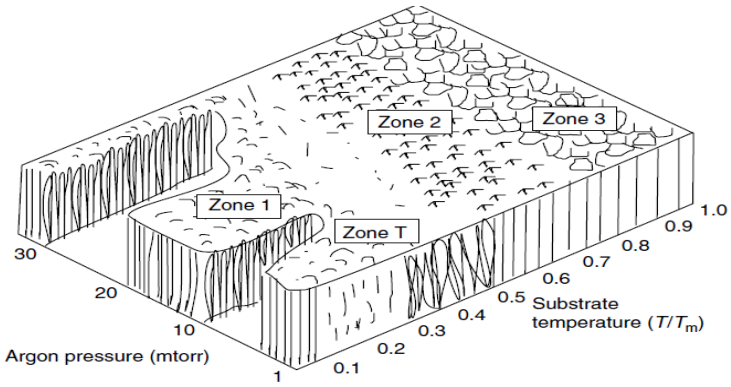

Figure 2.6. The extended Structural Zone Model (SZM) proposed by Thornton [2.4]

Although the proposed SZM were correlate a variety of deposition parameters with thin film parameters, however the need for expansion of the existing SZM concerning the deposition parameters was imperative due to the rapid increment in use of new or improved modes of deposition techniques i.e. High Power Impulse Magnetron Sputtering (HiPIMS). Thus, Andre Anders [2.39] proposes a new comprehensive SZM including plasma and ion-related deposition parameters (Figure 2.7).

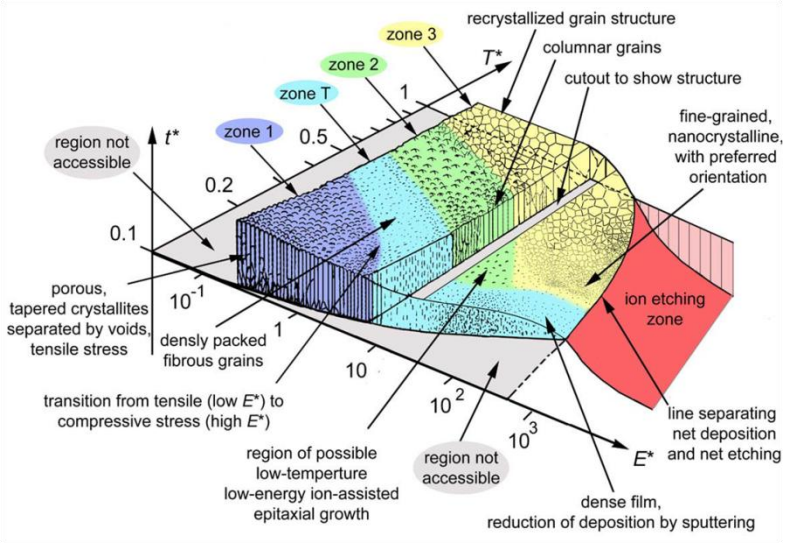

Figure 2.7 Upgraded SZM proposed by A. Anders where T^* is the generalized temperature, E^* is the normalized energy flex and t^* the net thickness respectively. [2.38].

2.3 PVD techniques

PVD technologies involve physical ejection of materials from a solid target and creation of condensated vapors. The movement of these vapors towards the substrate is responsible for the thin film growth. Evaporation and ionic impingement are some of the methods used for the

vapor creation thus sputtering and evaporation are of the most prevalent techniques for thin film deposition of various materials such as metals, oxides, and semiconductors.

Below we describe the basics for Sputtering and Pulsed Laser Deposition that used in the framework of the current thesis.

2.3.1 Sputtering

Sputtering is a momentum transfer process based on collisions between particles in the process chamber.

Initially, working gas, typically Ar is inserted into an evacuated deposition chamber. The material-target that we want to deposit is placed in the cathode while the substrate, where the material will be deposited is placed in the anode. A voltage is applied between target and substrate resulting to the ionization of the Ar gas and the creation of plasma. The Ar ionized atoms are accelerating towards the target due to the imposed electric field and the interactions with electrons.

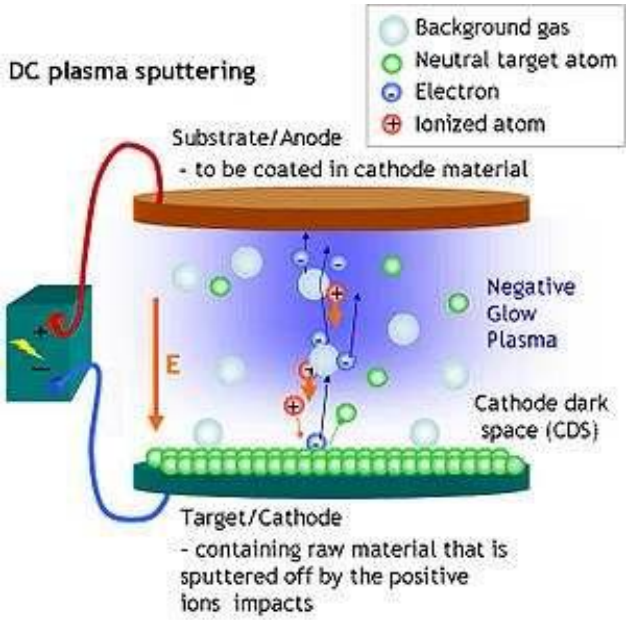

Figure 2.8. Schematically illustration of sputtering process (figure from www.etafilm.com).

Collisions of the accelerating ions with the target surface facilitate the momentum transfer. If the kinetic energy with which ions strike the surface is bigger than the binding energy of the atoms in surface then atoms of the material can be ejected and vapors are created. These vapors are responsible for the thin film growth. From the description of the sputtering process above we can see that we can distinguish three sections:

- Particle-target interactions

- Transport of the sputtered particles through the gas phase
- Deposition of the film.

Particle-target interactions

As stated above sputtering is a momentum transfer process thus depending on the kinetic energy of the ions that impinge in the target surface interesting phenomena occurs. For lower energies than the binding energies of the target surface atoms ions can be reflected on the surface while if the energy exceeds that energy, surface damage will occur as atoms forced into new lattice positions. Other phenomena that also can take place during the ion-target collisions are secondary electron emission from the atoms of the target, defects and voids in the target, backscattering or implantation of the incoming particles, X-ray emission etc. All possible processes that can occur during sputtering are illustrated in figure 2.9. The neutral atoms that reflected from the target surface can affect a wide variety of thin film properties especially when their kinetic energy is enough to arrive to the substrate.

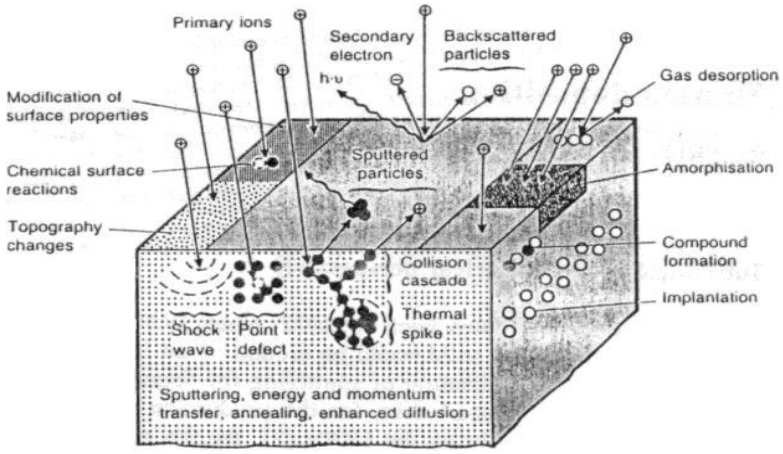

Figure 2.9. Ion interactions with solid [2.1]

The ability of ejection atoms from the target can generally described from the Sputtering Yield S which is the ratio of the atoms ejected per incident ion:

$$S = \frac{atoms\ removed}{incident\ ions}$$

and is proportional to the interactions that take place in the target through three parameters:

Kinetic Energy of the incident ions: Kinetic energy of the ions is directly related with the applied voltage between target and substrate, which is associated with the electrical power applied to the cathode, and is important parameter for the sputtering yield. The relationship of the ion energy and the sputtering yield is depicted in figure 2.10. As it can be seen there is minimum threshold energy in order to sputter atoms from the target (around 50 eV) which is depending on the nature of the incidence atom as well in the mass and atomic number of the target atoms. Also, an increase of the incidence ion energy leads to a respective increase of sputtering yield

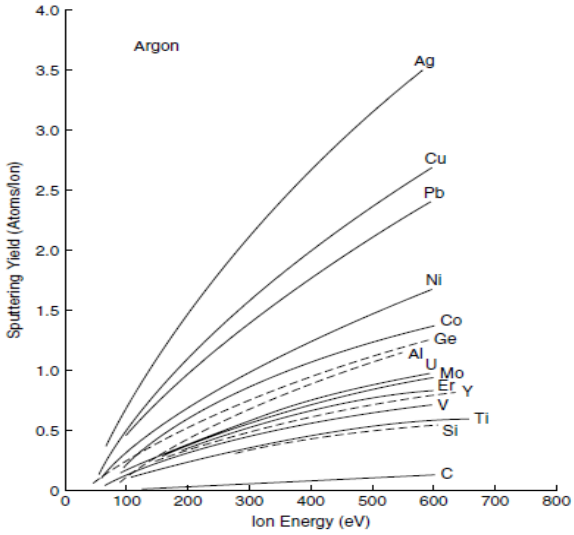

Figure 2.10. Sputtering Yield of different elements with respect to Ar ions energy. A minimum amount of energy is required for sputtering to occur [2.78]

Angle of incidence of the ions: The angle of incidence is one more parameter that can affect the sputtering yield. For normal incidence the accelerating ion will react with a small fraction of the surface and a small amount of target atoms will be emitted. However, as the angle is getting small the volume affected by the impact is moved closer to the surface and as result more atoms will be ejected from the surface. Finally, for a grazing incidence angle the ions will simply reflect from the surface and low sputtering will occur.

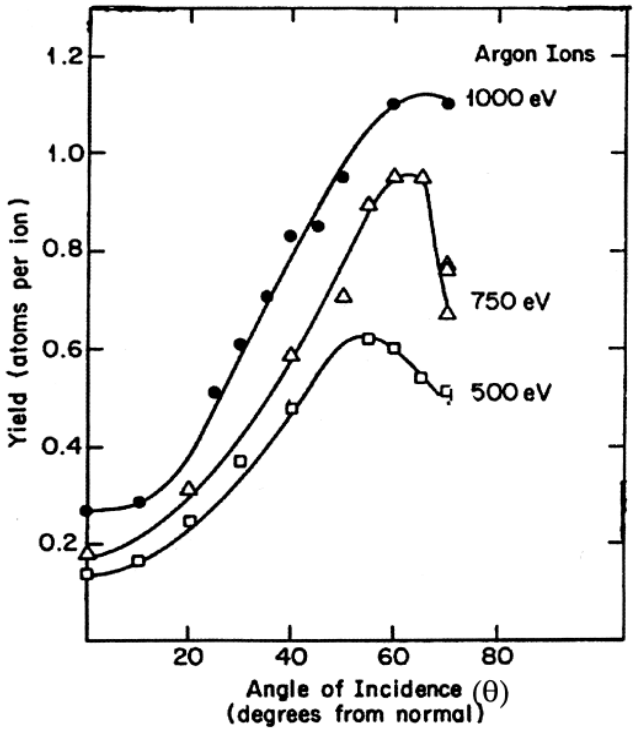

Figure 2.11. Sputtering yield of diamond s a function of sputtering angle for different Ar ions energy [2.15]

Transport of the sputtered particles through the gas phase

The ejected atoms from the sputtering target are transported through the gas phase to the substrate in order to deposit in the substrate. During their travel a number of collisions with other atoms in the chamber take place and this may reduce the ability the sputtered atoms to arrive in the anode.

Important role to this process plays the mean free path, the distance to be run by an ejected atom between two successive collisions with other atoms in the chamber. Mean free path depends on the pressure in the chamber, the temperature of the gas as well the size of the molecule. So by tuning, mainly, the pressure of the chamber we can tune the mean free path of the atoms.

Deposition of the film.

This is the final and most important stage as thin film growth occurs. Thus, there are some parameters such as substrate temperature and applied negative substrate bias with which we can change the flux and the kinetic energy of the species and consequently the desired properties of the grown film.

By heating the substrate we have the opportunity to provide the required energy to the atoms which are deposited to the substrate so that they can diffuse and form a film without defects and with a better crystallinity. Additional substrate heating can also be used as a means of surface cleaning from impurities such as oxides in the substrate surface.

A second possibility that also affects the flux of the deposited species as well the kinetic energy is the application of a negative bias on the substrate. This parameter can lead to better adhesion of the material to the substrate during the initial stages of the deposition. It can also contribute in grown more dense film or it can change the electric properties of some dielectric materials.

Finally, one very important process that occurs during the particle target interaction is the neutral backscattering ions that reflected and return to the substrate. The impingement of those ions in the film surface or even the implantation into the film can lead in changing the properties of the film such as surface topography modification, changes in interplanar spacing, reduction of film grain size and other. This is particularly important for high sputtering power densities such as those used for the sputter growth of crystalline w-AlN in this thesis.

2.3.1.1 DC-RF Sputtering

Direct Current (DC) and Radio Frequency (RF) sputtering are two different modes of sputtering that are used for thin film deposition, both in industrial and laboratory scale and schematically are depicted in figure 2.12

DC Sputtering historically, is the first sputtering mode that has been used for thin film growth and is based on the application of a direct current (DC) in the cathode leading in a DC plasma formation.

Although this configuration is very simple, it has some disadvantages and limitations such as the inability in deposition of insulating materials due to surface charging.

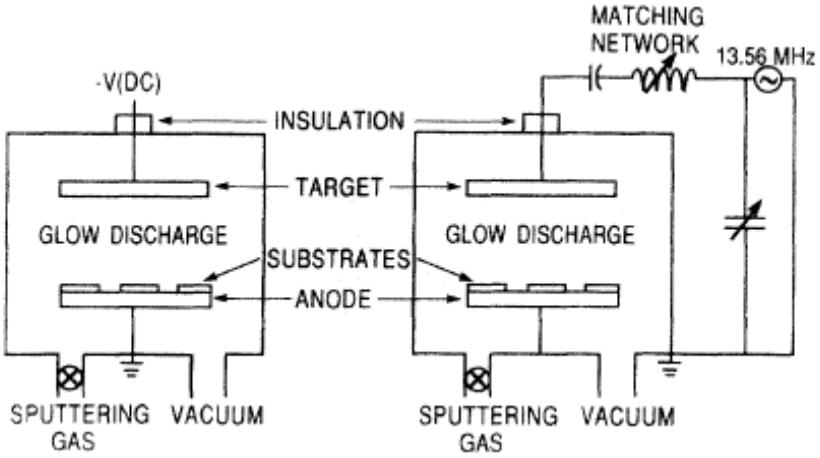

Figure 2.12. Schematically illustration of basic DC (left) and RF (right) sputtering configuration. In RF configuration a matching network is applied between the electrode and the power supply. [2.1]

Although an increase in gas density could be a solution for increasing the deposition rate due to increased ionic collisions in the gas face, however this option is not totally ideal because increasing gas density would simultaneously decrease the mean free path of the ions and thus fewer ions would reach to the anode.

The application of a Radio Frequency signal can eliminates the disadvantages and the limitations that discussed previously. Typical RF frequencies employed range from 5 to 30 MHz. However, 13.56 MHz has been reserved for plasma processing by the Federal Communications Commission (FCC) and is used in most industrial equipment.

Unlike to DC mode, in RF configuration an impedance –matching unit is placed between the power supply and the electrode so that the capacitor of the matching unit blocks the DC potential and minimizes the reflected power tuning the impedance accordingly.

In RF sputtering due to high frequency, electrons that oscillate in the glow region acquire enough energy to cause ionizing oscillations. Because of the high electron mobility the target is self-biased to a negative potential. As a result there is no charging of an insulating surface and sputtering of such a surface can be achieved. Moreover the trapped secondary electrons into the plasma can cause additional ionization, compared to the DC mode. This results in a high plasma density at the same pressure leading in high deposition rates.

2.3.1.2 Magnetron Sputtering

The simultaneous application of a permanent magnetic field together with an electric field during sputtering is the concept of magnetron sputtering technique. The applied magnetic field can be applied either as parallel or perpendicular to the electric field. The parallel magnetic field

is not efficient enough and the only benefit is that prevents secondary electrons from being lost is the chamber walls. Furthermore, a delay to the backscattering electrons to arrive at the substrate is observed. Contrarily, a perpendicular, to the electric field, magnetic field optimizes the sputtering operation. Specifically, secondary electrons are trapped close to the target surface, increasing the number of collisions leading in a greater number of ejected atoms from the target and thus in higher depositions rates

Usually magnetrons are placed just below the target and their form depends on the form of the target while a cooling system for the magnetrons is also used. It is worth noticing that magnetrons are placed in that way so that dynamic lines of the magnet field enfold the target.

Magnetron Sputtering is a widely used form of sputtering for thin film growth mainly due to the high depositions rates that are achieved while through the years different configurations are manufactured such as planar, toroidal, toroidal-conical etc.

2.3.1.3 Reactive Sputtering

In reactive sputtering simultaneously with the carrier gas a reactive gas is used as well, in order to grow compound films from pure metallic targets, for example growth of AlN from Al metallic target in Ar and N_2 ambient.

The most widely used compound films that are deposited based on reactive sputtering are:

- Oxides (e.g. Al_2O_3, SiO_2) using reactive O_2
- Nitrides (e.g. AlN, TiN) using reactive N_2
- Carbides (e.g. SiC) using reactive volatile hydrocarbons (e.g. CH_4, C_2H_2)

Although reactive sputtering is used extensively, the formation of high purity compound targets for the deposition of compound films is also an option. There are some parameters that can guide us in making the choice between reactive sputtering or the use of a compound target:

Target Purity: Preparation of high purity metallic targets is much easier and cost effective instead of creating high purity compound targets. Moreover, because a mixture of powders is used in the second case impurities are inevitable.

Deposition Rate: The usage of the reactive gas leads in the formation of compounds on the target surface, a process also called “target poisoning”. Furthermore, sputtering yield of compound targets is very low possible due to contaminations that reaches the sample or the different bonding between the target atoms which affects the effective sputtering yield γ_{ell} [2.76, 2.77]. Generally, deposition rate is proportional to the reactive gas pressure while a pre-sputtering with the initial gas is indispensably for the removal of the compounds from target surface.

Stoichiometry and Properties: Depending on the deposition conditions and in combination with the reactive gas we can provide different stoichiometry and properties to the growing film.

2.3.2 Experimental Set Up

The depositions of the thin films within this PhD thesis were performed by a dual-cathode RMS (DCRMS) in a custom made, high vacuum($P_b=2\times10^{-6}$ mbar) deposition chamber (Figure 2.13),. The DCRMS consisted of two 2 inch unbalanced magnetrons in confocal geometry (45^o angle of incidence) and a target placed 5 cm away from the magnetrons' surface. The growths were carried out at room temperature while the substrate was able to rotate during the depositions. For the binary AlN-Ag system growth a DC and RF voltage were applied to the Al and Ag targets respectively while the deposition took place in an Ar/N_2 mixed environment. In addition, in order to grow the ternary AlInN system pure In pieces were placed onto the Al surface target while by varying the number of the In pieces we could control the concentration x in our films. Finally, in all cases a pre-sputtering process, with gun shutters closed, was performed for cleaning the targets surfaces using only Ar as sputtering gas.

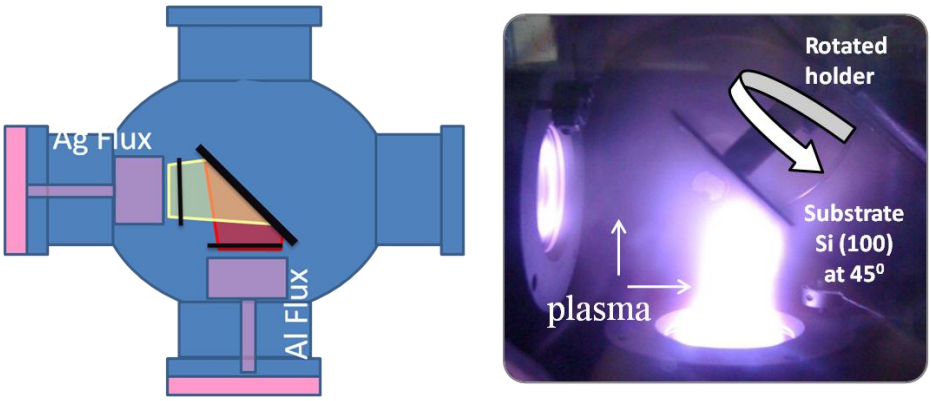

Figure 2.13. *Left:* Schematically illustration of the experimental set up. *Right:* Image inside of the chamber during Al and Ag cosputtering in Ar/N_2 mixed environment.

2.3.3 Pulsed Laser Deposition (PLD)

The development of powerful, high photon flux, Q-switched lasers has drastically changed our perception of light-matter interactions and opened new ways of implementing laser sources for the growth and processing of nanostructured materials. Thus, Pulsed Laser Deposition has become a well-established technique for the growth of carbon nanotubes [2.63-2.65], diamond

like carbon and ultra nano-crystalline diamond [2.66-2.68], nanocomposite films and coatings with finely controlled dispersion of nanoparticles (NPs) and super lattices [2.69-2.71].

The utilization of a powerful laser beam gives the opportunity to prevail over other techniques like evaporation and sputtering for some materials where it is not possible to be applied such as in case of high temperature superconductors (HTS) where high temperatures are required [2.72].

The wide use of PLD is based on its unique combination of assets such as:

1. Clean character, since usually no carrier or precursor gas is required for PLD; the cleanliness of PLD is usually comparable to molecular beam epitaxy (MBE).
2. Retaining the targets composition in the grown film, unlike sputtering and evaporation.
3. Fine control of the kinetic energy of the deposited species.
4. Extremely high deposition rate and nucleation density during the laser pulse (although the effective deposition rate is usually very low due to the pulsed mode, which incorporates immense dead times), which as a result alter the kinetic and thermodynamic conditions of growth.

The basic instrument for all laser processes of materials is the laser source itself. The laser source consists of a power source used for the optical pumping, which might be electricity or a strong light source (e.g., the flash lamps of the typical Nd:YAG solid state lasers or another laser source), the active medium and the resonator (or cavity). The active medium can be either a mixture of gases (e.g., He–Ne) or liquids (e.g., various dyes) or a solid state crystal with a controlled concentration of optically active impurities, e.g., Nd impurities in an Yttrium–Aluminum Garnet for Nd:YA lasers or Ti color centers into an Al_2O_3 crystal for Ti:Sapphire lasers. The stimulated optical emission takes place into the active medium. The resonator is usually a tube with two assembled mirrors. The one mirror is highly reflective and the other is semi-reflective (the latter is also called the aperture) and the active medium is located between them. The stimulated optical emission occurs along the central axis of the resonator

The laser sources can be categorized to CW and to pulsed Q-switched lasers. The CW-lasers operate resonators with one partially reflective (50–80%) mirror out of which a continuous optical beam is emitted continuously. On the other hand, a Q-switched laser (Figure 2.14), is based on the introduction of an electro-optic or acousto-optic modulator (e.g., Kerr cell, Pockel cell, etc.) intersecting the central axis of the resonator.

The modulator for low-Q (low quality factor) conditions is transparent to the emitted laser light along the central axis of the resonator while for high-Q conditions transmits the emitted photons to another direction and through an aperture the laser beam is emitted out of the

resonator. In this mode of operation, the modulator is in low-Q conditions, for most of the time, building the appropriate intensity of the laser beam through successive passages of the emitted photons through the active medium. When the desired laser intensity is built, the modulator is switched to high-Q conditions. This results in high peak power (usually in the range 10^8–10^{16} Watt/cm^2) as the average power of the laser is packed into an ultrashort time frame and, thus, a laser pulse of immense power is emitted through the aperture.

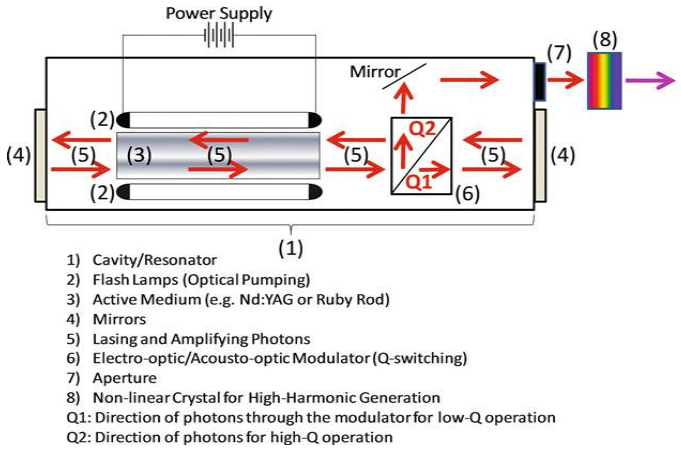

Figure 2.14. An internal view of a Q-switched pulsed laser source [2.40]

The pulse duration can range from several tens of ns (10^9 s) to a few tens of fs (10^{15} s). Special crystals can be adapted on the aperture of the laser source in order to generate high harmonics of the light and, thus, emit laser beams of various wavelengths (e.g., for the most popular Nd:YAG lasers the emitted wavelengths can be 1,064, 532, 355, 266, and 213 nm). The most common types of lasers that used in PLD technique are presented in Table II below.

Table II. The most common types of lasers used for PLD and their basic features [2.40]

Laser type	Pulse duration	Wavelength (nm)	Spectral region
Excimer ArF	ns	193	Far UV
Excimer KrF	ns	248	UV
Nd:YAG	ns-ps	1,064(fundamental) 532 (2nd harmonic 355 (3rd harmonic) 266 (4th harmonic) 213 (5th harmonic	IR Green UV UV UV
Ti:Sapphire	fs	800 (fundamental) 400 (2nd harmonic)	NIR Violet

PLD is based on the phenomenon of laser ablation which at a superficial level, might be viewed simply as a rapid boiling of material within a localized interaction volume at, and close to, the surface of the target, while a focused pulsed laser beam of high fluence illuminates the target material (Figure 2.15) [2.31].

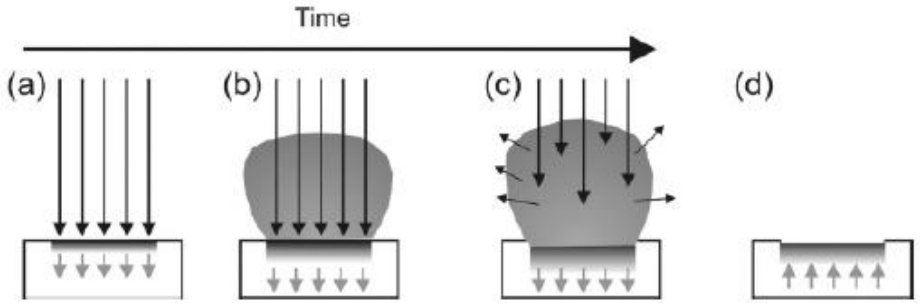

Figure 2.15. Schematic illustration of the PLD mechanism.(a) Absorption of the laser beam. (b) Melting and vaporization of the target-plume formation (c) Absorption of the incident laser beam by the plume and plasma formation. (d) Melt front recedes leading to eventual re-solidification [2.31]

The usual fluence used in PLD with pulse duration of the order of ns ranges from a few mJ/cm^2 to several tens of J/cm^2. The fluence when shorter laser pulses (e.g., ps or fs range) are used is lower but the radiation power is still higher. The used fluence is usually equivalent to 1–100 billion times the power density of arriving sunlight on the surface of the earth for the pulse duration and for the specific illumination area. The laser irradiation induces vaporization, via heating of the target, and formation of plasma via ionization of the target atoms. In particular, the removal of atoms from the bulk material is usually done by a Coulomb explosion due to multi-photon ionization of near surface atoms, given that the laser fluence is of the order of some J/cm^2 (high fluence is a prerequisite for this process, since it ensures a high probability of multi-photon ionization, which is taking place in a time interval of the order of few ps). Subsequently the electrons that become free after the ionization process oscillate within the electromagnetic field of the laser (given that the pulse duration is relatively longer than the ionization process, i.e., pulse duration in the range of ns) and can interact with the target atoms inducing electron–phonon interactions resulting to target heating and vaporization.

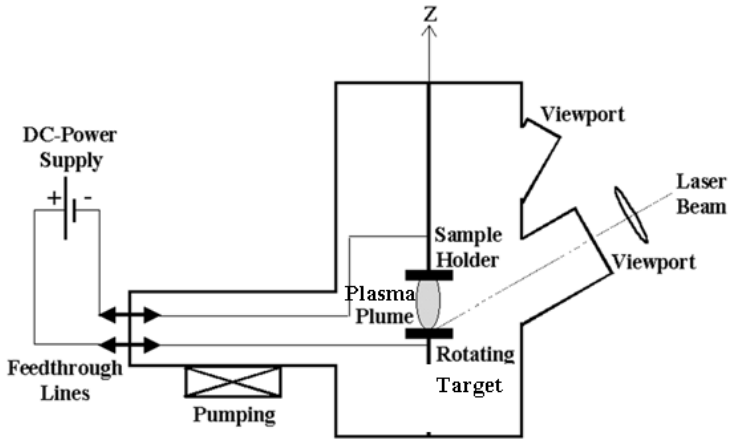

Figure 2.16. Basic configuration of a PLD set up.

The mixed vapors and ions of the target material are called the plume. The kinetic energy of the ablated species may vary with the laser wavelength and fluence in the range from a few eVs up to hundreds of eVs. After the creation of the plume the material expands within a cone, whose axis is parallel to the normal vector of the target surface toward the substrate due to Coulomb repulsion (for ions) and adiabatic expansion of the pressurized vapors. These processes are displayed schematically in figure 2.17.

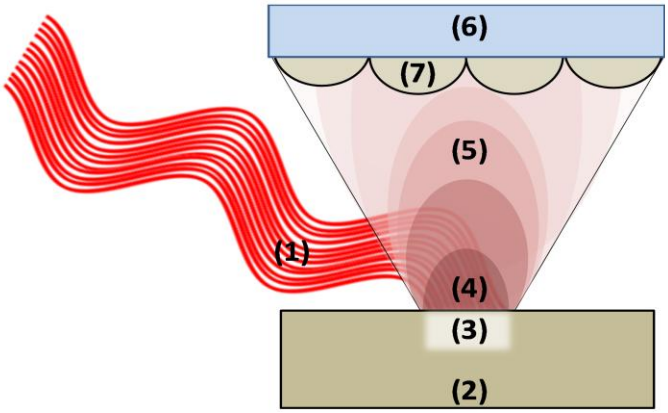

Figure 2.17. Illustration of laser-mater interactions that take place in the target. (1) laser beam, (2) the material-target, (3) interaction region of laser-mater, (4) laser-gas interactions (plume), (5) ionized gases, (6) substrate, (7) vapor condensation and thin film growth [2.40].

PLD combines many assets of thermal techniques (such as MBE and evaporation) like the clean character, and of ionic techniques (such as sputtering) like the flexibility in controlling the kinetic energy of the deposited species. The main advantages of PLD can be summarized as:

- Flexibility in creating high/low-energy species,
- Low working pressures resulting to higher diffusion of arriving species and subsequently to better crystalline quality of the produced films,
- Ion–solid interactions (implantation, cascades, etc.),
- Clean character; no impurities
- Growth of metastable phases

However, PLD has also some drawbacks like:

- Thickness inhomogeneity (i.e., smaller samples compared to other physical or chemical vapor deposition techniques),
- Relatively high surface roughness (droplets/clusters),
- Low-effective deposition rate (few nm/min).

We should point out that although the apparent deposition rate for PLD is very low, compared to other PVD-techniques, such as sputtering, and it is usually of the order of few nm/min, the real deposition rate is in the order of magnitudes higher because of the pulsed character of deposition (Figure 2.18). Thus, the deposition takes place in a time interval which is comparable to the pulse duration (a few ns or ps or fs), followed by a dead time which is in the range of 0.1–100ms for 10Hz to 10 kHz repetition rate. In conclusion the real deposition rate during the laser pulse is about
10^{-2} nm/pulse, which is equivalent to about 106 nm/s and it is much higher than any other PVD technique. The real deposition rate is not so significant for the industrial applications (where the apparent or average deposition rate is the key parameter). On the other hand, the immense real deposition rate is very important for the kinetics and thermodynamics of growth, especially for multi-component films.

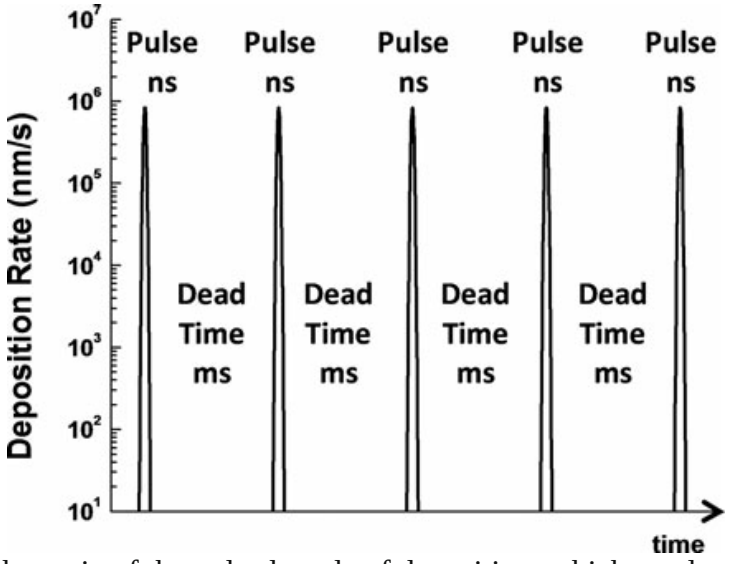

Figure 2.18. A schematic of the pulsed mode of deposition, which results to a succession of immense deposition rate during the pulse followed by a dead time [2.40]

Although the description above gives the impression that PLD is a versatile technique, in fact the processes that take place during laser beam-material interaction is quite complicated. The mechanism that takes place in the target and is responsible for the material evaporation can be sub-divided into primary and secondary processes.

We must also point out that we have the ability to introduce reactive gases into the vacuum chamber in order to grown films like nitrides and oxides [2.73-2.75]. Background gas can affect the plume distribution which presents an ellipsoid configuration. Specifically, for low gas pressures (< 1 Pa) plume expansion is the same as in vacuum without reactive gas. When the gas pressure is about 10-100 Pa a compression is applied to the plume shrinking it. Finally when the gas pressure is over 100 Pa a strong confinement of the plume is observed. Plume characteristics can also be affected from the kinetic energy of the plume species which are associated with parameters such as laser wavelength and power density.

Kinetic energy of the plume species is a crucial factor, as in sputtering, for the desired properties of the deposited thin film. Nonetheless, there are also, parameters that can determine the properties of the film such as laser wavelength, repetition rate, substrate temperature.

Laser wavelength: laser wavelength can lead in thermal or non thermal process.

Repetition rate: Can define the degree of the supersaturation of the evaporated material that affects on the growth mode of films. Island growth (*Volmer-Weber growth*), layer growth (*Frank-Van der Merwe growth) or Stranki-Krastanov* are also occur in PLD thin film deposition

Substrate temperature: is usually applied in order to give extra mobility to the arriving species usually for epitaxial growth. At room temperature, amorphous thin films are usually grown.

2.4 POST GROWTH THIN FILM PROCESSING

Sometimes the grown films exhibit different properties such as crystallinity or microstructural features that are undesirable like stresses, microstructural defects etc. Thus a further processing is necessary. In addition, post-growth annealing can be used for the dewetting of films of low melting point materials, such as Ag. This is beneficial in order to promote LSPR.

A process that films are usually subjected to, in order to improve their properties is annealing. A variety of different annealing processes have been developed through the years ranging from the usage of a conventional furnace, in vacuum or not, up to a more modern and very promising process of laser annealing where a laser (usually UV) is used for the annealing. Hot plate annealing (HP) [2.41-2.44] and Microwave annealing (MW) [2.45-2.48] are techniques that can be used as well.

In this PhD thesis samples were subjected to laser annealing, meanwhile HP annealing has also been used in some cases. Basic aspects of these techniques are presented below

2.4.1 Hot Plate Annealing

Hot plate annealing is actually based on heating of a spiral resistance which is surrounded by a metal plate. Simultaneously, the heat that is emitted from the resistance is transferred to the plate leading to Hot Plate.

Based on the above we can say that hot plate annealing is an indirect process which can be distinguished in two steps. Firstly, heat transfer from the hot plate to the substrate which are in direct contact and subsequent heating of the film.

Figure 2.19. *Left:* Hot plate set up. *Right:* Heated resistance.

Although hot plate annealing is a fast and user-friendly technique and applicable in all materials, however the uneven thermal distribution is a major disadvantage (Figure 2.20) causing reproducibility issues,

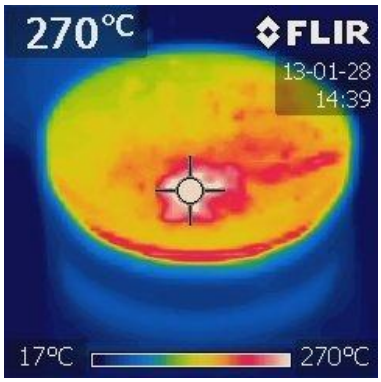

Figure 2.20. Hot plate image using a thermo camera. An uneven thermal distribution can be observed.

2.4.2 Laser Annealing

Laser annealing is a rapid thermal process where extensive diffusion effects can be avoided. This major advantage as well as its applications in industrial scale has lead in its rapid growth in recent years in the material science, turning it into a powerful technique [2.48-2.62].

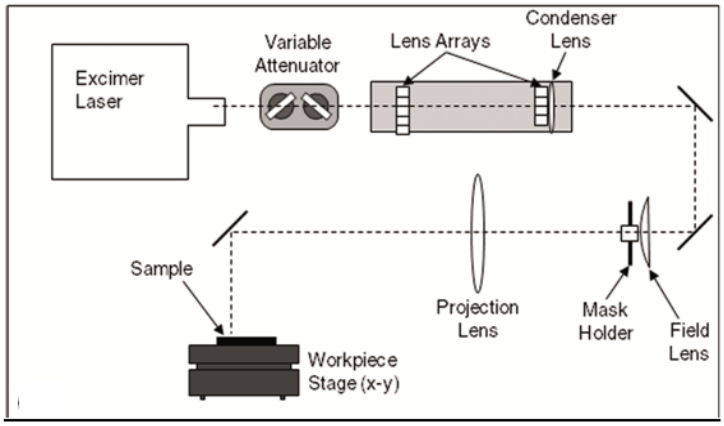

Figure 2.21. Basic configuration of laser annealing [2.56].

This process is based in the photon absorption through inter- or intra-band electronic transitions. The absorptions cause an alteration in the electron distribution of the materials that thermalizes via electron-electron and electron phonon interactions, as already reported in a

variation of works in laser-solid interactions [2.34, 2.35]. Thus, the electronic and lattice dynamics must be taken into account in order to understand the effect of the laser annealing.

Consequently, two interrelated equations (Eqn. 2.14, 2.15) can be applied for the total description of the heat transfer in a material [2.24]:

$$C_e \frac{\partial T_e}{\partial t} = \nabla(k_e \nabla T_e) - H(T_e T_L) + S(t) \tag{2.13}$$

$$C_L \frac{\partial T_L}{\partial t} H(T_e T_L) \tag{2.14}$$

where C_e and C_L are the electronic and lattice specific heat ($Jm^{-3}K^{-1}$) respectively, $S(t)$ is the absorbed laser power per unit volume (Wm^{-3}), $H(T_e T_L)$ is the rate of energy transfer between lattice and electrons (Wm^{-3}) and $\nabla(k_e \nabla T_e)$ is the diffusive electronic heat transfer.

The processes taking place when the laser radiation hits a material depend on the amount of deposited laser energy. This energy and its spatial and temporal distribution determine what kind of material modification will occur. The main laser-solid interaction process is the excitation of electrons from their equilibrium states to some excited states by absorption of photons. These typical single photon processes are well-known in a wide field of physics. Other possible excitations involve multiphoton electronic transitions. At a constant laser fluence, a shorter laser-material interaction time favors multiphoton excitation processes, because the probability of nonlinear absorption increases strongly with a growing laser intensity.

In laser annealing process both material and substrate parameters such as transparency, thermal conductivity, optical band gap etc. can play dominant role. Thus, we need lower laser fluence for lower thermal conductivity substrates.

References

[2.1] Ohring M. *The Materials Science of Thin Films,* Academic Press (1992).

[2.2] Seshan K., *Handbook of Thin Film Deposition Processes and Techniques. Principles, Methods, Equipments and Applications (second edition)*, Noyes Publications (2002).

[2.3] Powell A. R., Rossnagel S., *PVD for Microelectronics: Sputter deposition applied to semiconductor manufacturing*, Volume 26, Academic Press (1999).

[2.4] Harsha S.K.S. *Principles of Vapor Deposition of Thin Films (first edition),* Elsevier (2006).

[2.5] Freund L.B., Suresh S., *Thin Films Materials: Stress, Defect Formation and Surface Evolution*, Cambridge University Press (2003).

[2.6] Robins J.L., *Applied Surface Science.* **33/34** (1988), pp. 379-394.

[2.7] Grabow H.M., Gilmer H.G., *Surface Science*, **194** (1988), pp. 333-346.

[2.8] Bay H.L., Bohdansky J., *Appl. Phys.*, **19** (1979), pp.421-426.

[2.9] Yoshitake M., Yamauchi Y., Bose C., *Surf. Interface Anal*., **36** (2004), pp. 801-804.

[2.10] Sedehi A., Meiksin H., Blachere J.R., *Thin Solid Films,* **98** (1982), pp. 49-58.

[2.11] Musil J., Baroch P., *et al., Thin Solid Films*, **475** (2005), pp. 208-218.

[2.12] Seah M.P., *Thin Solid Films*, **81**(1981), pp. 279-287.

[2.13] Stowell M.J., Hutcinson T.E., *Thin Solid Films*, **8** (1971), pp. 41-53.

[2.14] Reichelt K., *Vacuum,* **38**(1988), pp. 1083-1099.

[2.15] Smentkowski V.S., *Progress in Surface Science,* **64** (2000), pp.1-58.

[2.16] Iverson M.S., Litster D.J. *et al., Powder Technology,* **117** (2001), pp. 3-39.

[2.17] Evans J.W., Thiel P.A., Bartelt M.C., *Surface Science Reports,* **61** (2006), pp. 1-128.

[2.18] Harsdorff M., *Thin Solid Films*, **90** (1982), pp. 1-14.

[2.19] Stringfellow, *Journal of Crystal Growth*, **137** (1994), pp. 212-223.

[2.20] Kinbara A., Kusano E., Kondo I., *Vacuum*, **51** (1998), pp. 475-478.

[2.21] Berg S., T. Nyberg, *Thin Solid Films,* **476** (2005), pp. 215-230.

[2.22] Ratsch C., Zangwill A., *Surface Science*, **293** (1993), pp. 123-131.

[2.23] Venables A.J., *Surface Science*, **299/300** (1994), pp. 798-817.

[2.24] Schaaf Peter, *Laser Processing of Materials. Fundamentals, Applications and Developments*, Springer (2010)

[2.25] Boardman D.A., Cresswell B., Anderson J., *Applied Surface Science*, **96/98** (1996), pp. 55-60.

[2.26] Lowndes H.D., Geohegan B.D., *et al., Science*, **273** (1996), pp. 898-903.

[2.27] Aziz M.J., *Appl. Phys. A.,* **93** (2008), pp. 579-587.

[2.28] Scharf T., Krebs H.U., *Appl. Phys. A.,* **75** (2002), pp. 551-554.

[2.29] Habermeier H.-U., *Applied Surface Science,* **69** (1993), pp. 204-211.

[2.30] Krebs H.U., *Advances in Solid State Physics*, **43** (2003), pp. 505-518.

[2.31] Ashfold, M.N.R., Claeyssens F. et al., *Chem. Soc. Rev*., **33** (2004), pp. 23-31.

[2.32] Palani I.a., Vasa N.J., Singaperumal M., *Materials Science in Semiconductors processing*, **11** (2008), pp. 107-116.

[2.33] Cheng Yi-Ting, Uang Rough-Huey et al., *Microelectronic Engineering,* **86** (2009), pp. 865-867.

[2.34] Von der Linde D., Sokolowski-Tinten K., Bialkowski J., *Applied Surface Science,* **109/110** (1997), pp. 1-10.

[2.35] Wood R.F., Giles G.E., *Physical Review B,* **23** (1981), pp. 2923-2942.

[2.36] http://en.wikipedia.org/wiki/Contact_angle

[2.37] Morchan B., Deuchishin A., *Phys. Met. Metallogr*., **28** (1969), pp. 653660.

[2.38] Thornton A.J., *J. Vac. Sci. Technol.,* **11** (1974), pp. 666-670.

[2.39] Anders A., *Thin Solid Films*, **518** (2009), pp. 4087-4090.

[2.40] Patsalas P., *Nanoscience & Technology*, **59** (2012), pp. 59-83.

[2.41] Yong-Hoon K., Kwang-Ho K., Sung Kyu P., *J. Nanosc. Nanotechn,* **13** (2013), pp. 7779-7782(4).

[2.42] Li, Q., Li, X.-F., Zhang, J.-H., *Gongneng Cailiao/J. Funct. Mater.* **, 44** (2013), pp. 442-445.

[2.43] Shin, H.-S., Yun, H.-J., Baek, K.-H., *et al., J. Nanosc. Nanotechn.,* **12 (**2012), pp. 5325-5329.

[2.44] Chung, Y.-D., Cho, D.-H., *et al., Current Applied Physics***, 11** (2011), pp. S65-S67.

[2.45] Chuen-Yuan H., Jing-Wen H., *et al, Nanotechnology*, **21** (2010), 035302 (6pp).

[2.46] Filippo E., Manno D., *et al*., *Superlattices and Microstructures*, **47** (2010) pp. 66-71.

[2.47] Minfeng Chen, Hung-chun Chang, *J. Quantum Electronics*, **45** (2009) pp1558-1562.

[2.48] Stepanov A. L., Valeev V. F. , *et al, Technical Physics Letters*, **34** (2008).

[2.49] Nedyalkova N.N., Nikova R, *et al*., *Applied Surface Science*, **258** (2012) pp. 9162– 9166.

[2.50] Takami A., Kurita H., Koda S., *J. Phys. Chem. B,* **103 (**1999), pp. 1226-1232.

[2.51] Henley J.S., Beliatis J.M. *et al*., *Nanoscale,* **5** (2013), pp. 1054–1059.

[2.52] Beliatis J.M., Henley J.S., *et al*., *Phys.Chem. Chem. Phys.,* **15 (**2013), pp. 8237-8244.

[2.53] Peng P., Hu A., Zhou Y., *Appl Phys A*, **108** (2012), pp. 685–691.

[2.54] Yang Y., Zhang Y.M., Cheng J.G,, *Appl. Phys. Lett*., **99** (2011), pp. 091901.

[2.55] Tseng M.L, HuangY-W, Hsiao M-K, *et al., ACS Nano*, **6** 2012, pp. 5190–5197.

[2.56] Siozios A., Koutsogeorgis D. C.,*et al., Nano Lett.,* **12** (2012), pp. 259-263. [2.57] Bazioti C., Dimitrakopulos G.P.,*et al., J. Mater. Sci.,* **49** (2014), pp. 3996-4006.

[2.58] Siozios A., Zoubos H.,*et al.,Surf. Coat. Technol*., **255** (2014), pp. 28-36.

[2.59] Grochowska K., Śliwiński G., *et al*., *Plasmonics*, DOI 10.1007/s11468-012-9428-3.

[2.60] Rao, S.S., Lee,Y.F., *et al., App. Phys. Let*., **105**, (2014).

[2.61] Koutsogeorgis, D.C. , Cranton, W.M., *et al*., *J. Alloys and Compounds*, **483**, (2009), pp. 526-529.

[2.62] Tsakonas C, Cranton W.M., *et al., J. Phys. D: Appl. Phys*., **46** (2013), pp. 095305.

[2.63] Zhang M., Yudasaka M., S. Iijima, *Chem. Phys. Lett*. **336** (2001), pp. 196.

[2.64] Zhang Y., Gu H., Iijima S., *Appl. Phys. Lett*. **73** (1998), pp.3827.

[2.65] Yang E.H., Strauf S., Fisher F., *D.S. Choi, Proc. SPIE* **7318** (2009), art. no. 731813.

[2.66] Cappelli E., Scilletta C., *et al*., *Appl. Phys. A* **93** (2008).

[2.67] Yoshitake T., Nagano A., *et al.. J. Appl. Phys. L*. **46** (2007).

[2.68] Patsalas P., Kaziannis S., *et al*.,, *J. Appl. Phys*. **101** (2007), art. no. 124903.

[2.69] Lotsari A., Dimitrakopulos G.P. *et al., Surf. Coat. Technol*. **204**, (2010), pp. 1937-1941

[2.70] Pinakidou F., Paloura E.C., *et al., Surf. Coat. Technol*. **204** (2010)
, pp. 1933-1936

[2.71] Matenoglou G.M., H. Zoubos, *et al., Thin Solid Films* **518** (2009), pp. 1508-15011 .

[2.72] Zheng, B.J., Lian, J.S., *et al., Applied Surface Science*, **256** (2010), pp. 2910-2914.

[2.73] Koutsokeras L.E. *et al., App. Physic. Lett*., **93** (2008), 011904

[2.74] Matenoglou G.M., *et al., App. Physic. Lett*., **94** (2009), 152108.

[2.75] Matenoglou G.M, *et al., Thin Solid Films*, **518** (2009), pp. 1508-1511

[2.76] Depla D., *Nuclear Instruments and Methods in Physics Research B*, **328** (2014) pp. 65–69

[2.77] M P Seah and T S Nunney., *J. Phys. D: Appl. Phys*., **43** (2010), 253001 (13pp)

[2.78] Tractor Arthur A. *Coatings Technology: Fundamentals, Testing and Processing techniques*, CRC Press, Taylor & Francis Group (2007).

Chapter 3 *THIN FILM CHARACTERIZION*

3.1 Introduction

As mentioned previously, thin film growth has led in the development of new and at the same time unknown structures and properties, respectively. Thus, it is important every time to be able to identify the properties of the film.

A large number of techniques (destructive or not) has been developed and applied for full characterization of the thin films properties (structural, morphological and optical). X-ray Diffraction (XRD), X-Ray Photoelectron Spectroscopy (XPS) and Atomic Force Microscopy (AFM) are some of the most widly used techniques.

In this chapter we present the basics of the techniques that were used in this PhD for the thin film characterization.

3.2 Structural Characterization

Structural and microstructural characterization is a very important part of materials analysis as it gives the opportunity to identify the crystal structure and other structural parameters such as the lattice constant, grain size and lattice strain.

X-Ray Diffraction (XRD) is a common and non-destructive technique that is widely used for the derivation of structural parameters of new unidentified samples in thin film form.

3.2.1 X-Ray Diffraction (XRD)

Diffraction of an electromagnetic wave takes place when this wave encounter a number of periodically arranged "obstacles" on the length scale of the wavelength and it scatters around. X-rays are part of electromagnetic radiation with wavelength comparable to the interatomic distances in crystals. Thus, constructive and destructive interferences can be observed when a crystalline solid is exposed to X-rays.

When X-rays enter in a material, they are elastically scattered from the crystal atoms with the same wavelength λ of the incident radiation. If $\mathbf{K_0}$ is the wave vector of the incident beam and **K** wave vector of the scattered beam we can define an important parameter called scattering vector **Q,** which is equal to the difference $\mathbf{K}$-$\mathbf{K_0}$ (Eqn. 3.1) as illustrated in figure 3.1 while angle between **K** and the prolonged direction of $\mathbf{K_0}$ is the scattering angle 2θ (Fig. 3.1).

$$Q = \frac{4\pi \sin\theta}{\lambda} \qquad (3.1)$$

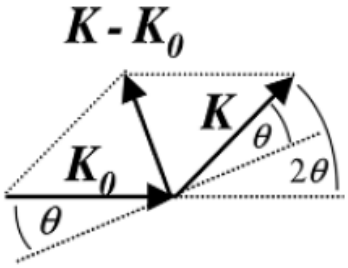

Figure 3.1. The scattering vector **Q** is the difference of the wave vector of the scattering beam **K** and the wave vector of the incidence beam $\mathbf{K_0}$.

Scattering vector Q is the parameter that gives the positions in space where constructive interferences occurs and diffraction peaks are observed. Using Laue conditions for maximum intensity and after some mathematical calculations [3.1, 3.2] we get (Eqn. 3.2) for cubic crystals [3.25].

$$\frac{Q}{2\pi} = \frac{\sqrt{h^2 + k^2 + l^2}}{\alpha} \qquad (3.2)$$

where *h, k, l* is Miller indices and α is cell parameter.

Substituting equation 3.1 to equation 3.2 we get equation 3.3:

$$\frac{2a}{\sqrt{h^2 + k^2 + l^2}} \sin\theta = \lambda \qquad (3.3)$$

The distance of two adjacent planes is given by the interplanar spacing d_{hkl} with respect to the Miller indices and the lattice parameters. For instance, in case if a cubic lattice has been found that (Eqn. 3.4):

$$d_{hkl} = \frac{\alpha}{\sqrt{h^2 + k^2 + l^2}} \qquad (3.4)$$

Rearrangement of equation 3.4 using equation 3.3 leads to equation 3.5 which is the known *Bragg's law* and gives the positions where diffraction peaks are observed.

$$n\lambda = 2d_{hkl} \sin\theta \qquad (3.5)$$

where n is the order of diffraction, λ the X-ray wavelength, d_{hkl} the interplanar spacing and θ is the scattering angle.

Bragg's law can also be extracted with geometrical considerations, as visualized in figure 3.2

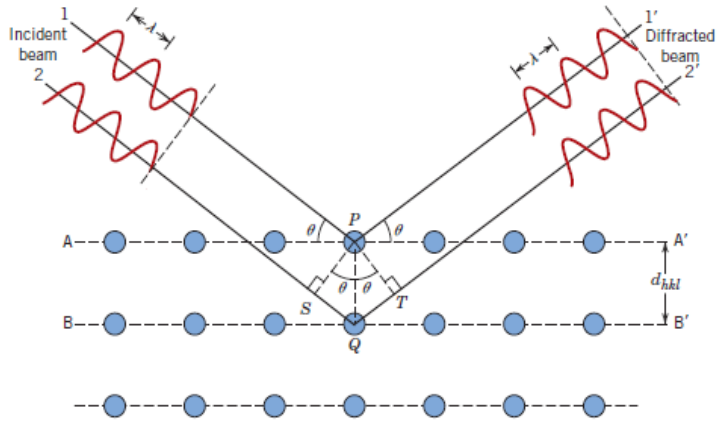

Figure 3.2. Geometrical representation of the Bragg's law [3.4]

Consider two parallel lattice planes AA′ and BB′ with spacing d_{hkl} and a monochromatic, parallel, in-phase x-ray beam of wavelength λ and with angle of incidence at both planes θ. Two rays of the x-ray beam named 1, 2 respectively will be scattered from atoms P, Q. Constructive interference of the scattered rays 1′,2′ occurs when the sum of the paths SQ and QT is equal to any multitude of a wavelength (nλ). That condition can be further written as (Eqn. 3.6):

$$n\lambda = SQ + QT = d_{hkl}\sin\theta + d_{hkl}\sin\theta = 2d_{hkl}\sin\theta \qquad (3.6)$$

which is exactly the Bragg's law (Eqn. 3.5)

X-Ray Diffraction Configurations

XRD measurements can be performed using two configurations Bragg Brentano (BBXRD) and Grazing Incidence (GIXRD), respectively.

Bragg-Brentano mode (BBXRD)

Bragg Brentano XRD (BBXRD) is the most widely used configuration for the structural characterization of a material.

In this mode the X-ray tube and the detector are simultaneously moving in a wide range of angles, clockwise and anticlockwise respectively. Although the angle of incidence and the scattering angle (detector) are varying throughout the measurement, they remain equal (θ_{in} = θ_{sca}). During the measurement the intensity of the scattering beam is monitored as a function of the 2θ angle, where 2θ is defined the angle between the scattering angle and the extinction of the angle of incidence as it is illustrated is figure 3.3. The rotation of both the X-ray tube and the detector is achieved through the rotation of the goniometer, which is placed in the center of the diffractometer.

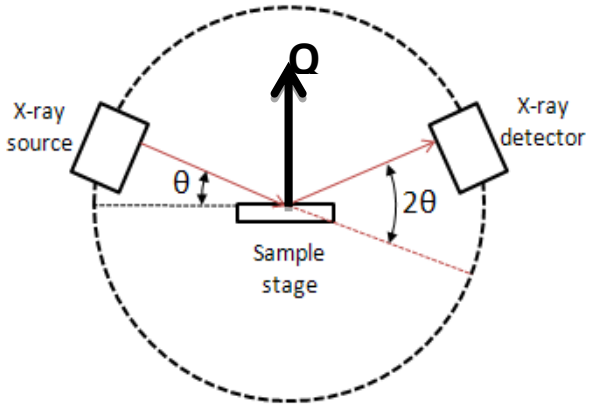

Figure 3.3. Bragg Brentano XRD geometry. X-ray tube and detector are moving simultaneously.

In Bragg Brentano mode the scattering vector **Q** is always parallel to the specimen surface normal, thus only the lattice planes that are oriented parallel to the surface give diffraction signal.

Grazing Incidence mode (GIXRD)

The second configuration that is also can be performed for the extraction of structural parameters is the Grazing Incidence XRD (GIXRD), which in this case, the incoming x-ray beam penetrates to the sample's surface at a small glancing angle α which remains constant during the measurement while the detector is moving in a 2θ mode. Nevertheless, the intensity of the scattering beam is also recorded as a function of the 2θ angle which described exactly as in BBXRD. In contrast to the BBXRD, now the angle between the outgoing beam and the sample surface is 2θ-α as depicted in figure 3.4.

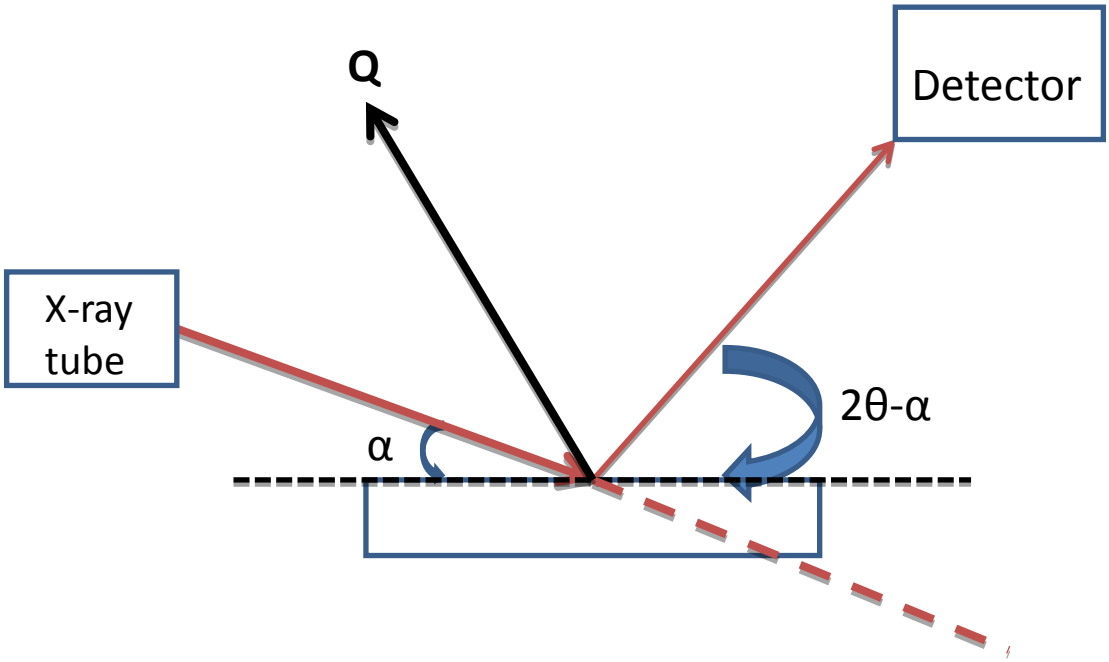

Figure 3.4. Grazing Incidence XRD configuration. Angle of incidence is remaining constant and only the detector is moving in 2θ mode.

GIXRD is usually performed for thin film characterization because the small angle of incidence increases the footprint of the measured x-ray beam on the sample surface. This results in substantially increased measured signal, but in the expense of angular resolution (thus the GIXRD peak profiles are broader). Further enhancement of the measured signal is achieved due to the longer optical path in the film as a consequence of the glancing angle of incidence.

Due to the different geometrical configuration, the scattering vector **Q** is not perpendicular to sample surface. As a result diffraction caused by lattice planes that are neither parallel with the surface nor with each other. For this reason, if a single-crystal substrate (like Si wafer) is used, there is contribution from the substrate to the diffraction pattern.

Grain Size analysis

XRD pattern analysis can be used for crystalline size estimation through the well-known Scherrer equation (Eqn. 3.7), which correlates the FWHM of the diffraction peak with the crystal size [3.25]:

$$D(\mathrm{nm}) = \frac{K\lambda}{\beta\cos\theta} \qquad (3.7)$$

where D is the grain size in nanometers, K is a shape factor with a typical value of about 0.9, λ is the wavelength of the radiation, β is the FWHM of the diffraction peak in 2θ scale and θ the respective Brag diffraction angle.

Scherrer equation is limited to nanoscale particles and is not applicable for grain larger than 0.1 to 0.2 μm and is usually applied for size estimation and not for an accurate calculation of the grain size. This is because a variety of factors like inhomogeneous strain and crystal lattice imperfections which can also contribute to the width of the diffraction peak. For stressed nanoparticles a more sophisticated analysis (Williamson Hall) is required [3.21].

Experimental set up

X-Ray Diffraction (XRD) measurements were acquired in a BRUKER D8 diffractometer equipped with an X-ray tube ($Cu_{K\alpha}$= 0,154nm), parallel beam optics (focusing Göbel mirror) and a linear strip detector with 192strips (spatial resolution of 75 micrometers) providing high resolution XRD diffractograms.

3.3 Chemical Characterization

The identification of the chemical bonding of a specimen is an integral part of material characterization. Chemical characterization is more imperative when our studies are focusing on amorphous materials where the formed phases cannot be identified by X-ray Diffraction.

X-ray Photoelectron Spectroscopy (XPS), Auger Electron Spectroscopy (AES) and Wavelength Dispersive X-ray Fluorescence (WD-XRF) are some of the most common techniques for the qualitative analysis of a sample.

3.3.1 X-Ray Photoelectron Spectroscopy (XPS)

X-Ray Photoelectron Spectroscopy (XPS) is among the most prevalent surface techniques for the quantitative and qualitative analysis of the elements that exists within the material as well the estimation of the chemical state (e.g. oxidation state) and the electronic distribution. The popularity of XPS as a surface analysis technique is attributed to its high information potential, its flexibility in addressing a wide variety of samples and its sound theoretical basis. It should be noted that although X-rays penetrate deeply into the sample, electrons from only a

few nanometers of the sample are able to escape and be emitted thus XPS is a surface sensitive technique.

Photoelectric effect is the dominant mechanism that XPS technique relies on and it is illustrated in figure 3.5. X-rays illuminate a sample causing interactions with the atom's electrons with total transfer of the photon energy to the electron leading to electron emission (photoelectrons) from the atoms.

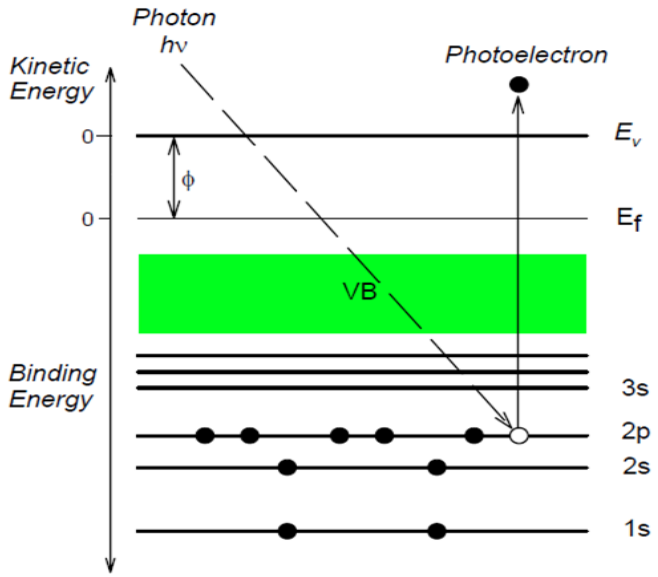

Figure 3.5. The photoelectric effect. An incident photon interacts with the atom transfers its energy to the atom leading to electron emission from the atom.

The kinetic energy of each emitted atom is recorded and the binding energy is estimated using the equation 3.8:

$$\mathrm{E_B} = \mathrm{E_{ph}} - \mathrm{E_{kin}} - \mathrm{W} \qquad (3.8)$$

where $E_B$is the binding energy of the electrons in the atomic orbital, E_{ph} is the photon energy, E_{kin} the kinetic energy of the emitted atoms and W is the work function depended on the spectrometer and the material.

The energy of the photoelectrons is related to the atomic and molecular environment from which they originated, thus it is unique fingerprint for each element.

Performing a wide scan (Figure 3.6) all the photoelectrons, from core up to valence level, is observed and elemental identification is performed. Note that all the measurements are required in UHV conditions. The background of the xps spectra is attributed to the electrons inelastic

collisions while the increased energy at binding energy 1200eV and above is due to the photon energy that were used for photoionization.

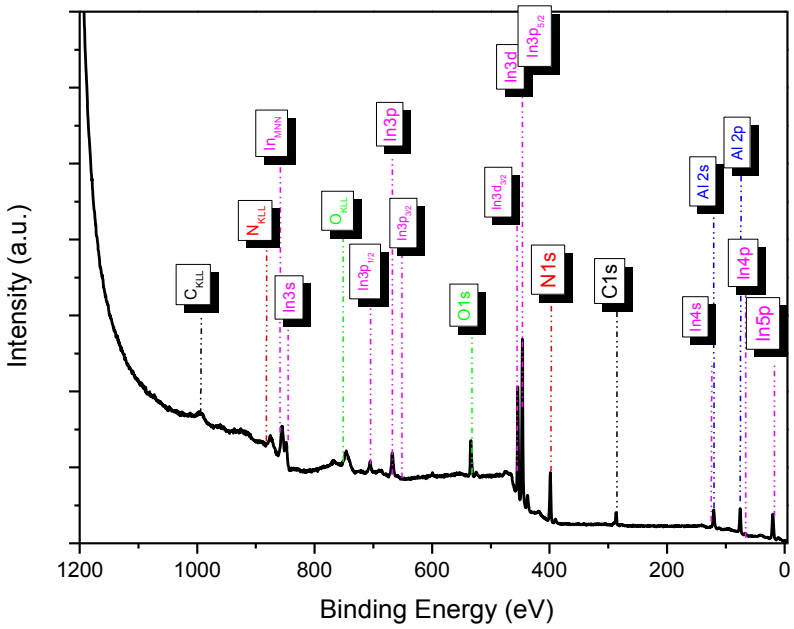

Figure 3.6. Wide scan XPS measurement of a ternary AlInN film. Through the binding energy of each peak an elementary analysis can be achieved.

Besides the elemental analysis a chemical state estimation can be held by core-level XPS measurements where we focus on the peak we are interested on and a high resolution scan is performed. Core-level XPS measurement of Al 2p electrons is illustrated in figure 3.7.

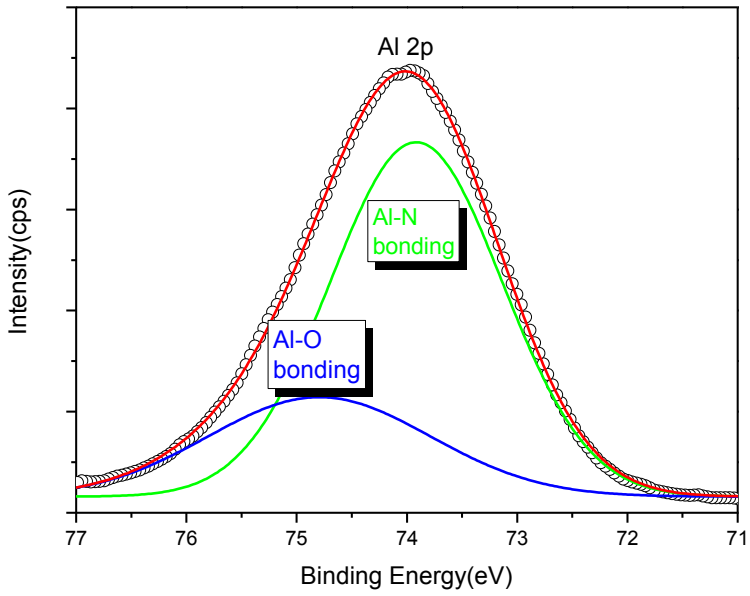

Figure 3.7. High Resolution XPS of Al 2p peak.

Experimental set up

The XPS measurements were performed in a UHV chamber (Pb=1.2x10^{-9} mbar) using a SPECS GmbH system, equipped with a non-monochromatized twin Al-Mg anode X-Ray source and a multi-channel Hemispherical Sector electron Analyzer (HSA-Phoibos 100) and schematically illustrated in figure 3.8. The base pressure in the spectrometer was 2.2×10^{-9} mbar during all measurements. The pass energy[3] was set at 20 eV providing a full-width at half maximum (FWHM) value of 1.18 eV at Ag 3d XPS peak and thus minimizing sample exposure to electron beam (measuring time). The photoelectron take-off angle was 90°.

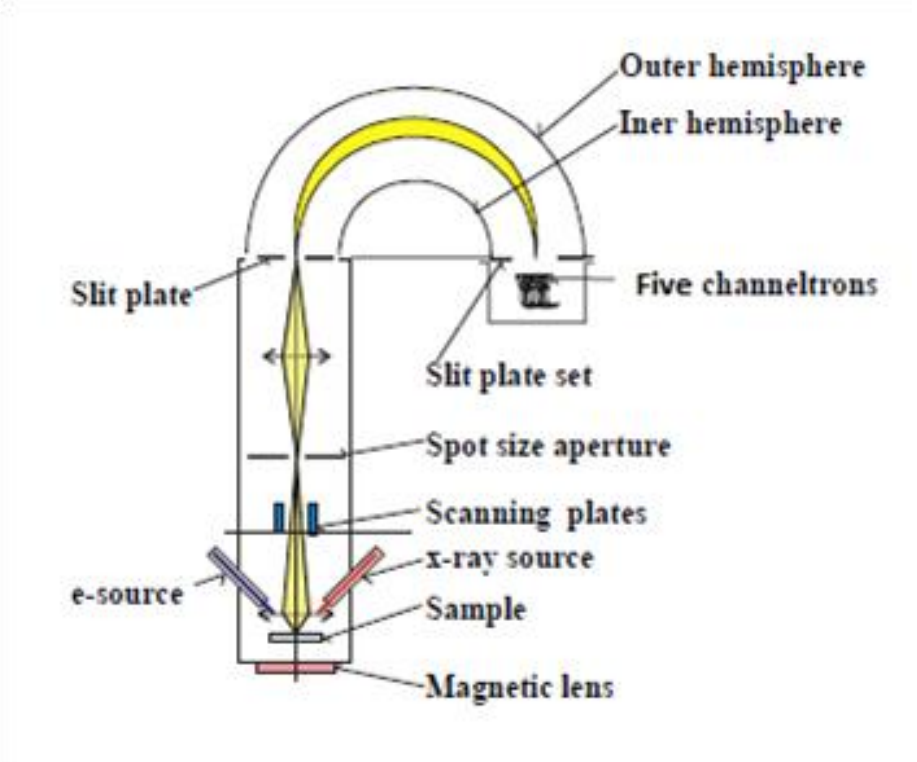

Figure 3.8 Schematic illustration of the XPS set up with the Hemispherical Sector electron Analyzer (HSA-Phoibos 100) respectively.

[3] The pass energy determines the energy resolution of the analyzer in both spectrometer mode and imaging mode. Higher pass energy reduce the energy resolution of the analyzer but increase sensitivity.

3.4 Morphological Characterization

Morphological characterization is an important chapter in thin film characterizations as it gives us the opportunity to estimate structural and microstructural characteristics like defects, grain boundaries, and roughness.

X-ray Reflectivity, Electron Microscopy and Atomic Force Microscopy are some of the widely used technique due to their advantages (high accuracy and resolution, non-distractive character except of TEM) for the morphological characterization of the films.

3.4.1 X-Ray Reflectivity

X-ray Reflectivity (XRR) is a non-destructive technique, which gives the opportunity to extract critical information about density, roughness of surface and interfaces and thickness of a film.

XRR is essentially a θ/2θ X-Ray scan but in contrast with Bragg Brentano XRD it takes place in much smaller angles, usually 0^o to 5^o degrees. The reflectogram that is recorded during the measurement can be divided in two regions, as illustrated in figure 3.9: *region I (blue)*, where an almost constant intensity (plateau) is observed and a total reflection of the beam occurs and *region II (green)* where the intensity is steeply decreasing. Between region I and region II is the critical angle θ_c which is related with the electron density [3.2] and thus the density of the specimen can be extracted. In Region II two parameters are usually investigated. Firstly, the distance between the periodical intensity oscillators (known as Kiessig oscillations) and secondly how steeply the intensity decreases. The first parameter can lead in thin film thickness estimation, while the second parameter is related with the surface roughness of the specimen and can be described by the distorted wave Born approximation as an exponential decay [3.22-3.24].

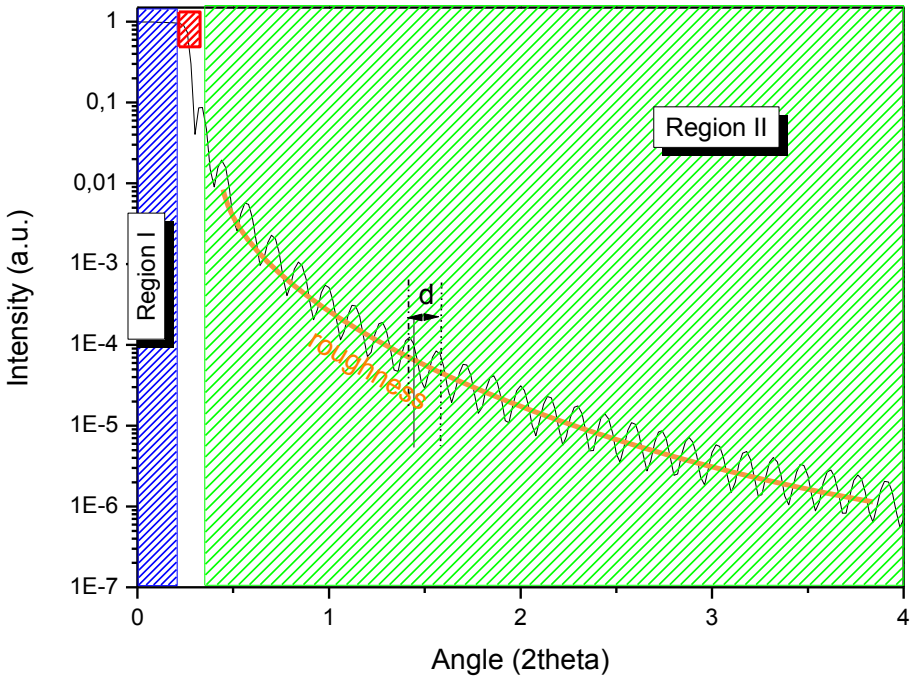

Figure 3.9. XRR measurement of AlN 30nm.

3.4.2 Electron Microscopy (EM)

Electron Microscopy (EM) exploits the electron properties when they impinge on a material surface. The basic mechanism that can take place when electrons interact with matter is illustrated in figure 3.10. Thus secondary electrons (SE) or backscattering electrons (BSE) can be observed while X-rays or Auger electron emission is also possible to occur.

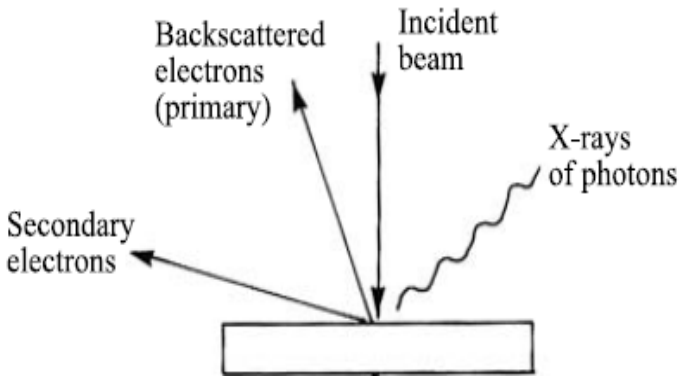

Figure 3.10. Electron-Matter interactions. Backscattering electron and Secondary electrons are produced through inelastic and elastic collisions respectively. X-ray photoemission can also be observed.

The EM exploits the wave character of the electrons and gives the opportunity to achieve higher resolution (typically down to 1nm without taking into account the instrumental

restrictions), unlike to optical microscopy where due to the wave character of the light a resolution down to 200 nm can be achieved (Figure 3.11) due to the longer wavelength of the visible light.

Scanning Electron Microscopy (SEM) and Transmission Electron Microscopy (TEM) are two of a wide variety of techniques that fall into the Electron Microscopy category. They provide information relating to several characteristic such as topographical features, morphology, phase distribution, crystal orientation and defects.

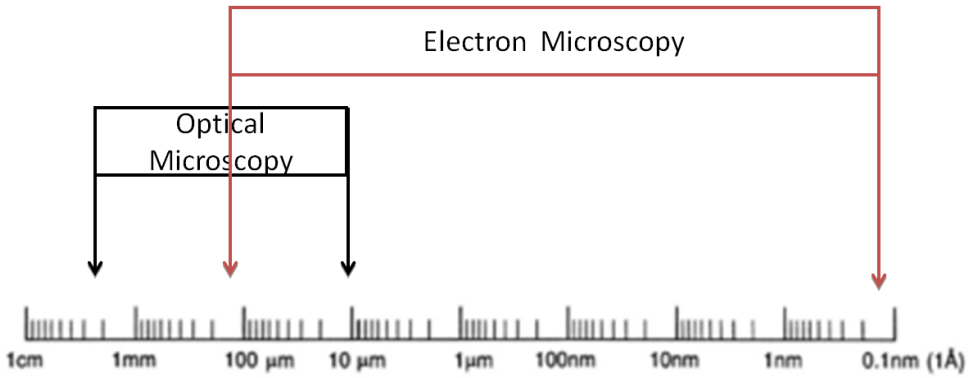

Figure 3.11. Resolution of Electron and Optical microscopy respectively. Due to the wave character of electrons Electron microscopy can provide higher spatial resolution.

3.4.2.1 Scanning Electron Microscopy (SEM)

Scanning Electron Microscopy (SEM) is based on formation, acceleration and recording of electrons that are impinging and scattered on a sample surface.

An electron gun, typically tungsten[4], is used for the emission of electrons after its heating by applying an electrical current. Electrons are accelerated by a negative voltage to the cathode (sample holder). Emission of electrons occurs at high temperatures thus a high vacuum (or ultra-high vacuum in case of field emission gun) is required.

Scanning, positioning and focusing of the electron beam on the sample surface is accomplished by the use of electromagnetic or electrostatic fields. These fields consist of various lenses which are tending to magnify and focus the beam spot onto the sample surface. A typically magnification ranges for the SEM between 10x and 100,000x.

When electrons are impinging on the sample surface, some of them can undergo inelastic collisions transferring their energy to the specimen. As a result secondary electrons (SE) are

[4] Tungsten, Lanthanum hexaboride thermionic electron guns and field emission gun are the most common electron guns that used widely today.in this PhD the used SEM employ thermionic tungsten filaments

emitted. Elastic interactions between electron and the matter can also observe leading in backscattering electrons (BSE).

Secondary electrons are low energy electrons (2-5 eV) that usually are ejected near the surface of samples. If we take into account the small penetration depth of electrons, they will be affected more from the surface properties of the specimen.

Contrarily, backscattering electrons are emitted after collision of the primary electrons with the sample surface without any loss of energy exhibiting higher energies. The measuring intensity is related to the atomic number of the elements that comprises the sample. Higher atomic number elements produce more backscattering electrons. As a result higher Z phases appear brighter and thus physical features of the surface can be observed.

As it is illustrated in figure 3.10 inelastic electron-matter interaction can lead in characteristic X-ray and Auger electrons that can used for quantitative and qualitative chemical analysis of the sample.

Finally, secondary electron or backscattering electrons, are recorded using a cathode-ray tube (CRT) or a recording device leading in the image formation.

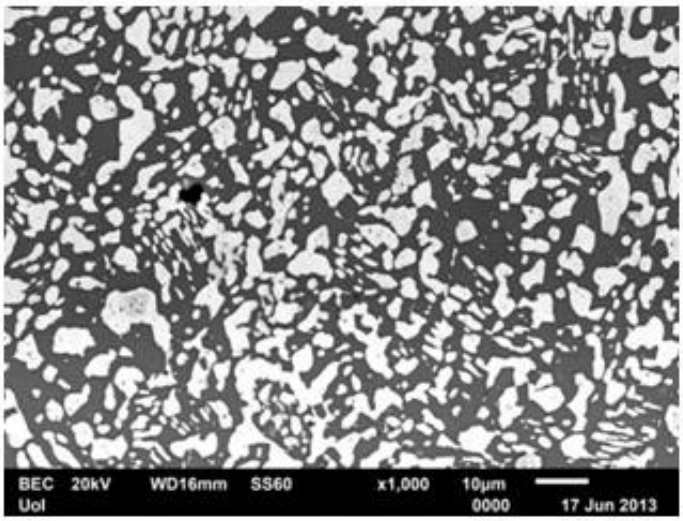

Figure 3.12. SEM image of a PbSnAg alloy using backscattering electrons. Region with brighter color (white) corresponds to Pb due to his high atomic number Z while black regions correspond to Sn and Ag [3.20].

3.4.2.2 Transmission Electron Microscopy (TEM)

Transmission Electron Microscopy (TEM) is usually performed for structural features observation, such as the crystal structure, defects and dislocations of materials. Unlike to SEM, TEM relies on the recording of diffracted, transmitted or inelastically scattered electrons which

have passed through a very thin(less than 50nm) specimen. In order the electron beam to penetrate and pass through the sample a high accelerating voltage, typically 100kV up to 1MeV is applied to the electrons after their emission from the cathode.

Three different imaging modes can be employed in this technique:

- *Bright Field (BF) imaging*: Only the transmitted electrons are recorded leading in the image formation. As a result, the bright areas in this kind of images correspond to regions where the electrons have not been diffracted while the dark areas correspond to regions where electrons have been diffracted.
- *Dark Field (BF) imaging*: In this mode one or more of the diffracted beams are selected by the aperture. Consequently, the transmitted beams and the remainder of the diffracted beams are blocked. The bright regions of the image thus correspond to the areas of the specimen giving rise to the selected diffracted beams, whereas the remainder parts of the specimen appear dark in the image
- *Selected area diffraction:* In diffraction mode, the diffraction pattern formed at the focal plane is projected onto the viewing screen. The diffraction pattern contains information on the periodicity of crystalline phases. The diffraction information can be limited to a selected area of the specimen by inserting an aperture at the image plane of the objective lens. This technique is known as selected area electron diffraction (SAED) or simply selected area diffraction (SAD). Lattice resolution can be obtained from phase contrast by selecting both the direct-transmitted beams and diffracted beams. This procedure is known as high-resolution TEM (HRTEM) imaging.

In all cases the electrons are recorded in a photosensitive film or a fluorescent screen or a CCD camera leading in the investigating area imaging.

Important role in TEM plays the optical system that is used for the magnification of the electron beam which comprises from electromagnetic and electrostatic lenses as well as apertures where the objective lens stands for this utility.

As mentioned before, in TEM, electrons pass through the sample. Thus, except from the high accelerating voltage a thin specimen is also required. This requirement gives a crucial role in the sample preparation and depending on the materials involved sample preparation may be the bulk of the work in TEM.

The specimen preparation can be distinguished in two major categories:

- *Mechanical preparation:* A thin slice of the material can be made by sawing or cutting.
- *Chemical preparation:* a chemical solution dissolves the original surface and reduces the specimen thickness.

3.4.2.3 Atomic Force Microscopy (AFM)

Atomic Force Microscopy (AFM) is a reliable characterization technique for the morphological characterization of surfaces and thus is used in a wide range of materials. The procedure that is taking place during AFM measurements is based on a raster scan across the surface with a sharp and force sensitive tip (Figure 3.13 right). This tip is part of cantilever on the back of which a laser beam is incident and reflected. Variations in scanning surface leads in different force interactions between surface and tip and as a result different deflections of the cantilever occur. These deflections alter the reflected laser beam which is recorded from a position sensitive detector and appears as height difference reproducing the surface topography (Figure 3.13).

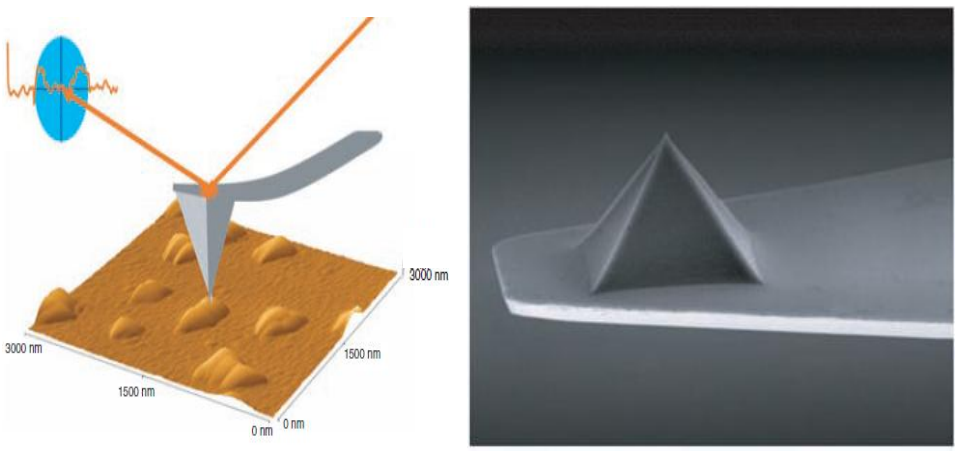

Figure 3.13. *Left:* Schematically representation of the operation of the AFM. *Right:* SEM image of a tip at the apex of a probe

AFM signal is based mainly on interatomic repulsive forces which are of an extreme short-range nature because, although long range forces are also taking place, deformation of the surface can occur or even sample destruction due to tip scratching across the surface can be present.

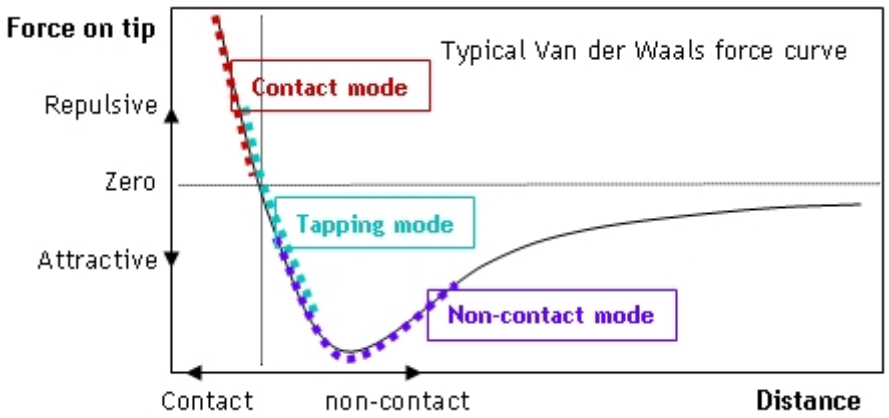

Figure 3.14. Applied force directions of the basic AFM operation modes

AFM operation is usually described as one of three modes, according to the nature of the tip motion:

- contact mode
- tapping mode, also called intermittent contact
- non-contact mode

In ***tapping mode***, the cantilever is driven to oscillate up and down at near its resonance frequency by a small piezoelectric element mounted in the AFM tip holder similar to non-contact mode. However, the amplitude of this oscillation is greater than 10 nm, typically 100 to 200 nm. The interaction of forces acting on the cantilever when the tip comes close to the surface, Van der Waals forces, dipole-dipole interactions, electrostatic forces, etc. cause the amplitude of this oscillation to decrease as the tip gets closer to the sample. An electronic servo uses the piezoelectric_actuator to control the height of the cantilever above the sample. The servo adjusts the height to maintain a set cantilever oscillation amplitude as the cantilever is scanned over the sample. A *tapping AFM* image is therefore produced by imaging the force of the intermittent contacts of the tip with the sample surface

3.5 Optical Characterization

Except from the materials' structural and morphological characterization in our study is necessary to determine the optical constants like refractive index or dielectric functions.

Spectroscopic Ellipsometry (SE) and Optical Reflectance Spectroscopy (ORS) are two dominant techniques for the optical characterization of the materials as they are based in the reflectance and absorption of the light from the material.

3.5.1 Optical Reflectance Spectroscopy (ORS)

The optical reflectance spectroscopy is based in the interaction of the electromagnetic radiation with matter, which can be analyzed from Fresnel equations as already was discussed in chapter 2.

Specifically the studied parameter is the reflectance of a specimen when it is illuminated by light while it is taking into account and the absorption that may be present.

The basic configuration is depicted in figure 3.14 and composes of optical fibers that transfer the light from the sources to the specimen and a central fiber that collects and leads the reflected beam to the spectrometer. In order to cover the visible and UV spectra two light sources are utilized, Halogen and Deuterium, which combined cover a photon range from 1.5eV to 5.25eV (figure 3.15).

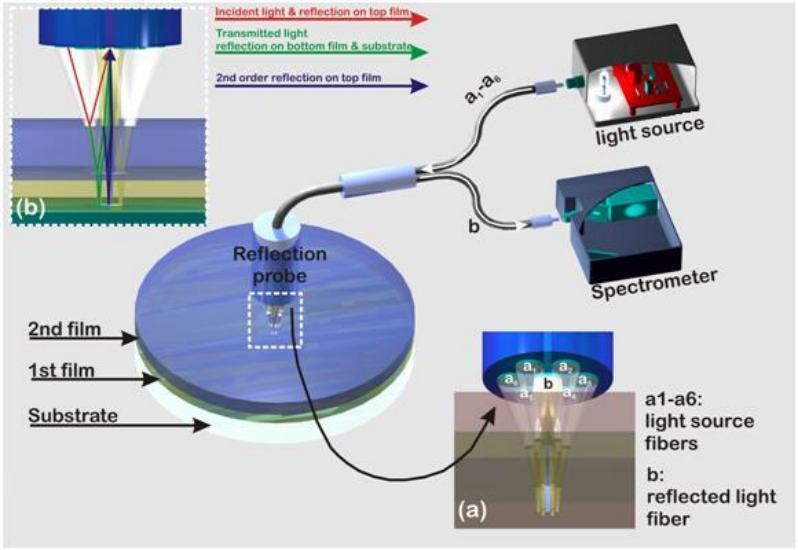

Figure 3.15. Schematic illustration of an Optical Reflectivity Spectroscopy configuration.

The reflected beam is the result of the reflections that take place in the surface and the interface sample-substrate and is connected to the refractive index and the thickness of the material.

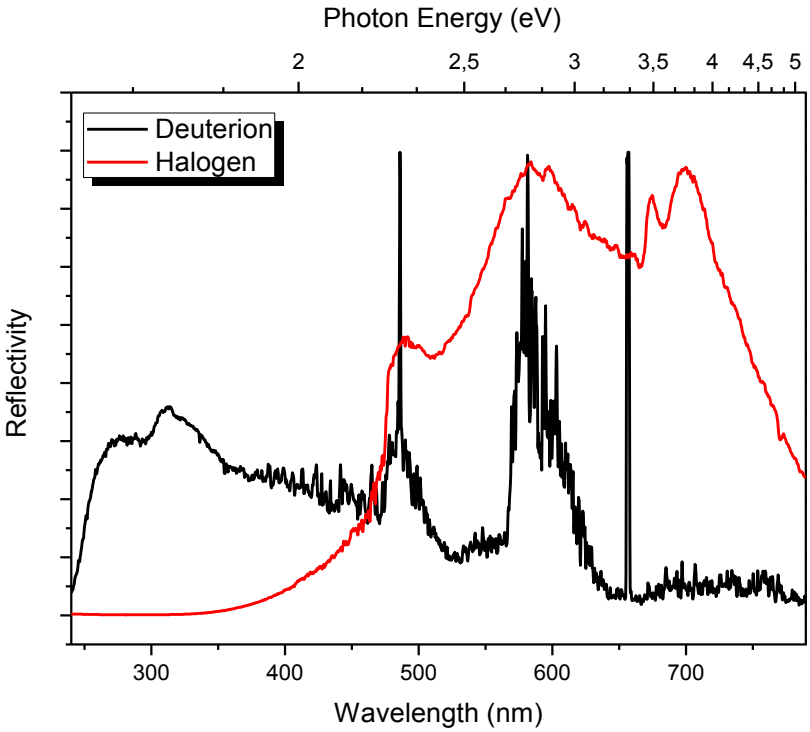

Figure 3.16. Spectra of deuterium (black) and halogen (red) sources, respectively using a silver mirror with high reflectivity.

References

[3.1] Culity B.D., *Elements of X-ray Diffraction,* Addison-Wiley (1956).

[3.2] Birkholz Mario, *Thin Film Analysis by X-ray Scattering,* Wiley-VCH (2006).

[3.3] Shmueli Uri, *Theories and Techniques of Crystal Structure and Determination,* Oxford Science Publications, (2007).

[3.4] Callister D. William,Jr. *Materials Science and Engineering. An introduction,* John Wiley & Sons Inc. (2007).

[3.5] Gibaud A., Hazra S., *Current Science-Surface Characterization*, **78**(2000), pp. 1467-1477.

[3.6] Friedbacher Gernot and Henning Bubert, *Surface and Thin Film Analysis*, Wiley-VCH (2011).

[3.7] Turner H. Noel, Schreifels A. John, *Anal. Chem.*, **66**(1994) , pp. 163R-185R

[3.8] Hofmann Siegfried, *Auger and X-Ray Photoelectron Spectroscopy in Materials Science*, Springer (2013).

[3.9] Kaufmann N. Elton, *Characterization of Materials (Volume 1),* Wiley-Interscience (2003).

[3.10] Riviera C. John, Myhra Sverre, *Handbook of Surface and Interface Analysis. Methods for problem-Solving* (Second Edition) CRC Press (2009).

[3.11] Vickerman C., John, Gilmore S. Ian, *Surface Analysis. The principal techniques (Second edition),* John Wiley & Sons Inc. (2009).

[3.12] Amelinckx S., D. van Dyck, J. van Landuyt, G. van Tendeloo, *Electron Microscopy. Principles and Funtamentals.*Wiley-VCH (1997).

[3.13] Egerton F. Ray, *Physical Principles of Electron Microscopy. An introduction to TEM, SEM and AFM,* Springer (2005).

[3.14] Nan Yao, Zhong Lin Wang, *Handbook of Microscopy for Nanotechnology*, Kluwer Academic Publishers (2005).

[3.15] Fultz Brent, Howe M. James, *Transmission Electron Microscopy and Diffraction of Materials (Third edition),* Springer.

[3.16] Williams B. David, C. Carter Barry,*Transmission Electron Microscopy. A textbook for Materials Science,* Springer (2009).

[3.17] Bhushan B. Fuchs H, *Applied Scanning Probe Methods XII*, Springer (2009).

[3.18] Kaupp G., *Atomic Force Microscopy, Scanning Near field Optical Microscopy and Nanoscratching. Application to Rough and Natural Surfaces*. Springer (2006).

[3.19] Morita S., *Roadmap of Scanning Probe Microscopy*, Springer (2007).

[3.20] Panagiotidis L., Undergraduate thesis, Ioannina (2013).

[3.21] Prablu Y.T., Veneateswara Rao K., Inter. *Journ. Engin. Advanc. Technol*., **2** (2013), pp. 268-274.

[3.22] Patsalas P., Logothetidis S., *et al.*, Diamon. Relat. Mater., **14** (2005), pp.1241-1254.

[3.23] Sinha S.K., Sirota E.B., *et al*., *Phys. Rev. B*, **38** (1988), pp2297-2311.

[3.24] Nevot L., Croce P., Rev. Phys. Appl., **15**(1980), p. 761.

[3.25] Azaroff L. V., "*Elements of X-ray Crystallography*", McGraw-Hill, New York (1968)

Chapter 4 *OPTICAL PROPERTIES OF THIN SILVER FILMS*

4.1 Introduction

Silver is a well-known noble metal, involved in plasmonic applications as it exhibits a strong Surface Plasmon Resonance in the visible region [4.1-4.3], while its biocompatibility makes it a candidate for bio-applications [4.4, 4.5].

Although a number of papers related with laser annealing (LA) of metals and its optical properties [4.2, 4.7-4.14] are listed in literature, a complete study of the behavior of a metal under LA is not yet completely understood.

In this chapter the optical properties of thin silver films subjected to laser annealing are studied extensively and a systematic investigation of plasmonic behavior as a function of various LA parameters is presented.

4.2 Sputtered thin silver films

4.2.1 Sputter deposition of Ag

Silver thin films of various thicknesses were deposited using RF Magnetron Sputtering in Ar ambient using a 3 inch diameter metallic target. Power and Ar flow were constant in all cases while only the deposition time was changing. The growth parameters are presented in detail in table III

Table III. Deposition details for the deposition of Ag thin films.

Sample ID	Deposition time (sec)	RF Power (Watt)	Ar Flow (sccm)	Working Pressure (mTorr)
#1	5 min	40	8	5
#2	10min	40	8	5
#3	15 min	40	8	5

Initially, X-ray BBXRD and specular reflectivity (XRR) were performed in order to estimate the structural and morphological features of the samples.

From the XRD patterns were observed the (111) and (200) diffraction peaks corresponding to FCC crystal structure. Both diffraction peaks are not shifted relative to the pdf values [4.16]. This can be attributed to the absence of stresses in our films.

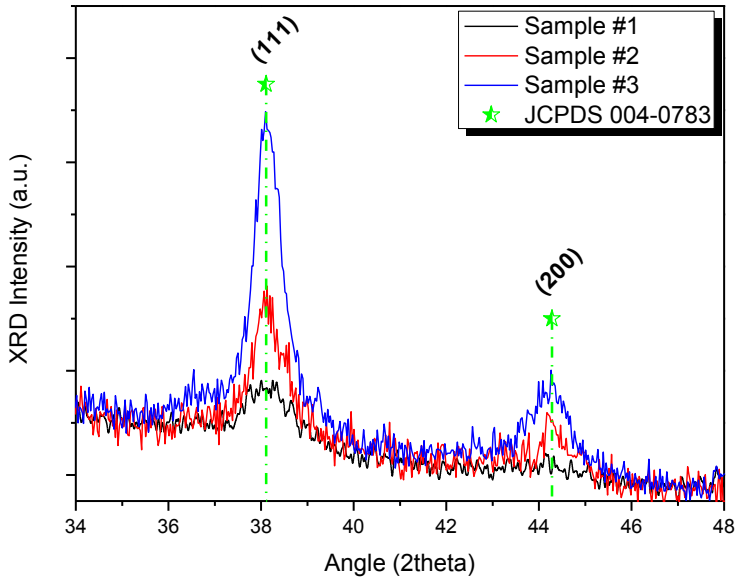

Figure.4.1. XRD pattern of the as grown films.

For the XRR analysis an $Ag/SiO_2/Si$ model was used. The experimental results (black squares) and the fitting with the model (red solid line) for all three samples are depicted in figure 4.2 while the numerical values obtained from the analysis are summarized in table IV.

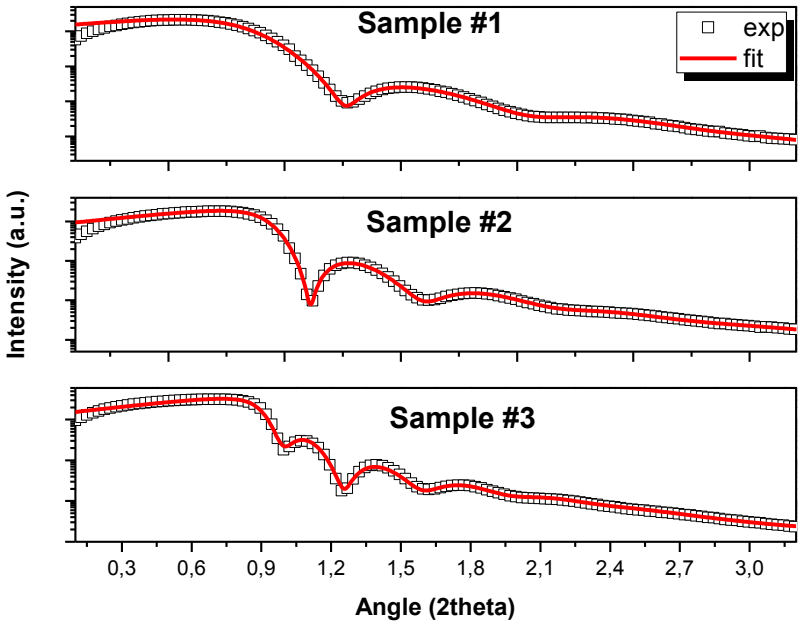

Figure 4.2. X-Ray Reflectivity of the as deposited samples (squares) with the corresponding fit (red line) for thickness, density and roughness estimation.

Table IV. XRR parameters of the as deposited films

Sample ID	Thickness (nm)	Roughness	Density (gr/cm^3)
#1	9.18±0.03	1.84±0.02	8.45±0.03
#2	13.05±0.02	2.05±0.01	10.52±0.01
#3	19.77±0.04	2.28±0.02	10.44±0.02

The estimated results from the XRD and XRR analysis are plotted in figure 4.3 with respect to the film thickness. Thin film density (Figure 4.3a) for the thinner films is lower than bulk while the other two films present a density close to that of bulk Ag. Taking into account the results of the grain size estimation, where for the thinner film the grain size is comparable to thin film thickness, we can rationally assume that sample #1 is not a uniform film but it is consists from small islands of silver nanocrystals i.e. its thickness is below the coalescence threshold [4.15].

A grain size determination applying the Scherrer formula (Eqn. 4.7) and using the profile of the Ag (111) diffraction peak (figure 4.3b) was also performed. The size of the crystallites increases with the film thickness, however the mean crystallite size is smaller than the film thickness, indicating that the film does not consist of single Ag crystals in the entire of the thickness.

Finally, the same behavior with the grain size is observed in the surface roughness results (Figure 4.3c).

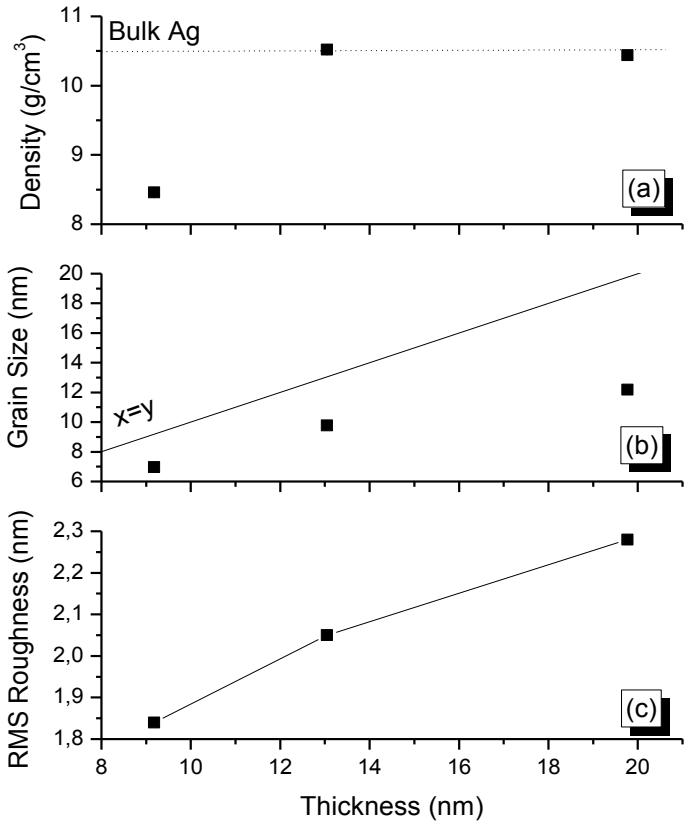

Figure 4.3. Extracted results (density (a), grain size (b), surface roughness (c)) as a function of thin film thickness as resulting from XRD and XRR analysis.

The morphological characterization of the Ag films was deduced from AFM topography measurements in the as deposited samples. As it can be seen, sample #1 (Figure 4.4) is a dense network of small islands with voids while sample #2 presents a totally dense film confirming the XRR results. Moreover a rougher surface of sample #2 is observed.

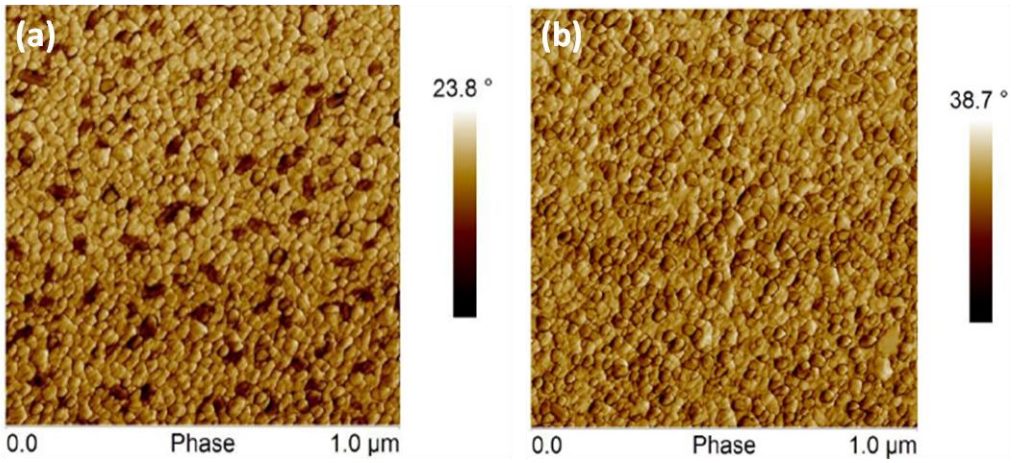

Figure 4.4. AFM phase images and the respective phase image for sample #1 (a) and sample #2 (b) respectively.

Combined XRD (Figure 4.3b) and AFM measurements (Figure 4.5) showed films consisted of oblate particles and not hemispheres. In particular, the XRD analysis estimates the grains size regarding the z axis while the AFM results corresponds to the grains size in the x-y plane respectively. Moreover, taking into account the fact that in case of a hemisphere the crystallite size value estimated from the AFM technique should be twice the value estimated from the XRD technique respectively, i.e. 2 $crystille\ size_{XRD} = crystille\ size_{AFM}$ with a contact angle $\theta_c = 90^0$ s. On the contrary, if the contact angle is lower i.e.$\theta_c < 90^0$, then we have 2 $crystille\ size_{XRD} < crystille\ size_{AFM}$ which is in agreement with our results. Thus, we conclude that indeed our films consist of oblate particles with a contact angle $\theta_c < 90^0$.

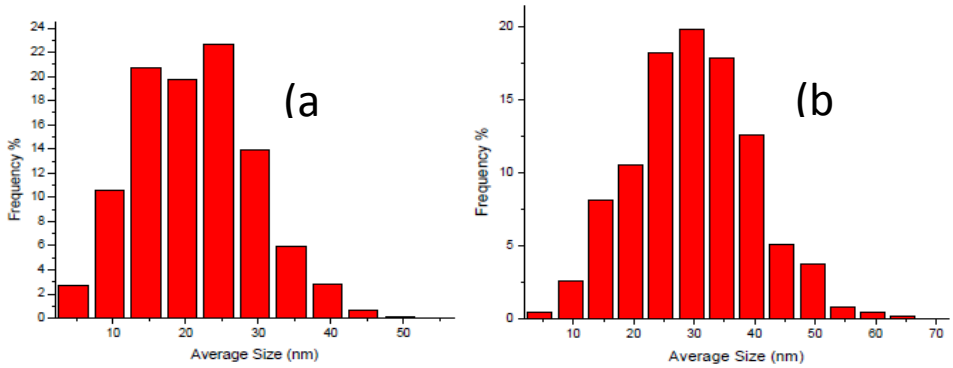

Figure 4.5. Size distribution of sample #1 (a) and sample #2 (b) derived from AFM analysis.

Finally, the successful deposition of metallic thin films of silver was also confirmed from ORS measurements (Figure 4.6). Samples exhibit a strong reflectance which varies with sample thickness. Thus, as the film is getting thicker the reflectance is increased with the maximum intensity being above the 350nm. Due to the small thickness of the Ag films, they are transparent to UV light, thus substrate features can be also observed.

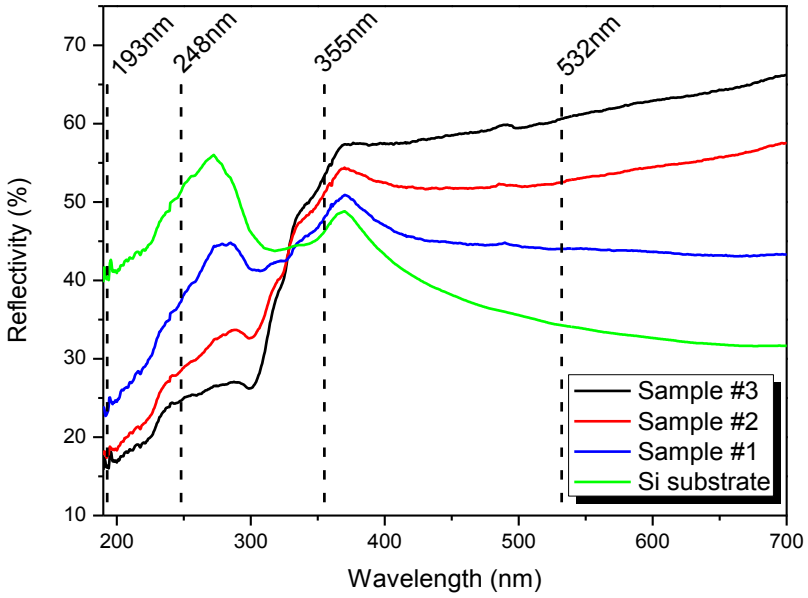

Figure 4.6. Reflectivity of Ag samples and silicon substrate in the near UV-visible range. Substrate features are observed due to thin thickness.

4.2.2 Laser Annealing

The as grown samples subsequently were subjected in laser annealing process. Single shot Uv-eximer lasers with 193nm wavelength (ArF) and 248nm (KrF) respectively were used with 25nm pulse duration. The samples were mounted on a computer controlled X-Y translation stage for easy sample manipulation and exposed to atmospheric air. In order to investigate the effect of fluence in the optical properties of the films a wide range of fluencies were used starting from 200mJcm^{-2} up to 800mJcm^{-2} with a step of 100mJcm^{-2}.

Finally, the modification that different number of pulses made to the films was also studied. Thus, 1, 2, 3, 5 and 10 pulses respectively were employed. After annealing ORS measurements were performed in order to study the optical properties of the dewetted Ag. Moreover, AFM measurements were also carried out, in the standard tapping mode in order to correlate the plasmonic behavior with the morphological features of the laser annealed samples.

.

Sample #1:

The optical reflectivity spectroscopy (ORS) measurements of sample #1 for laser annealing at 193nm and 248nm with various fluencies and number of pulses are summarized in figure 4.7 and figure 4.8 respectively. All spectra are normalized with the Si reflectivity in order to minimize the substrate features. In most cases an SPR peak manifestation is observed which provides some optical characteristics according to the treatment parameters.

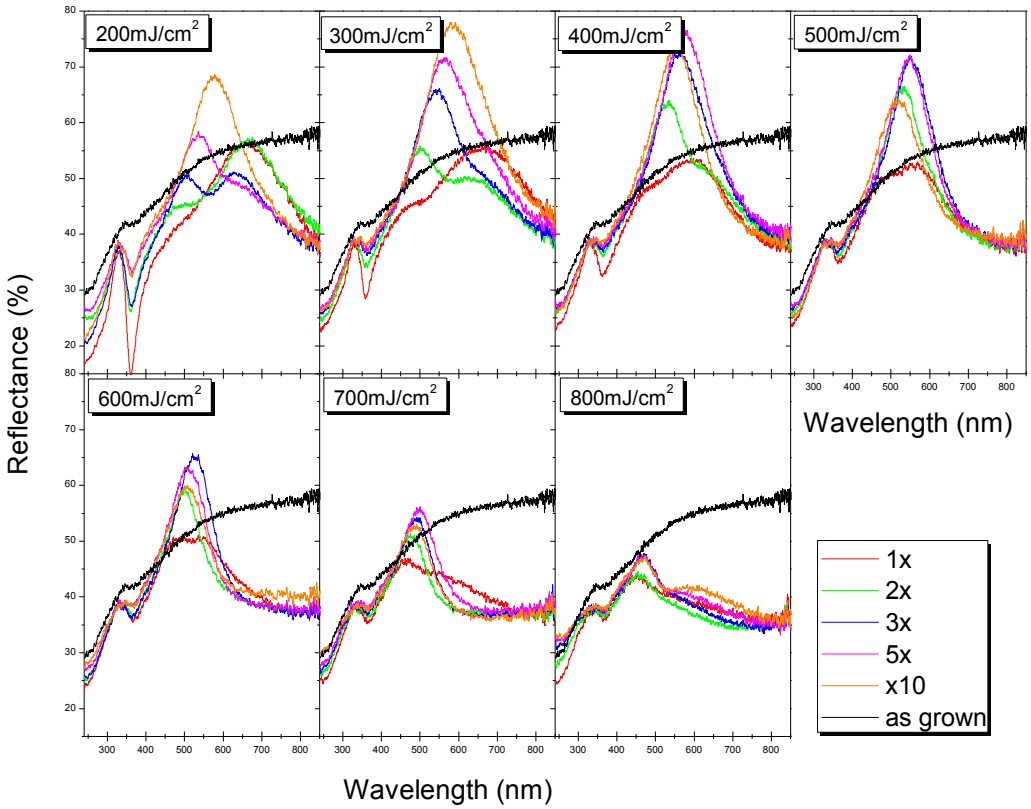

Figure 4.7. ORS spectrums of Sample #1 after laser annealing at 193nm, with various fluencies and number of pulses.

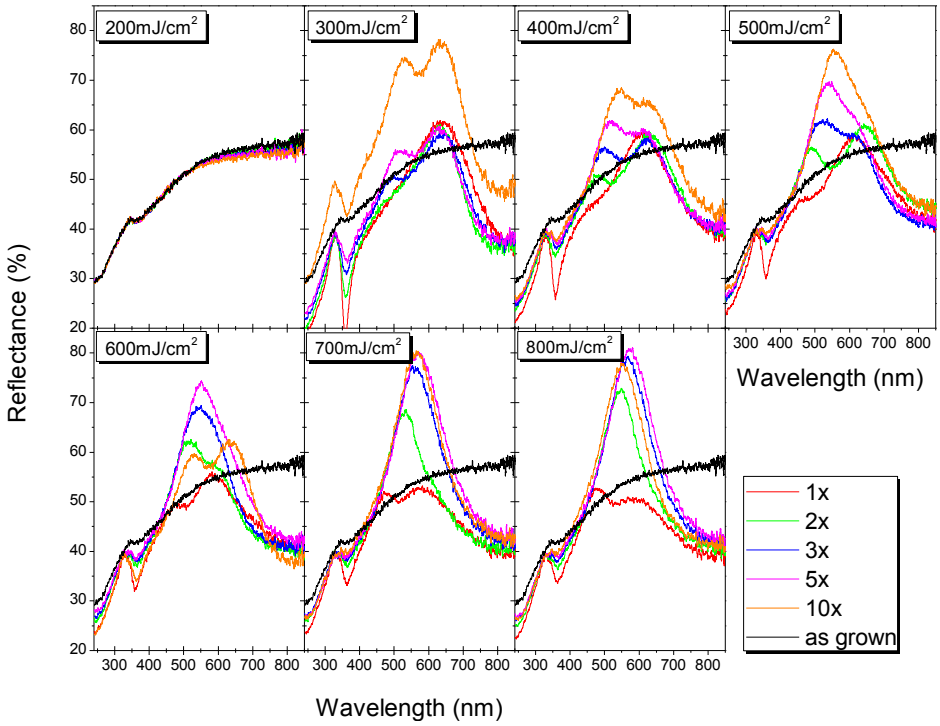

Figure 4.8. ORS spectrums of Sample #1 after laser annealing at 248nm, with various fluencies and number of pulses.

In order to estimate and correlate LSPR peak features such as position and intensity with laser fluence and number of applied pulses, all LSPR peaks emerged was fitted using a Lorentzian model after background subtraction as it is illustrated in figure 4.9 below.

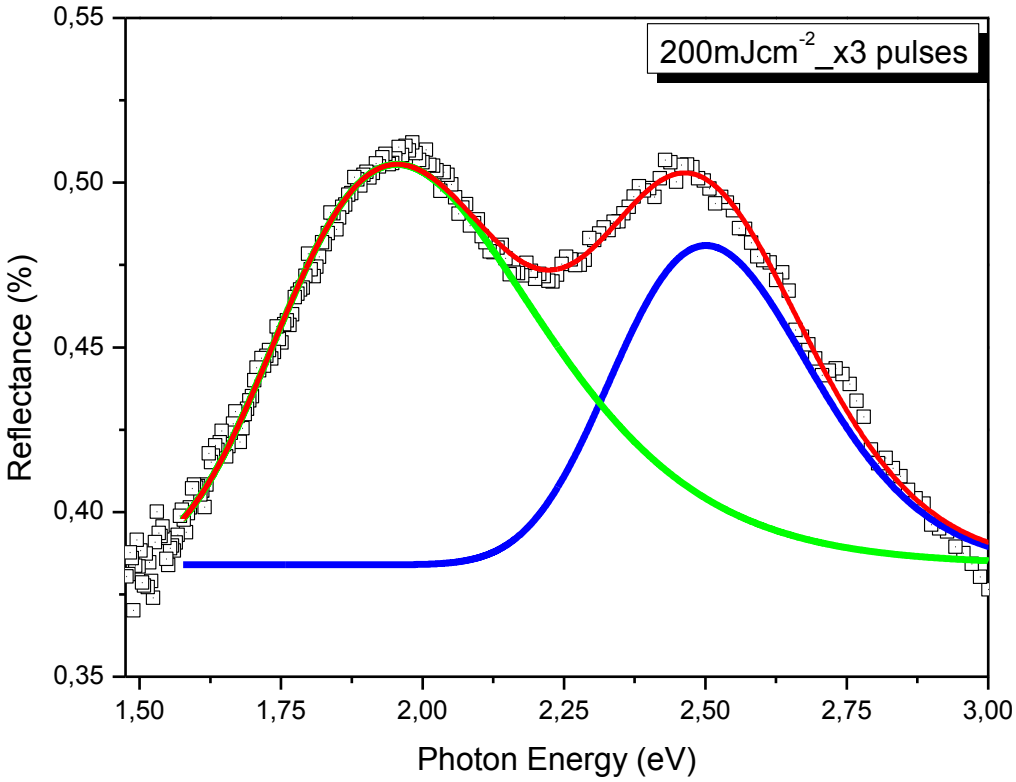

Figure 4.9. Optical Reflectivity Spectra for sample #1 for 3 pulses at 200mJcm^{-2} using 193nm wavelength fitted with two Lorentzian functions in order to feature the bimodal distribution.

Effect of no of pulses:

Among the parameters that can affect the laser annealing procedure, the effect of the numbers of the applied pulses was first considered. Thus, as it can be seen in figure 4.9 the implementation of 1 pulse for 200 mJ/cm^2 (black filled squares) in case of 193nm laser wavelength an LSPR peak emerged at around 660nm wavelength while after two successive pulses a blues shift was observed which can be attributed in the recreation of smaller nanoparticles after the second pulse. On the other hand the implementation of higher number of pulses causes a gradual shift of the LSPR peak in higher wavelengths and a LSPR enchansment indicating the coalescence of the existing nanoparticles and the formation bigger. On the other hand, for 300mJ/cm^2 (red filled circle) the implementation of up to 10 successive pulses leads to the peak displacement on higher wavelengths (red shift) possibly due to the coalescence of the pre-existing nanoparticles and the formation new of bigger size.

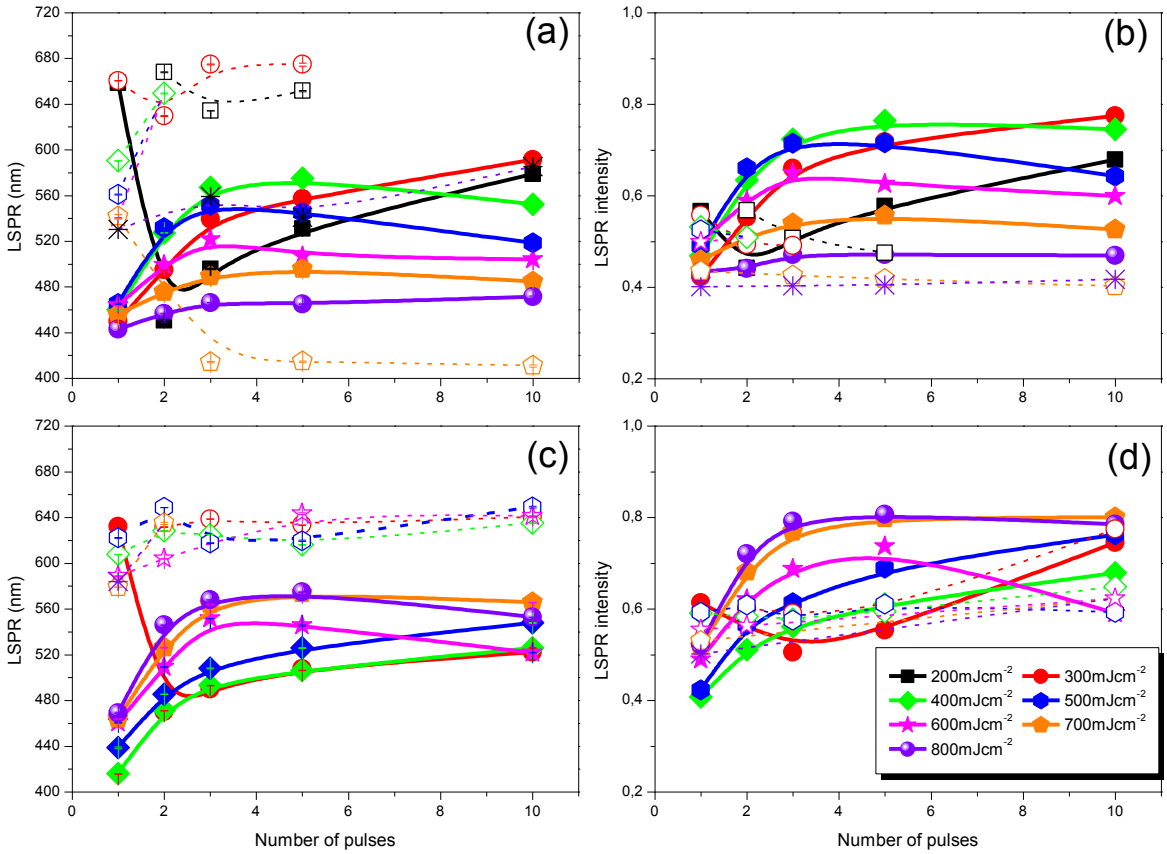

Figure 4.10. LSPR peak position and intensity for 193nm (a, b) and 248nm (c, d) laser wavelength respectively with respect to number of applied pulses. Dashed lines corresponds to the second peak that occurs in case of bimodal systems

Similar behavior in the optical response of the sample it was also observed in case of 248nm laser wavelength (Figure 4.9 (c, d)). A major difference in this case is that due to lower delivered energy, the lower limit in order LSPR peak to be emerged is 1 pulse at 300mJ/cm^2 unlike to 193nm wavelength where 200mJ/cm^2 fluence could alter the optical properties of the film.

From the ORS measurements revealed that for both 193nm (Figure 4.7) and 248nm (Figure 4.8) laser wavelength bimodal systems was observed indicating the formation of different particles size distribution. As a result a second LSPR emerged in higher wavelengths compared to the other which remained unaffected with the implementation of different number of pulses (dashed lines in figure 4.9). Exception is only the case of 700mJ/cm^2 for 193nm (Figure 4.9, orange open trapezoid with dashed line) where the implementation of successive number of pulses induces a blue shift of the second peak indicating the particles segregation into smaller.

From morphological point of view, the transition from 2 to 10 successive pulses did not induce significant differences in particles size distribution in case of 193nm wavelength (Figure 4.10) which is in agreement with the optical response of the sample.

.

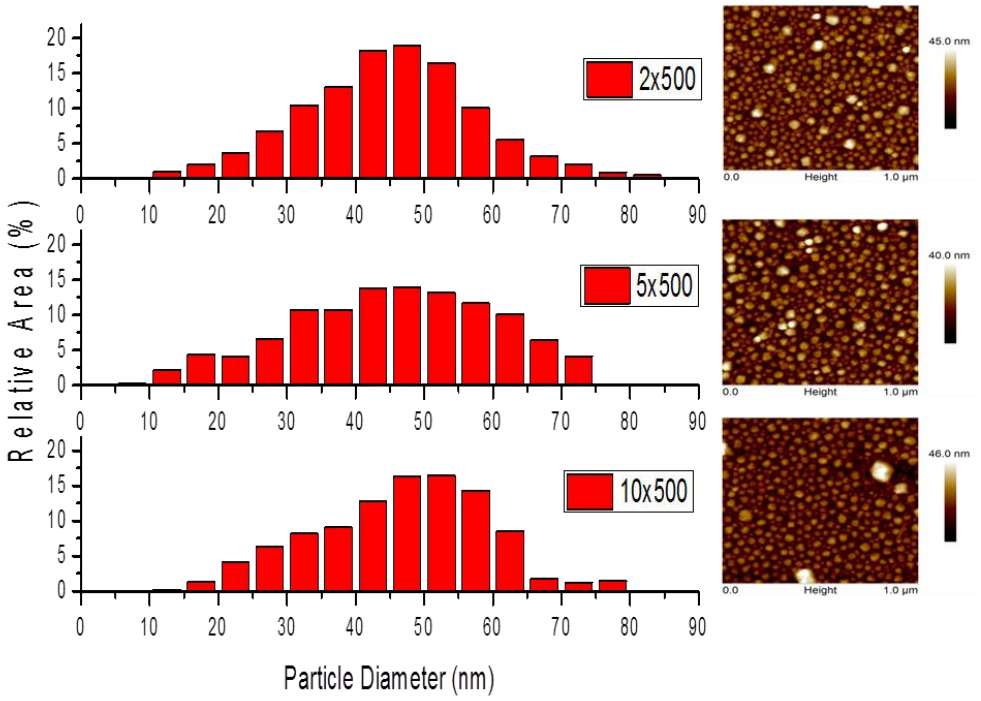

Figure 4.11. Size distribution of particle size for 500mJ/cm^2 fluence for different pulses with respective AFM topography images (insert).

On the contrary, when 248nm laser wavelength was used, as it is illustrated in figure 4.11 the implementation of 1 pulse at 400mJ/cm^2 causes a broad size distribution with particles size ranging from 5 up to 140nm while further increase of the applied pulses provides a more narrow size distribution mainly from the dissolution of the bigger nanoparticles. Thus, now the maximum particles size did not excide 100nm. The AFM analysis complements the optical results justifying the bimodal behavior in that case.

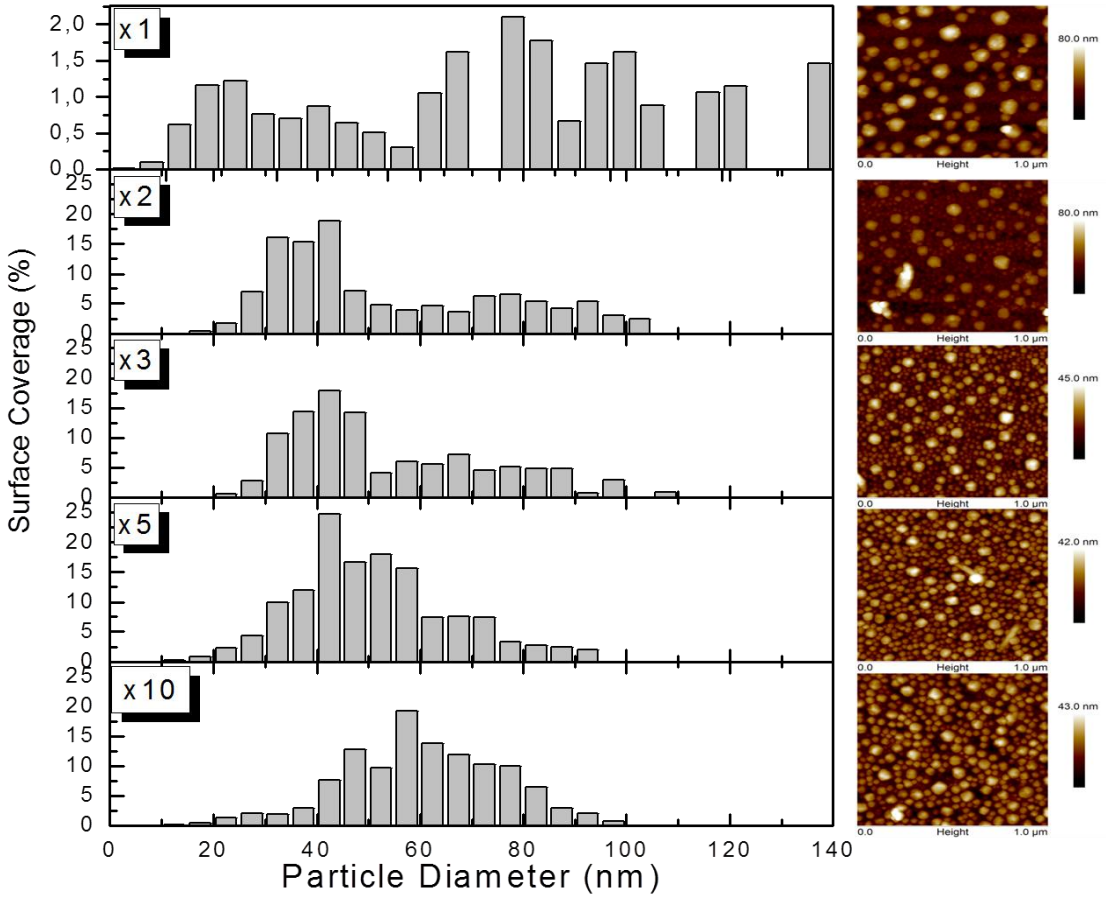

Figure 4.12. *Left:* Size distribution of formed nanoparticles as a function of the number of pulses for sample #1 with 400mJ/cm^2 fluence for 248nm wavelength. *Right:* respective AFM topography images.

Effect of fluence:

The fluence of the laser beam was the second parameter that investigated in this task of the chapter for both 193nm and 248nm wavelength. From the ORS spectra it was found that for 1 pulse at 193nm wavelength promotes a bimodal behavior in all fluence range (Figure 4.12).In particular, for the first peak (black filled squares) increasing the fluence from 200mJ/cm^2 to 300mJ/cm^2 an abrupt blue shift of the LSPR peak occurs indicating the reduction of the size of the nanoparticles. Unlike, for 400mJ/cm^2 and 500mJ/cm^2 a minor shift of the LSPR peak in higher wavelengths while increasing fluence further relocates LSPR peak in lower wavelengths. On the other hand increasing fluence up to 600mJ/cm^2 induces a gradually blue shift in its spectral position (black open squares) with a corresponding reduction of the peak intensity was observed while for higher fluencies no significant difference were recorded.

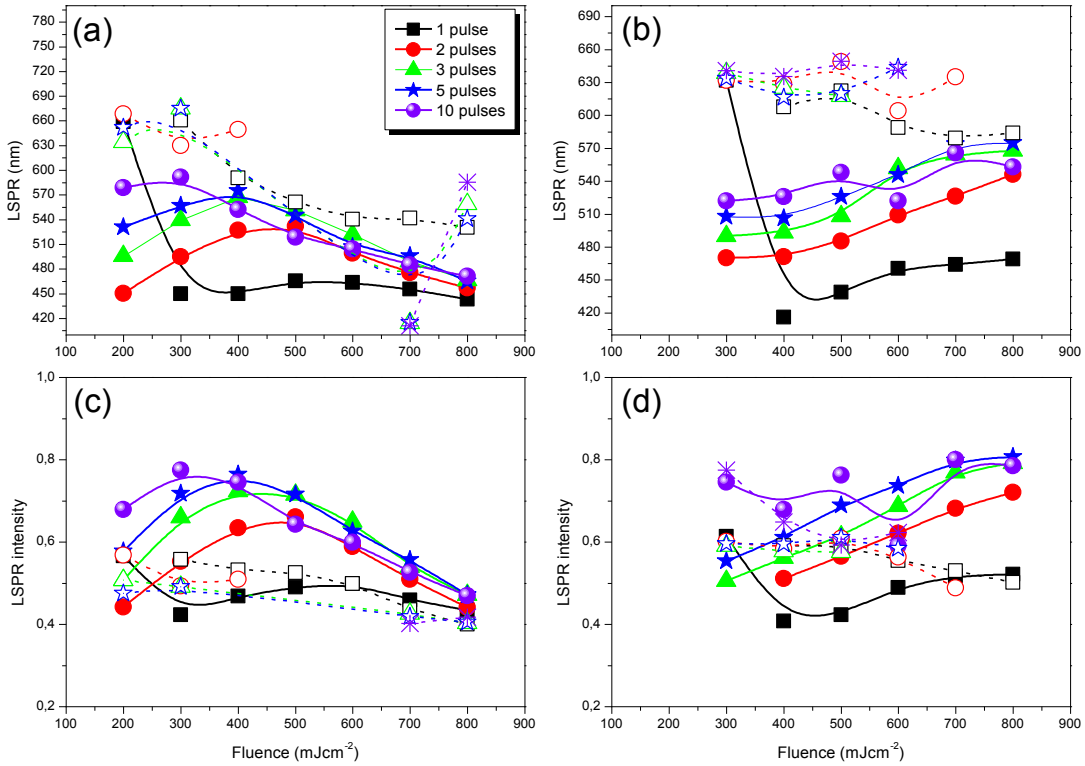

Figure 4.13. Effect of laser fluencie in LSPR peak position and intensity for 193nm (a, c) and 248nm (b, d) laser wavelength respectively. Dashed lines corresponds to the second peak that occurs in case of bimodal systems

On the contrary, in case of two successive pulses increasing fluence up to 500mJ/cm^2 works constructively leading in the agglomeration of the existed from the first pulse nanoparticles into bigger. As a result a red shift of the LSPR peak was observed in the ORS spectrums (Figure 4.12 a, red filled circles) and the intensity of the LSPR increases respectively due to lower ohmic losses (Figure 4.12 c, red filled circles).In case of higher fluencies the delivered energy works distractively. Thus, now nanoparticles with lower particle size were formed and as a result blue shift of the LSPR peaks was recorder in the ORS spectrums with a simultaneous reduction of the LSPR intensity. Similar effects of the fluence were also observed for 3 (Figure 4.12, green filled triangles), 5 (Figure 4.12, blue filled stars) and 10 pulses (Figure 4.12, purple filled sphere) except that red shift of the LSPR was observed up to 400mJ/cm^2 for 3 and 5 pulses while in case of the 10 pulses the LSPR peak shifts in higher wavelengths (bigger nanoparticles formed) was observed only in the transition from 200mJ/cm^2 to 300mJ/cm^2. Additional, in case of bimodal behavior for higher laser pulses LSPR emerged in higher wavelengths indicating the growth of a second size distribution bigger than the first. Laser fluence did not alter significant the spectra position and intensity of this second LSPR peak.

In case of 248nm wavelength the effect of laser fluence is different compared to 193nm wavelength due to lower deliver energy (Figure 4.12b, d). Thus, 200mJ/cm^2 leaves unaffected the sample even after 10 successive pulses. For 1 pulse at 300mJ/cm^2 an LSPR peak at 630nm emerged. Increasing fluence at 400mJ/cm^2 a blue shift of the LSPR peak was observed indicating the formation of smaller nanoparticles while going further in higher fluencies bigger nanoparticles were formed each time and as a result a gradual shift of the LSPR peak was observed a corresponding increase of the LSPR intensity (Figure 4.12 d). On the other hand, for higher number of pulses fluence worked only constructively. As a result a gradual red shift of the peak was observed in all cases. Similar behavior of the second peak it was also observed in case of 248nm laser wavelength

In order to further explore the effect of the laser fluencies, AFM measurements were performed which confirm the results from the optical reflectivity spectroscopy. In particular, from the AFM measurements (Figure 4.13) it appears that the fluence affects not only the mean size of the formed nanoparticles but the particle density as well [4.9, 4.11, and 4.13]. Thus, for 10 pulses and 500 mJ/cm^2 delivered energy, a broader size distribution is observed whilst with 700mJ/cm^2 the particle size presents a more narrow distribution with the maximum size not exceeding 50nm. The same behavior was observed after annealing with 248nm wavelength as representative AFM measurements shows in figure 4.14. At 300mJ/cm^2 a very broad range of particle sizes is formed from 15nm up to 105nm. The implementation of higher fluencies alters the size distribution and quantity, which is now getting narrower and higher respectively. It should be also mentioned that only the upper limit of the particle size was altered while the lower retained almost unaffected.

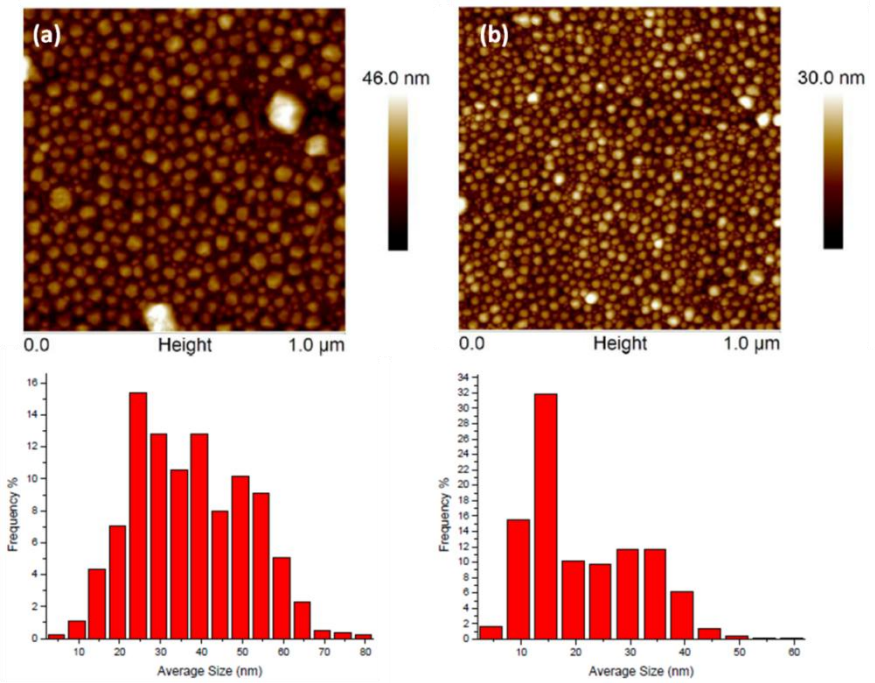

Figure 4.14. AFM images and size distribution after laser annealing with 10 pulses for 500mJ/cm^2 (a) and 700mJ/cm^2 (b) at 193nm wavelength respectively.

Finally, it is obvious that laser annealing with 248nm leads in formation of larger nanoparticles relative to laser annealing with 193nm. This is because the beam energy at 248nm is not as energetic as at 193nm, due to the lower photon energy in the first case and thus causes weaker modifications.

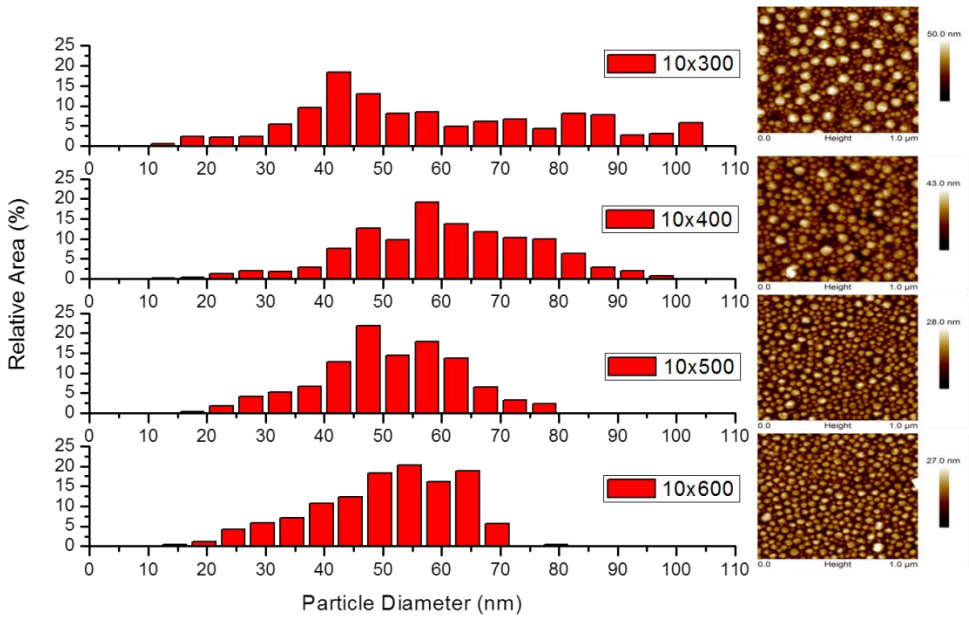

Figure 4.15. AFM images and size distribution after laser annealing with 10 pulses for 300mJ/cm^2, 400mJ/cm^2, 500mJ/cm^2 and 600mJ/cm^2 respectively at 248nm.

Sample #2:

The reflectance measurements of sample #2 for laser annealing at 193nm for various fluencies and number of pulses are summarized in figure 4.15, while the respective results with 248nm are depicted in figure 4.16. All spectra are normalized with the Si reflectivity in order to ignore substrate features.

In this case although the same effects are generally prevailing nevertheless, some differences in the effect of the applying pulses and fluencies, respectively, are observed for both wavelengths due to thicker film.

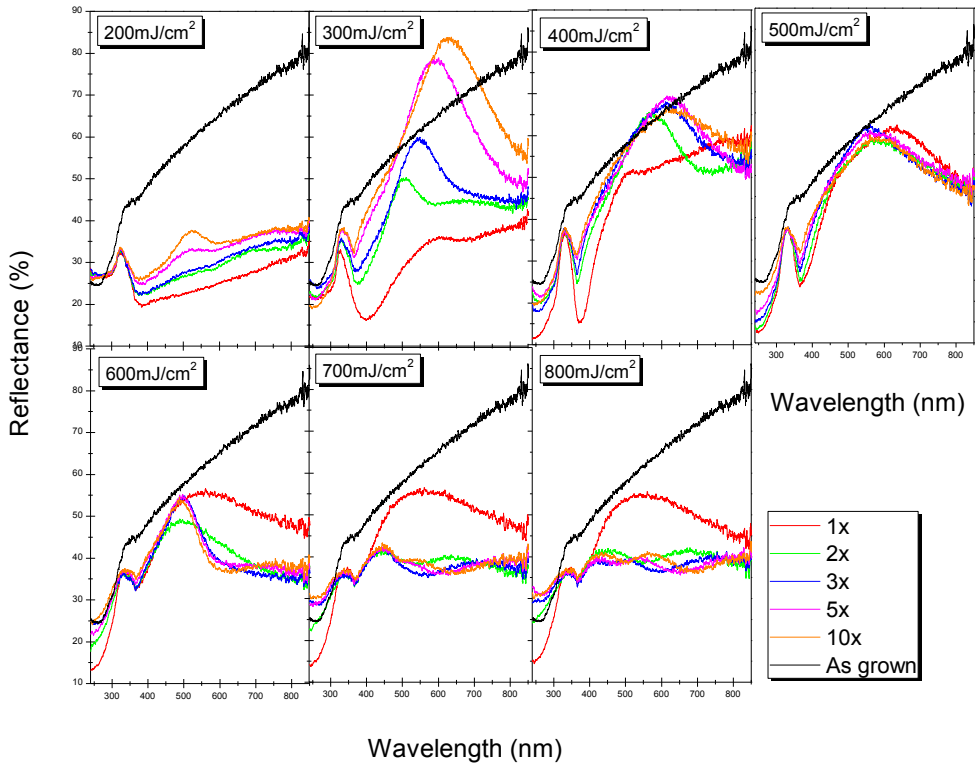

Figure 4.16. Reflectance measurements of sample #2 after laser annealing at 193nm, with various fluencies and number of pulses.

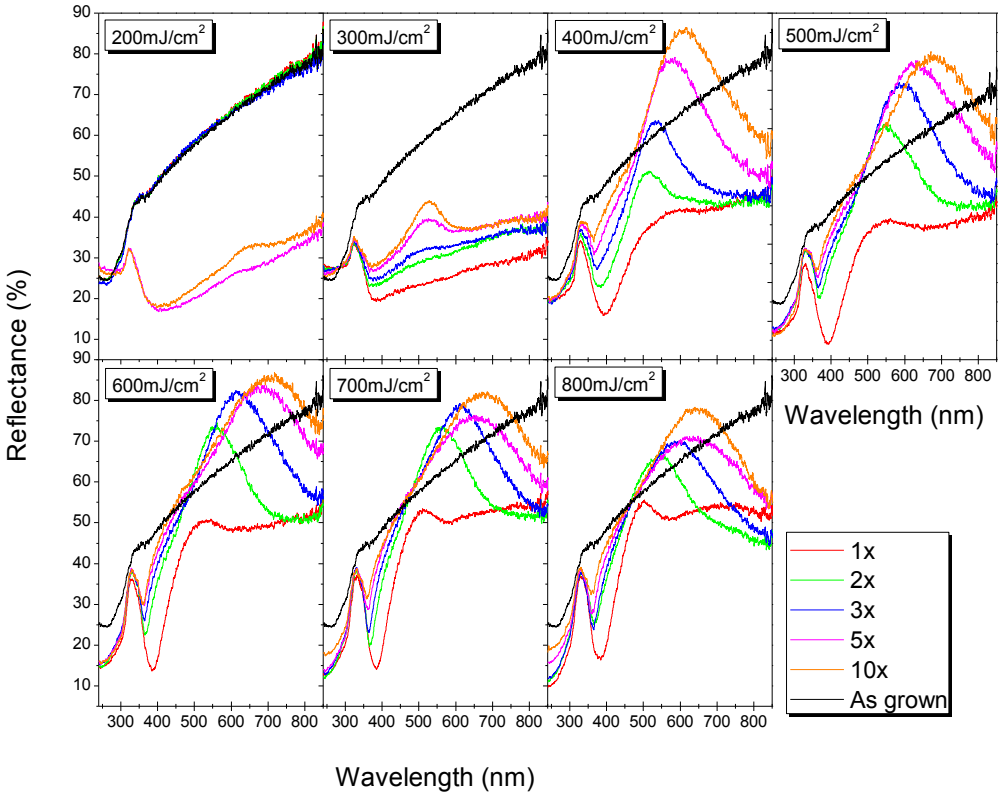

Figure 4.17. ORS spectrums of Sample #2 after laser annealing at 248nm, with various fluencies and number of pulses.

Effect of pulses:

For 193nm wavelength, the provided energy for 200mJ/cm^2 fluence, even after 10 successive pulses, is not enough to convert the initial film to metal nanoparticles. In case of the 300mJ/cm^2 (red filled circle) and 400 mJ/cm^2 (green filled sharp diamond) respectively, there is a consistent red shift of the LSPR with a simultaneous enhancement indicating the coalescence of the nanoparticles into larger. On the contrary, for higher fluencies, the implementation of consecutive pulses induces a blue shift of the LSPR peak with a corresponding reduction of its intensity that can be assigned in the dissolution of the nanoparticles into smaller due to higher delivered energy that reaches the sample.

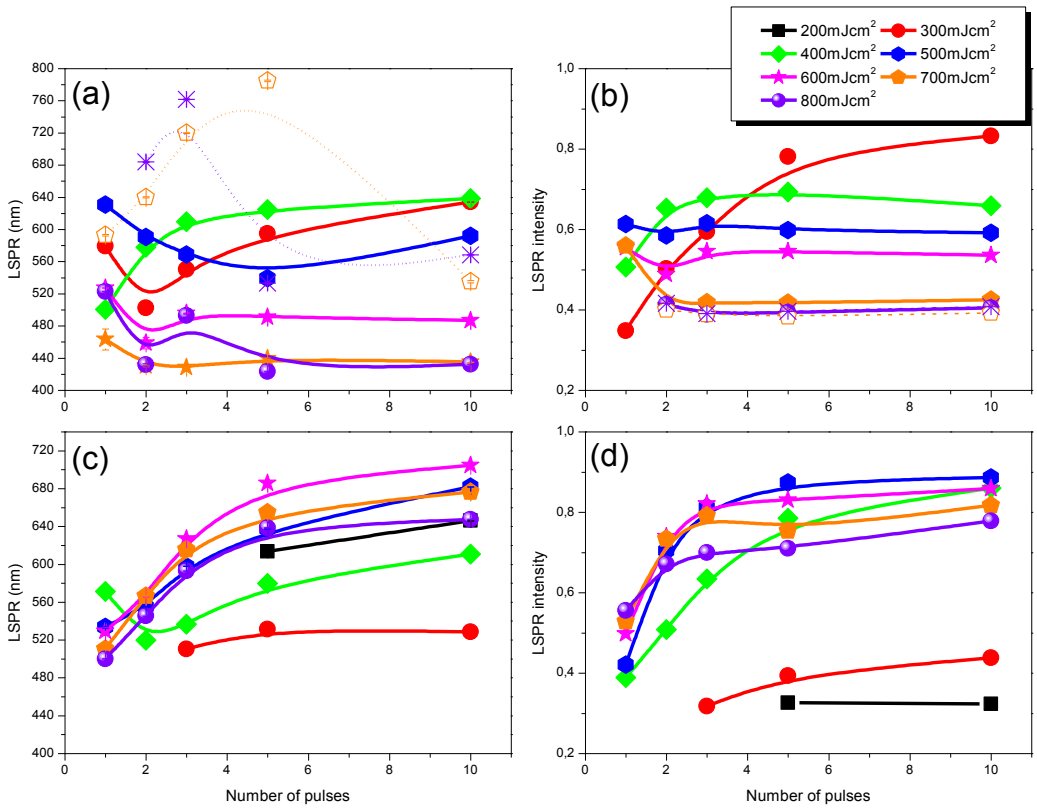

Figure 4.18. Effect of successive pulses on LSPR spectral position and intensity using 193nm (a, b) and 248nm (c, d) laser wavelength .Dashed lines corresponds to the second LSPR manifested in bimodal cases.

In case of sample #2 only for 700mJ/cm^2 (orange trapezoid) and 800 mJ/cm^2 (purple sphere) respectively a bimodal system was observed. In particular, in case of 700mJ/cm^2 the implementation up to 5 pulses induces a spectral shift of the LSPR position fro the second peak (orange opened trapezoid) while for 10 laser pulses a blue shift was observed. Common behavior was observed for 800 mJ/cm^2 but the second peak red shifts up to 3 successive pulses (purple star).

On the contrary, when 248nm laser wavelength was used a different behavior was observed due to lower amount of energy that reaches the film. In particular, regardless laser fluence, increasing laser pulses induces a spectral shift to higher wavelengths and enhancement of the LSPR intensity which are associated with enlargement of the silver nanoparticles particles. Moreover, for 248nm wavelength, LSPR emerged for 200mJ/cm^2 after 5 and 10 laser pulses unlike to 193nm wavelength

In figure 4.18 representative AFM topography images with the corresponding analysis of the size distribution for sample #2 after laser annealing using 248nm with 500mJcm^{-2} in various applied pulses are depicted.

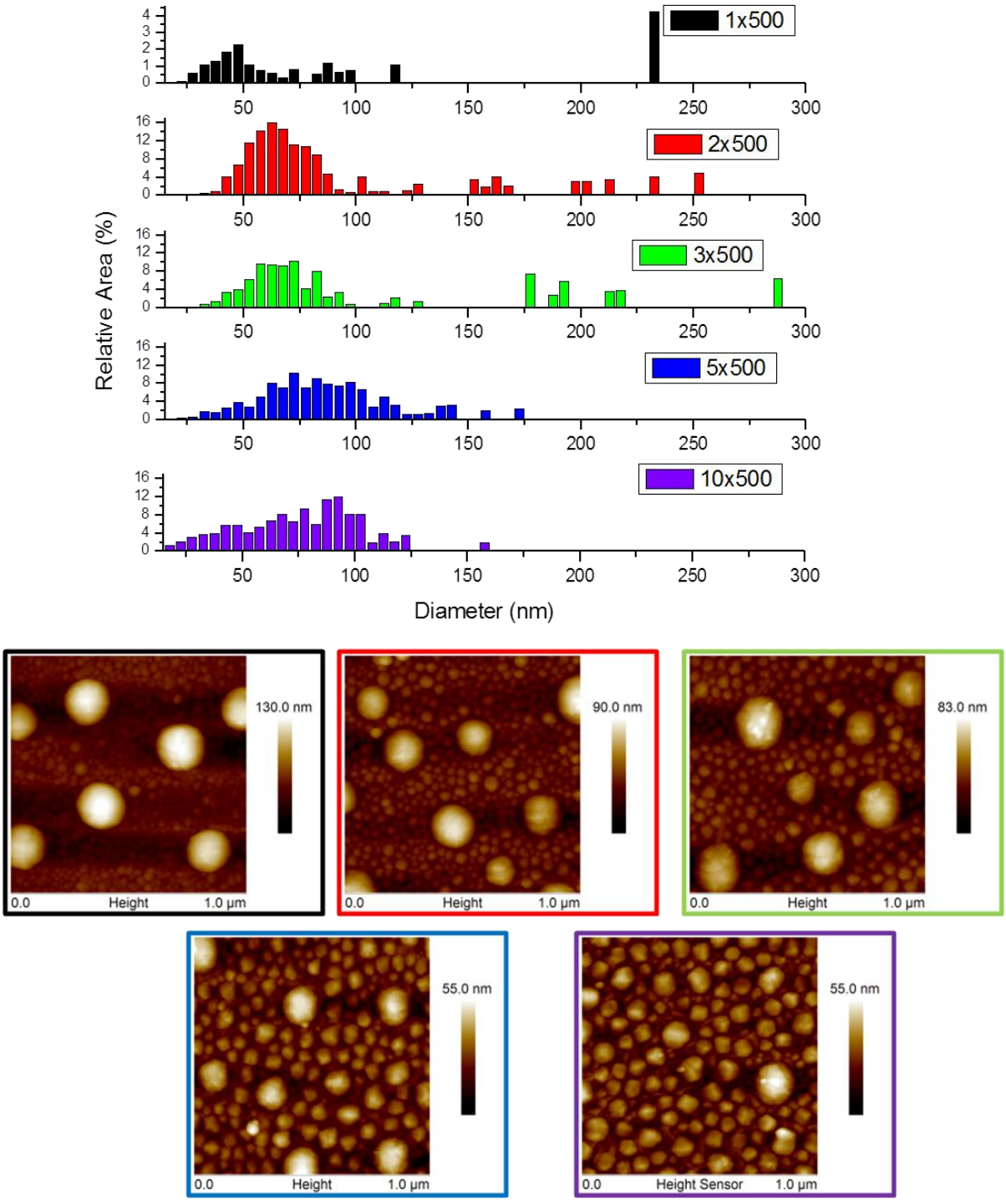

Figure 4.19 Size distribution and AFM topographies respectively of sample #2 after laser annealing at 500mJcm^{-2} with 248nm wavelength for various laser pulses..

The implementation of one pulse forms groups of nanoparticles of different particles sizes. In particular, the first group provides a size in the area 20 to 90 nm while the second group displays an average size at around 230nm. Although, it would be expected a bimodal LSPR, however this was not observed in ORS spectra. Nonetheless, a very broad LSPR peak emerged

which might suggests this broad size distribution. On the other hand, the implementation of a second pulse caused fragmentation of the bigger nanoparticles into smaller while a small amount of initial particles was retained. Increasing further the number of the laser pulses induces a more narrow size distribution. Thus, in case of 10 successive pulses particles size ranged up to 120nm.

Effect of fluence:

The effect of the laser fluencies on the optical properties of sample #2 was investigated as well.

For sample #2, in case of 193nm laser wavelength, increasing fluence from 300mJ/cm^2 to 800mJ/cm^2, for 1 pulse (Figure 4.19, black filled square), leads to spectral shift of the LSPR peak position which can be either blue or red according to nanoparticles enlargement or dissolution. Two successive pulses leads to a red shift of the LSPR in its spectral position for transition from 300mJ/cm^2 to 500mJ/cm^2 laser fluence while beyond that further increase induces a blue shift of its spectral position and a reduction on the LSPR intensity, as it is illustrated in figure 4.19a, c respectively, indicating the formation of smaller nanoparticles. On the contrary, the implementation of 4 successive pulses causes a red shift of the LSPR peak position after increasing fluence from 300mJ/cm to 400mJ/cm^2 followed by a relocation of its spectral position to lower wavelengths up to 700mJ/cm^2 while for 800mJ/cm^2 laser fluence a shift of the LSPR spectral position in higher wavelengths was observed which can be assigned in respective particles size alterations (enlargement, reduction, enlargement). The spectral position relocations with respect to laser fluence are accompanied with respective changes of the LSPR peak intensity (figure4.19 d) which is also associated in the particles size alterations. Finally, the augmentation of the laser fluence from 300mJ/cm^2 to 400mJ/cm^2 causes a minor red shift of the LSPR peak position while rising laser fluence further up to 800 mJ/cm^2 induces a consistent blue shift of the LSPR peak position and a gradual reduction of its peak intensity which are respectively associated with the dissolution and the formation smaller due to the higher deliver energy. In case of 248nm wavelength for 1 and 2 laser pulses respectively 400mJ/cm^2 fluence is the threshold for LSPR to be emerged as it demonstrated in ORS spectrums (Figure 4.19b). So, for 1 pulse increasing fluence from 400mJ/cm^2 to 800mJ/cm^2 induces a gradual spectral shift in higher wavelengths which associated with changes in particles size (each time bigger nanoparticles are formed).

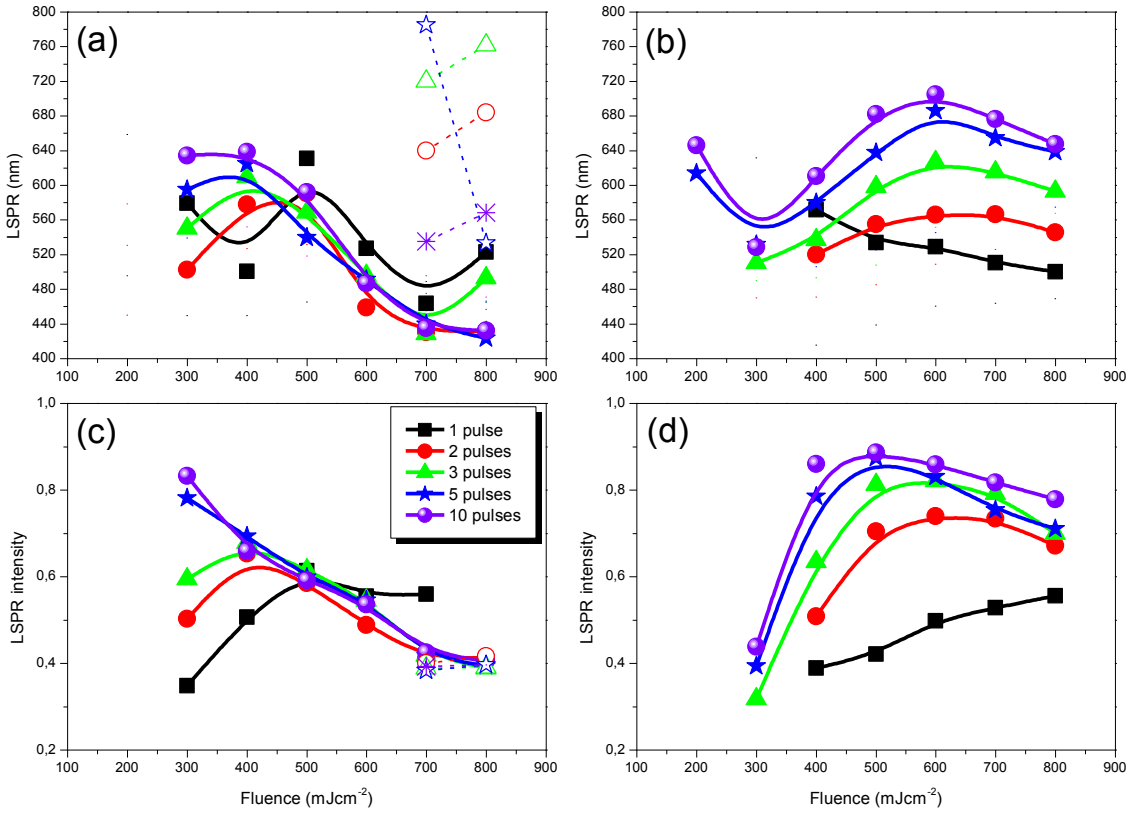

Figure 4.20. LSPR spectral position and intensity as a function of laser fluence using 193nm (a, c) and 248nm (b, d) laser wavelength respectively for sample #2.

On the contrary for two successive pulses (Figure 4.19. red filled circle) this spectra shift occurs only up to 600mJ/cm^2. Further increase of laser fluence at 700mJ/cm^2 and 800mJ/cm^2 leads to blue shift with corresponding reduction of the LSPR intensity which can be attributed in the reformation of the nanoparticles from the first pulse into smaller. Similar behavior was observed in case of three pulses but now three pulses were getting effective in particles formation for 300mJ/cm^2. Finally, for 5 (blue filled star) and 10 (purple filled sphere) laser pulses respectively, LSPR emerged for 200mJ/cm^2.Thus, increasing laser fluence from 200mJ/cm^2 to 300mJ/cm^2 induces a blue shift of the LSPR in its spectral position indicating the formation of nanoparticles with smaller size. Further increase of the laser fluence induces similar spectral shifts as in case of four laser pulses. It should be noticed that the alterations of the LSPR spectral position for various laser fluencies accompanied by corresponding changes of peak intensity which is also associated with particles size alterations.

AFM analysis (Figure 4.21) demonstrated that indeed the implementation of higher flux of energies (higher fluencies) shifts particles size in a narrow size distribution and smaller particles sizes justifying the blue shift in LSPR spectral position that as observed from the ORS spectrums.

.

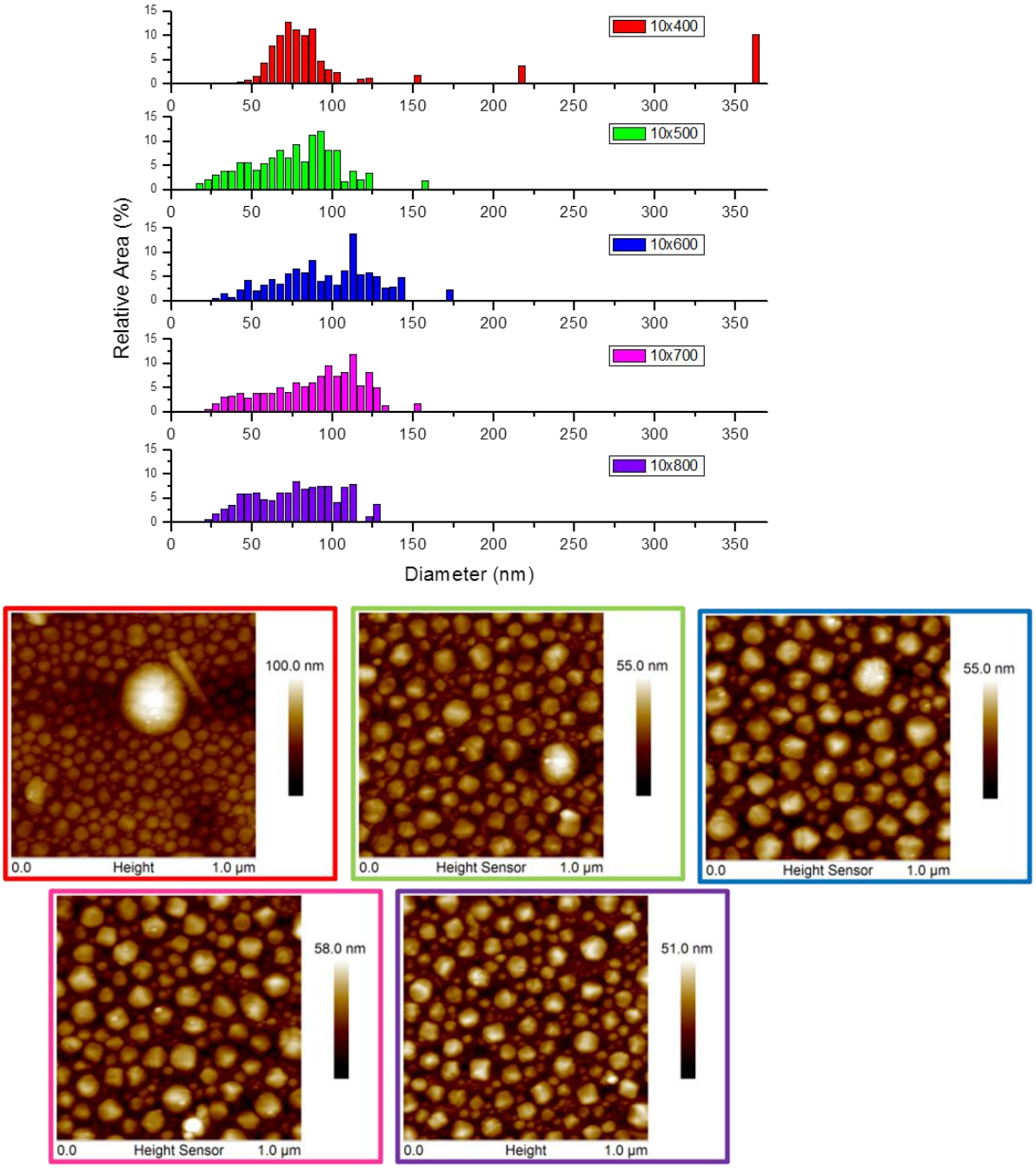

Figure 4.21. Particles size distribution with the corresponding topographies with respect of laser fluence after 10 successive pulses using 248nm laser wavelength

Sample #3:

Finally, The ORS measurements of sample #3, which is the thickest of the three, are illustrated below. Figure 4.22 shows the reflectance of the sample after laser annealing with 193nm wavelength at various fluencies and number of pulses while the respective reflectances

for laser annealing at 248nm wavelength with various fluencies and number of pulses are presenting in figure 4.23.

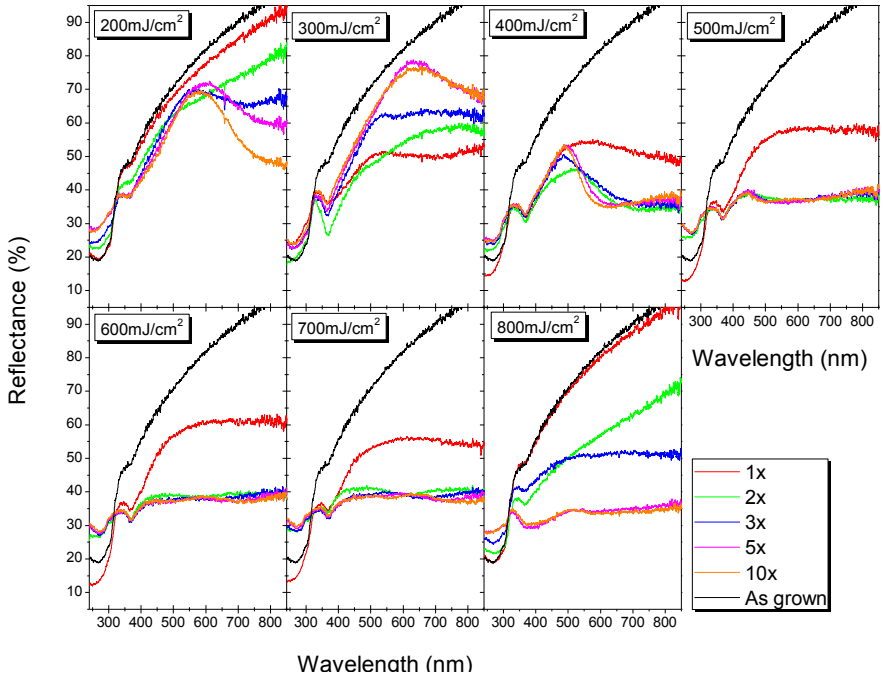

Figure 4.22. Reflectance of sample #3 by varying fluence and number of pulses for laser annealing with 193nm wavelength.

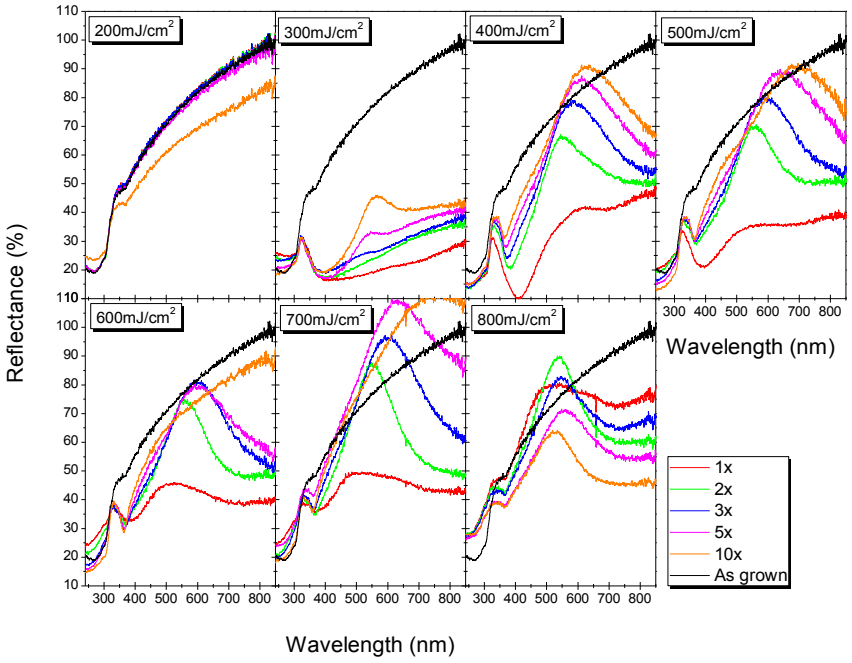

Figure 4.23. Reflectance of sample #3 with respect to various fluencies and number of pulses using 248nm wavelength.

Effect of pulses:

In case of the thicker sample for 200mJ/cm^2 even after 10 pulses the sample is still retain the metallic behavior. The lower limit in order LSPR peak to emerged is the case of 3 pulses at 300mJ/cm^2 where a plasmon peak was manifested at around 550nm (Figure 4.24 a) while the implementation of 5 consecutive pulses red shift the LPSR peak at 600nm indicating the coalescence of the existence particles and the formation bigger once. Further increase at 10 pulses leads to nanoparticles with small size and thus a blue shift of the LSPR peak was observed.

Contrariwise for 400mJ/cm^2 and above the LSPR manifestation was observed even from the first pulse. Thus, in case of 400mJ/cm^2 for 1pulse and LPSR peak emerged at 525nm. The implementation of an extra pulse (2 pulses) deconstructs the existing particles producing smaller nanoparticles. As a result a blue shift of the LSPR peak was observed. Unlike to two successive pulses, in case of 3 and 5 pulses a red shift was recorded in the ORS spectrums indicating the formation of bigger nanoparticles than previously. Finally, the implementation of 10 successive pulses causes a minor blue shift of the LSPR peak.

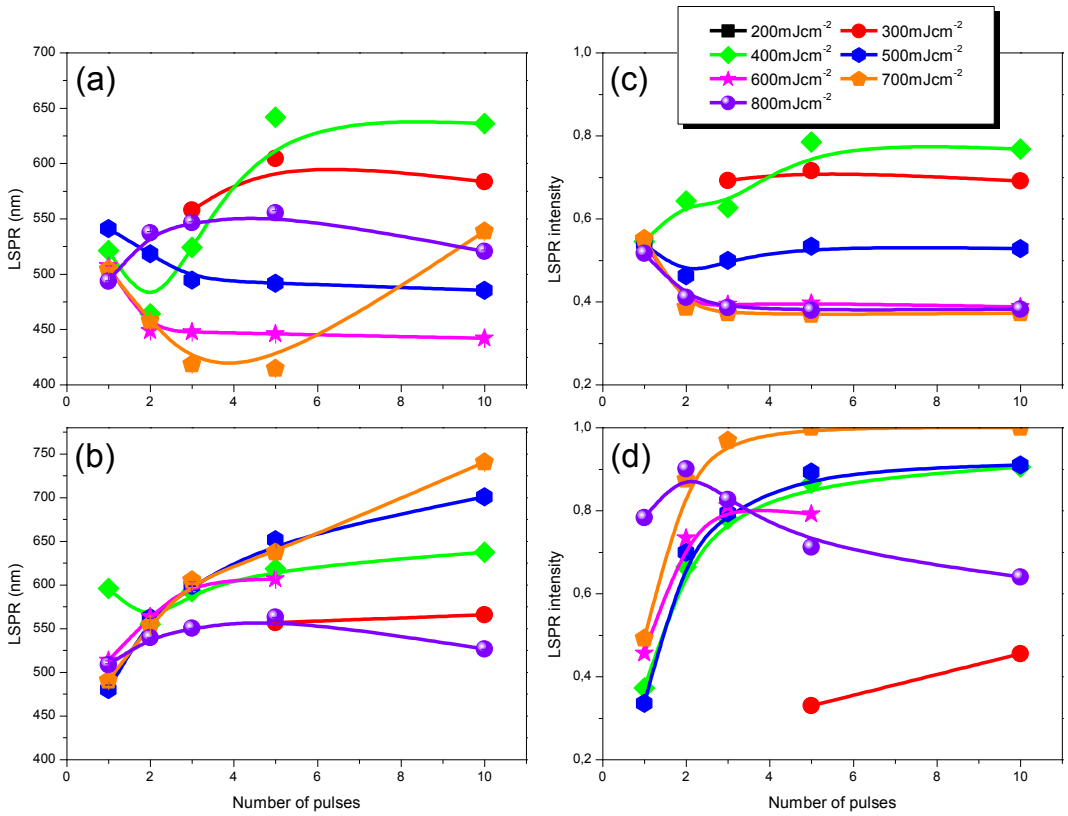

Figure 4.24. LSPR peak position and intensity for various number of applied pulses for 193nm (a, c) and 248nm (b, d) laser wavelength respectively.

For 500mJ/cm^2 and 600mJ/cm^2 respectively increasing the number on the applied pulses leads to a gradual blue shift of the LSPR peak indicating the continuous size reduction of the formed nanoparticles. Similar effects were observed for 700mJ/cm^2 up to 5 applied pulses while after 10 pulses a significant peak shift in higher wavelengths (red shift) was observed. Finally, the implementation up to 5 pulses at 800mJ/cm^2 red shifts the LSPR peak while 10 pulses at the same fluence reduces the size of the formed particles and thus a blue shift was recorded in the ORS spectrums. According to the LSPR peak relocation and particles formation a similar behavior of the LSPR intensity was observed as it is demonstrated in figure 4.24 c

When 248nm wavelength was used the optical properties of the sample are different mainly due to the lower delivered energy. Thus, the threshold for LSPR manifestation is at 300mJ/cm^2 after 5 pulses.

In case of 248nm, the implementation of each extra pulse work constructive in the formation of bigger nanoparticles. As a results a gradual red shift of the LSPR peak position was observed which is reflected in the intensity of the LSPR peak as it is already discussed above (Figure4.24 c) while only after 10 successive pulses for the highest fluence (800mJ/cm^2) a blue shift of the LSPR peak was observed.

Effect of fluence:

In case of fluence, the second parameter that was considered in this study, for 193nm laser wavelength (Figure 4.25a) 400mJ/cm^2 was the threshold for LSPR manifestation for 1 and 2 applied pulses respectively. In case of 1 pulse, increasing fluence leads to a continuous red shift of the LSPR position indicating the formation of smaller nanoparticles due to the increase of the deliver energy each time.

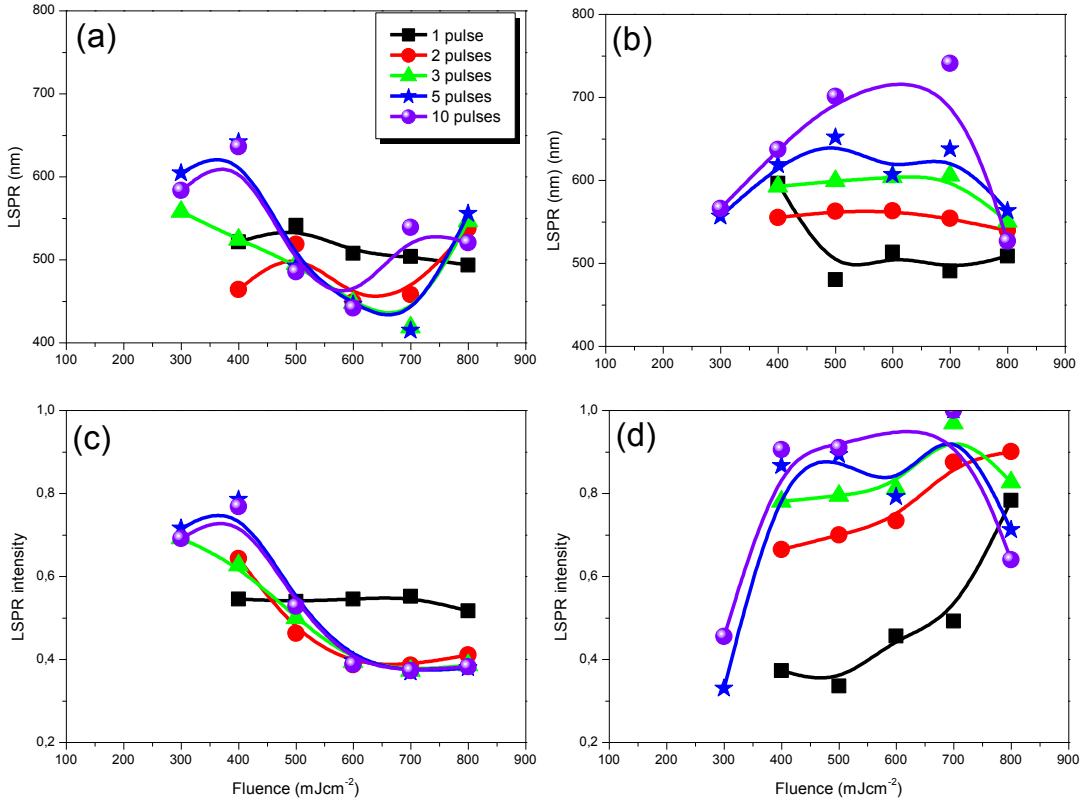

Figure 4.25. Effect of laser fluence in LSPR spectral position and intensity using 193nm (a, c) and 248nm (b, d) wavelength respectively in case of sample #3.

For 2, 5 and 10 pulses respectively the implementation of higher fluencies can act constructively or distractively with simultaneous enlargement or reduction of particles size.

Finally in case of 3 successive pulses, increasing fluencie up to 700mJ/cm^2 relocation the LSPR peak position in lower wavelengths (blue shift). On the contrary, for 800mJ/cm^2 a red shift of the peak was observed which can be assigned in the enlargement of the existing particles.

In case of 248nm laser wavelength and for 1, 2 and 3 pulses respectively the lower limit of fluence for LSPR to be emerged was at 400mJ/cm^2 while for higher number of applied pulses the corresponding threshold was at 300mJ/cm^2.

For 1 pulse (Figure 4.24b) the transition from 400mJ/cm^2 to 500mJ/cm^2 causes a blue shift of the LSPR peaks while for 600mJ/cm^2 LSPR peaks moves to higher wavelengths. Further increase of the fluence (700mJ/cm^2) causes afresh a blue shift of the LSPR while the maximum value of fluence shifts the LSPR peak at higher wavelengths.

In case of 2 pulses, the increase of the fluence up to 600mJ/cm^2 causes a minor red shift of the LSPR peak while for higher fluencies a blue shift was recorded in the ORS spectrums that can be attributed in the dissolution of the existing particles in smaller. Similar behavior was also

observed in case of 3 and 10 successive pulses up to 700mJ/cm^2. Beyond this value a blue shift of the LSPR peak was observed.

Nevertheless, in case of 5 successive pulses the increase of laser fluence can work either constructively (enlargement of the nanoparticles-red shift) or destructively (smaller nanoparticles-blue shift) as it is demonstrated in figure 4.25b

It is worth noticing that the LSPR intensity is strongly related with the effect of the fluence in the particles size for both 193nm and 248nm laser wavelength. Thus, in case of a red shift in LSPR peak position, possible due to particles enlargement, a simultaneous increase of LSPR intensity was observed, on the contrary for blue shift of the LSPR peak a reduction of the peak intensity was observed as well.

4.3 Conclusions

In this thin silver films were grown using magnetron sputtering technique and were subjected to a new, widespread cold annealing process namely laser annealing and the optical and structural properties with respect to laser parameters such as wavelength, fluence, number of pulses and film thickness was considered.

Combined optical (ORS) and morphological (AFM) measurements respectively demonstrated that though laser annealing we managed to accurate control of the silver size and quality nanoparticles.

The analysis of the optical response of the annealed samples show that LSPR peak position and intensity was strongly related to laser parameters while the thickness of the starting film was a critical factor for laser annealing.

Thus, as regards laser wavelength, it was revealed that 193nm was more effective due to higher delivered energy leading to more narrow particles size distributions. On the contrary, 248nm laser wavelength induces more broad particles size distributions and as a result bimodal systems were observed in some cases.

On the other hand, in case of consecutive pulses a spectral shift of the LSPR peak position in higher wavelengths (red shift) and an LSPR enhancement was induced which was associated with nanoparticles enlargement while increasing fluence it was demonstrated a blue shift of the LSPR peak position indicating dissolution of the initials nanoparticles to smaller due to higher energies reached the sample.

Finally, concerning film thickness was evidenced that higher amounts of energy was needed as film thickness increased for LSPR manifestation.

References

[4.1] Zoubos H. *et al., Solar Energy Materials and Solar Cells*, **117** (2013), pp. 350-356.

[4.2] Henley S.J., *et al., Nanoscale*, **5** (2013), pp. 1054-1059.

[4.3] Kim Seok-Soon *et al., Applied Physics Letters*, **93** (2008), pp. 073307_1-073307_3.

[4.4] Kooyman R.P.H., *et al., Journal of Molecular Structure*, **218** (1990), pp. 345-350.

[4.5] Guo L., Yuan W., Lu Z., Li C.M., *Colloids and Surfaces A: Physicochem. Eng. Aspects*, **439** (2013), pp 69-83.

[4.6] Chaloupka K. Malam Y., Seifalian A.M., *Trends in Biotechology* , **28** (2010), pp. 580-588.

[4.7] Peng P., Hu A., Shou Y., *Applied Physics A: Materials Science and Processing*, **108** (2012), pp. 685-691.

[4.8] Grochowska K. et al., *Plasmonics*, **8** (2013), pp. 105-113.

[4.9] Yang Y., Zhang M.Y., Cheng G.J, *Applied Physics Letters*, **99** (2011), pp. 091901_1-091901_3.

[4.10] Tseng M.L., Huang Yao-Wei *et al*., *ACS Nano*, **6** (2012), pp. 5190-5197.

[4.11] Beliatis M.J. *et al*., *Optics Letters*, **36** (2011), pp. 1362-1364.

[4.12] Kurita H. *et al., Applied Physics Letters*, **72** (1998), pp. 789-791.

[4.13] Takami A. *et al., J. Phys. Chem. B*, **103** (1999), pp. 1226-1232.

[4.14] Pyatenko A. *et al., J. Phys. Chem. B*, **113** (2009), pp. 9078-9085.

[4.15] Seal K., Nelson M.A., *et al.*, Phys. Rev. B Cond. Mat. Mater. Physic., **67** (2003), pp. 353181-3531813.

[4.16] JCPDS 00-004-0783

Chapter 5 *Metal-Dielectric Binary Systems in Various Formations*

5.1 **Introduction**

Nanocomposite materials consisting of a metallic phase and a ceramic host although have been long established as important category of materials, they are still a growing field of because by exploiting the exceptional flexibility in tailoring their functional properties makes it suitable candidates for new emerging technologies such as biointerfaces [5.1,5.2], high-density magnetic storages [5.3,5.4], magneto resistive devices [5.5,5.6], solar photothermal coatings [5.7,5.8], advanced catalysts and electrochemical devices [5.9]. Moreover, the ability of LSPR resulting from the interaction of the metal conduction electrons with light makes them applicable in various plasmonic applications [5.10, 5.11].

In this chapter, a thorough study of the optical and structural properties of AlN- based nanocomposite films with silver inclusions in various morphologies is presented.

Aluminum nitride (AlN) is a very well known wide band gap semiconductor (E_g = 6.2 eV) which exhibits several high quality characteristics such as pure transparency in the visible spectral region and high refractive index (n=2). In addition, it has excellent mechanical properties and substantial chemical and metallurgical stability make it suitable for a wide range of applications such as antireflection [5.12] and protective coatings [5.13]. On the other hand, silver is the archetypical material for plasmonic applications [5.14] due to the low dielectric losses and the absence of any interband transition in the visible range resulting in the strongest LSPR in the visible range among all metals.

Firstly, the metal phase distribution into the ceramic matrix before and after LA with different laser parameters is investigated, for samples that were grown by Pulsed laser Deposition. These films consist of Ag nanospheres (<4nm) in an amorphous AlN matrix [5.15]. Secondly, our studies focus to nanocomposite films that were gown by Magnetron Sputtering with two different approaches. The first approach includes the dispersion of the metallic phase into the AlN host by co-sputtering of AlN and Ag and the effect of thermal and laser annealing on the structural and optical properties is investigated. In a second and different approach the transformation of Ag layers to nanoparticles is attempted. For that reason, multilayers consisting of alternately AlN and Ag layers are deposited and the effect of laser annealing is extensively investigated.

5.2 AlN:Ag nanocomposite films grown by Pulsed Laser Deposition

5.2.1 Thin Film Deposition

The deposition parameters and structural informations about the samples that were used in this section of the chapter have already reported extensively [5.15], so regarding to structural characterization we will give some general features of the as grown samples based on the work that has already done.

As it can be seen in figure 5.1 PLD samples provide a totally XRD amorphous AlN phase. On the other hand the XRD diffractogram revealed two diffraction peaks at around 38^o and 45^o degrees respectively. These diffraction peaks can be attributed in pure metallic Al droplets as it was identified from SEM observations and EDX qualitative analysis of the samples (Figure 5.2).

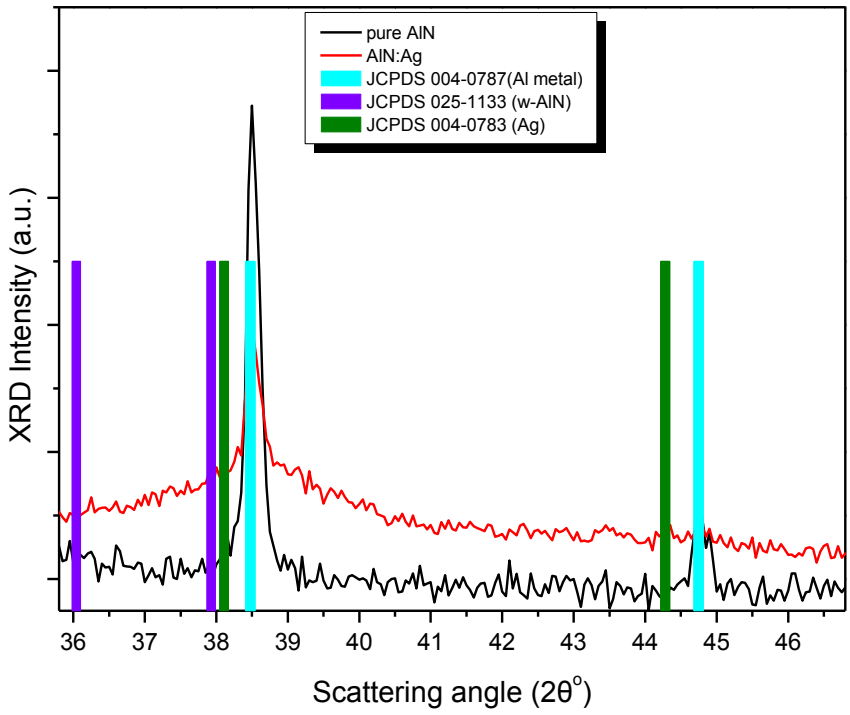

Figure 5.1. XRD pattern of the pure AlN (black line) and PLD AlN:Ag nanocomposite sample (red line) film.

Finally, the presence of Ag in AlN:Ag nanocomposite films is demonstrated for the broadening of the main XRD peak at around 38^o.

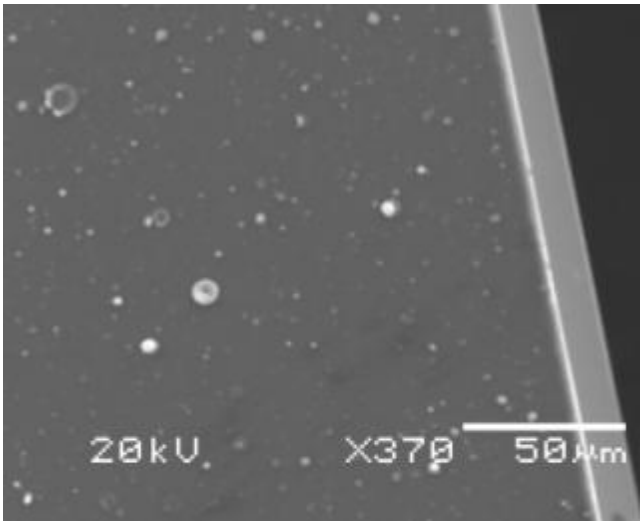

Figure 5.2. SEM image of a pure AlN surface. Al droplets are presenting in the surface as a part of the deposition process.

The structural and morphological characterization was also studied by Transmission Electron Microscopy (TEM) observations in order to investigate the distribution of the metallic phase within the matrix. As it is illustrated in figure 5.3 the as deposited film gives no trace of crystalline AlN, while the density and the refractive index of the AlN matrix have values inferior to crystalline w-AlN [5.15] confirming the amorphous nature of the matrix, while the formation and homogeneous distribution of the silver nanoparticles into the matrix is verified.

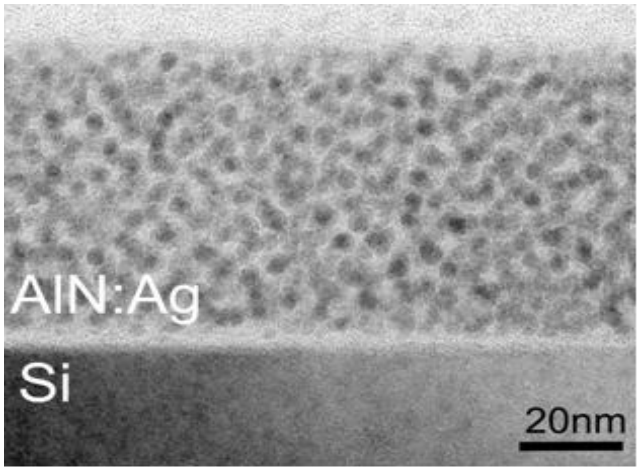

Figure 5.3. Cross section TEM observation of the as grown sample. A narrow distribution of the silver nanoparticles into an amorphous matrix is observed.

Moreover, the formed nanoparticles present a narrow size distribution as follows from the TEM measurements and depicted in figure 5.4

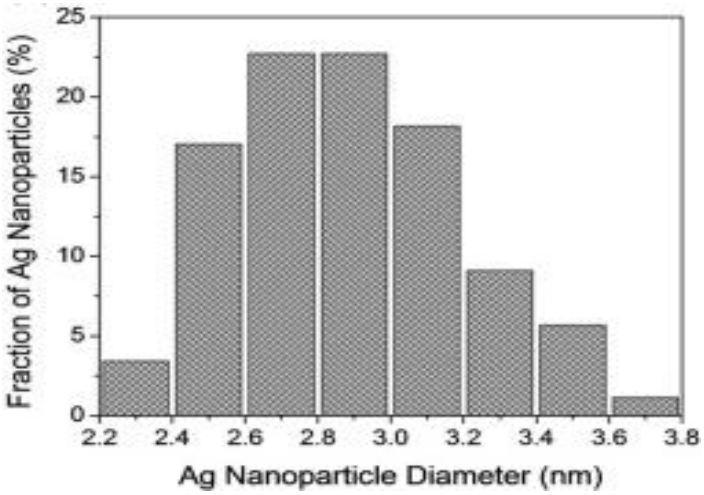

Figure 5.4. Representative particle size histogram of the as grown nanocomposite film.

On the other hand the successfully formation of silver nanoparticles linking to a Surface Plasmon Resonance manifestation around 420nm as it was observed from Optical Reflectivity Spectroscopy measurements (Figure 5.5) .

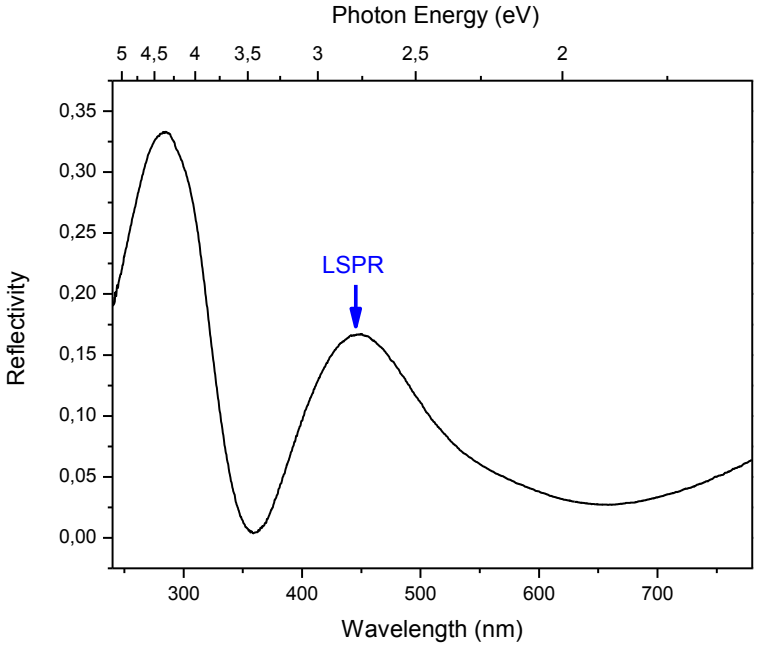

Figure 5.5. Reflectivity spectrum of an as grown sample.

5.2.2 Thin Film Processing

The as deposited films were further subjected in two different annealing approached, thermal and laser annealing respectively, with various parameters and the optical and structural changes of the treated samples were studied.

5.2.3 Thermal annealing

In a first step the as-grown films were thermally annealed in various temperatures starting from 400 ^{o}C up to 800^{o}C for 1 hour under argon ambient in order to avoid film oxidation.

In figure 5.6 the optical response of the sample after thermal annealing in various temperatures is summarized.

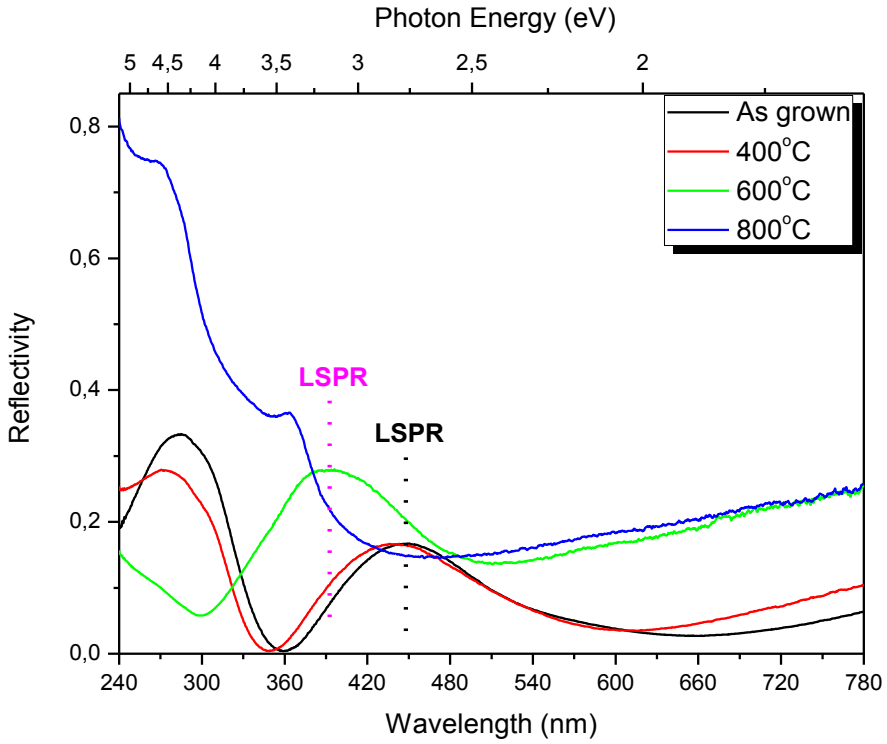

Figure 5.6. Reflectivity spectrums for different annealing temperatures.

As it can be seen annealing at 400^{o}C causes a minor alteration in spectral position and intensity is observed according to the as deposited. For annealing at 600^{o}C and 800^{o}C respectively, disruption of the nanoparticles and outdiffusion of the silver in the surface occurs.

5.2.4 Laser annealing

In order to anticipate outdiffusion effects our films were subjected to UV laser annealing due to its ultrafast character (~20 ns), which drastically reduces the diffusion phenomena as well as

the uneven distribution of the delivered energy according the optical absorption of the constituent phases. The effect of various parameters such as the wavelength, number of pulses and fluence in the structural and optical properties was examined. In particular, ArF (193nm) and KrF (248nm) UV-excimer lasers (20nm pulse duration) were applied for laser annealing of samples with fluencies in the range of 200mJ/cm^2 to 600 mJ/cm^2 while 1, 2, 3 and 5 pulses were applied.

As a starting point, we begin with the interaction of the laser beam with a pure AlN film deposited by PLD on Si (100) substrate, in order to identify and evaluate the potential structural and morphological changes upon laser annealing.

The optical reflectivity spectra of an AlN/Si sample before and after laser annealing using the 248 nm laser beam (magenta up and down triangles for 400, 500 mJ/cm^2, respectively, and denoted as LA@248 nm) and the 193 nm laser beam (purple up and down triangles and diamonds for 100, 300, and 400 mJ/cm^2, respectively, and denoted as LA@193 nm) are displayed in figure 5.7. It is evident that for low fluence (λ=193 nm, 100 mJ/cm^2, purple up triangles) the changes in the optical reflectivity spectra are minor and maybe attributed to the interface roughening and amorphization of Si due to the delivery of the laser energy directly to the substrate. The laser beam does not interact with the AlN layer itself because of the transparency of AlN; note that the fundamental gap of AlN has been reported to be above E_g=6.2 eV.

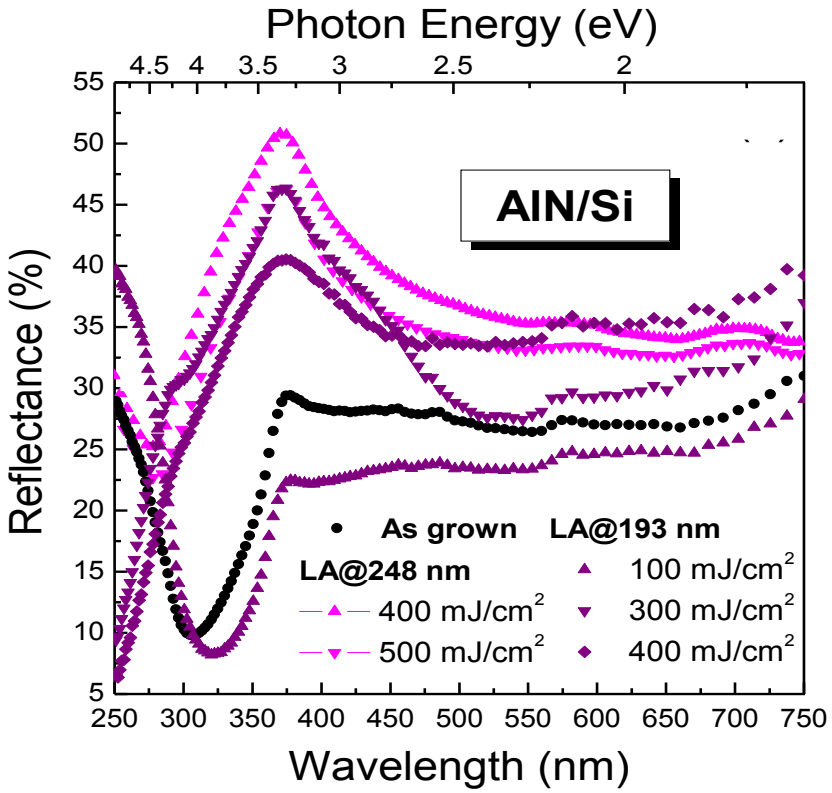

Figure 5.7. ORS spectra of pure AlN on Si substrate as a function of the laser fluence.

For fluencies in the order of the laser damage threshold of Si which is about 350mJcm^{-2} for laser annealing using 248nm wavelength, the film is removed from the substrate and now the characteristic Si-relevant reflectivity peak at about 330 nm is observed in ORS spectra. Delamination of the film from the substrate is also confirmed by electron microscopy measurements with corresponding image depict in figure 5.8.

Finally, for further higher laser fluencies (500 mJ/cm^2 for 248 nm, and 400 mJ/cm^2 for 193 nm) the AlN is removed, as well, but the Si peak at 330 nm is broadened due to Si damage and amorphization to a larger extend.

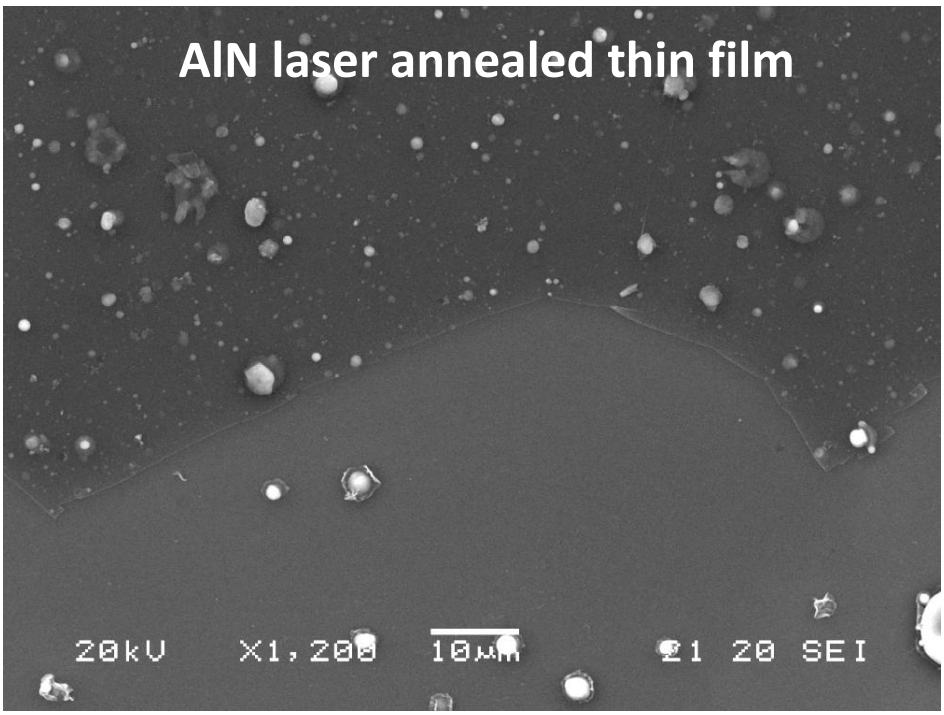

Figure 5.8. SEM image of pure AlN after laser annealing. Film delamination is observed for fluencies near the laser damage threshold.

Despite the fact that delamination of the film has been attributed in the absorption of the laser beam from the film in our cases lift-off of the film resulting from substrate damage as the film does not interact with the laser beam.

On the contrary, the AlN:Ag/Si samples endured the laser irradiation (193 nm, 300 mJ/cm^2), as it is shown in the plane view secondary electron image of figure 5.9, where no removal of AlN:Ag has been observed (the horizontal red line denotes the border between the treated and untreated areas of the sample's surface); the film remained intact and only its reflectivity changed after laser annealing. This is because the Ag nanoparticles absorb and scatter the incoming laser light reducing the power that arrives to the Si substrate below the damage threshold.

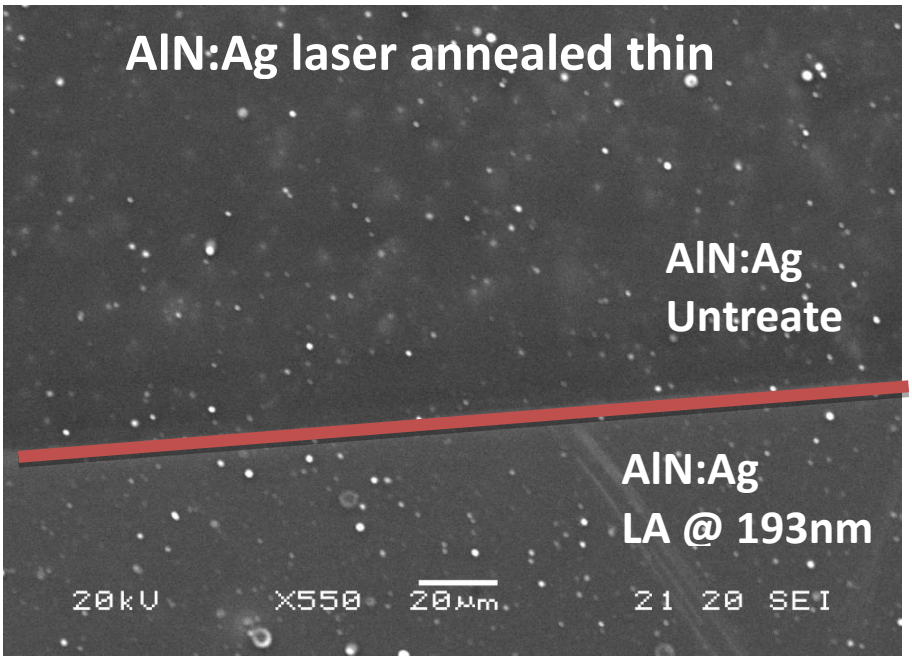

Figure 5.9. SEM image of the nanocomposite sample after laser annealing.

A major factor that can affect the process of laser annealing is the laser wavelength, because of the different values of absorption coefficient of the amorphous AlN matrix for the two laser wavelengths (193 and 248 nm), as well as of the Ag nanoparticles.

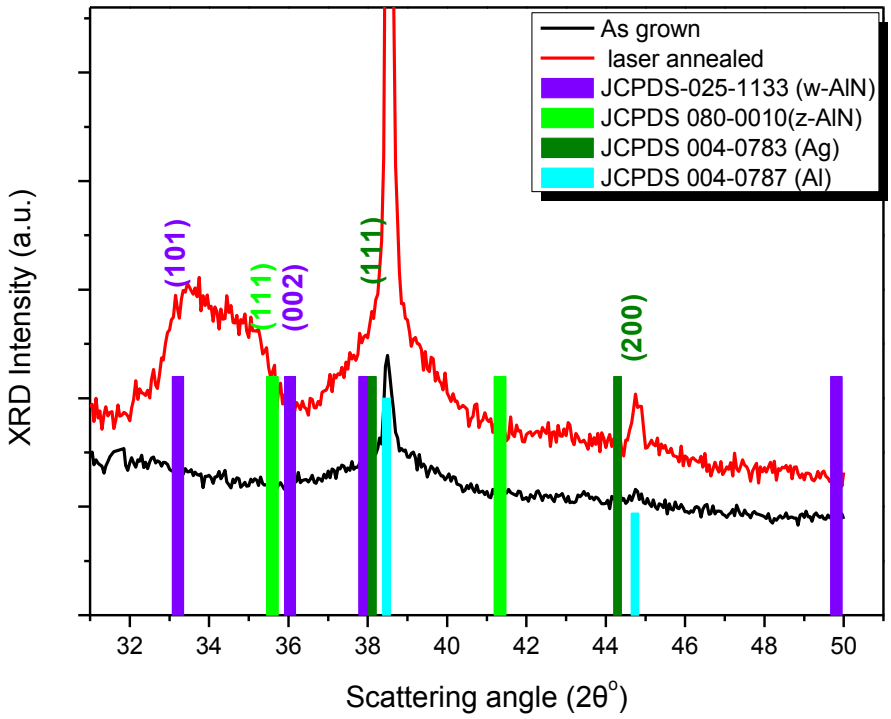

Figure 5.10. XRD pattern of the nanocomposite film after laser annealing with 1 shot, 200mJcm^{-2} at 193nm wavelength.

The X-ray diffractogram (Figure 5.10) of the laser annealed a-AlN:Ag samples reveals crystallization of the AlN matrix to form w-AlN and possibly strained z-AlN (an AlN polytype of similar structure to w-AlN, but with differently stacked basal planes).This. The location of the crystallized AlN is attributed to the Ag nanoparticles acting as hot spots during the laser pulse inducing an immense temperature increase at the neighborhood of the AlN/Ag interface. However, HRTEM cross section images of the laser treated areas that displayed in figure 5.11 revealed even more significant structural modifications after laser annealing for both wavelengths. In particular, laser annealing with 193nm wavelength (Figure 5.11 g, h, i) leads to Ag np's agglomeration and formation of larger while a more significant structural alteration is the partial recrystallization of the matrix especially in the shell of the nanoparticles. Similar results but to a lesser extend occurs after laser treatment using 248nm wavelength (Figure 5,11 d, e, f,) which can attributed in the lower delivered energy which is lower than the AlN optical band gap (6.2eV) and only interaction with Ag nanoparticles occurs. As a result the delivered energy to the substrate is higher and thus more rough AlN/Si interfaces were observed.

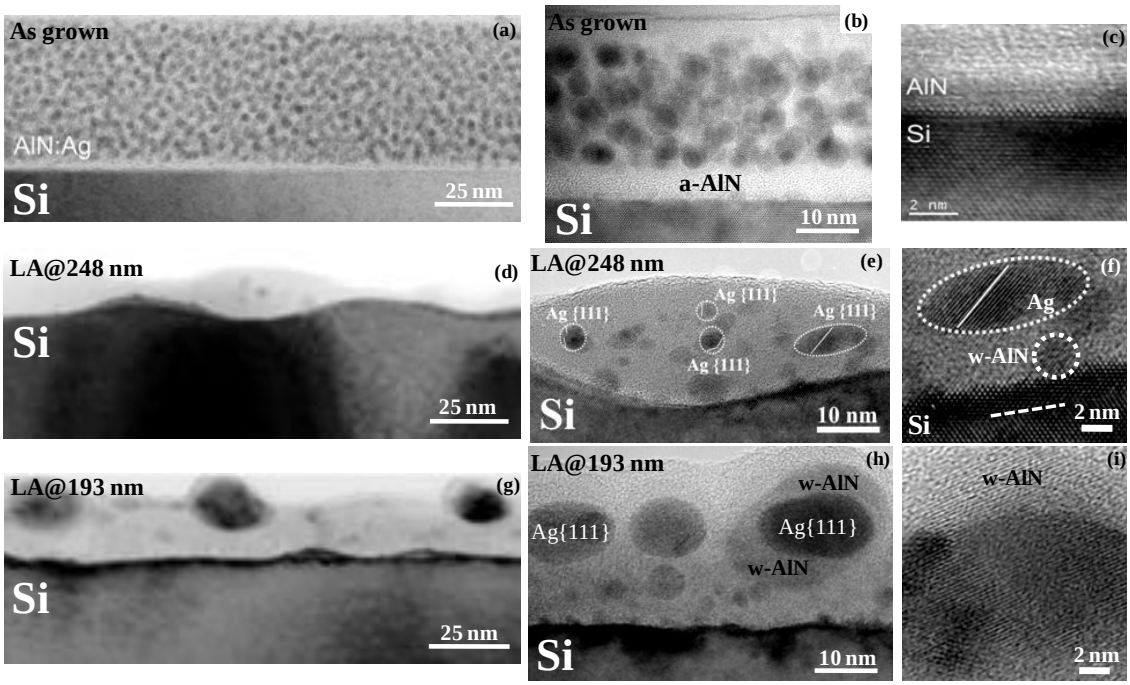

Figure 5.11. Cross section TEM images of increasing resolution from AlN:Ag/Si: (a,b,c) as-grown, (d,e,f) laser annealed with two pulses of 248 nm/400 mJ/cm^2, and (g,h,i) laser annealed with one pulses of 193 nm/400 mJ/cm^2.

These structural modifications after laser annealing alter the optical properties of the films as ORS measurements revealed (Figure 5.12). Thus, a significant LSPR enhancement after LA was observed comparing to the as grown film for both wavelengths while the np's enlargement and matrix recrystallization leads to a red shift of the LSPR spectral position. On the other hand,

the matrix recrystallization gives a more transparent character to our films. As a result, substrate features are reflected to the reflectivity spectra.

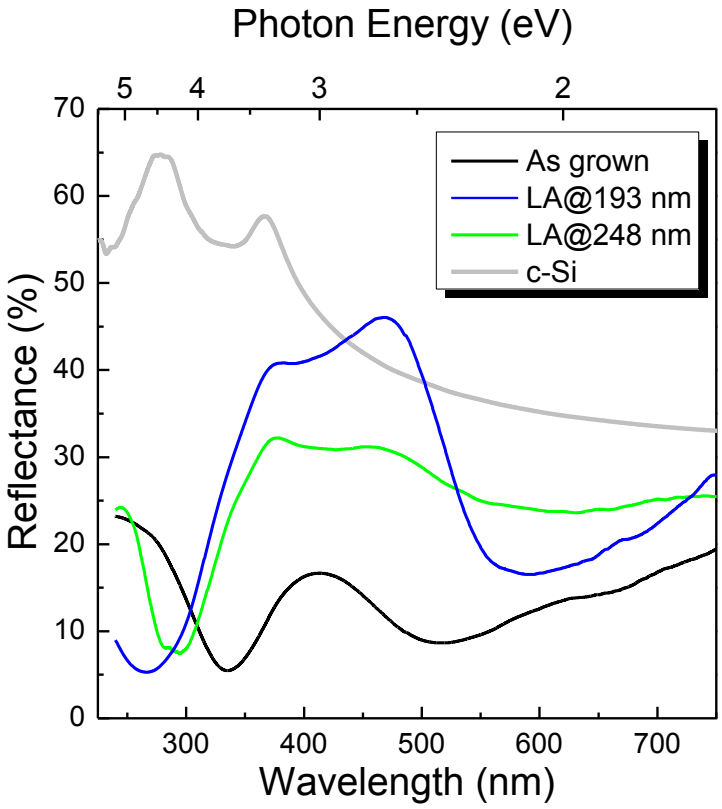

Figure 5.12. Optical reflectivity of AlN:Ag: as grown, LA with a 193 nm-400 mJ/cm^2 pulse, and LA with two 248 nm-400 mJ/cm^2 pulses respectively..

Then, the effect of the applied number of pulses was investigated as well. The optical reflectivity spectra for various successive pulses are depicted in figure 5.13. For various fluencies the one pulse causes a significant red shift, from around 400nm to 470nm, on the LSPR peak with a simultaneous SPR enhancement. As it can be seen for low fluencies (200mJ/cm^2) at 193nm wavelength (Figure 5.13a) each successive pulse leads to an LSPR enhancement while substrate features can be observed due to film's transparency. On the contrary when higher fluencies are used (300mJ/cm^2) the effect is more effective and thus for three successive pulses Ag massive outdiffusion is observed. On the other hand, when 400mJ/cm^2 fluence is used at 248nm wavelength two additional pulses provides an LSPR enhancement while for 3 consecutive pulses a blue shift of the LSPR peak position is observed due to formation of smaller nanoparticles the structural features of the laser annealed samples were studied through XRD and TEM measurements respectively.

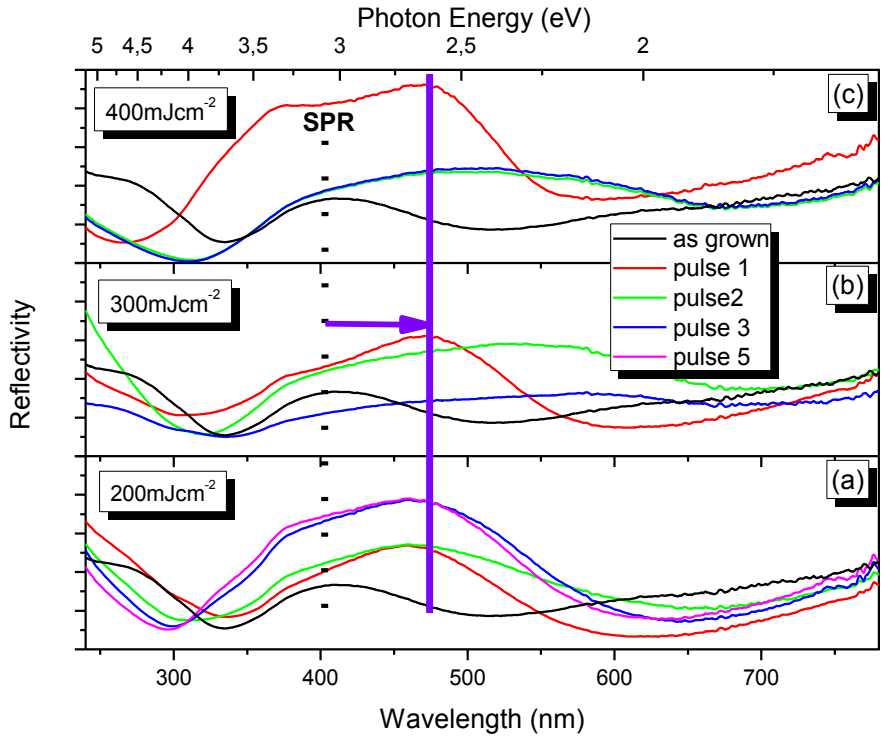

Figure 5.13. Effect of the applied pulses in the LSPR behavior at 193nm wavelength.

Unlike to laser annealing with 193nm wavelength, using 248nm the LSPR enhancement is less intense while the red shift of the LSPR peak is also observed. From TEM cross section image, that is depicted in figure 5.11, it can be seen that now, although crystallization of the matrix occurs, due to lower energy smaller particles are formed leading in lower LSPR peak intensities

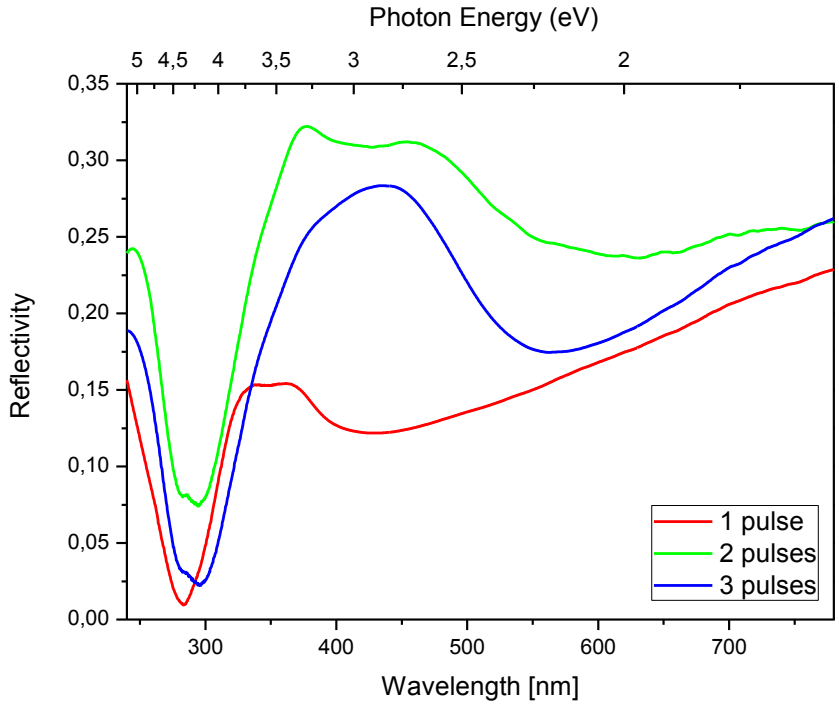

Figure 5.14. LSPR performance after laser annealing at 400mJcm^{-1} with 248nm wavelength and different number of pulses.

The effect of the fluence in structural and optical features of the nanocomposite films was another factor that was studied.

The ORS spectra of the laser annealed samples with various fluencies are depicted in figure 5.15 for both 193nm and 248nm wavelength respectively.

For laser treatment at 193nm wavelength a significant and consistent enhancement of the SPR peak efficiency is observed as the fluence increasing up to 400mJcm^{-2} while a red shift in the SPR peak position is caused. For 600mJcm^{-2} Si substrate features are clearly observed in the ORS spectrum which evidence that the 600mJcm^{-2} delivered energy is sufficient for ablation.

Unlike to laser annealing with 193nm wavelength, at 248nm wavelength the enhancement of the LSPR intensity is not as intense as previously due to smaller nanoparticles that are formed after laser annealing in comparison with 193nnm. On the other hand a red shift of the SPR peak is for 400mJcm^{-2}. For fluencies 500mJcm^{-2} and 600mJcm^{-2} a blue shift of the SPR peak is caused with a simultaneous reduction of the intensity.

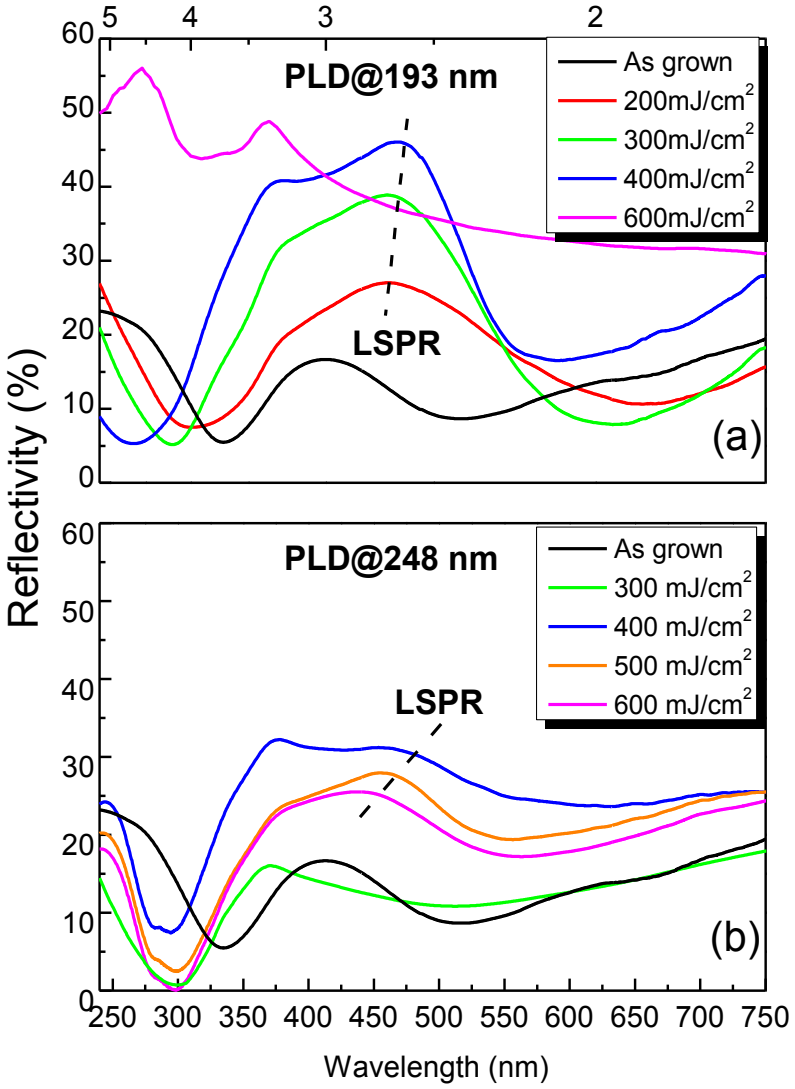

Figure 5.15.Reflectivities of the laser annealed sample as a function of the fluence using 193nm (a) and 248nm wavelength (b) respectively.

The combination of the LSPR enhancement with simultaneous structural changes that occurs after laser annealing leads to a strong reflectivity contrast which can be used for spectrally selective patterns into AlN:Ag nanocomposite films.

In order to investigate this opportunity we encode the pattern "*AlN:Ag*" into the nanocomposite film consisting of 60μm pixels of annealed sample. The encoded pattern illustrated in figure 5.16.

Figure 5.16. The annealed pattern under white illumination. Each pixel of the pattern is approximately 60µm

The formed pattern was illuminated using four different colored lights covering the visible region of the electromagnetic spectrum. Indeed, as it is illustrated in figure 5.16 our samples are spectrally selective only in the blue-violet region which is in agreement with the optical results. The reflectivity contrast ΔR in this region is maximum around 470nm (ΔR=35%). On the other hand in the red region (ΔR= 5%) pattern is totally invisible, while in the green region ΔR= 15%) the pattern is barely visible.

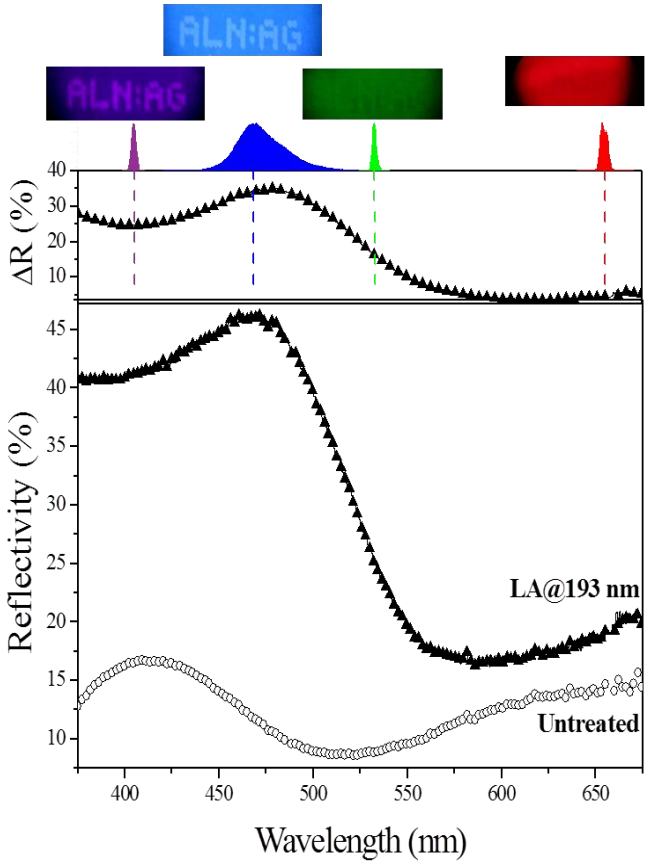

Figure 5.17. Reflectivity contrast (ΔR) between the treated and untreated sample. The maximum ΔR is observed in the blue region.

5.3 AlN-Ag co-sputtered thin films

5.3.1 Thin Film Deposition

In this section nanocomposite films were grown with simultaneously deposition of Al and Ag in N_2 and Ar environment using a Confocal Dual Magnetron Sputtering (DCMS). The sputtering power of the Al cathode was varied in order to vary the degree of matrix crystallinity, while the sputtering power of the Ag cathode was varied in order to control the Ag concentration into the films. The structural and morphological features of the as-deposited films were investigated by X-ray diffraction and X-ray reflectivity, while the chemical state and the concentration of the Ag into the AlN was identified using X-ray Photoelectron Spectroscopy (XPS).

The main deposition conditions of the studied samples are summarized in Table V.

Table V. Deposition parameters of the co-sputtered nanocomposite films.

Sample ID	**Al Power (Watt)**	**Ag Power (Watt)**	**Ag concentration (% at.)**	**Ar flow(sccm)**	**N_2 flow (sccm)**	**Deposition time (min)**
Sample #4	100	0	0	12	8	30
Sample #5	15	0	0	12	8	30
Sample #6	100	3	6	12	8	30
Sample #7	100	15	11	12	8	30
Sample #8	100	25	32	12	8	30
Sample #9	15	3	7	12	8	30

The XRD patterns of the pure AlN films (Figure 5.17) show that Sample #4 that was grown with 100 Watts applied power exhibits characteristic diffraction peaks corresponding to the (002) and (101) crystal planes of w-AlN, which indicates a preferential growth along these crystal orientations. Contrariwise, when the sputtering power is lowered the degree of crystallinity decreases as well. Thus sample #5 did not exhibit any peak assigned to AlN in the X-ray diffractogram. In both cases a diffraction peak at around 32.9^o is observed which corresponds to (002) of Si [5.16].

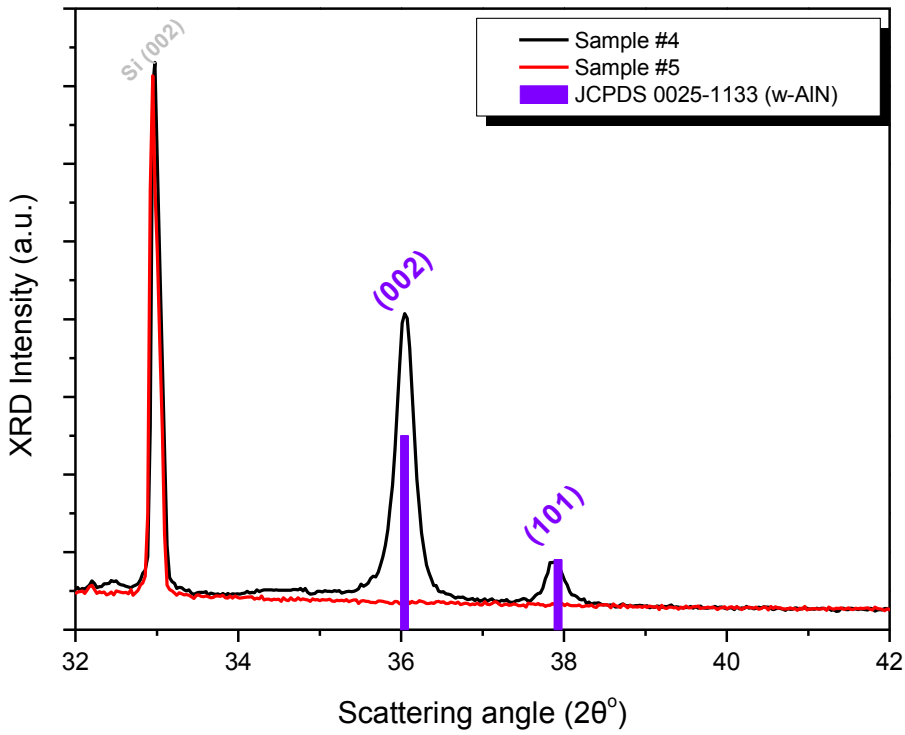

Figure 5.18. Bragg-Brentano XRD pattern of pure AlN with different sputtering power.

On the other hand the incorporation of Ag into AlN films induces severe changes in their microstructure and morphology, especially for the case of sputtered w-AlN. So, as it was revealed from the XRD measurements (Figure 5.18) for small [Ag] concentration (Sample #6), there is no indication of diffraction from Ag and the recorded pattern resembles that of powder w-AlN suggesting that Ag is very finely dispersed into the w-AlN matrix (i.e. atomically dispersed or in clusters of <2 nm that cannot be probed by XRD). For higher silver concentration the film becomes even less textured indicating a gradual transformation from columnar morphology for w-AlN to globular morphology for w-AlN:Ag (11%, Sample #7). In addition, a very broad peak emerges around the expected angular value for the Ag (111) diffraction peak, indicating segregation of Ag.

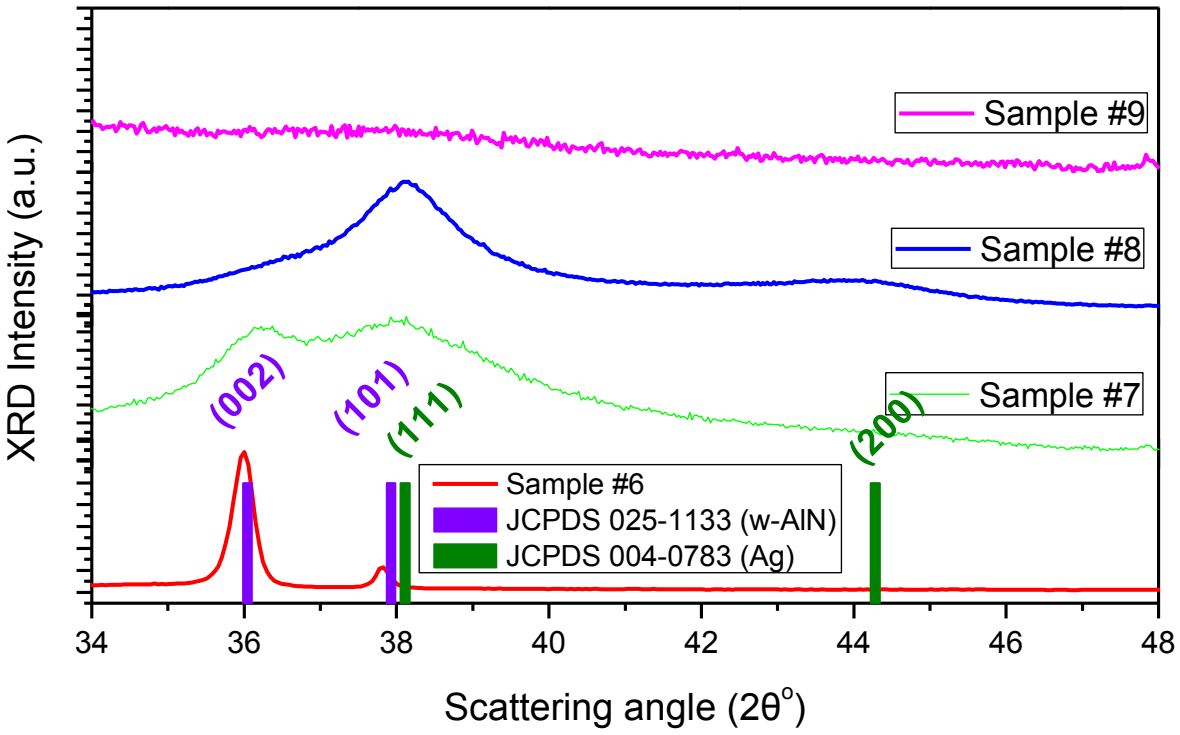

Figure 5.19. XRD pattern of the co-sputtered nanocomposite films.

For Ag concentration 32% *at.* (Sample #8) the diffraction pattern of w-AlN is not observed at all, instead two characteristic peaks of Ag (111) and Ag(200) are manifested. The profile of the Ag (111) is asymmetric possibly due to contribution of AlN(101) and non-uniform strain and concentration gradients. The manifestation of an Ag diffraction pattern indicates that a total segregation occurred in this later case. In the case of the sputtered a-AlN:Ag (Sample #9),the AlN is completely amorphous and its diffraction does no exhibit no trace at all. A very faint modulation of the background around the expected angular position of Ag (111) peak might indicate a small segregation of Ag. In order to estimate structural features like grain size and strain of the studied samples Williamson- Hall and Scherrer analysis respectively were performed. Moreover, thickness and density of the as-grown samples were estimated from X-ray reflectivity measurements. Representative XRR patterns of the studied samples are depicted in figures 5.19

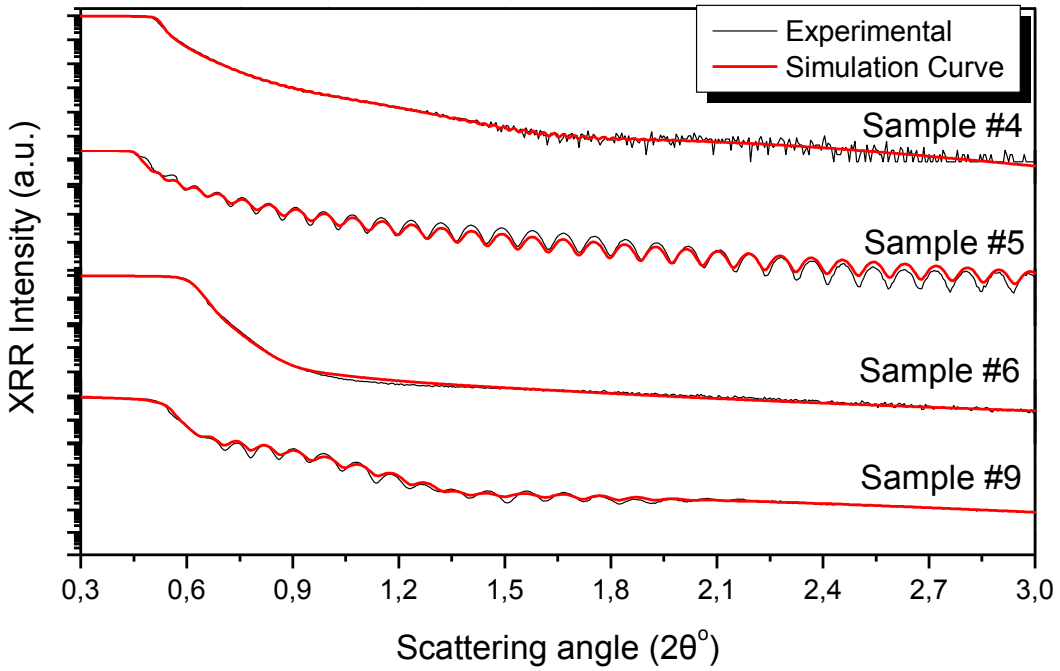

Figure 5.20. X-Ray reflectivity spectrums (black line) with the fit curves (red line) for pure AlN and nanocomposite films.

The results revealed from the grain size and XRR analyses are summarized in table VI.

Table VI. Structural results of the co-sputtered nanocomposite films.

Sample ID	**[Ag] (% at)**	**AlN Grain Size (nm)**	**Ag Grain Size (nm)**	**Thickness (nm)**	**Density (g/cm^3)**
Sample #4	0	123, 41	0	302	3.11
Sample#5	0	0	0	97	2.55
Sample#6	6	32, 15.7	0	530	3.20
Sample #7	11	18.5, 18.7	1.5	507	4.50
Sample #8	30	-	4.5	472	4.77
Sample #9	7	-	-	84	3.17

The results from the XRR analysis revealed that the different degrees of crystallinity that we achieve by applying the sputtering power affect the density of the growing films. Thus, when high sputtering powers are used dense films are produced close to bulk(3.26gr/cm^3). On the contrary, when lower sputtering powers are applied we produce less dense films as it is illustrated in figure 5.20.

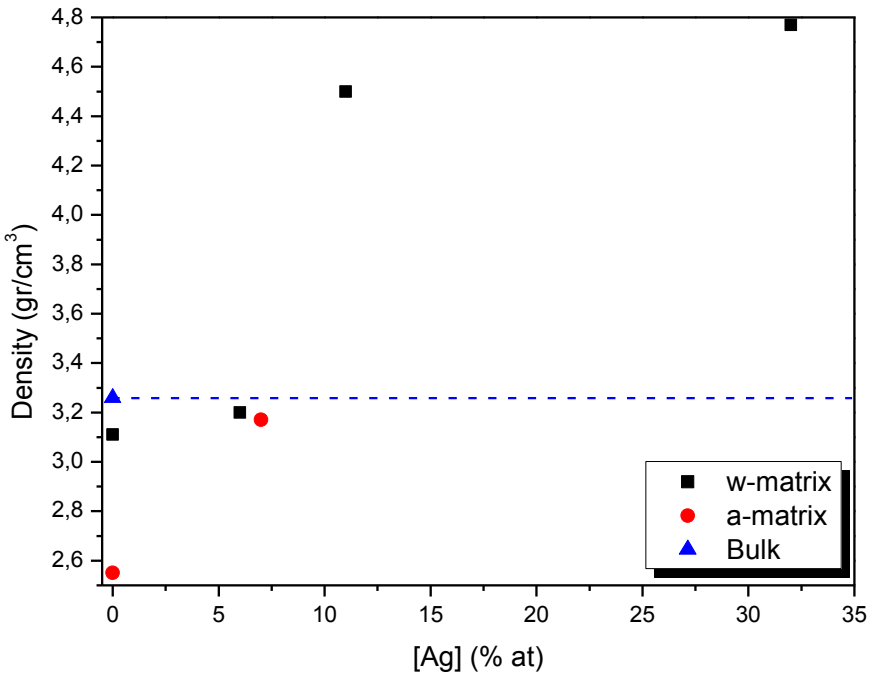

Figure 5.21. Density (gr/cm^3) of the nanocomposite films as a function of the Ag concentration for the co-sputtered films. Amorphous nanocomposite films provide a lower density that the crystalline once.

Finally, X-ray photoelectron spectroscopy measurements were performed in order to identify the Al-N bonding, especially for the amorphous nanocomposite films as well the segregation and self-organization of the Ag into the AlN matrix. Wide scans obtained from our films presented in figure 5.21 where an identification of the XPS and AES peaks had been done for the quantitative and qualitative analysis. Furthermore, high resolution measurements of Al 2p photoelectron peak (Figure 5.22) and Ag 3d (Figure 5.23), respectively, were performed. Charging effects were eliminating using C 1s as reference.

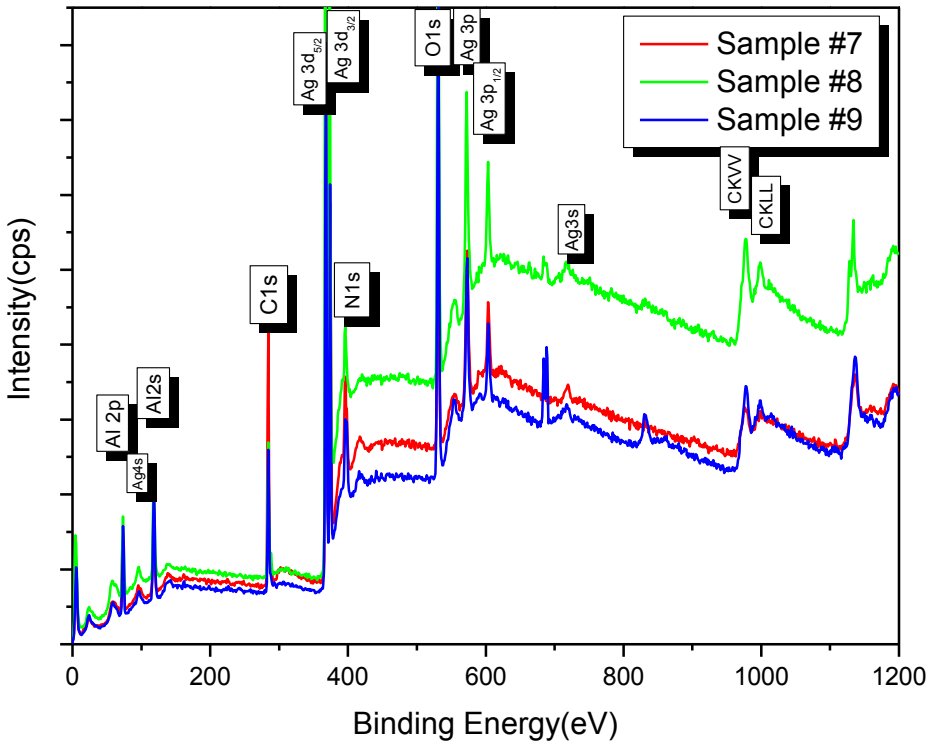

Figure 5.22. Wide scan XPS measurements of as deposited nanocomposite films with the respective qualitative analysis.

Al 2p photoelectron peak, which depicted in Figure 5.22, is deconvoluted with one Gaussian peak which located at binding energies about 73.6 eV corresponding in Al-N bonding [5.17]. The characteristic Ag-3d doublet corresponding to the Ag-3$d_{3/2}$ and Ag-3$d_{5/2}$ due to spin-orbit splitting was observed for all samples. The Ag-3$d_{5/2}$ peak was deconvoluted to two Gaussian peaks located at binding energies of 367.9 eV and 368.4-368.6eV. The former, which is an extremely sharp peak, corresponds to metallic Ag. The presence of silver oxides would induce a shift of the Ag-3$d_{5/2}$ peak to a lower binding energy (367.4 eV for Ag_2O [5.18] and 367.3 eV for AgO [5.19]). The Ag oxide peaks also are broader compared to the corresponding metallic peak [18] this further supports the assignment of the peak at 367.9 eV to metallic Ag. Therefore, the peak observed around 368.5 eV cannot be assigned to Ag oxides.

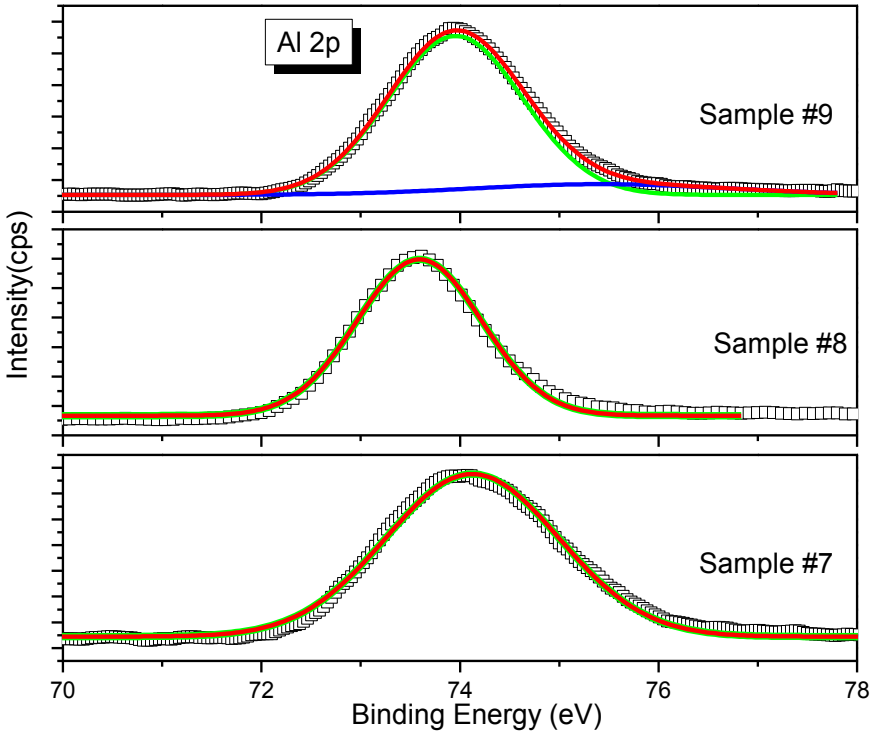

Figure 5.23. High resolution XPS measurements of Al 2p and respective deconvolution for samples #7, #8, #9

Contrariwise, shifts of the core level spectra of various metals (Au [5.20,5.21], Pd [5.21], Pt [5.22], Ag [5.23]) to higher binding energies have been observed for finite size clusters, due to size-dependent shifts of the Fermi level [5.23] and, ultimately, for clusters below 2 nm due to metal-insulator transition [5.21]. Based on these previous studies, we can assign the peak observed around 368.5 eV to nano-Ag participating in clusters of sizes less than 2 nm.

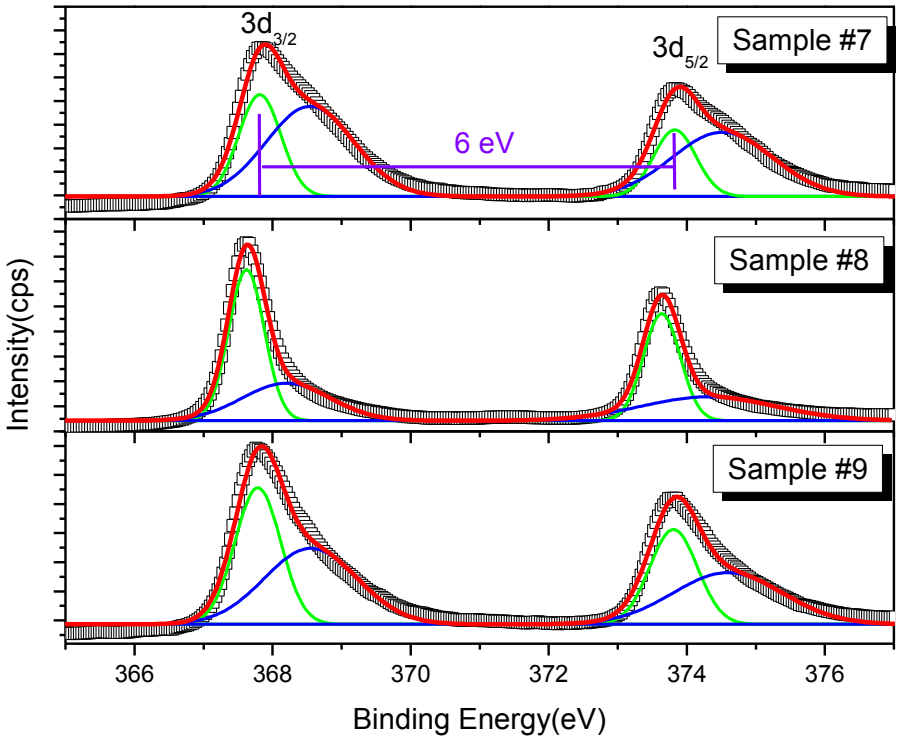

Figure 5.24. High resolution measurements of Ag 3d doublet photoelectron peak and respective deconvolution for samples #7, #8, #9

Comparing the areas below the $3d_{5/2}$ peaks of the metallic Ag and nano-Ag we can determine the fractions of Ag atoms that participate either in small sized clusters (<2 nm), that cannot be probed by XRD, or in bigger metallic Ag crystal grains (Figure 5.24). This correlation between the atomic fractions of nano-Ag ([nano-Ag]/[Ag], where [Ag] =[nano-Ag]+[metallic-Ag]), *vs.* the total [Ag] concentration in the AlN:Ag films, confirming the XRD findings that were presented previously. The absolute concentration of nano-Ag (<2 nm) in AlN:Ag has been also determined by the area of the corresponding peak. The [nano-Ag]/Ag concentration was found to be constant at approximately 4% *at*. This defines the solubility limit of Ag in AlN; for higher concentrations of Ag, the rest of the Ag segregates and self-organizes in metallic Ag crystals. On the contrary, in order to achieve self-organization of Ag higher concentrations should be provided.

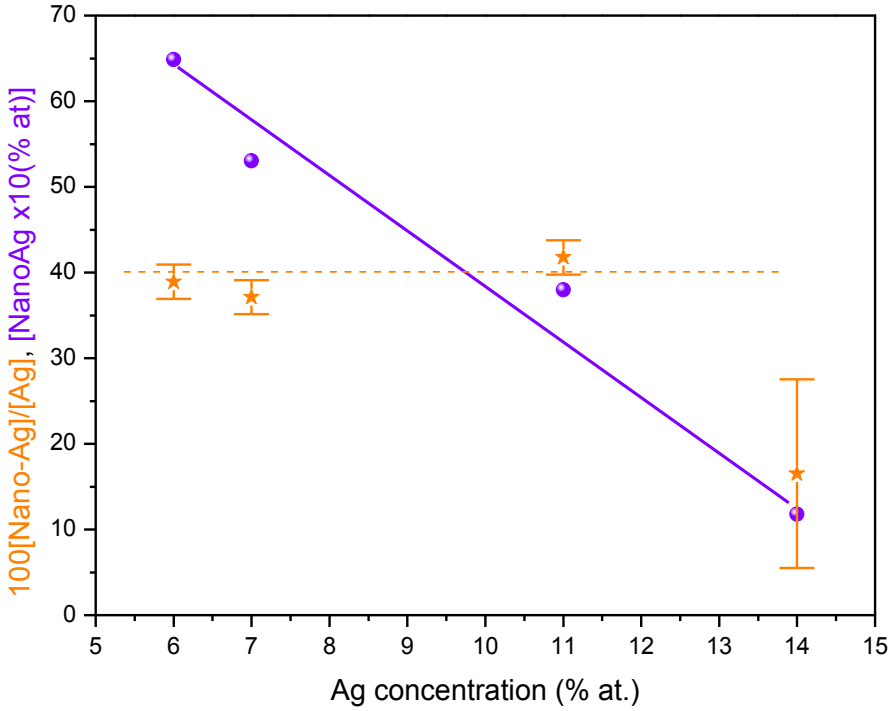

Figure 5.25. Atomic fractions of nano-Ag ([nano-Ag]/[Ag], as a function of the total [Ag] concentration in the AlN:Ag nanocomposite films.

The structural results that reported above are in agreement with the optical properties of the films as it is illustrated in figure 5.25. Thus, for the lower silver concentration (sample #6) the film is still transparent comparing to pure w-AlN film (sample #4). Unlike to sample #6, sample #7 and sample #8, where a phase segregation of the metallic phase occurs, our films are less transparent and a metallic behavior is observed. Especially, for sample #7, a weak broad peak around 460nm is manifested. This might be attributed to LSPR peak. Finally sample #4 (pure w-AlN) the ORS spectrum consists of multiple reflection due to sample transparency while sample #5 (pure a-AlN) due to thin thickness provide two peaks corresponding to the substrate features. On the other hand sample #9, although provides similar Ag concentrations with sample #6 exhibits a weak LSPR peak at around 460nm wavelength while no interference fringe were observed in its ORS spectra possible due its thin thickness.

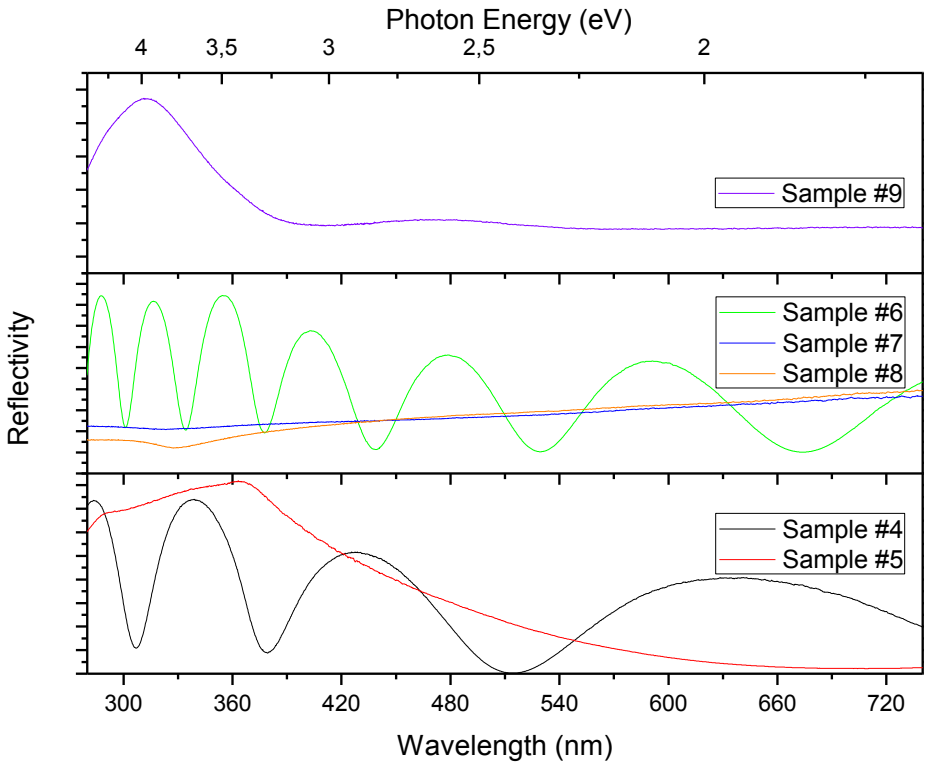

Figure 5.26. Optical reflectivity spectrums of the nanocomposite films. Different optical behaviors are observed according to the silver concentration.

5.3.2 Thin Film Process

The structural and morphological stability of the studied samples have been evaluated by applying thermal and laser annealing respectively. Moreover the effect of these two approaches in the optical properties of the samples was also investigated.

Thermal annealing experiments were carried out in Ar ambient for two hours in 400^{o}C and 600^{o}C, respectively. For laser annealing experiments 1 pulse was applied to our samples for fluencies from 200mJcm^{-2} up to 600mJcm^{-2}, using 193nm and 248nm wavelengths, respectively.

5.3.3 Thermal annealing

As it revealed from the XRD measurements for the nanocomposite films with wurtzite matrix (Figure 5.26) no structural changes for the AlN observed even at 600°C. On the other hand, due to its high diffusivity silver at 600°C is affected by thermal annealing as it is close to its melting point

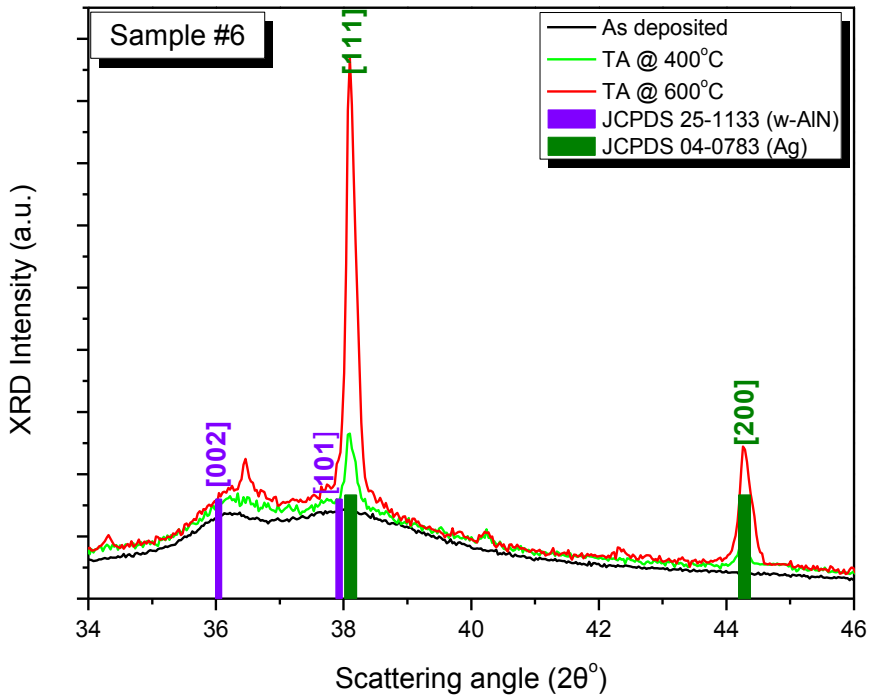

Figure 5.27. XRD pattern of sample #6 after thermal annealing in carious temperatures.

SEM observations confirm the diffusive character of the metallic phase as it can be seen in figure 5.27. Outdiffusion of the silver in the surface is observed and the formation of nanoparticles with size ranging within 40-310nm.

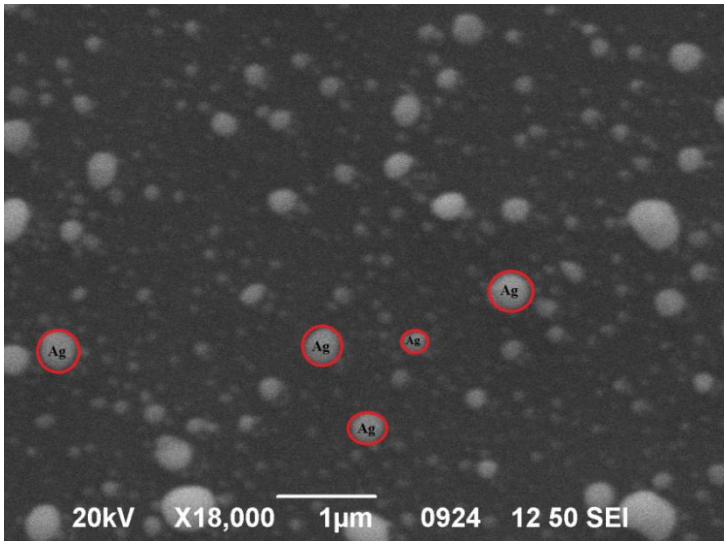

Figure 5.28. SEM image of sample #6 after thermal annealing at 600 ^{o}C. Outdiffusion of the silver in the surface and formation of broad metallic nanoparticles

A similar behavior was observed also for the a-AlN:Ag (sample #9). No trace of crystallization of a-AlN upon thermal annealing was observed in the corresponding X-ray pattern (Figure 5.28).

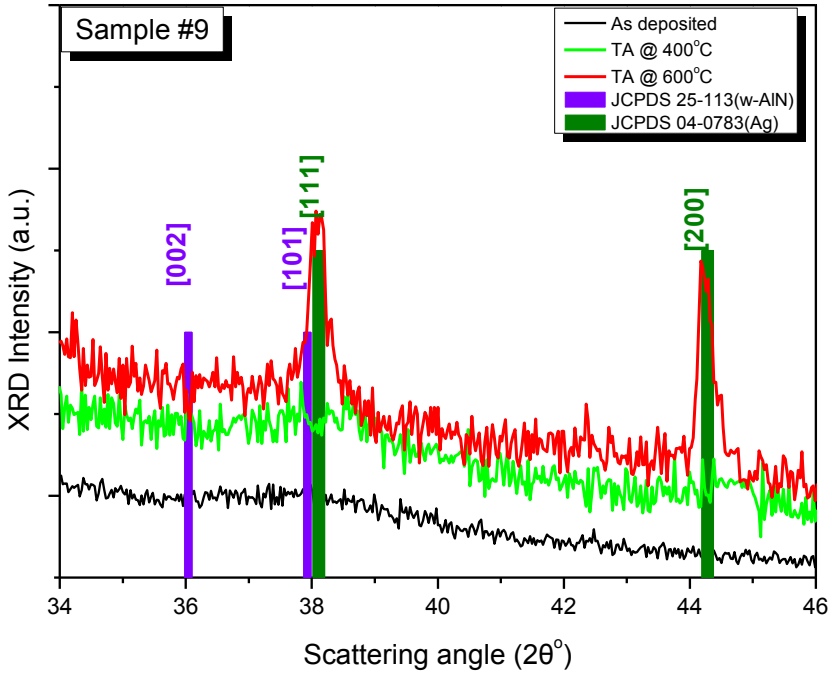

Figure 5.29. XRD pattern of sample #9 after thermal annealing at different temperatures. Thermal annealing does not affect the amorphous matrix. Outdiffusion of the Ag occurs only in 600 ^{o}C

However, the outdiffusion of Ag did occur, but it was less pronounced in this case, since it was observed only for thermal treatment at 600 ^{o}C and resulted in the formation of Ag crystals

of average size of 34 nm this is also confirmed by SEM observations of Ag particles of average size of 75 nm on the surface (Figure 5.29).

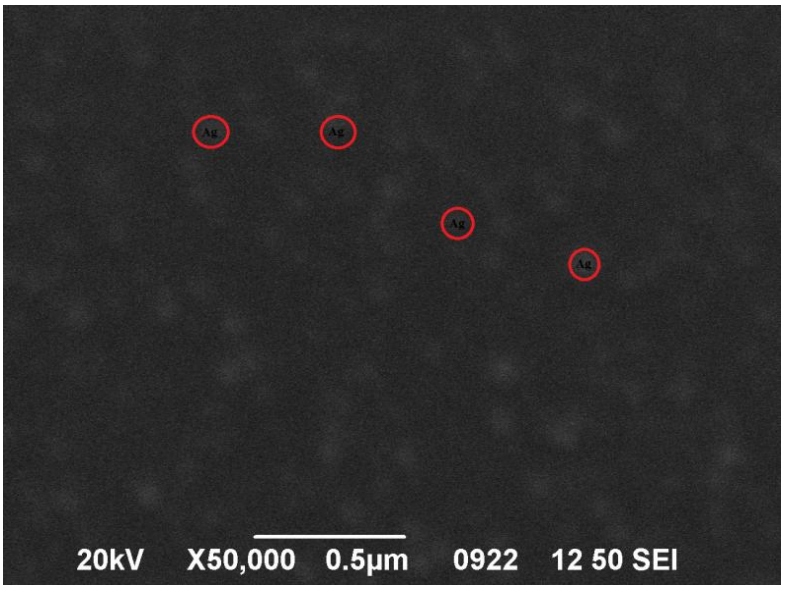

Figure 5.30. SEM image of sample #9 after thermal annealing at 600^{o}C. Outdiffusion of the Ag is also observed with simultaneous creation of smaller nanoparticles.

The formation of the nanoparticles on the surface after thermal annealing linked with the Surface Plasmon Resonance manifestation as it is illustrating in the Optical Reflectance spectrum in figure 5.30. Due to the broad size distribution of the nanoparticles a broad SPR peak is observed at around 600nm. In contrast, in sample#9 thermal annealing induces the emergence of a significant LSPR band in the blue region (~460 nm). Spectral position of the observed LSPR is consistent with the observed size of Ag nanoparticles [5.24].

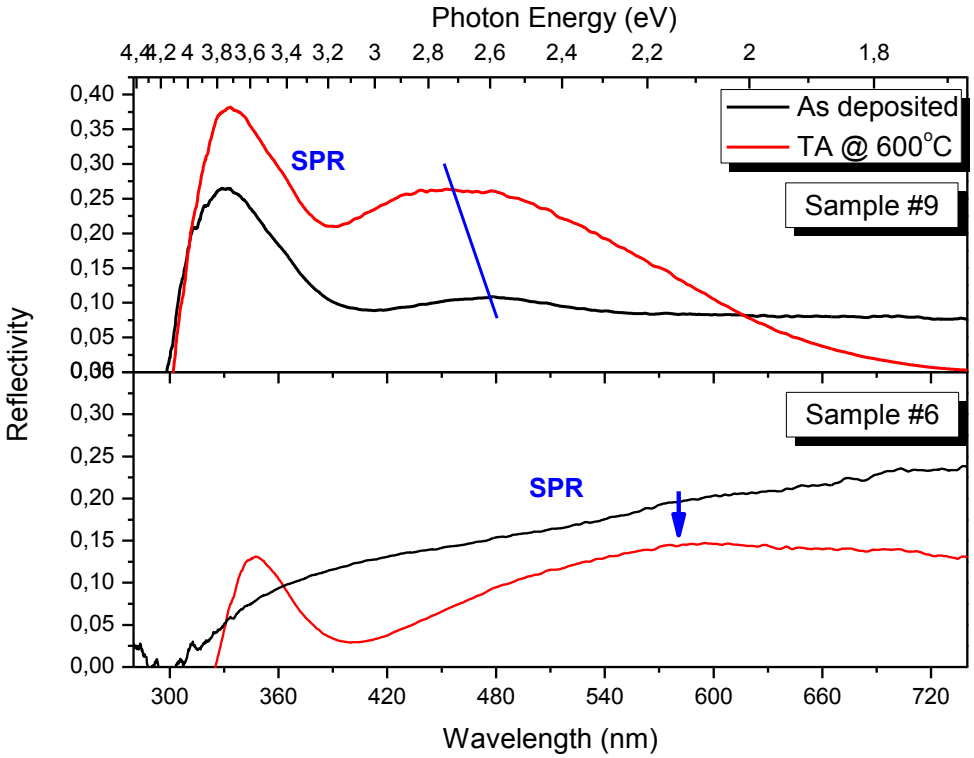

Figure 5.31. Reflectivity spectrum of samples #9 (up) and #6 (down) of the as deposited and after thermal annealing at 600°C. In case of sample #9 a more intense LSPR peak is manifested.

5.3.4 Laser annealing

The changes of the structural and morphological features of the co-sputtered samples after laser annealing were also investigated. Representative XRD difractogramms after laser annealing of samples #6 and sample #9 are demonstrated in figure 5.31. As it was revealed from the XRD measurements the changes occurring after LA are radically different to those after thermal annealing.

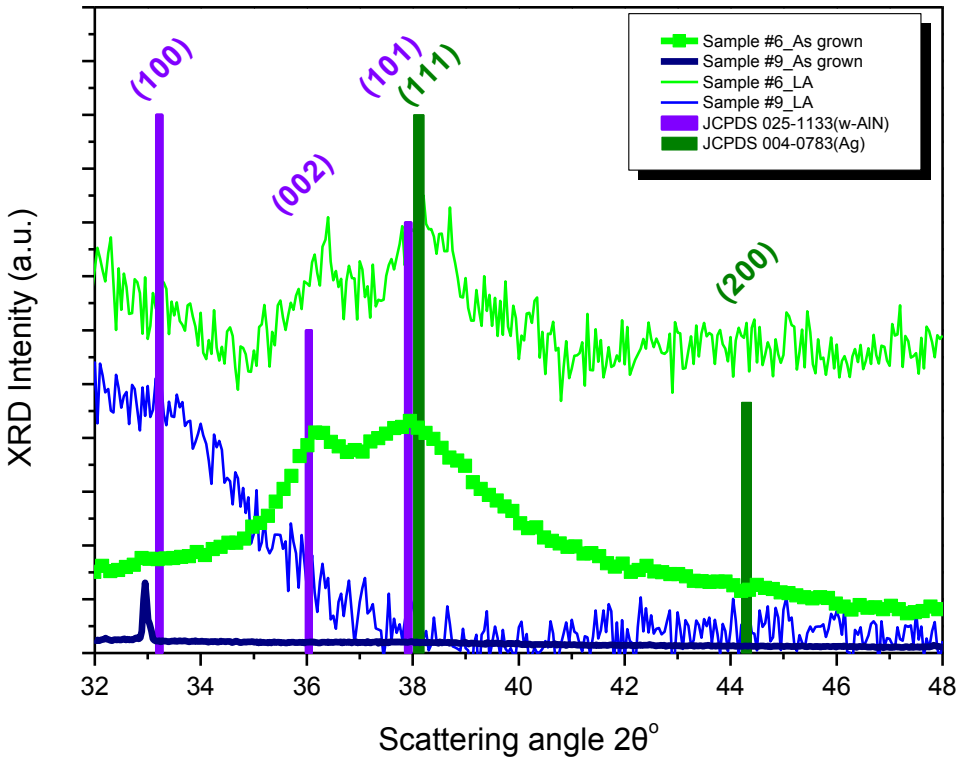

Figure 5.32. XRD pattern of nanocomposite films after laser annealing.

For sample #6 with wurtzite matrix no significant changes are observed after laser annealing in contrast with the AlN:Ag nanocomposite films grown by PLD where recrystallization of the matrix is observed. On the other hand for sample #9 (aAlN:Ag) is an intermediate case. The AlN matrix does remain intact as in the case of sample #6 and in its X-ray diffraction pattern a feature emerges in the angular vicinity of the expected w-AlN(002) peak which is, however, too broad and ambiguous in order to be safely assigned to w-AlN. Possibly, in sample #9 there are less pure metallic Ag domains that can act as hot spots and nucleation sites of w-AlN and thus the diffraction signal of w-AlN after laser annealing is exceptionally weak. From XRD measurements is it obvious that the variations in Ag distribution after LA are negligible which verified by SEM images (Figure 5.32). This is reasonable taking into account that laser annealing is an ultrafast process that does not provide the appropriate time for significant macroscopic Ag diffusion.

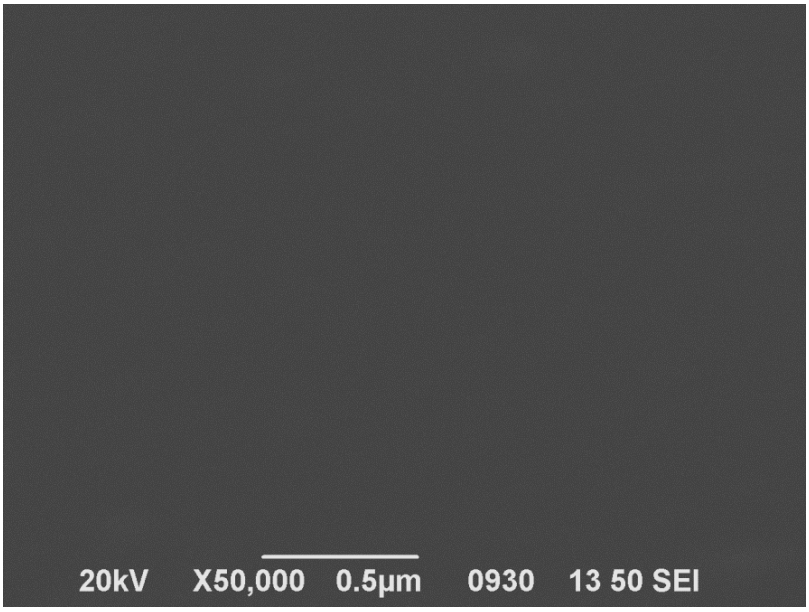

Figure 5.33. SEM image of sample #6 after laser annealing. Laser processing seems to leave unaffected the sample surface due to ultrafast character.

The situation is totally different for sample #8 with the highest Ag concentration. As it can be seen from SEM image (Figure 5.33) there is a massive outdiffusion of Ag upon LA due to the exceptionally high optical absorption of this sample.

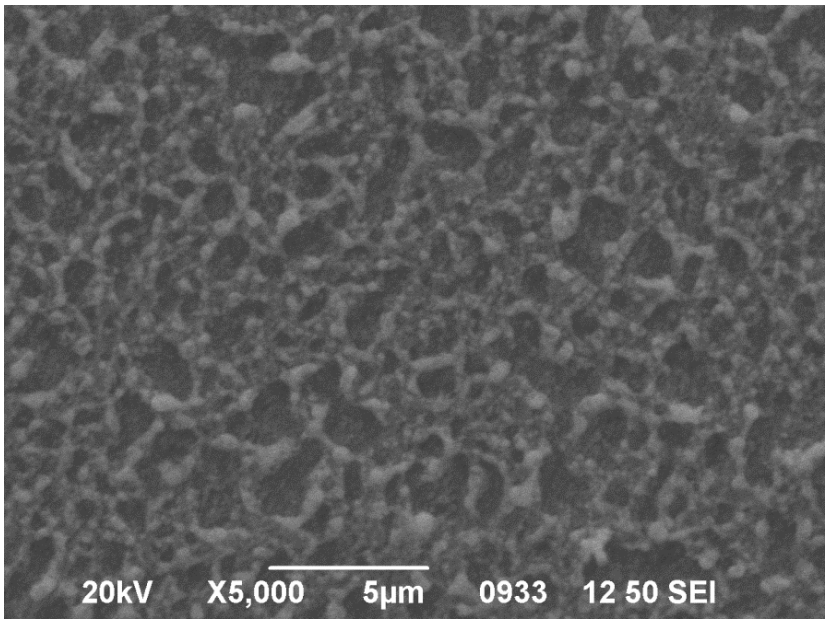

Figure 5.34. SEM image of sample #8 after laser annealing. A metallic network is created due to silver outdiffusion.

The structural results were verified from the ORS measurements that were performed in the studied samples. Thus, for laser annealing with 193nm wavelength for the group of samples with crystalline matrix (representative spectra of sample #6 for various fluencies are depicted in (Figure 5.34a) the existence of interference fringes, manifesting at similar wavelengths before

and after LA, testifies that the integrity of the sample was maintained and there was no significant change of the value of the refractive index. The minor changes on the lineshape of the interference fringes might be attributed to some interfacial effects. This is reasonable, taking into account that AlN is transparent in the UV-Visible range as well as laser wavelength corresponds to 6.2 eV which is similar to the band gap of the AlN, thus there is no interaction between AlN and laser beam. Unlike to wurtzite matrix, in aAlN:Ag nanocomposite films laser annealing at 200mJcm^{-2} and 300mJcm^{-2} seem to roughly improve the SPR peak, while for higher fluencies the LSPR intensity reduces due to outdiffusion and evaporation of Ag..

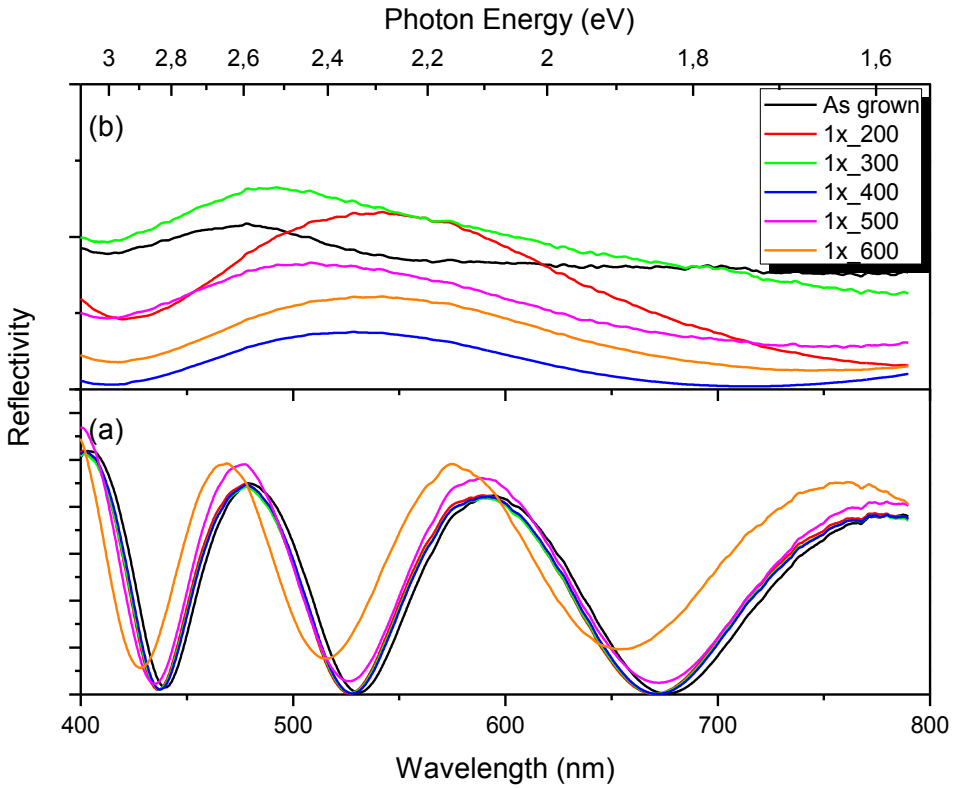

Figure 5.35. ORS spectra of samples #6 (a) and sample #9 (b) after laser annealing at 193nm for different fluencies.

The same situation is revealed from ORS measurements for laser annealing with 248nm wavelength as well (Figure 5.36) for 1 and 2 pulses. As it was earlier mentioned for the wAlN:Ag films the subtle changes of interference fringes shape and position after laser annealing denote no optical and structural changes of the annealed sample. In aAlN:Ag cases only the implementation of one pulse with 200mJcm^{-2} fluence seems to improve the LSPR peak with a subsequent red shift. Contrariwise, the implementation of higher fluence operates reversibly, for one and two subsequent pulses as well, degrading the LSPR peak manifestation up to 600 mJcm^{-2} where silver outdiffusion occurs for one and two pulses respectively.

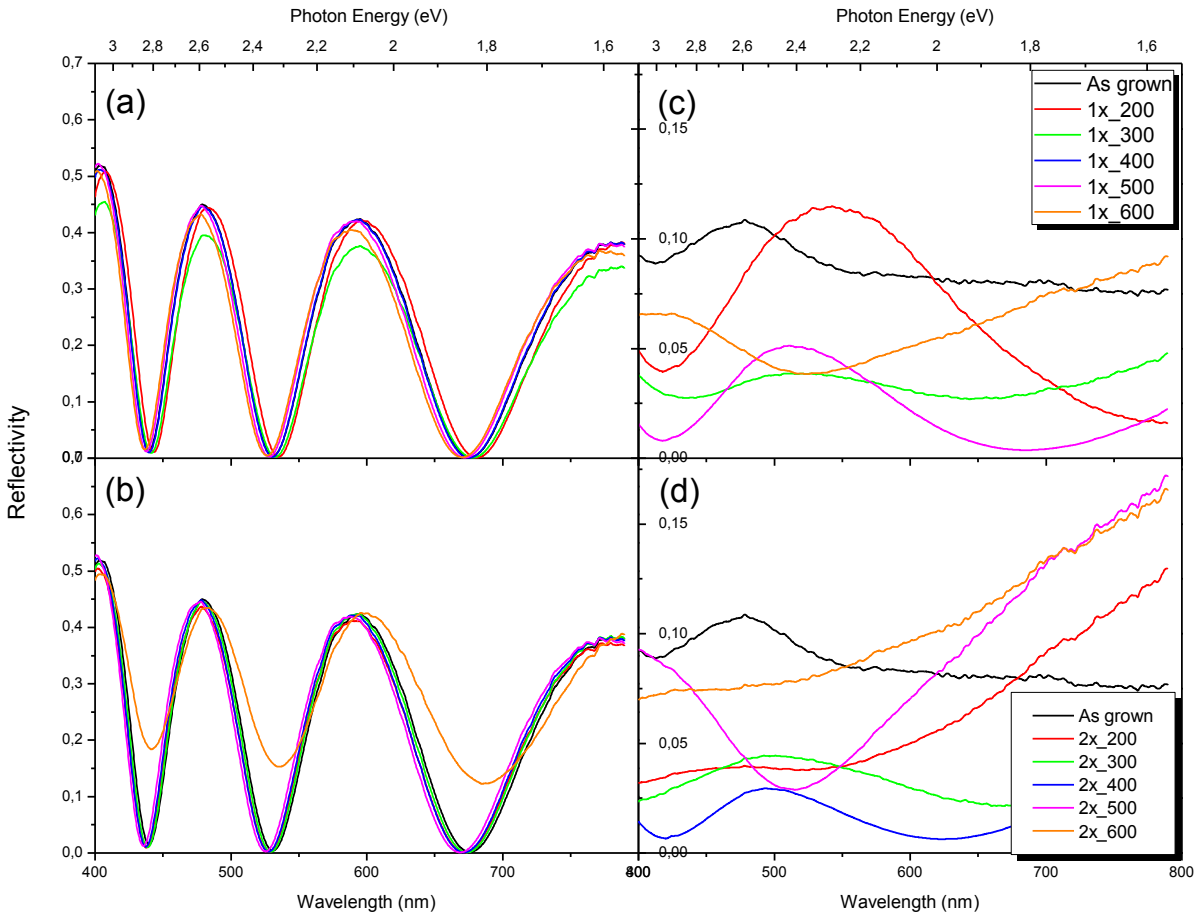

Figure 5.36. ORS spectrums of samples #6 and sample #9 after laser annealing with 248nm for various fluencies. (a) samples #6 1pulse, (b) samples #6 2pulses. (c) sample #9 1 pulse, (d) samples #9 2 pulses

5.4 AlN/Ag multilayers

5.4.1 Thin Film Deposition

Stratified nanostructures consisting of alternate thin layers of AlN and Ag were also studied in this PhD thesis. The deposited samples can be divided into two different categories based on the AlN degree of crystallinity. Thus, the first group of samples consists of alternative crystalline AlN and Ag layers while in second group our samples consist of thin amorphous ceramic layers. This variation in the AlN crystallinity was achieved by varying the applied power in the Al target. On the other hand, in both categories the thickness of the silver layer was varying by using different deposition times. Each sample started and ended with AlN layer ensuring the insulation of the metal phase by ambient conditions. The depositions took place in

a reactive Ar-N_2 mixed environment. Table VII summarizes the growth and structural features of the AlN/Ag samples studied in this section

Table VII. Deposition parameters of the as grown multilayers

Sample ID	Power Al (Watt)	Power Ag (Watt)	AlN deposition time (sec)	Ag deposition time (sec)	Ag grain size (nm)	Number of repetitions
Sample #10	100	10	66	10	4.7	20
Sample #11	100	10	57	30	4.7	20
Sample #12	100	10	47	50	2.7	20
Sample #13	15	10	438	10	4.3	20
Sample #14	15	10	375	30	4.4	20
Sample #15	15	10	312	50	2.5	20

In order to clarify the crystallinity of the as deposited samples XRD measurements were carried out. For the first group of samples under study, with 100 watt Al power, diffraction peaks indicating the formation of the hexagonal structure emerged in their difractogramms (Figure 5.37). On the flipside, at 15W the samples demonstrate a reduction in crystallinity, evident by the absence of any characteristic peaks for AlN (Figure 5.38). Finally, diffraction peaks corresponding to the Ag phase were also observed. The Ag (111) peaks of all samples were fitted with Voigt curves and the corresponding Lorentzian broadenings were used to determine the grain size (shown in table VII) from Scherrer's formula. The broad profile of the observed diffraction peaks for both AlN and Ag is attributed to the thin thickness of the layers taking into account that the deposited layers were as thin as just to approach the island coalescence threshold.

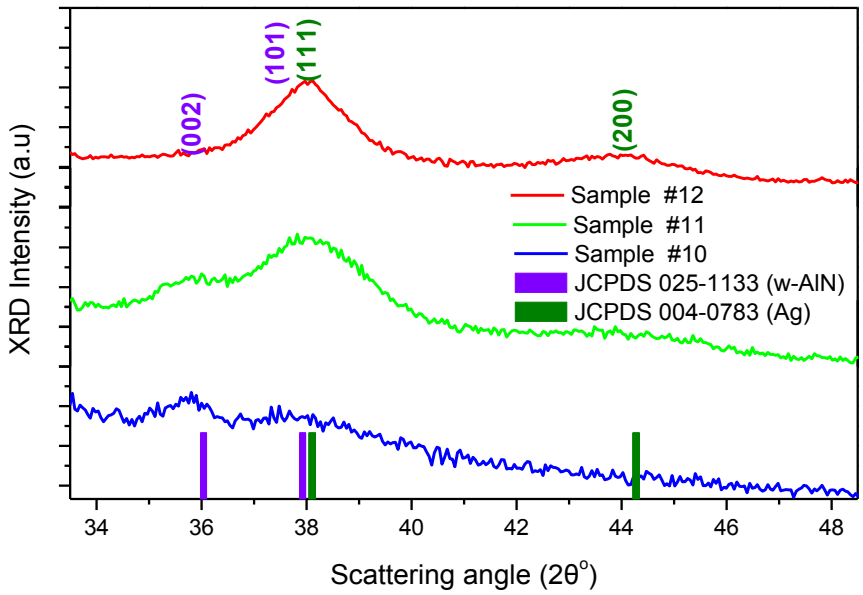

Figure 5.37. XRD patterns of the w-AlN/Ag multilayers.

Unlike to the first group of samples, in the second one with 15 Watt applied power in Al cathode the XRD measurements (Figure 5.37) emerged only diffraction peaks corresponding to the (111) and (200) diffraction planes of Ag FCC structure were only observed. On the contrary, no trace of crystallinity was revealed for the AlN layers. So the determination of the chemical state of the samples, especially for the amorphous multilayer was imperative in order to identify the Al-N bonding.

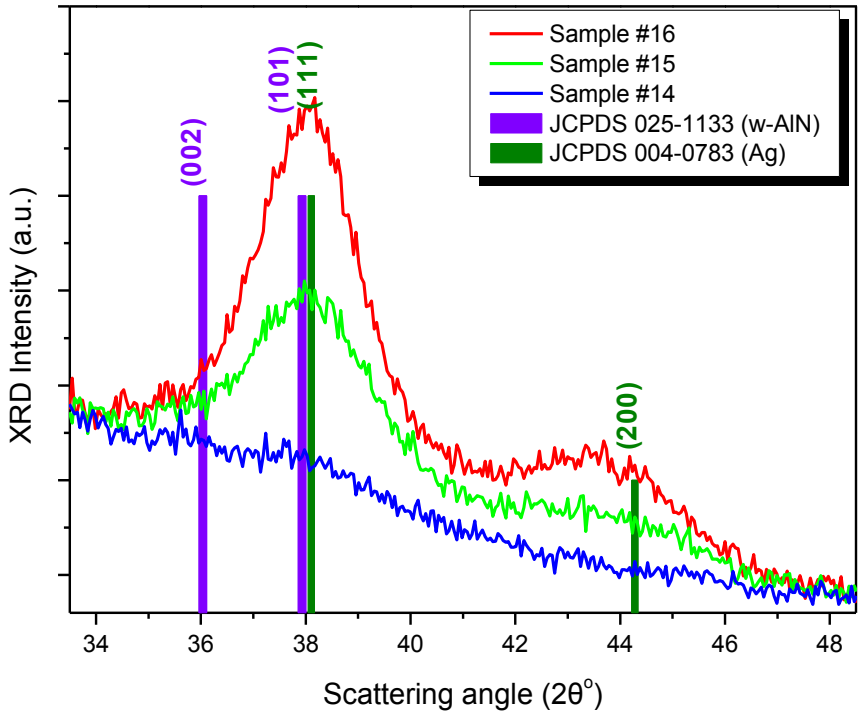

Figure 5.38. XRD patterns of the w-AlN/Ag multilayers

Thus, XPS measurements were performed. Representative wide scans obtained of our samples, where the photoelectron and Auger peaks have been identified are depicted in figure 5.38. The XPS measurements were carried out after 3 min of sputtering with Ar^+ ions thus the corresponding XPS peaks of Ar can be observed. Furthermore, high resolution XPS (HRXPS) measurements of Al 2p, Ag 3d and N 1s were performed respectively (Figure 5.39). XPS measurements were carried out even for the group of samples with the crystalline AlN, although the phase identification was achieved from the XRD measurements. In order to eliminate charging effects Ar 2p XPS peak was used as reference.

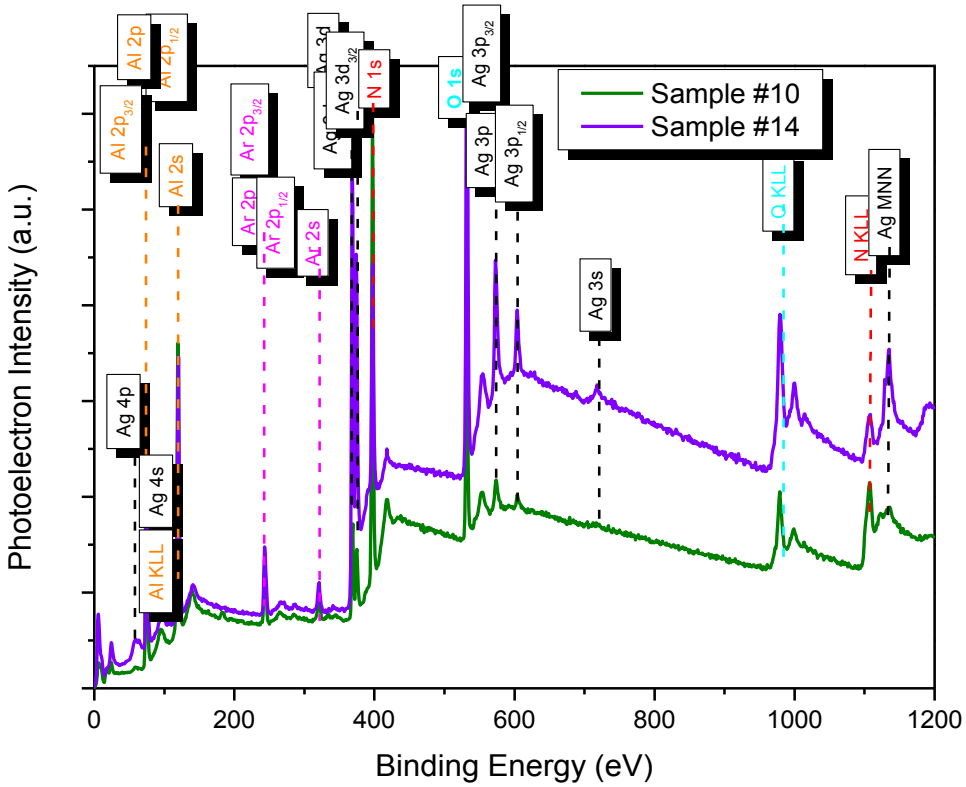

Figure 5.39. Representative wide scan XPS measurements of wAlN/Ag (Sample #10) and aAlN/Ag (Sample #14) respectively. Photoelectron peak identification has been performed.

Al 2p XPS peak of the first group (Figure 5.39 c,) is deconvoluted from two components with binding energies 73.6eV and 73.0 eV respectively. The major component can be attributed to Al-N bonding [5.24] while the second component can be attributed to Al-O bonding [5.25]. The formation of Al-N bonds is confirmed from the N 1s peak which is at 396.2 eV [5.24]. Al 2p XPS analysis of the aAlN/Ag group (Figure 5.37d) is also deconvoluted with two components located in similar values. Thus, the major component is at 73.5 eV while the second component is at 72.8 eV. It is worth noticing that Al-O bonding is further supported

from the strong O 1s XPS peak which clearly observed in the wide scan of both categories of materials, which can attributed in oxygen contaminations within the chamber during film deposition. In Ag 3d XPS peak the characteristic Ag-3d doublet corresponding to the Ag-3$d_{3/2}$ and Ag-3$d_{5/2}$ due to spin-orbit splitting was observed for all samples (Figure 5.39 a, b). For w-AlN/Ag sample(Figure 5.39a) the Ag-3$d_{3/2}$ peak was deconvoluted to two Lorentzian-Gaussian peaks located at binding energies of 367.1 eV and 368.1eV while for the Ag-3$d_{5/2}$ the two components located at binding energies 373.1 and 374.1 eV respectively. Similar values of Ag-3$d_{5/2}$ and Ag-3$d_{3/2}$ analysis are revealed for the a-AlN/Ag multilayers (Figure 5.39b). Thus, for the second group of materials Ag-3$d_{3/2}$ is located at around 366.5eV and 367.2eV while Ag-3$d_{5/2}$ two components located at binding energies 372.5eV and 373.2 eV respectively.

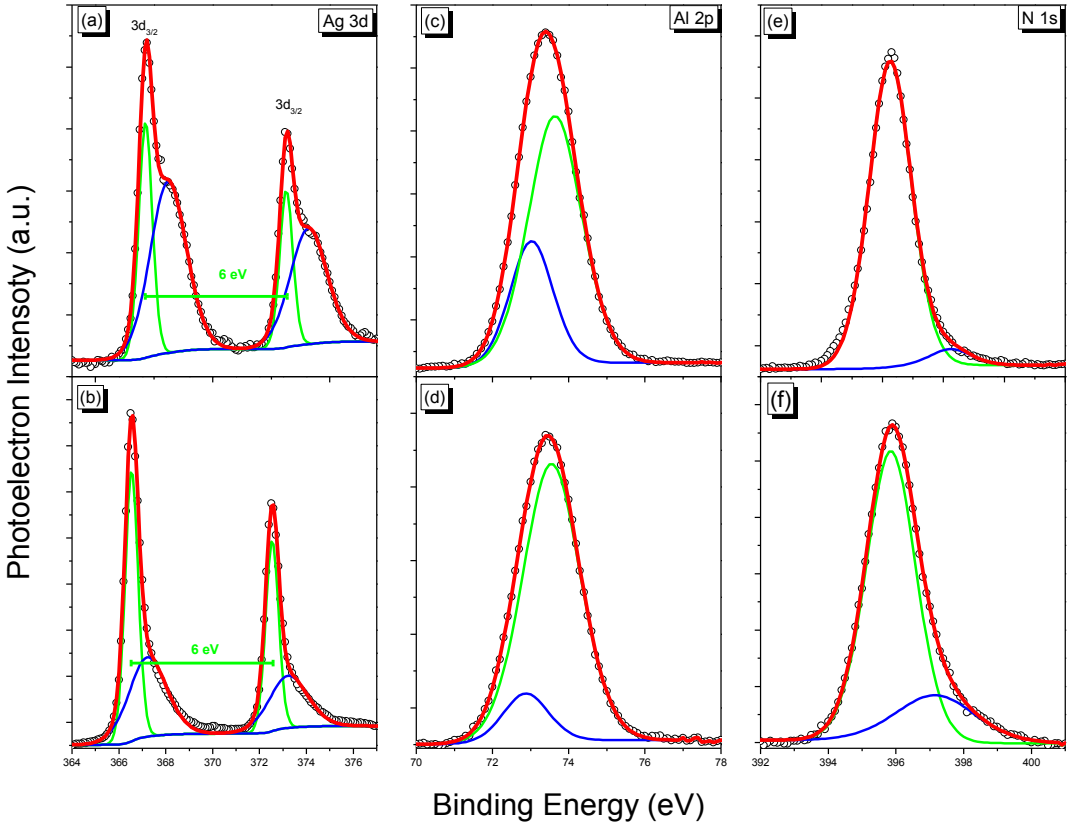

Figure 5.40.High resolution XPS of Ag 3d(a,b), Al 2p (c, d), N 1s(e,f) for a w-AlN/Ag (up) and a-AlN/Ag (down) multilayers.

The successful deposition of periodical structures was confirmed by TEM observations for both categories of samples as it is illustrated in cross-section images in figure 5.40. The structural characterization of the AlN layers show no trace of crystallinity which is agreement with the XRD results for the second group of multilayers (Figure 5.40c).

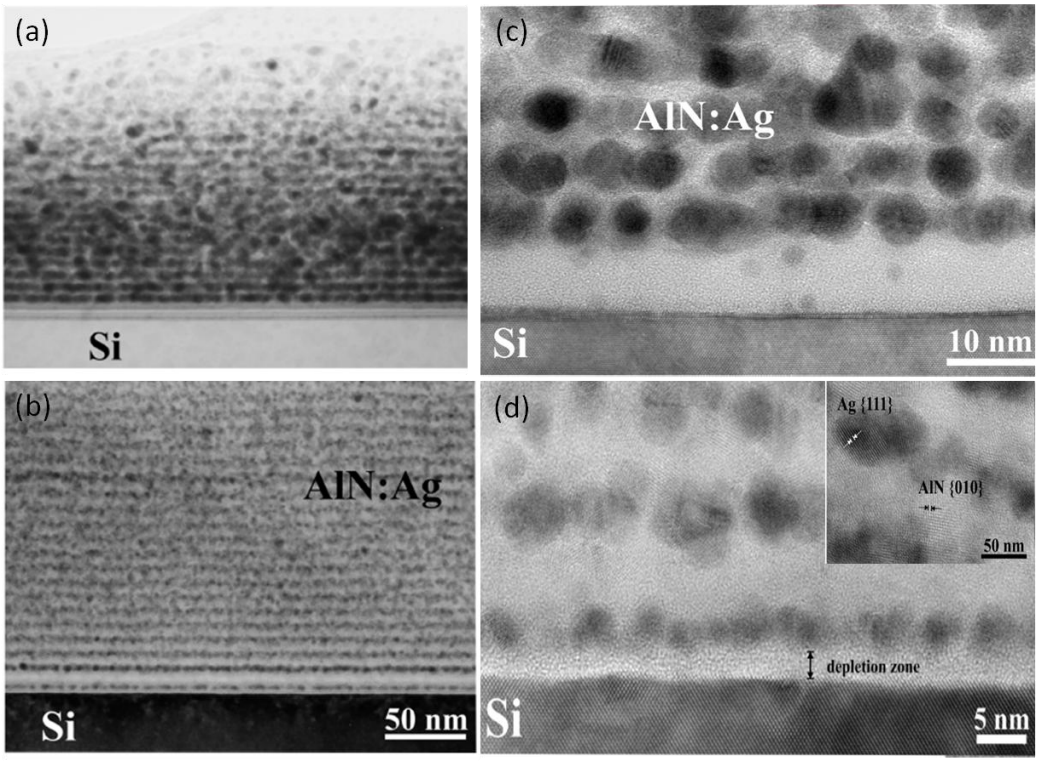

Figure.5.41. (a) Cross section TEM image of as grown sample #14. (b) Cross section TEM image of as grown sample #10.

On the other hand the characterization of the metallic phase of the multilayer verifies that indeed we have single phase with (111) orientation (Figure 5.40 c, d) something that is in agreement with the XRD results. Moreover, TEM characterization reveals that the metallic layer consists of overall spherical shapes which are abutting each other. ORS for both 'families' of sputtered materials are shown in figures 5.43. The spectra are in general featureless, resembling the optical response of a bulk metal, except for the two cases of very thin Ag layers (ML#10 and ML#13), were a continuous Ag film has not been achieved and multiple reflections begin to appear accompanied by plasmonic peaks in the lower wavelengths (peaks around 420 and 450 nm forML#3 and ML#6 respectively).

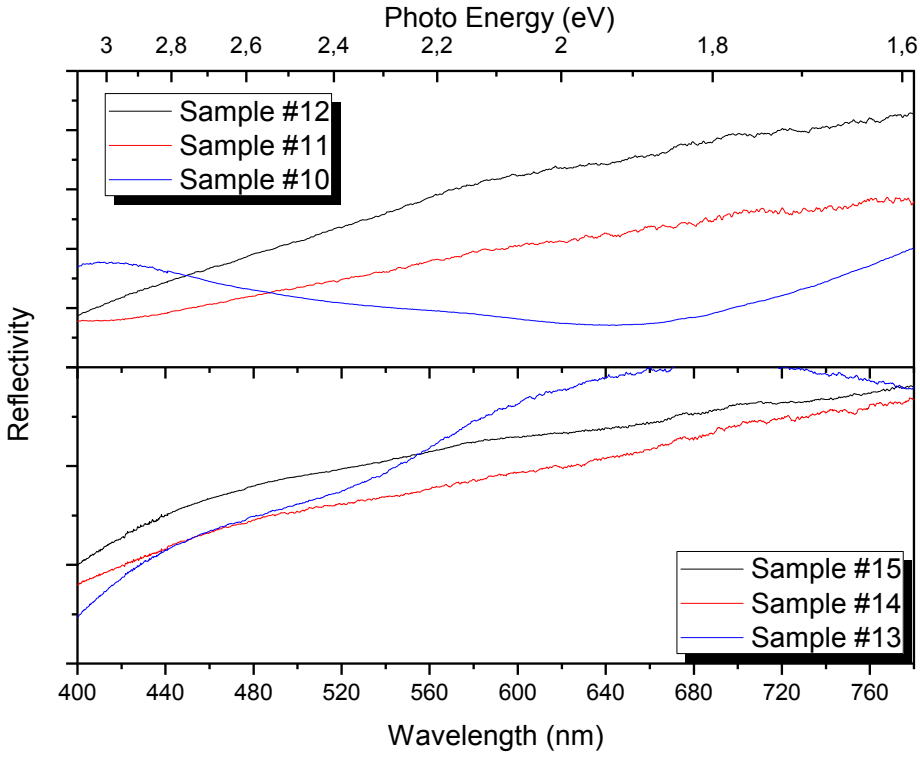

Figure 5.42. ***Up:*** ORS of the wAlN/Ag multilayers. Spectra are the combination of multiple reflections due to the transparent character of the AlN with a higher reflection due to the metallic character of the Ag. ***Down:*** ORS of the aAlN/Ag multilayers. A similar behavior is observed. In both cases there is no LSPR manifestation.

5.4.2 Laser processing

The as grown samples were subjected to laser annealing which is our major processing technique in this PhD study. 193nm (ArF) wavelength was used for laser annealing both in ambient and under high pressure, 150 psi Ar, respectively. Unlike to previous sections only one and two pulses were applied.

5.4.3 Structural properties

The structural modification after laser annealing in a first step was studied by X-ray diffraction. As it is illustrated in figure 5.42, for the aAlN/Ag multilayers, the diffraction peaks corresponding to (111) and (200) diffraction planes of silver emerged that can attributed in the enlargement of the Ag grains. On the other hand at around 36^{o} diffraction angle a weak "shoulder" is also observed. This can be evidenced that after laser annealing a partial recrystallization of the aAlN occurs.

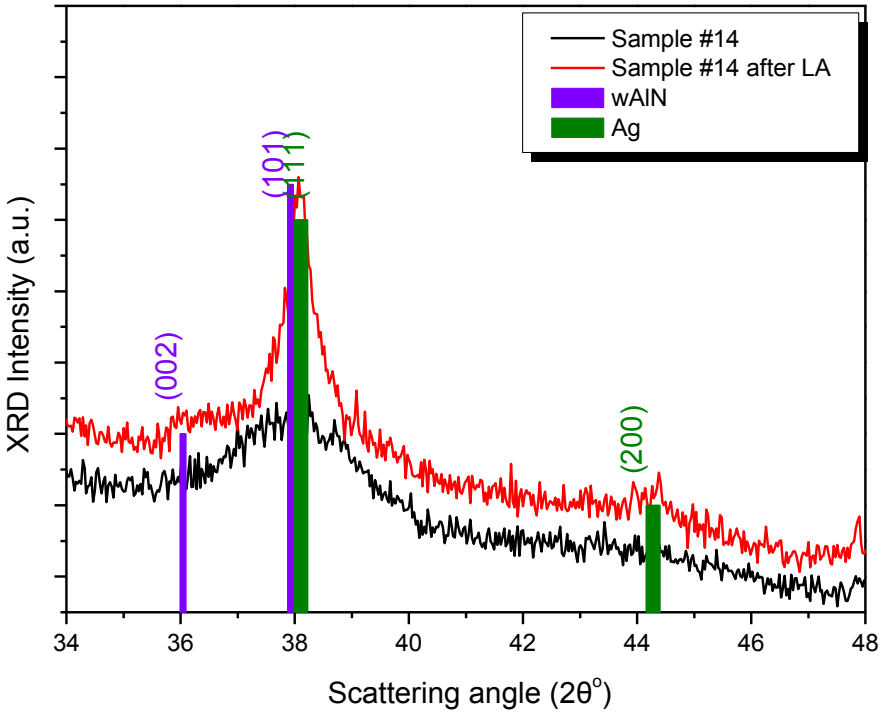

Figure 5.43. XRD pattern for sample #14 before (black line) and after laser annealing (red line). A "weak" shoulder at around 36° is manifested that suggests structural modification of the aAlN.

Extended structural and morphological examinations of the annealed samples were performed based on TEM observations. For aAlN/Ag multilayers cross section TEM images (representative observations of sample #14 are illustrated in figure 5.43) reveal that after laser annealing in ambient the upper layers of the multilayered morphology is destroyed and isolated silver nanoparticles are formed. Except of Ag nanoparticles formation, the upper part of the film appears highly affected by laser annealing, resulting in a kind of film dissolution and concurrent roughening while the first ~13 layers (~ 75 nm film thicknesses) appear unaffected by laser annealing, conserving their overall morphology, thickness and spacing. The metallic nanoparticles provide a gradual enlargement according to their location. Thus, nanoparticles with size of 5 nm are observed in the bottom layers (unaffected area) to 8-12 nm at the middle of the film and to ~25 nm towards the surface of the film.

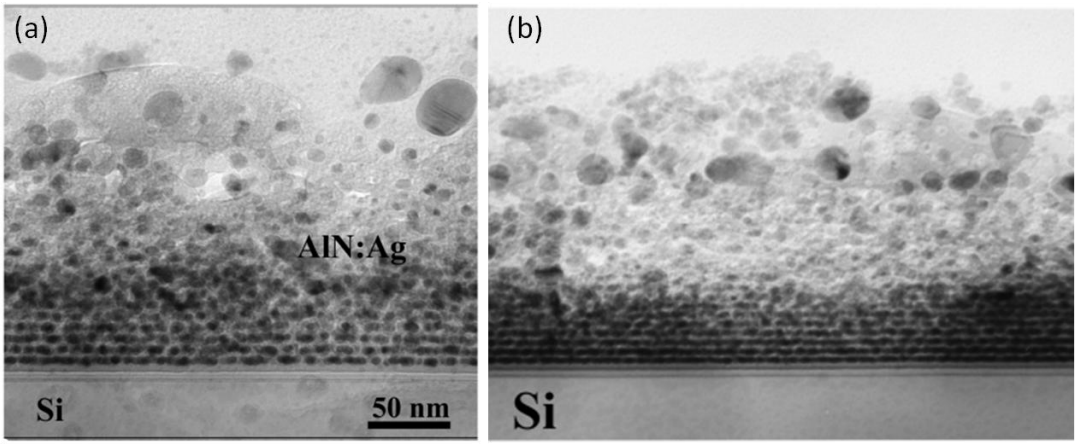

Figure 5.44. HRTEM observations of Sample #14 after laser annealing with193nm, at 600mJcm^{-2} with one 1pulse in ambient (a) and under high pressure (b).

Similar results revealed from TEM observations for laser annealing under high pressure (Figure 5.43b). The periodical structures are destroyed after laser annealing with a simultaneous formation of Ag nanoparticles providing similar sizes as above. Unlike to previous laser processing parameters, now only approximately 9 layers are unaffected after laser annealing. It is also worth noticing that recrystallization of the aAlN matrix is not observed unlike to XRD results as well as to PLD nanocomposite films. On the contrary the crystalline AlN/Ag multilayers seems to be affected in a lesser degree, compared to the amorphous AlN/Ag group of samples, after laser annealing as it can be seen from representative TEM cross section observations from sample #10 in ambient and under high pressure that depicted in figure 5.44. The gradually enlargement of the nanoparticles is also observed in this group of films with nanoparticles of 3-5nm diameter being in the bottom of the sample and the larger once with approximately 20nm diameter being on the top of the sample. Finally, in contrast to the aAlN/Ag nanoparticles, wurtzite AlN/Ag multilayers exhibited much less roughening after laser annealing.

It should also point out that multilayers provide a better interfacial AlN/Si quality after laser compared to PLD sample. This can be assigned in the thicker films that were produced in case of multilayer which are approximately 300nm while the PLD samples are 70nm thick. Thus, in case of multilayer laser beam can not reach the substrate.

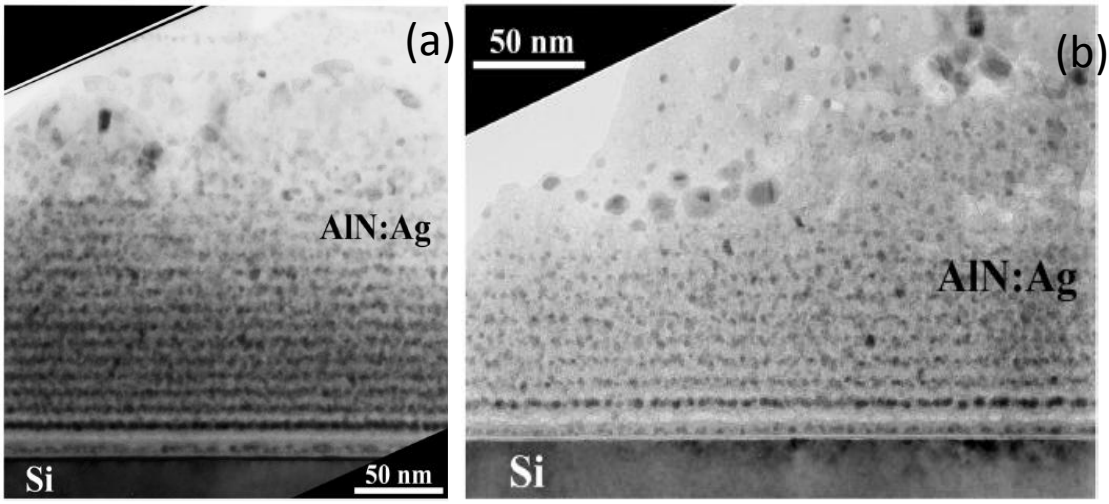

Figure 5.45. HRTEM observations of Sample #10 after laser annealing with193nm, at 600mJcm^{-2} with one 1pulse in ambient (a) and under high pressure (b).

5.4.3.1 Optical properties

The formation of metallic nanoparticles after laser annealing alters the optical properties of the samples since Surface Plasmon Resonance peak is manifested as it was observed from ORS measurements. Representative spectra are illustrated in figure 5.45.

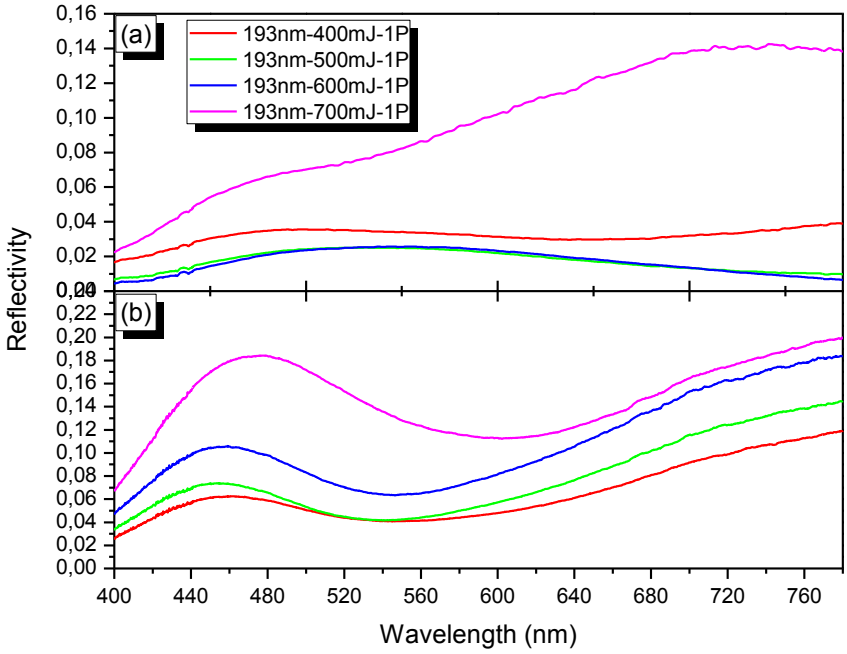

Figure 5.46. Optical Reflectivity Spectrums of Sample #12 (a) and Sample #14 (b) at 193nm wavelength with 1 pulse for various fluencies.

The analysis of the of the SPR peak position and the intensity of the peak for the aAlN/Ag group of materials are illustrated in figure 5.46. It must be noticed that the analysis includes the

SPR profile for samples #13and #14 only. On the contrary sample #15 did not exhibit any SPR in the visible range. This can be attributed in the thick thickness of the Ag layer (approx. 9nm) which is thick enough so that laser beam can not affect it drastically as it happens with the other two samples.

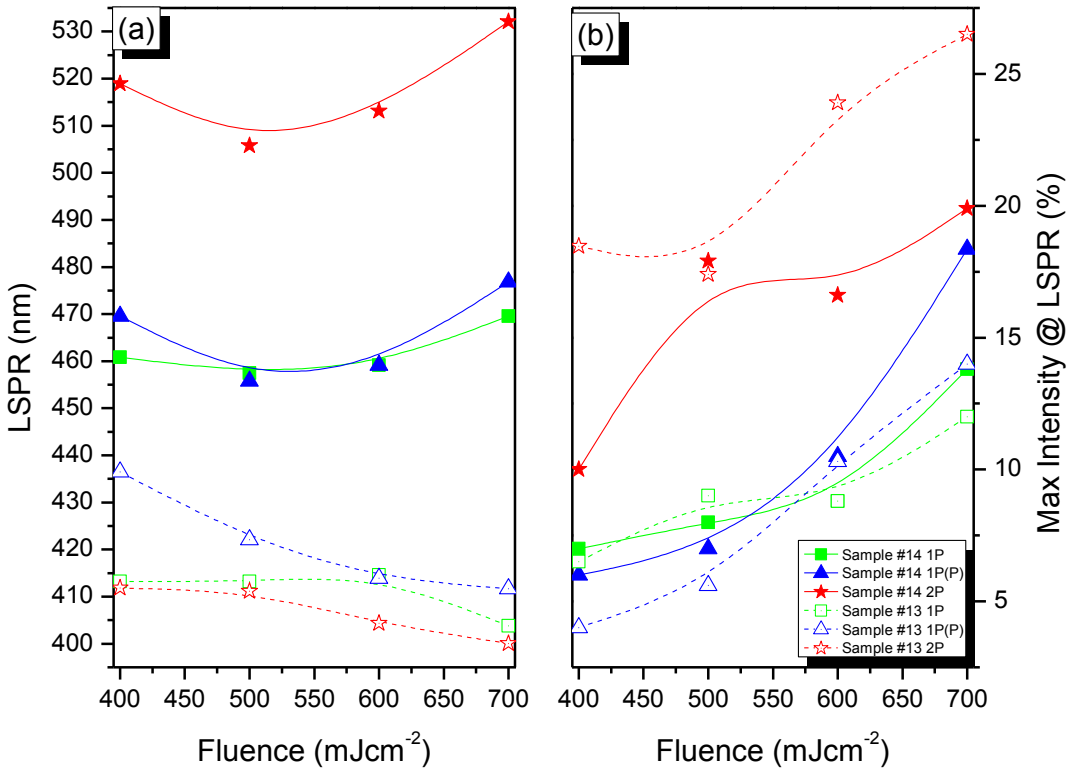

Figure 5.47. Effect of laser fluence in the spectral position of the LSPR peak position (a) and intensity (b) respectively after laser annealing in ambient conditions and under pressure (P).

From figure 5.46a it can be seen that LSPR peak position is depended both on the thickness of the initial metallic layer and the thickness of the AlN. Thus for sample #13 due to the thinner silver layer, LSPR peak is manifested in lower wavelengths, small nanoparticles are formed, comparing to the higher wavelengths that SPR manifested for sample #14, bigger nanoparticles are formed.

The dependency of the LSPR peak from the laser fluence was a factor that examined in this part of the chapter. For sample #14 one pulse in ambient (green filled squares), 500mJcm^{-2} fluence leads in a weak blue shift comparing to SPR wavelength at 400mJcm^{-2} fluence. This can be attributed in the formation of smaller nanoparticles. On the other hand for 600mJcm^{-2} and 700mJcm^{-2} fluencies a red shift is observed. This is evidenced that bigger nanoparticles are formed relative to lower fluencies. Red shift could also be achieved from alteration of the refractive index of the host e.g. recrystallization of the amorphous host, something that is not

confirmed from TEM observations. The LSPR behavior does not seem to change significantly when laser annealing took place under high pressure (blue filled triangles) or if 2 pulses are applied (red filled stars). The formation of bigger nanoparticles is supported from the simultaneous enhancement of the LSPR intensity (Figure 5.46b). For sample #13 the SPR peak follows the opposite path and now the fluence increment leads in a blue shift. This can be attributed in the thin thickness of the silver (approx. 1nm) which can be described as small islands. Now the increasing intensity of the LSPR intensity can attributed in the creation of higher number on particles each time.

A red shift of the LSPR is also observed for sample #12 (filled violet square) and sample #10 (empty violet square) after laser annealing with 1 pulse in ambient (Figure 5.47a), which can attributed in the formation of bigger nanoparticles after laser annealing with higher fluencies. As a result increment of the SPR intensity is observed due to lower ohmic losses. On the contrary, laser annealing with 1 pulse under pressure leads on a blue shift of the LSPR, which can possibly attributed in the obstruction of the silver outdiffusion and formation bigger nanoparticles. Corresponding behavior is observed to the LSPR intensity (Figure 5.47c). Finally the application of a second pulse in both conditions (Figure 5.47b) leads in a blue shift of the LSPR, indication that the second pulse cleaves the initial formed nanoparticles to lower.

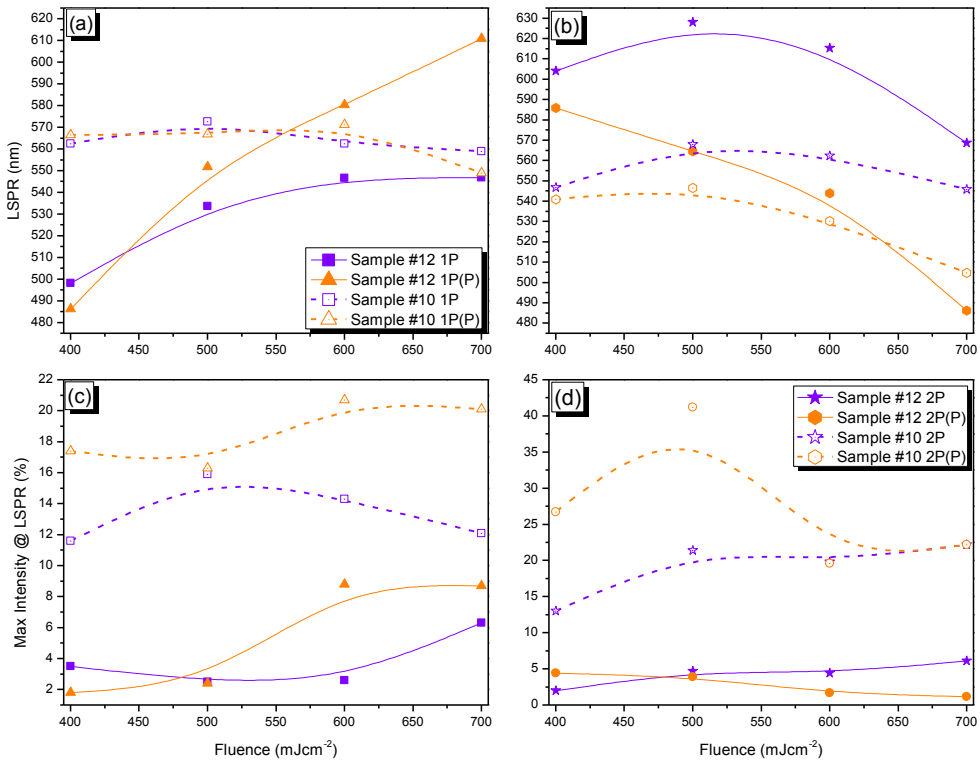

Figure 5.48. (a, b) Alteration of the LSPR position for 1 pulse and 2 pulses as a function of different fluencies respectively. (c, d) Variation of the LSPR intensity for different used fluencies.

5.5 Conclusions

In this chapter the structural and optical properties of the AlN-Ag system in various configurations using Pulsed Lased Deposition and Magnetron Sputtering deposition techniques were studied in an effort to understand their self-organization mechanisms and optical properties. Depending on the method and growth conditions we managed to produce either amorphous or crystalline AlN matrix. Starting with the sputtered films, in case of co-sputtered nanocomposite films incorporation of Ag into w-AlN results in disruption of columnar growth, reduction of texture and development of globular grains. The combined XRD and XPS analyses identified a solubility limit of 4% *at.* for Ag into AlN. Further increase of the Ag concentration results in segregation of Ag and self-organization in Ag crystal grains. On the other hand, in case of periodical structures TEM observations revealed that the metallic layer is not a continues layer but consists of overall spherical shapes which are abutting each other due to very thin thickness. On the contrary, in the case of PLD samples, the implementation of a sector target as well as the low miscibility of the two phases leads in the formation of Ag nanoparticles with an average size 3-5nm into the AlN host. Unlike to sputtered samples, in case of PLD the formation of Ag crystal grains occurs even for Ag concentrations below the solubility limit, due to the pulsed and successive deposition.

Each category of samples was subjected to thermal and laser annealing in order to investigate its effect on the structural and optical properties of the produced samples based on the different annealing mechanism that occur in each case.

Thermal annealing of AlN:Ag co-sputtered and PLD samples respectively results in outdiffusion of Ag, which is more pronounced in w-AlN:Ag samples of low Ag concentration, due to their columnar morphology that provides diffusion paths. The outdiffused Ag self-organized in nanoparticles of sizes 40-310 nm and had strong plasmonic response. Contrariwise, the structural features of AlN itself did not alter after thermal annealing due to the high melting point of AlN. On the other hand, laser annealing induces only nanometric outdiffusion, identified only by surface sensitive Auger spectroscopy, due to the ultra-short annealing time. In case of PLD samples the selective delivery of laser energy to metallic hot spots promotes local over-heating resulting in local crystallization of the AlN matrix as well as in particles enlargement. As a result, significant changes in the optical properties of the samples were observed. In particular, the localized surface plasmon resonance in the optical reflectance spectra can be tuned to cover a wide part of the visible range from violet to green by applying

the appropriate annealing procedure producing high spatial selectivity miniature plasmonic devices

Finally, the implementation of UV laser treatment into multilayer structures results in the sub-surface modification of the metallic layer into metallic nanoparticles which alters the optical properties of the samples. Furthermore, TEM observations revealed that multilayers having a smooth AlN/Si interface compared to PLD samples which is associated with the higher thickness of the multilayers.

The LSPR emerged in case of multilayers reveal a new route for the fabrication of plasmonic templates due to the simplicity, flexibility and versatility of the proposed approach in combination with the capability to control the environmental sensitivity of Ag nanoparticles.

From the point of view of applications laser annealing of AlN:Ag nanostructures can lead to plasmonic template candidates for information storage, optical encoding and recording, security tagging, decorative and ophthalmic lenses.

References

[5.1] Narayan R.J., *Mater. Sci. Eng. C,* **25** (2005), pp. 398-405.

[5.2] Joerger R. *et al., Adv. Mater*., **12** (2000), pp. 407-409.

[5.3] Jaouen N. *et al., Phys. Rev. B,* **76** (2007), art. no. 104421.

[5.4] Panagiotopoulos I., *et al., J. Appl. Phys*., **87** (2000), pp. 4358-4361.

[5.5] Vovk A.Ya., *et al*., *J. Appl. Phys*., **91** (2002), pp. 10017-10024.

[5.6] Zhang X.X., Liu H., Pakhomov A.B., *Physica B,* **279** (2000), pp. 81-83.

[5.7].Zhang Q.-C, *Solar Ener. Mater. Solar Cells,* **62** (2000), pp. 63-74.

[5.8] Teixeira V., Sousa E., *et al , Thin Solid Films,* **392** (2001), pp. 320-326.

[5.9] Panagiotopoulos N.T., Diamanti E.K., *et al., ACS Nano,* **6** (2013), pp. 10475.

[5.10] Gadenne M., Podolskiy V., *et al*., *Europhys. Lett.,* **53** (2001), pp. 364-370.

[5.11] Dakka A., Lafait J., Sella C., *et al., Appl. Optics,* **39** (2000), pp. 2745-2753.

[5.12] Kaminski P.M., Bass K., Claudio G., *Phys. Solidi Status C,* **8** (2011), pp. 1311-1314.

[5.13] Godbole V.B., Narayan J., *Materials Science and Engineering B,* **39** (1996), pp. 153-159.

[5.14] Kalfagiannis N., Karagiannidis P.G., Pitalidis C, *et al. , Solar Energy Materials & Solar Cells*, **104** (2012), pp. 165-174.

[5.15] Lotsari A., Dimitrakopoulos G.P., Kehagias Th. *et al*., *Surf. Coat.Techn.,* **204** (2010), pp. 1937-1941.

[5.16] Bing-Hwai Hwang, *J. Phys. D: Appl. Phys.*, **34** (2001), pp. 2469-2474.

[5.17] Kovacich J.A., Kasperkiewicz J., *et al.,, J. Appl. Phys.* **55** (1984), pp. 2935-2939.

[5.18] Hoflund G.B., Weaver J.F., Epling W.S., *Surf. Sci. Spectra,* **3** (1994), pp. 157-162.

[5.19] Kaushik V.K., *J. Elec. Spec.. Relat. Phenom*., **56** (1991), pp. 273-277.

[5.20] Huang , P.-H. Chiu C.-J., Y.-H. *et al., J. Electrochem. Soc,* **153** (2006), pp. 193-198.

[5.21] Ramachandra Rao C. N., Kulkarni G.U., *et al., Chem. Soc. Rev*., **29** (2000), pp. 27-35.

[5.22] Liu F., Zhao Z., *et al.,, J. Surf. Anal*., **15** (2009), 271.

[5.23] Pászti Z., Petö G., *et al., Sol. State Commun*., **107** (1998), pp. 329-333.

[5.24] Evanoff Jr D.D., Chumanov G., *Chem. Phys. Chem*., **6** (2005), pp. 1221-1231.

[5.25] Barrie A., *Chemical Physics Letter*, **19** (1973), pp. 109-113.

Chapter 6 *TERNARY Al1-xInxN ALLOYS*

6.1 Introduction

The AlInN ternary system is an important chapter of III-V nitride alloys that although has not been studied extensively it is important due to the exceptional optical properties if the $Al_{1-x}In_xN$ that make them candidates to replace other ternary III-V systems in applications such as Light Emitting Diodes (LEDs) and Solar cells.

The growth of these alloys is performed mainly by Metal Organic Chemical Vapor Deposition (MOCVD) [6.1-6.6], which is based in chemical reactions at high temperatures, or Reactive Sputtering [6.7-6.14], which gives the advantage of depositions at low temperatures an important factor taking into account the differences occurred in the melting points between the Al (660.32 ^{o}C) and In (156 ^{o}C).

In this chapter Al reach ternary AlInN compounds have been grown and the structural and optical properties are studied. On a second step the as grown samples subjected to thermal annealing and the structural and optical changes that caused are studied.

Finally, it is attempted the growth of nanocomposite film consisting of Ag nanoparticles into AlInN matrix with different In composition and a study of the structural and optical properties is performed.

6.2 $Al_{1-x}In_xN$ ternary alloys

6.2.1 AlInN ternary alloys growth

$Al_{1-x}In_xN$ alloys ($x \leq 20\%$ at.) were grown using Magnetron Sputtering technique in a mixed Ar-N_2 environment using metallic Al target while different number of In pieces were placed on Al target in order to vary the In concentration into the samples. The deposition parameters are summarized in table VIII below. In order to investigate the structural and morphological characteristics X-Ray Diffraction (XRD) and X-ray Reflectivity (XRR) measurements were performed.

Table VIII. Deposition parameters of $Al_xIn_{1-x}N$ samples

Sample ID	Al target power [Watt]	In pieces	[In] (%at)	Ar Flow (sccm)	N_2 Flow (sccm)	Deposition time (min)
Sample #16	50	1	3	12	8	30
Sample #17	50	2	10	12	8	30
Sample #18	50	2	12	12	8	30
Sample #19	50	3	20	12	8	30

The composition x of the studied samples was evaluated from the XPS wide scan spectra (Figure 6.1) considering the integral strength of the Al2p and In 3d photoelectron lines and the relative sensitivity factors. Peak labeling of the emerged peaks at the wide scan spectra revealed that C 1s and O 1s photoelectron peaks, as well as, the C_{KLL} and O_{KLL} Auger peaks were manifested, which can be ascribed in the surface contaminations due to ex-situ XPS measurements. The concentrations for each sample are presented in Table VIII above.

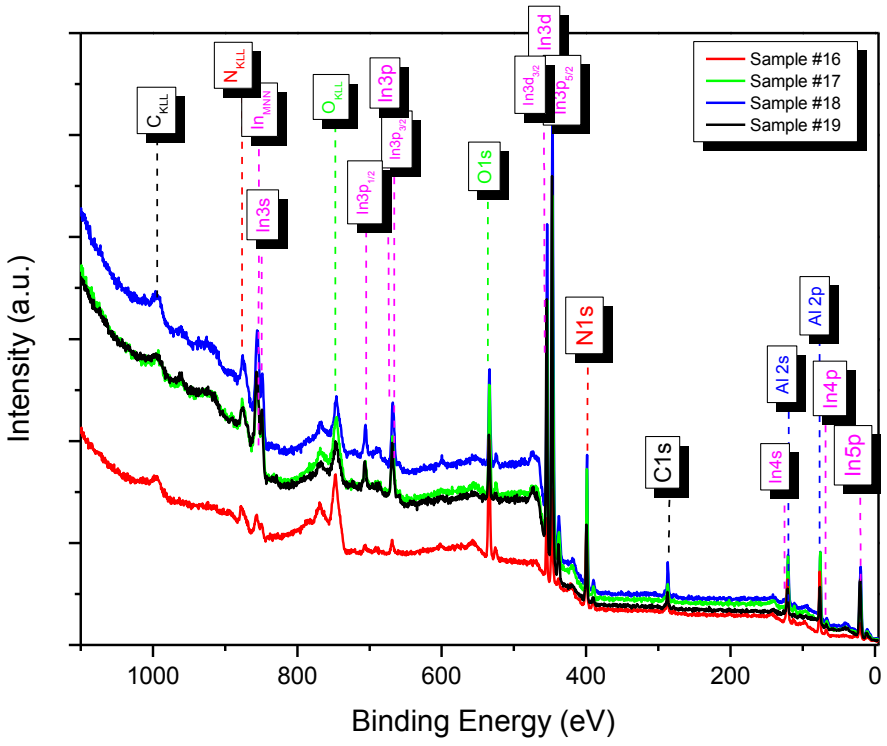

Figure 6.1. XPS Wide Scan measurements of the as grown samples were used for quantitative and qualitative analysis of samples

The GIXRD measurements of the as deposited $Al_{1-x}In_xN$ with increasing x concentration are illustrated in figure 6.2a. All films, irrespective of the x concentration, exhibits the wurtzite structure with (002) preferred orientation. A gradual shift of the diffraction peaks compared to the pure AlN was observed with increasing the In concentration which is an evidence of macro-strain in the films. This macro-strain can be attributed in strain which are developed due to deformation of the unit cell as the larger In atoms substitutes Al atoms in the lattice. The lattice deformation that caused from In incorporation is verified from calculations for the c axis of the wurtzite structure which deviates from Vegard's law (Figure 6.2b) especially for concentrations higher than 10% at.

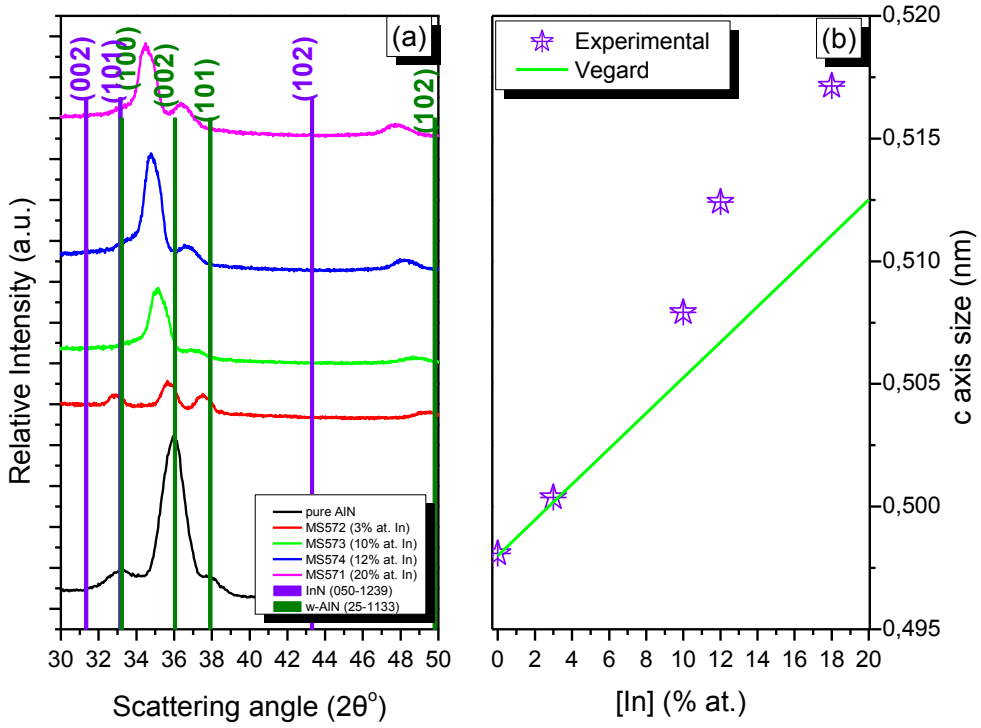

Figure 6.2. a)Evolution of the XRD (GIXRD) measurements of the as grown samples with increasing In concentration. b) Vegard's law for the as grown samples at c axis of the wurtzite structure along with the experimental values (stars).

X-ray Reflectivity measurements were also performed in order to investigate the variation of the sample's density as a function to the In concentration. Representative XRR patterns of the as grown samples with the theoretical fit are illustrated in figure 6.3a.

The analysis of the XRR measurements revealed that the density of the films was increasing with In composition (figure 6.3b), which is the result of Al substitution from larger In atoms into the lattice if N concentration remains the same

Finally, the chemistry that the as grown films provide was investigated by core level XPS (HRXPS) measurements of Al 2p, In 3d and N 1s photoelectron peaks. Charging effects in all

XPS spectra eliminated by considering C 1s photoelectron peak at 284.6 eV binding energy according to literature while a Gaussian-Lorentzian 30% (GL30) function was used for XPS photoelectron peak analysis.

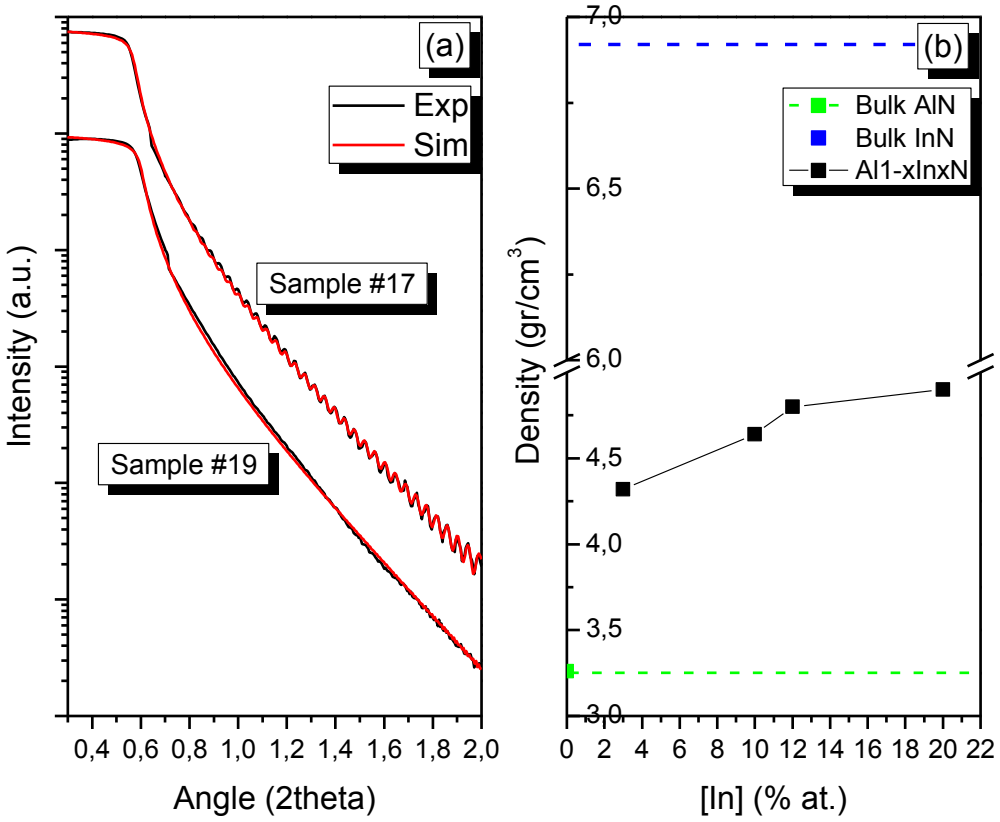

Figure 6.3. a) X-ray Reflectivity patterns with the theoretical fit for samples #17 and sample #19 respectively. b) Density alteration with respect to In composition of the as deposited films.

Al 2p photoelectron peak for all samples is deconvoluted with one component (figure 6.4a.b) taking a value within the range 73.2 eV to 73.6 eV which can attributed in Al-N bonding [6.15]. The characteristic doublet In 3d photoelectron peak (Figure 6.4c, d) corresponding to In $3d_{5/2}$ and In $3d_{3/2}$ respectively, due to spin-orbital splitting, was observed for all samples. The values of the In $3d_{5/2}$ was in the range of 444 eV while the value of the In $3d_{3/2}$ was at 7.6eV more at around 452 eV as it is referred to the literature. The values of the In 3d photoelectron peaks indicates the formation of In-N bonds [6.16] in our samples. Finally, in N 1s peak two different components were identified. The main peak provides a binding energy at around 396,4 eV and thus it can be assigned to Al-N bonding [6.15]. The minor component is exhibited in higher binding energies and can be attributed in N-C or N-H bonding due to the surface contaminations. On the other hand, indications of In-N from N 1s analysis could not be exported as the binding energy of N 1s for In-N bonding provides only 0.2eV difference from the corresponding value of Al-N N 1s.

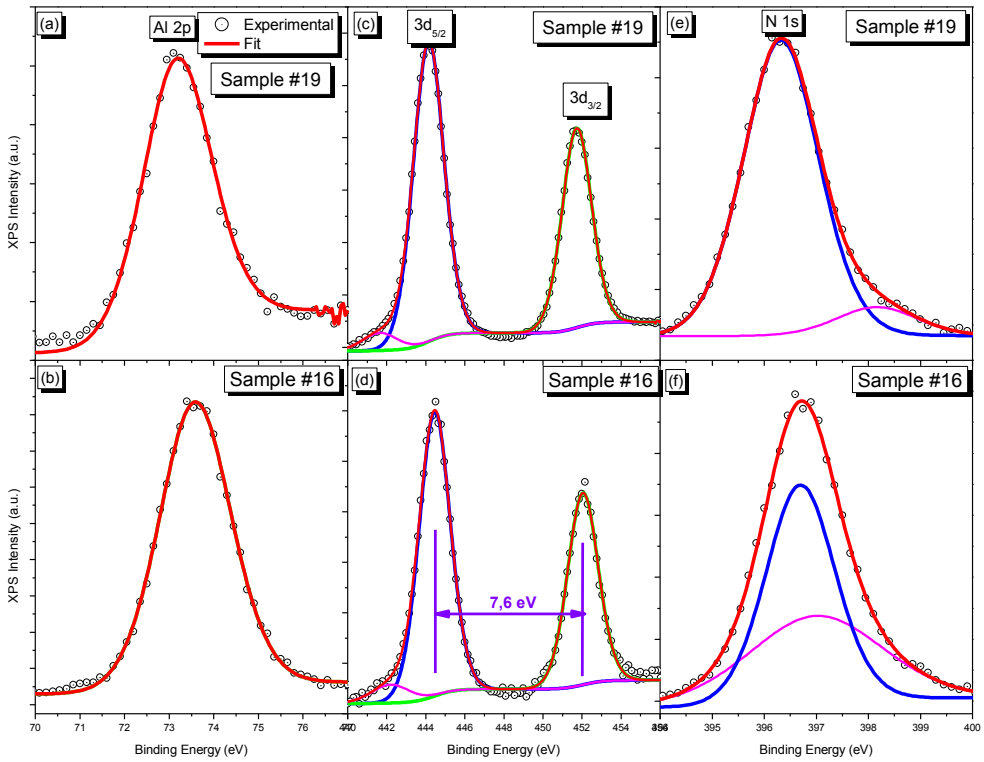

Figure 6.4. Representative High Resolution XPS (HRXPS) photoelectron peaks of Al 2p (a, b), In 3d (c, d) and N 1s (e, f) respectively.

The values of the photoelectron peaks that obtained after peak analysis and In concentration x are summarized in table IX below for all the as grown samples.

Table IX. XPS peak values obtained after peak analysis.

	Photoelectron Peak Binding Energy (eV)			
Sample ID	**Al 2p**	**N 1s**	**In $3d_{5/2}$**	**In $3d_{3/2}$**
Sample #16	73.58	396.32	444.14	451.73
Sample #17	73.20	396.69	444.45	452.05
Sample #18	73.21	396.27	444.10	451.70
Sample #19	73.17	396.37	444.17	451.77

As it was already reported the incorporation on InN into AlN alters the band gap of the film and therefore the optical absorption of the film. This behavior was confirmed by Optical Reflectivity Spectroscopy (ORS) measurements of the as deposited samples (Figure 6.5). In all cases interference fringes due to layer-substrate reflections are observed at a long energy range. Since the interference fringe begins to vanish in the vicinity of the energy related to the optical band gap, we can claim that the optical band gap is related with the concentration x in our samples. Thus, for 3% In (red spectra) the absorption is approximately at around 4.8 eV. On the contrary higher percentages of In, 10 % (green spectrum) and 12 % (blue spectrum) concentration respectively, leads on absorption at lower photon energies, approx 4.0 eV. Finally for the highest In composition (black spectrum) that used in this series of samples a further reduction on the optical absorption is observed, at approximately 3.6 eV.

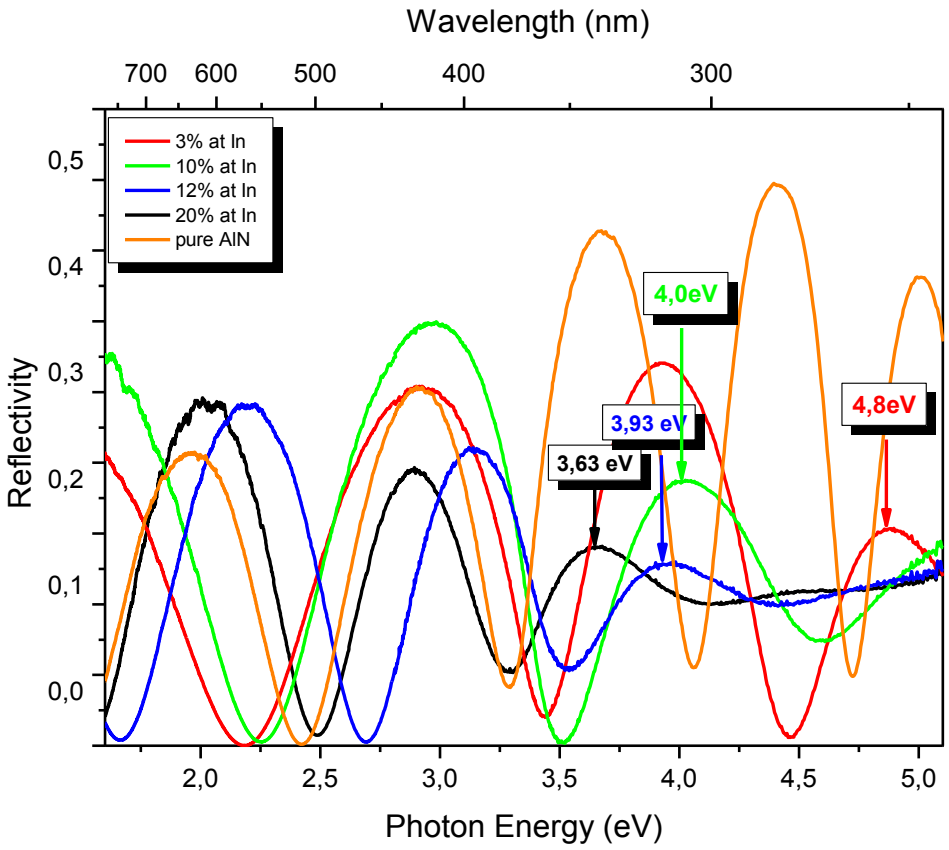

Figure 6.5. Reflectivity spectra of the as grown films with varying In concentration.

6.2.2 Thermal Annealing

The structural and morphological properties of the samples after annealing were investigated. Thus, samples #18 and sample #19, with the highest In composition, were subjected to thermal annealing at 800^{o}C for 1 hour in ambient in order to avoid oxidation of the films.

The XRD measurements of the treated samples (Figure 6.6) revealed that our films consist of polycrystalline w-AlN and w-InN with both structures provide a (002) preferred orientation while other diffraction peaks are also manifested. On the other hand, according to the difractogramms the annealed samples shift from the pdf values were also observed which can be attributed in the cell mismatch due to different atomic radius of Al and In respectively.

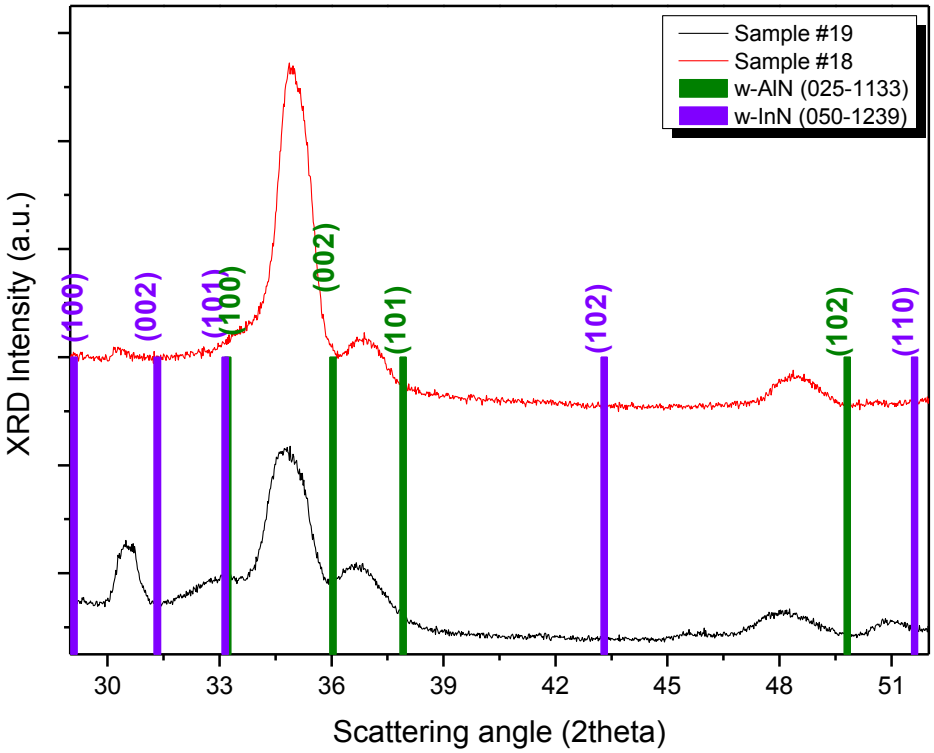

Figure 6.6. Grazing Incidence XRD measurements of annealed samples.

Although the XRD measurements revealed phase separation after thermal annealing, the chemical state was not varied according to the HRXPS measurements that were performed. Thus, Al 2p is taking a value in the range of 73.5eV binding energy which can attributed in Al-N bonding. The characteristic doublet In 3d photoelectron peak (Figure 6.4c, d) corresponding to In $3d_{5/2}$ and In $3d_{3/2}$ respectively, due to spin-orbital splitting, was observed as well. The values of the In $3d_{5/2}$ was in the range of 444 eV indicates the formation of In-N bonds.

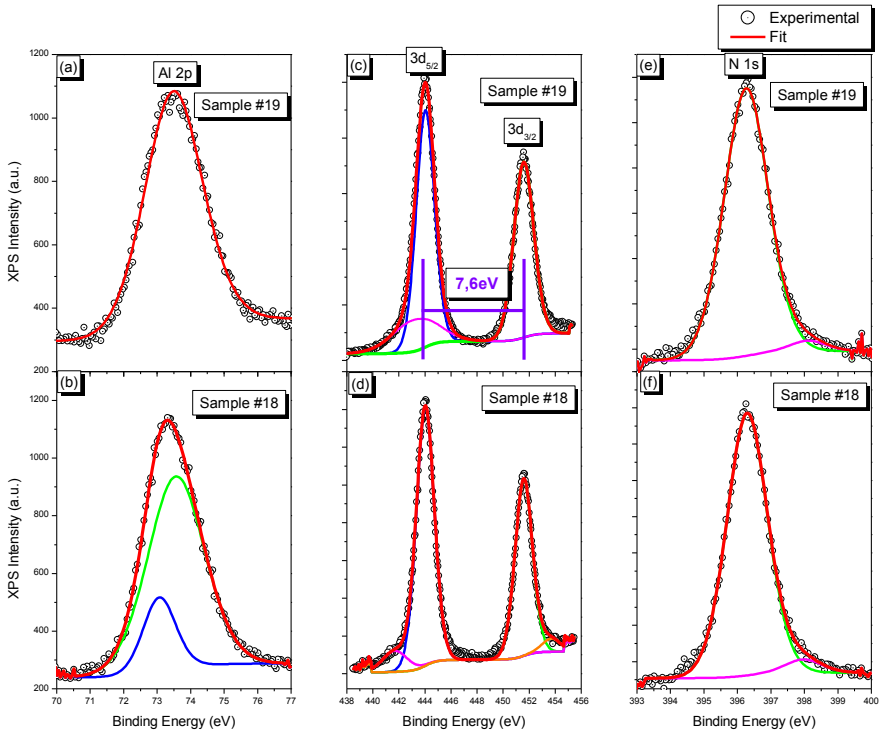

Figure 6.7. High Resolution XPS photoelectron peak analysis of Al 2p (a, b), In 3d (c, d), N 1s (e, f) for samples #18 and #19 respectively, after thermal annealing

The quantitative analysis revealed that after thermal annealing the In concentration was altered. Thus, sample #18 In concentration was 6.18% at, instead of 12% of the as grown sample, while sample #19 In concentration was 9.3% at, instead of 20% in the as grown. This variation of In composition can be attributed in the low melting point that In has. The results obtained from the XPS photoelectron peak analysis and the concentration x of the annealed samples are summarized in table X.

Table X. In concentration and XPS peak values obtained after peak analysis for the annealed samples.

	In conc. [%at.]	**Photoelectron Peak Binding Energy (eV)**			
Sample ID		**Al 2p**	**N 1s**	**In $3d_{5/2}$**	**In $3d_{3/2}$**
Sample #18	9.33	73.46	396.26	444.03	451.59
Sample #19	6.18	73.55	396.29	444.02	451.58

Thermal annealing and possibly the evaporation part of the In composition affects the morphology as it was revealed from the XRR measurements. Thus, the annealed samples display lower density values than the as grown (Figure 6.8) which can be assigned in the phase segregation and the formation of w-InN phase possible into w-AlN lattice.

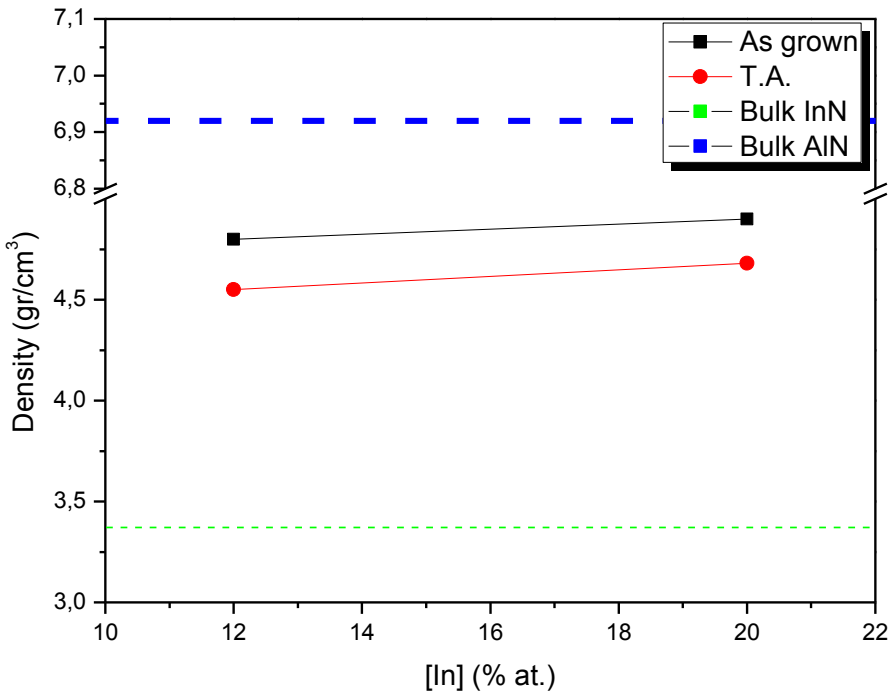

Figure 6.8. Density of the annealed samples with respect to the In composition.

The In evaporation mainly and the phase separation would affect the optical properties of the samples. Thus, reflectivity measurements that illustrated in figure 6.9 were performed. Interference fringes from layer-substrate reflections are also manifested. On the contrary, interference fringes intensity reduction which relates with optical band gap begins in a different energy comparing to the as grown films. Thus, sample #18 fringes vanish started at around 4.07 eV in contrast to 3.93eV of the as grown sample. A similar value is observed for sample #19 (4.04eV) relative to the 3.6eV of the as grown sample. This convergence of the annealed samples can be attributed in the similar In compositions that the samples have. This observation strengthens the argument that In evaporation during annealing is mostly altering the optical properties of the samples.

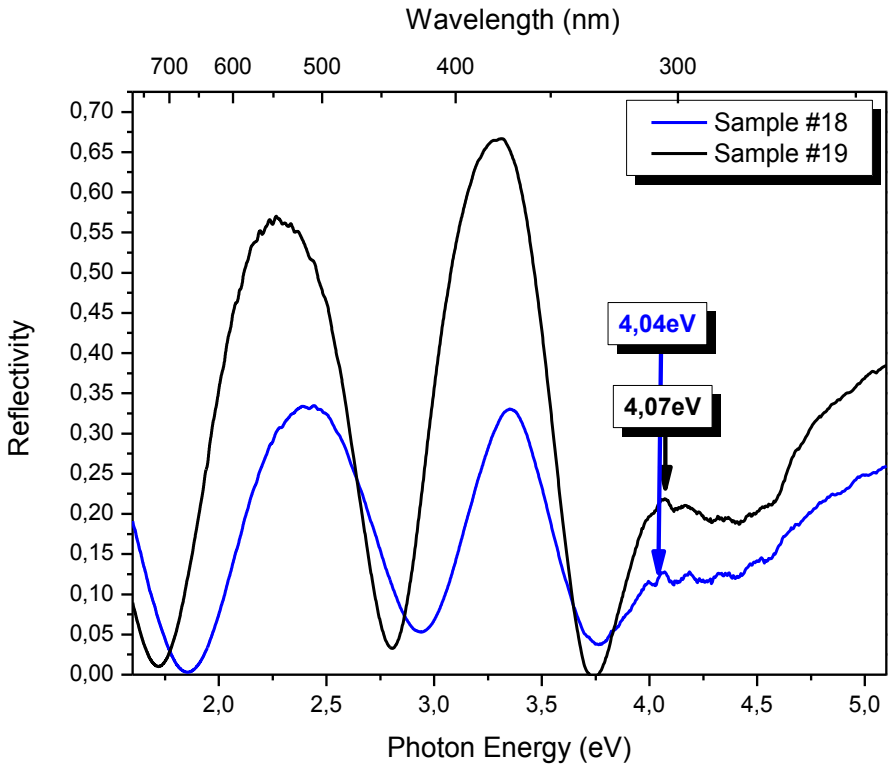

Figure 6.9. Optical Reflectivity spectrums of the annealed samples.

6.2.3 $Al_{1-x}In_xN$/Ag nanocomposite films

The last venture of this chapter was to grown nanocomposite films consisting of silver nanoparticles into an AlInN matrix. Thus, at first Ag films with different thicknesses were grown. XRR measurements were performed (figure 6.10) in order to estimate films parameters such as thickness, density and roughness

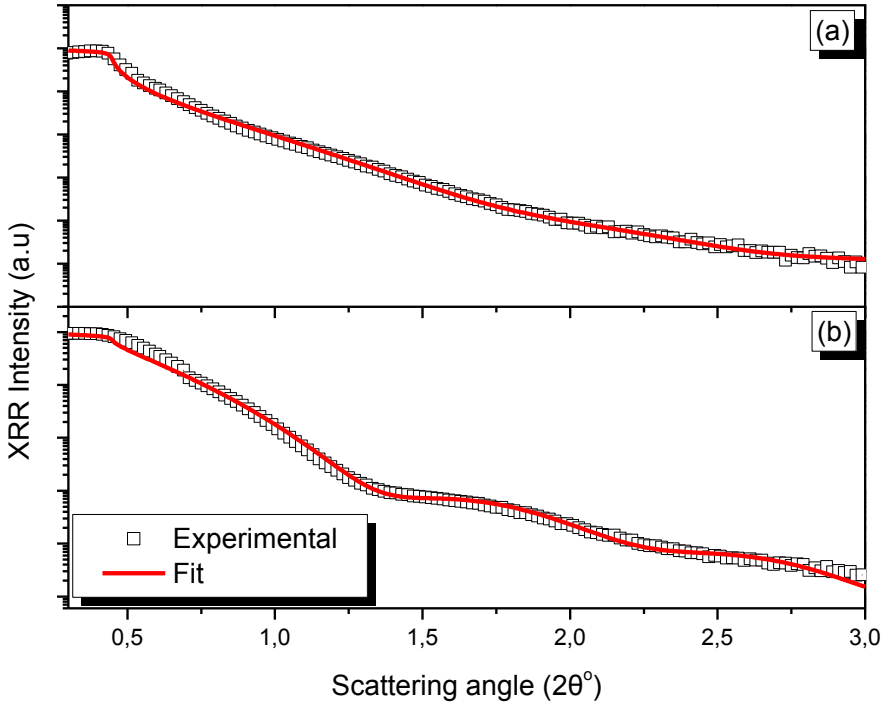

Figure 6.10. X-Ray reflectivity measurements (black squares) with the corresponding fit for samples #20 (a) and #21 (b) respectively.

The structural and morphological parameters of the as grown silver samples revealed from the XRR curves are summarized in table XI

Table XI. Structural and morphological parameters of as grown thin silver films

Sample ID	**Deposition time (sec)**	**Thickness (nm)**	**RMS Roughness (nm)**	**Density(gr/cm^3)**
Sample #20	5	4.48	0.70	3.875
Sample #21	10	6.30	0.77	5.04

By varying the deposition time we managed to grow films with thicknesses 4.5nm and 6.3nm respectively. Due to thin thicknesses both samples provide density values lower than bulk (Figure 6.11a) something reasonable taking into account that films in this range are not uniform but they are just approaching the percolating threshold. On the other hand both films had similar values of the RMS roughness as their thicknesses are of the same magnitude (Figure 6.11b).

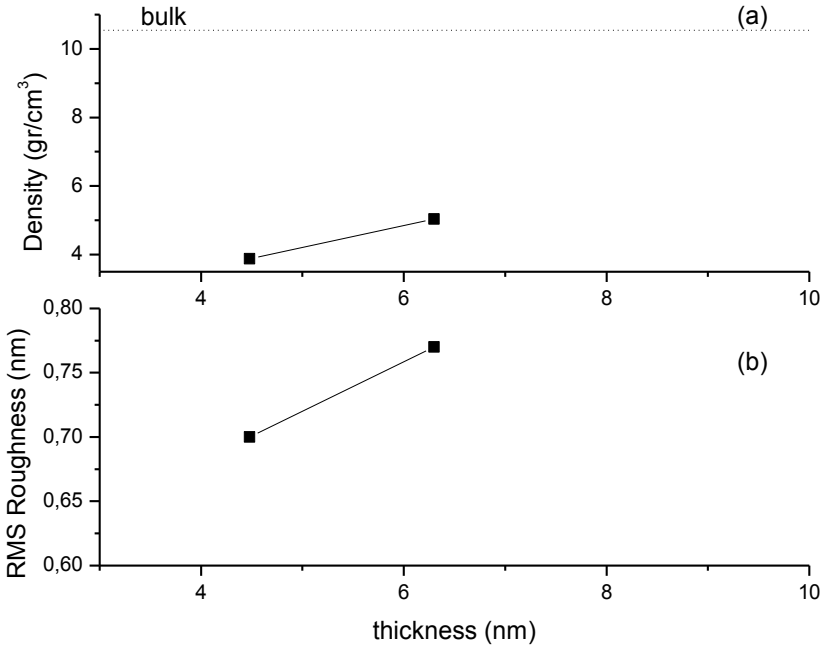

Figure 6.11. Density (a) and RMS Roughness (b) of samples #20 and #21 with respect to the film thickness.

The as grown samples were further subjected to hot plate annealing at 300^{o}C for 1 minute in order to convert the initial layer to metallic nanoparticles. From AFM images it was observed the formation of nanoparticles of different sizes. Thus in case of sample #20 (Figure 6.20), with the thinner silver film, nanoparticles with an average size of 15m, were performed while other with size at about 30nm were also observed.

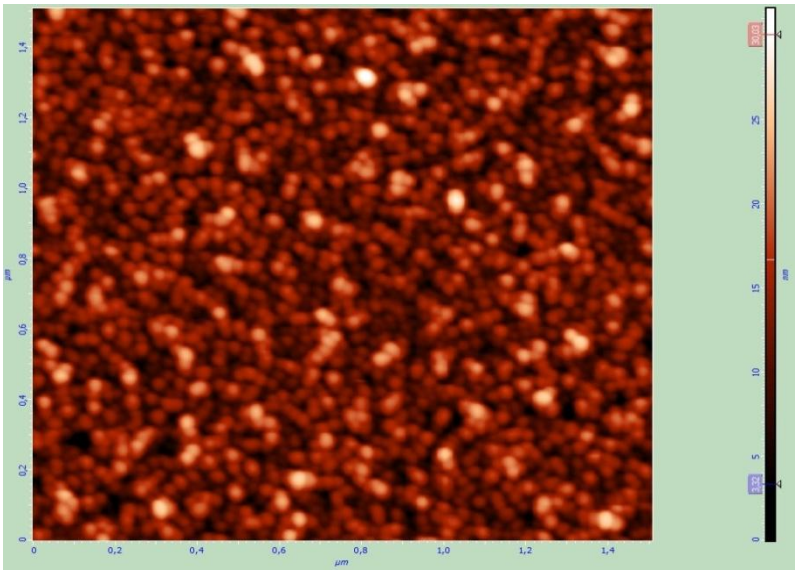

Figure 6.12. AFM image of sample #20 surface after hot plate annealing.

On the contrary, in case of sample #21 (Figure 6.13) bigger nanoparticles with an average size of 40nm were formed.

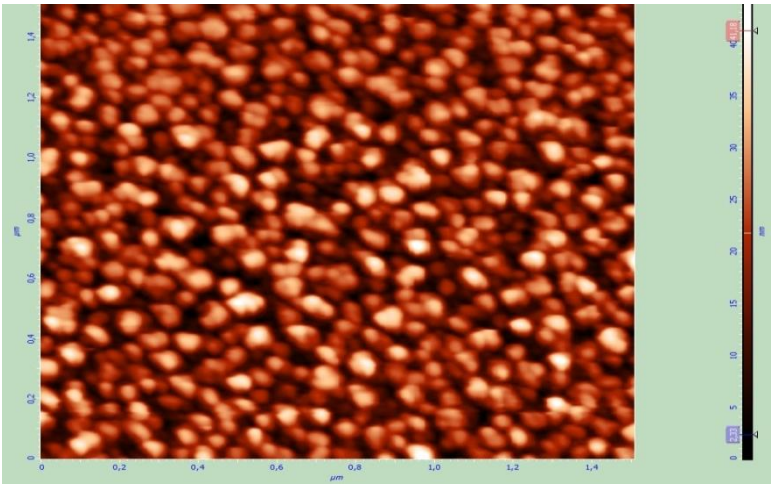

Figure 6.13. AFM image of sample #21 surface after hot plate annealing.

The formation of silver nanoparticles resulted in Localized Surface Plasmon Resonance (LSPR) manifestation in the reflectivity measurements (Figure 6.14).

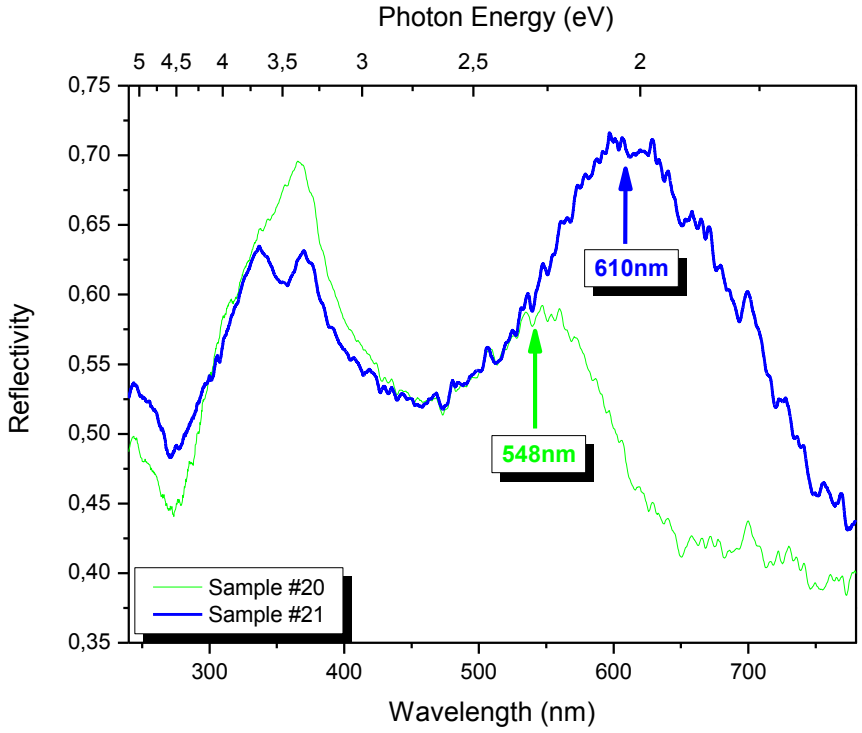

Figure 6.14. Optical Reflectivity spectrums of the annealed samples. According to the nanoparticles size LSPR at different wavelengths are manifested. Peaks at around 350nm can be attributed in substrate features.

The plasmon resonance wavelength is related to particles size. Thus, for the smaller particles (sample #20) an LSPR manifestation at 548nm was observed while for the bigger nanoparticles

(sample #21) a more intense SPR at higher wavelengths, 610nm, was observed. Except of the plasmon peaks, the ORS spectra exhibit peaks that can be assigned in substrate features. In both cases LSPR peak location was identified by fitting the ORS spectrum using a Lorentzian model after background subtraction which illustrated in figure 6.15.

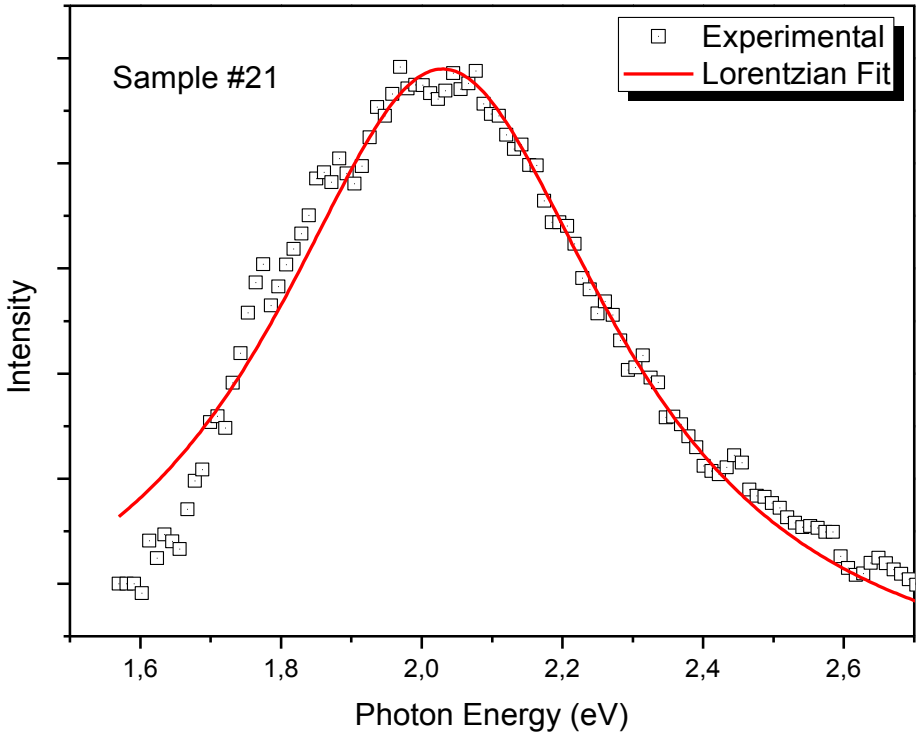

Figure 6.15. LSPR peak position (experimental) with the corresponding Lorentzian fit for sample #21.

Subsequently, each of the samples cut in two pieces and placed into the sputtering chamber in order, nanoparticles to be coated with a film of AlInN with different In concentrations. Specifically, for each In concentration a piece of sample #20 and sample #21, respectively, were placed simultaneously on the sample holder while a piece of silicon wafer was also placed as reference sample. Aim of this batch of experiments was to evaluate the effect of In concentration in the spectral position of the LSPR peak

XPS measurements were performed in order to identify In compositions on our samples. The compositional analysis in the wide scan spectrums (Figure 6.16) revealed that nanocomposite films with concentrations 7.7% at and 12.50% at respectively were grown.

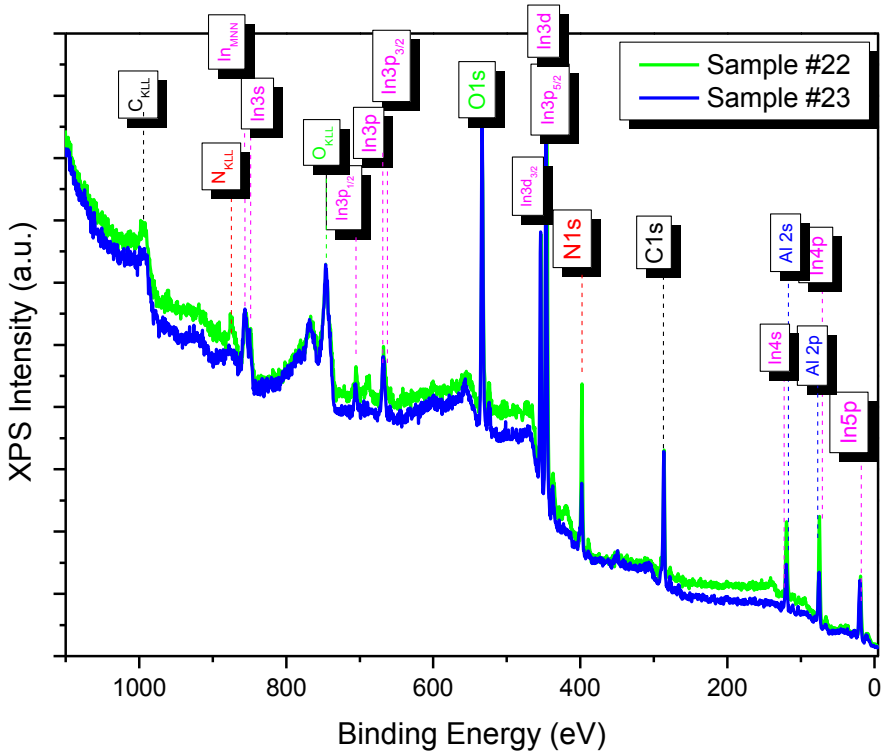

Figure 6.16. XPS wide scan spectrums of reference samples #22 and #23 respectively. Quantitative and Qualitative analysis has been performed.

The deposition parameters and In compositions for all samples are aggregated in Table 6.4.

Table XII. Deposition parameters of the nanocomposite samples

Sample ID	**Power DC(Watt)**	**[In] % at.**	**Ar/ N_2 flow (sccm)**	**Deposition time (min)**	**Si substrate reference**	**LSPR peak position (nm)**
Sample #22	50	7.7	12/8	10	reference	-
Sample #23	50	12.50	12/8	10	reference	-
Sample #24	50	7.7	12/8	10	Sample #20	548
Sample #25	50	7.7	12/8	10	Sample #21	610
Sample #26	50	12.50	12/8	10	Sample #20	548
Sample #27	50	12.50	12/8	10	Sample #21	610

The XRD measurements performed in grazing incidence (GIXRD) mode within the range 32^o to 52^o scattering angle while the tube was at 2^o. From the diffraction patterns observed that only diffraction peaks corresponding to Ag (111) and (200) diffraction planes in contrast to the as grown samples where diffraction peaks of the ternary system was manifested which can be attributed to the thin film thickness, which was approximately at 80nm. This thin thickness was preferred in order to avoid the overlap of the LSPR peak with the interference fringes due to the film transparency.

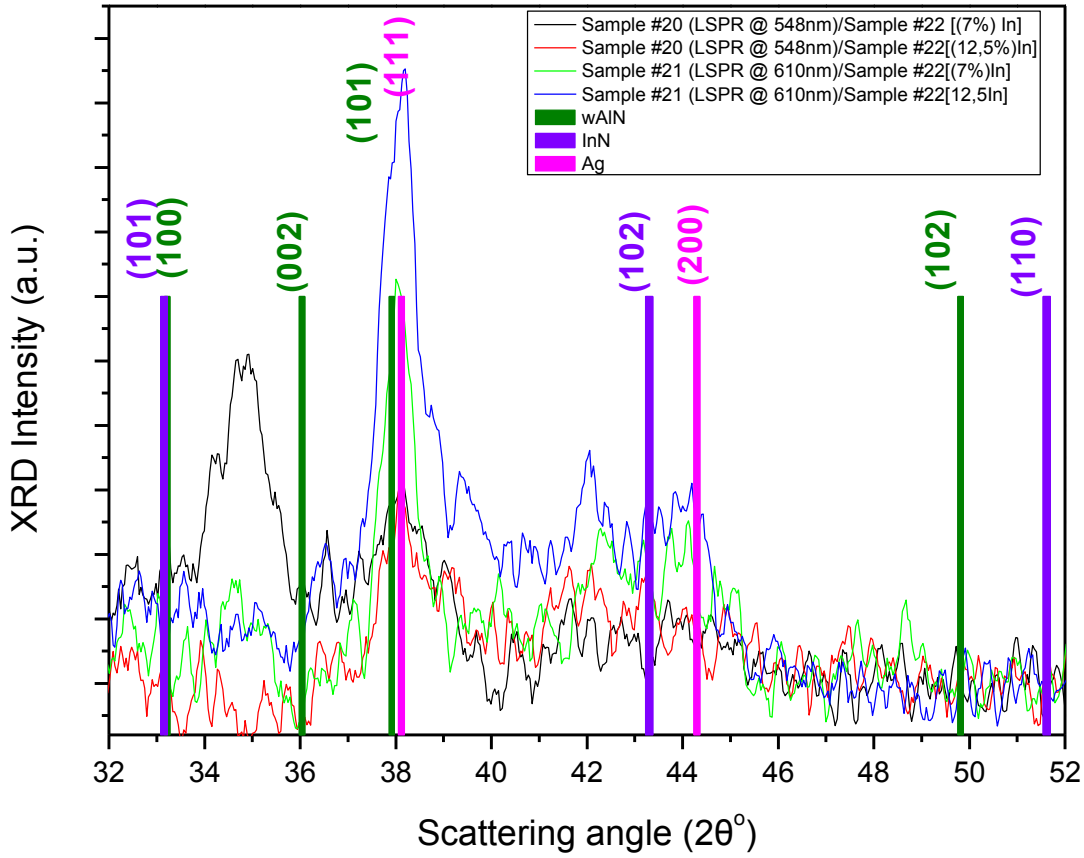

Figure 6.17. Grazing Incidence XRD pattern of the as-grown nanocomposite films.

Optical properties of the nanocomposite films were studied as well by Optical Reflectivity Spectroscopy (ORS). For sample #22 ORS spectrum (Figure 6.19a) consisted of a peak that can be attributed in interference fringes. On the contrary, samples #24 and #25 (Figure 6.19a) revealed a complex behavior. Thus, their reflectivity spectrums consisted of a broad peak which is the deconvolution of interference fringes with the LSPR peak. A blue shift of the LSPR peak is observed in these cases, although theory predicts a red shift of the SPR when nanoparticles are embedded in a denser surrounding. Thus, while the initially LSPR position was at 540 nm the coverage of the nanoparticles with AlInN film leads to a LSPR shift at 520nm for 7.7% In

and 502nm for 12.5% In. Similar behavior was observed for the rest samples as well (Figure 19b). So, sample #23 ORS spectrum consisted from interference fringe due to its transparency while the nanocomposite films (samples #25 and #27 respectively) revealed a complex behavior with the LSPR peak shifted to blue as well.

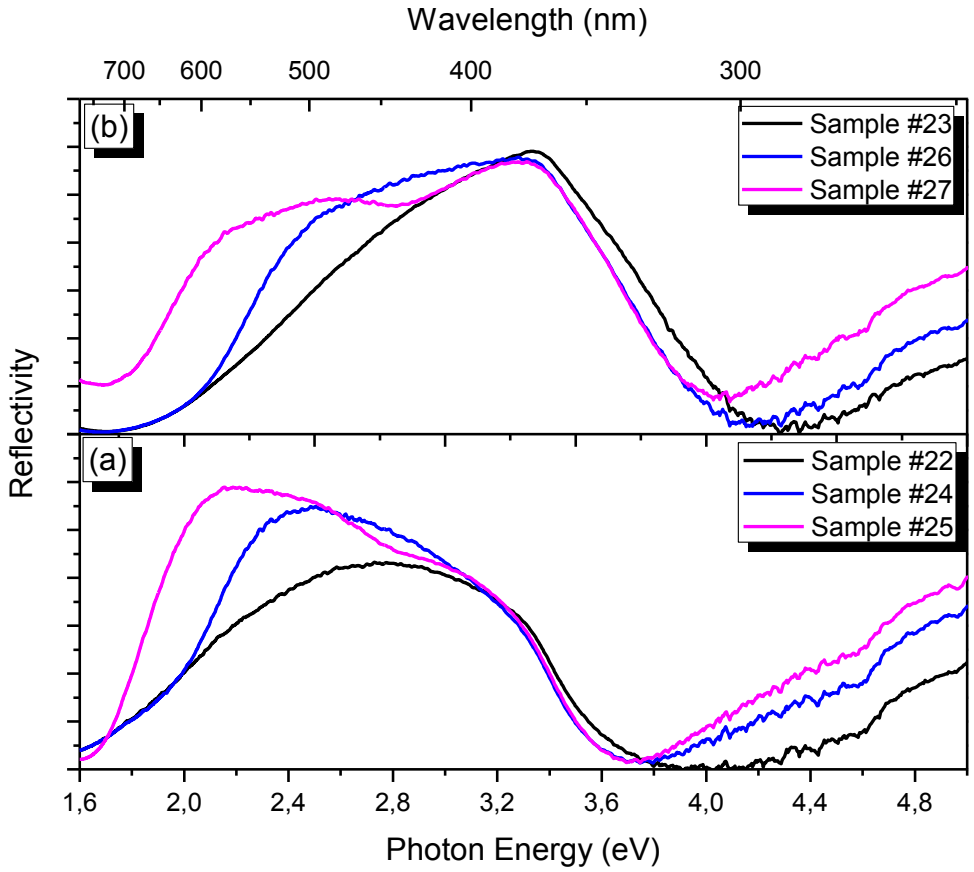

Figure 6.18. Reflectivity spectrums of the nanocomposite films for various LSPR peaks and In concentrations.

Finally, the estimation of the LSPR peak position and its variation with respect to the In concentration was investigated. In order these estimations to be accurate the analysis of the ORS spectrums included background subtraction and a Lorentzian fit to the LSPR peak.

The LSPR peak position with respect to the In concentration is plotted in figure 6.20a. As it is already mentioned, a blue shift was observed in all cases which are unlike to theory. One possible reason for that is that during the deposition of AlInN film the plasma flux could "melt" the already formed nanoparticles reducing nanoparticles size. On the other hand, In concentration altered LSPR variation, (Figure 6.20b). Thus, as In composition increased the LSPR variation, DR, increased linearly which can attributed in the fact that a more optically dense film was grown.

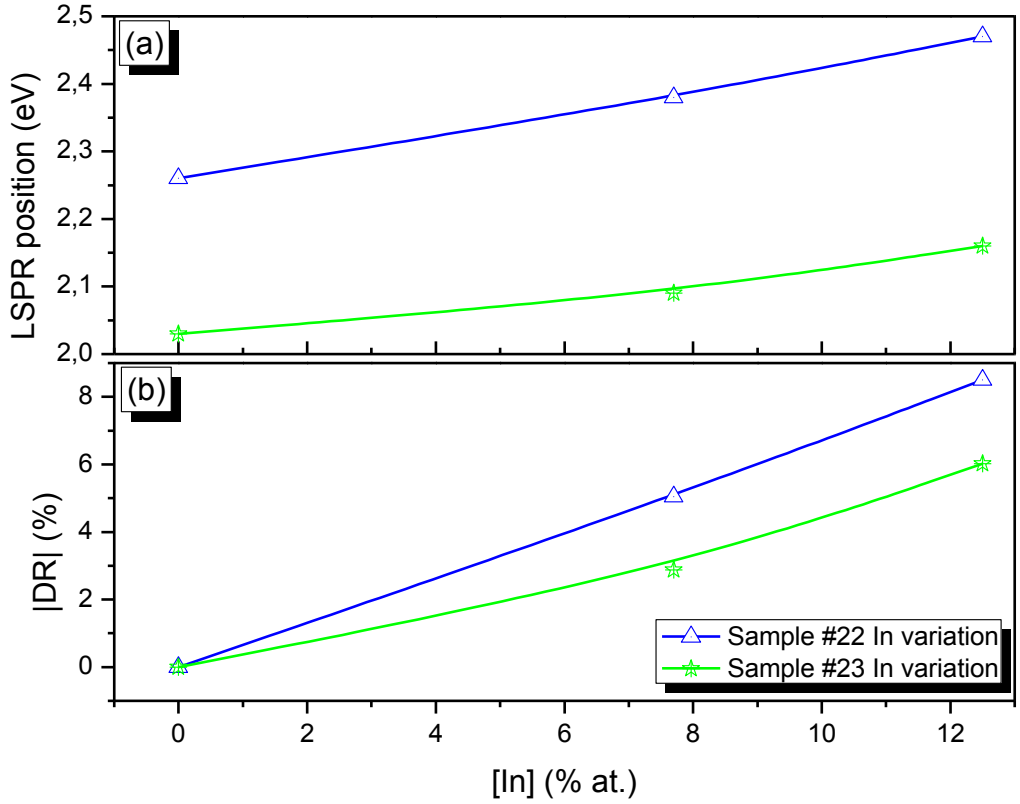

Figure 6.19. LSPR peak position (a) and variation, in absolute values, (b) with respect to In concentration.

6.3 Conclusions

In this chapter, binary Al-rich $Al_{1-x}In_xN$ and nanocomposite films consisted of Ag nanoparticles capped with $Al_{1-x}In_xN$ layer respectively were grown using reactive magnetron sputtering with In concentrations ranging up to 20% at.

Combined XPS and XRD analysis identifies that the variation of In concentration leads in the formation of stressed films due to cell deformation as larger In atoms substitutes Al atoms in the lattice while in terms of optical properties, In incorporation induces changes in the optical absorption of the film as it was demonstrated for the optical reflectivity spectra.

On the other hand, spinodul decomposition of the samples was demonstrated after thermal annealing. The quantitative analysis of the annealed samples revealed an alteration in In concentration possible due to sublimation during the annealing without any changes in the chemical state of the samples.

Finally, in order to form nanocomposite films, Ag nanoparticles of different particles size were covered with an $Al_{1-x}In_xN$ layer. The XRD analysis revealed no significant differences compared to the pure ternary $Al_{1-x}In_xN$ films while the optical response of the nanocomposite

film are not clear indicating that the deposition of the capping layer could affect the silver nanoparticles. Thus, a detailed and in depth analysis is required.

References

[6.1] Hums C., Bläsing J., *et al., Applied Physics Letters*, **90 (**2007), pp. 022105.

[6.2] Kelekci O., Tasli P., *et al., Current Applied Physics,* **12** (2012), pp. 1600-1605.

[6.3] Minj A., Cavalcoli D., Cavallini A.,*Phys. Status Solidi C,* **9** (2012), pp. 982–985.

[6.4] Mosca M., Nicolay S., *et al., Phys. Status. Solidi*, **204** (2007), pp. 1100–1104.

[6.5] Yamaguchi S., Kariya M., *et al., J. Cryst. Growth,* **195** (1998), pp. 309-313.

[6.6] Kim-Chauveau H., *et al., J. Cryst. Growth*, **316** (2011), pp. 30–36.

[6.7] Peng T., Pipreka J., *et al., Applied Physics Letters*., **71 (**1997), pp. 2439-2441.

[6.8] Tung-ShengYeh, Jenn-MingWu, Wen-HowLan, *J. Cryst. Growth*, **310** (2008), pp. 5308–5311.

[6.9] Guo Q., Yahata K., Tanaka T., *Phys. Status Solidi C,* **0** (2003), pp. 2533–2536.

[6.10] Han Q., Duan C., *et al., J. Electr. Mater.*, **39** (2010), pp.489-493.

[6.11] Seppänen T., *et al., J. App. Phys.*, **97 (**2005), 083503.

[6.12] Guo Q.X., *et al., J. Cryst. Growth,* **300** (2007), pp. 151–154.

[6.13] Guo Q., *et al., Jn. J. App. Phys.*, **47** (2008), pp. 612–615.

[6.14] Jiang L. F., Shen W.Z., Guo Q. X., *J. App.Phys.*, **106** (2009), 013515.

[6.15] Evanoff Jr D.D., Chumanov G., *Chem. Phys. Chem*., **6** (2005), pp. 1221-1231.

[6.16] Nagata T., *et al., App. Phys. Lett.,*, **95** (2009), 132104.

Chapter 7

CONCLUSIONS-OUTLOOK

7.1 **Conclusions**

The optical properties of nanocomposite films consisting of AlN or Al-In-N matrices and Ag inclusions and the effect of laser annealing, a new and very promising technology were studied in this PhD framework.

Specifically, in depth analysis of the optical properties of pure Ag after UV-laser annealing and their dependence from a variety of parameters such as film thickness, laser wavelength, fluence and number of pulses, respectively, was performed and presented in chapter 4.

A general conclusion was that laser annealing leads in nanoparticles formation and as a result LSPR manifestation was observed in the Optical Reflectivity spectra, at various wavelengths.

Film thickness is an important factor taking into account that for the thicker film only for high fluencies nanoparticles are formed. On the contrary, for thinner thicknesses alterations were observed for all fluencies.

Moreover, laser parameters such as wavelength, fluence and number of the applied pulses play a crucial role in the LSPR position. Thus, we can tune the LSPR position covering all the visible range according to the requirements. Lower fluencies and number of pulses result in bimodal particle distribution, while high fluencies and lot of pulses create particles of a very narrow unimodal distribution.

In chapter 5 the optical properties of the system AlN:Ag in various formations were studied while a correlation with the structural features was performed. The first formation consists of small Ag nanoparticles with a narrow size distribution (2-5nm diameter) into an amorphous AlN host. As a result an LSPR at 2.8eV is manifested. Thermal annealing of the as-grown samples did not cause significant changes in both the structural and optical properties. On the contrary, UV-laser annealing, at both 193nm and 248nm, led to important alterations of the films. Thus, after laser annealing Ag nanoparticle enlargement was observed and extensive diffusion was prevented. One more very important feature after laser annealing with 193nm was the partial recrystallization of the matrix around the nanoparticle leading in a significant LSPR red shift and enhancement and so, our films became spectrally selective. *This is the first time reported in the literature that inorganic films are photosensitive*.

Subsequently, we focus our study in formations produced by Magnetron Sputtering technique which meets the large-scale industrial standards. The first one was nanocomposite films, where Ag was atomically dispersed into crystalline and amorphous AlN matrix, respectively. In this case we have the simultaneous deposition of Ag and Al into Ar-N_2 mixed environment. By varying the power of the Ag electrode we managed to control the Ag concentration, while by varying the Al power we managed to control the matrix crystallinity.

The solubility limit of the Ag into AlN matrix (4% at.) was calculated by XPS analysis for the as-grown samples. This result was confirmed from the ORS measurements taking into account that sample with the lower Ag concentration reserves its transparency; while for higher Ag concentrations a different behavior is observed. In case of a-AlN:Ag (7% at.) a broad peak at around 460nm was manifested which can be attributed to LSPR. The as-grown films were first subjected to vacuum thermal annealing at 400^{o}C to 600^{o}C respectively, in Ar ambient. AlN phase was not affected from thermal annealing at both temperatures. On the contrary SEM images show Ag outdiffusion in the surface for all cases. In the case of w-AlN:Ag nanocomposite films extended Ag diffusion was observed with simultaneous nanoparticles formation providing a broad size distribution (40-310nm).On the other hand, in case the of a-AlN:Ag silver diffusion was less pronounced and Ag nanoparticles with average size 75nm was observed. The structural modification of the samples after thermal annealing led in the LSPR manifestation with a broader peak profile due to broad size distribution.

The as grown samples were subjected to UV-laser annealing with 1 pulse at 193nm and 248nm; afterwards, the structural and optical features of the samples were observed. In the case of w-AlN:Ag samples the integrity of the samples was maintained and no significant changes were observed. Unlike, for the a-AlNAg samples laser annealing increased the SPR peak in some cases.

The second formation that was studied was multilayers consisting of 20 alternating bilayers of AlN and Ag, while a final layer of AlN was deposited on the top. In this case also by varying the Al target power we managed to grow multilayers with a-AlN and w-AlN layers, while by varying the deposition time of the silver we alter the Ag layer thickness. The as grown metallic layers consist of silver particles with 5nm diameters, nonetheless they did not exhibit LSPR because they are in touch with each other. The as-grown samples were subjected to laser annealing using only 193nm wavelength with 1 and 2 pulses in air and under pressure. TEM observations show that laser annealing affect the structural features of the samples to a greater extent in case of a-AlN/Ag multilayers that w-AlN/Ag. Thus, after laser annealing subsurface transformation of the initial metallic layer to nanoparticles was observed. The formed nanoparticles exhibit a broad size distribution according to their location. So, nanoparticles of around 5nm were observed in the bottom of the film, 8-12nm in the middle of the film while approximately 25nm towards the surface of the film. On the contrary, the crystalline w-AlN/Ag multilayers seem to be affected in a lesser degree, compared to the amorphous AlN/Ag group of samples. The gradual enlargement of the nanoparticles is also observed in this group of films with nanoparticles of 3-5nm diameter being in the bottom of the sample and the larger once with approximately 20nm diameter being on the top of the sample. Finally, wurtzite w-AlN/Ag

multilayers exhibited much less roughening after laser annealing. The formation of metallic nanoparticles after laser annealing altered the optical properties of the samples since LSPR peak is manifested as it was observed from ORS measurements. The analysis of the optical measurements revealed that the LSPR peak position and intensity is related both to the laser conditions and Ag layer. *This subsurface nanostructure modification is the first time reported in the literature.*

Finally, in chapter 6 the growth of ternary $Al_{1-x}In_xN$ films and nanocomposite films $Al_{1-x}In_xN$/Ag with In composition being in the range 0% at < x≤ 18% at. was investigated. The XRD measurements of the pure ternary as grown samples revealed that polycrystalline films were grown with (002) preferred orientation while a gradual shift of the diffraction peaks from the powder values with increasing In concentration was observed. These shifts can be attributed to elastic strain in our films, which are developed due to deformation of the unit cell as the larger In atoms substitutes Al atoms in the lattice. The different In concentrations altered the optical properties of the as grown samples. Specifically, the incorporation on InN into AlN altered the band gap of the film and therefore the optical absorption which was at around 4.8 eV for 3% In while for the highest In composition a further reduction on the optical absorption at approximately 3.6 eV was observed.

The as grown samples were thermally treated at 800^{o}C for 1 hour in Ar ambient in order to avoid film oxidation. XRD measurements revealed phase segregation after thermal annealing. Moreover, In evaporation due to low melting point of In was caused from thermal annealing which altered the optical absorption in comparison to the as grown samples.

Finally, in case of nanocomposite AlInN/Ag films, Ag nanoparticles produced after hot plate annealing of thin Ag films of various thicknesses were capped with $Al_{1-x}In_xN$ with x= 7.7% at and 12.5 % at., as identified by XPS measurements. Significant structural modifications were not observed. On the contrary, the SPR peak position, intensity and variation |DR| is depended to the In concentration.

7.2 Outlook

Upon completion of this work new issues were raised which can complement the existing results of this PhD study or be the beginning of products with great scientific interesting.

- Optical properties of thin silver film laser annealing utilizing different wavelengths (532nm, 355nm, 1064nm) or pulse durations could be an interesting task. In the first case the different reflectivities of the Ag into the UV-Visible range could cause different absorption of the laser beam while in the second only electron vibrations would play role and not thermal effects. Additionally, polarization of the laser beam could also be an extra parameters to be considered in future work
- As it was mentioned above laser annealing is a very promising technique that is still has unexplored paths, such us the effect of the pressure in the laser annealing results. Although some preliminary results have been carried out, nonetheless a more extended study in required.
- In case of multilayers laser annealing using 248nm (4.99eV) wavelength could also an interesting work taking into account that only Ag will interact with the laser beam. On the contrary AlN will be totally unaffected due to higher band gap (6.2eV)
- Subsurface nanostructure modification that was presented in this study demonstrated that we could form nanoparticles from a single metallic layer. This technology could be applied in case of Al nanoparticles embedded in AlN on other nitride matrices because they are unstable, if not cap, due their fast oxidation. Thus, Ag layers could be replaced from Al once and the same procedure could be applied. Al nanoparticles have intense research interest, especially for optical encoding, due to LSPR manifestation in the UV range.
- The effect of the dielectric thickness in the particles formation could also be an interest task for future work.
- Furthermore the investigation of the smallest number of bilayers in combination with laser annealing could give an extra simplicity in this new technology.
- Finally, UV laser annealing of the ternary $Al_{1-x}In_xN$ films and the effect in the optical and structural properties could be an interesting future work.